UNIVERSITY OF COPENHAGEN

PhD thesis

Maria Thomsen

Subcutaneous injections:

Visualising and optimising device-tissue interactions

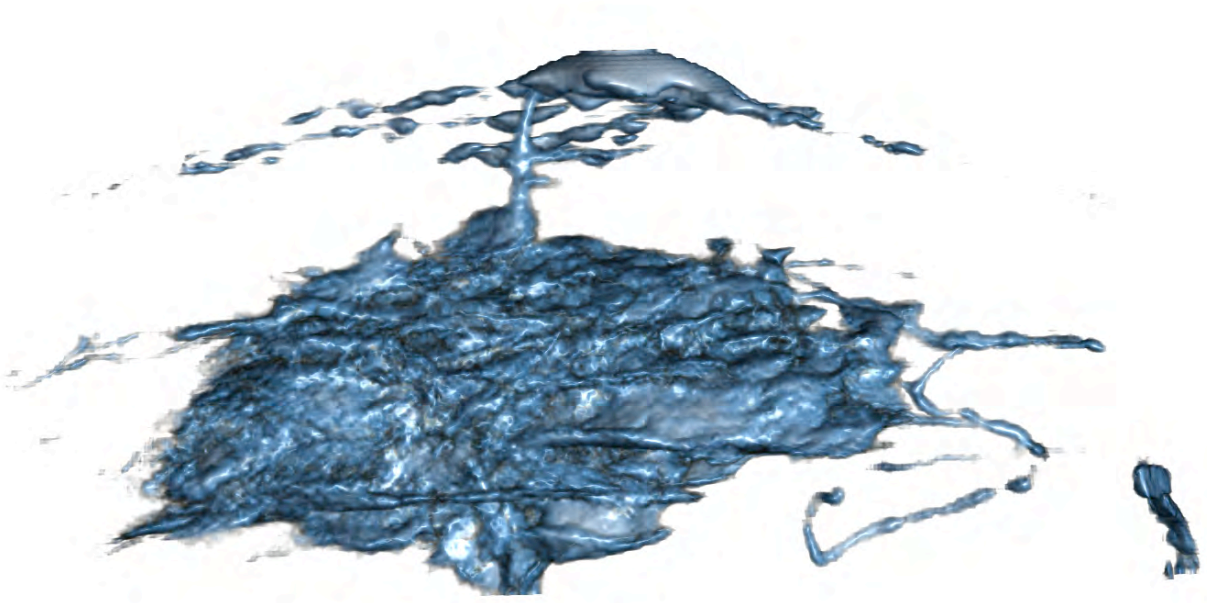

Academic advisor: Robert Feidenhans'l

Submitted: 2015/03/18

Subcutaneous injections:
Visualising and optimising device-tissue interactions

By: Maria Thomsen
Niels Bohr Institute, University of Copenhagen
Device R&D, Novo Nordisk A/A

Supervisors: Robert Feidenhans'l
Niels Bohr Institute, University of Copenhagen
Mette Poulsen
Device R&D, Novo Nordisk A/S

Submitted to: The PhD School of Science
Faculty of Science
Niels Bohr Institute
University of Copenhagen
Denmark

Font cover: X-ray tomographic reconstruction of a subcutaneous injection.

Abstract

This thesis is about visualization and characterization of the tissue-device interaction during subcutaneous injection.

The tissue pressure build-up during subcutaneous injections was measured in humans. The insulin pen FlexTouch® (Novo Nordisk A/S) was used for the measurements and the pressure build-up was evaluated indirectly from the changes in the flow rate between subcutaneous injections and air injections. This method enabled the tissue counter pressure to be evaluated without a formal clinical study approval. The measurements were coupled to a model for the pressure evolution in subcutaneous tissue, based on mass conservation and flow in a porous medium. From the measurements the flow permeability and bulk modulus of the tissue were determined.

In the adipose tissue the drug forms a bolus from where it is absorbed by the blood capillaries. The spatial distribution of the injected fluid in subcutaneous pig tissue was visualized by x-ray computed tomography. The insulin drug was represented by an iodine based contrast agent, and an experimental protocol was implemented and optimized. The tomograms provided quantitative information about the spatial drug distribution and enabled a characterization of how the drug distribution was influenced by the tissue morphology, and the injection parameters.

For *ex vivo* injections in subcutaneous pig tissue the bolus was characterized for different needle lengths, injected volumes and infusion flow rates. It was shown that the drug distribution at the injection site was influenced by the needle length and the injected volume.

Several imaging analysis tools were optimized for the characterization, and these tools were implemented also on subcutaneous injections in rats, visualized by low dose μCT, and used for characterization of the morphology in mouse tibia bone visualized *ex vivo* by high resolution μCT.

Dansk resume

Denne afhandling behandler visualisering og karakterisering af den subkutane injektionsproces.

Vævsmodtrykket, som dannes under injektion, er blevet målt for type 2 diabetikere. Vævsmodtrykket blev målt indirekte ved at måle ændringen i injectionsraten for subkutane injektioner og injektioner foretaget i luft. Målinger dannede grundlag for en model, baseret på massebevarelse og strømning i et elastisk porøst materiale. Fra målingerne kunne permeabiliteten og kompressibilitetsmodulet for vævet bestemmes.

I fedtvævet dannes et depot hvorfra insulinen diffunderer og bliver absorberet af kapilærerne. Fordelingen af insulin blev repræsenteres ved en jodbaseret røntgenkontrastvæske og den rummelige fordeling i vævet blev visualiseret vha. røntgentomografi. Røntgentomogrammerne dannede grundlag for en karakterisering af hvordan fordelingen af den injicerede væske var påvirket af morfologien i det subkutane væv og forskellige injektionsparametre.

Injektioner udført med forskellige nålelængder, injektionshastigheder og injektionsvolumener blev karakteriseret i subkutant grisevæv. Det blev vist at fordelingen af væsken i vævet var påvirket af nåle længden og det injecerede volumen.

Karakterisering blev gjort gennem anvendelse og optimering af forskellige billedanalyseværktøjer, som ogsåblev anvendt pålav-dosis μCT-tomogrammer optaget med en pre-klinisk μCT til gnavere, og til karakterisering af knoglevækst og tab. Knoglestrukturen i tibia knoglen fra mus blev karakteriseret ved højopløst *ex vivo* CT.

List of publications

Paper I

M. Thomsen, A. Hernandez-Garcia, J. Mathiesen, M. Poulsen, D.N. Sørensen, L. Tarnow, R. Feidenhans'l. *Model Study of the Pressure Build-Up during Subcutaneous Injection.* PLoS ONE (2014) 9(8): e104054. doi:10.1371/journal.pone.0104054
I participated in the design of the experiments, optimized the measuring procedure, and performed the measurements. The model calculations and manuscript were made in collaboration with HA and JM.

Paper II

M. Thomsen, E.B. Knudsen, P.K. Willendrup, M. Bech, M. Willner, F. Pfeiffer, M. Poulsen, K. Lefmann, R. Feidenhans'l. *Prediction of beam hardening artefacts in computed tomography using Monte Carlo simulations.* Nuclear Inst. and Methods in Physics Research, B (2014) 342, pp. 314-320. doi:10.1016/j.nimb.2014.10.015
I performed the experiments and designed the virtual experiment. The sample components were made by EK. I wrote the paper.

Paper III

M. Thomsen, M. Poulsen, M. Bech, A. Velroyen, J. Herzen, F. Beckmann, R. Feidenhans'l and F. Pfeiffer. *Visualization of subcutaneous insulin injections by x-ray computed tomography.* Physics in Medicine and Biology (2012) 57(21), pp. 7191-203. doi:10.1088/0031-9155/57/21/7191
I performed the experiment, made the data analysis and wrote the paper. The experiment was performed during my Master's thesis: *Inspection of subcutaneous injections by x-ray computed tomography* (Thomsen 2011). The data analysis and paper were made as a part of the PhD-project.

Paper IV

M. Thomsen, C. Rasmussen, H.H.F. Refsgaard, K.M. Pedersen, R.K. Kirk, M. Poulsen, R. Feidenhans'l. *Spatial distribution of soluble insulin in pig subcutaneous tissue: Effect of needle length, injection speed and injected volume.* European Journal of Pharmaceutical Science (submitted for internal review in Novo Nordisk A/S).
I performed the experiment, made the data analysis and wrote the paper.

Paper V

M. Thomsen, V. Andersen, C. Gunlach, M. Pedersen, A.D. Andersen, *A volumetric and morphological method for quantification of the growth plate in mice using high resolution μCT.* Journal of Bone Mineral Research (under preparation)
I performed the experiment in collaboration with CG, and made the data analysis and wrote the paper in collaboration with VA and AA.

Paper VI

M. Thomsen, M. Strobl, K. Lefmann *Neutron Imaging.* Book chapter in *Neutron Scattering: Theory, Instrumentation and Simulation* (2014) (lecture notes), University of Copenhagen.
I wrote the chapter under supervision from MS and KL.

Co-author publications

Paper VII

E. Bergback Knudsen, A. Prodi, J. Baltser, M. Thomsen, P. K. Willendrup, M. Sanchez del Rio, C. Ferrero, E. Farhi, K. Haldrup, A. Vickery, R. Feidenhans'l, K. Mortensen, M.M. Nielsen, H. Friis Poulsen, S. Schmidt and K. Lefmann. *McXtrace: a Monte Carlo software package for simulating X-ray optics, beamlines and experiments* J. Appl. Cryst. (2013). 46, pp. 679-696
I have contributed to the section about x-ray computed tomography.

Paper VIII

C.H. Rasmussen, M.M. Røge, Z. Ma, M. Thomsen, R.L. Thorisdottir, J. Chen, E. Mosekilde, M. Colding-Jørgensen. *Insulin aspart pharmacokinetics: an assessment of its variability and underlying mechanisms.* European Journal of Pharmaceutical Sciences (2014). 62(1) pp. 65-75.
I have contributed with visualization and quantification of the subcutaneous injection bolus, as input to the model established in the paper.

Acknowledgement

First I will like to thank my industrial supervisor Mette Poulsen, and my co-supervisor Dan N. Sørensen (Mechanical Engineering Support Department, Novo Nordisk A/S), and my academic supervisor Robert Feidenhans'l (Niels Bohr Institute, University of Copenhagen), for their great efforts on getting this PhD project established, and for enthusiasm and commitment along the way.

This PhD project have been co-financed by The Ministry of Science, Innovation and Higher Education, and Corporate Research Affairs at Novo Nordisk A/S. The experiments have been financed by the NEXIM project founded by The Danish Council for Strategic Research, the Mechanical Engineering Support Department (Novo Nordisk A/S), and the Insulin Pharmacology Research Department (Novo Nordisk A/S).

In the following I will appreciate all the people who have been involved in the work presented in this thesis. Without your help I would not have been able to complete this project.

Lise Tarnow and Bente Blaaholm (Steno Diabetes Center) for letting us perform measurements of the tissue counter pressure in humans.

Joachim Mathiesen and Anier Hernandez (Niels Bohr Institute, University of Copenhagen) for your valuable theoretical work on the tissue counter pressure measurements. It was of great importance and gave the measurements a higher impact for publication.

Franz Pfeiffer (Physics Department (E17) & Institute of Medical Engineering (IMETUM), Technische Universitat München) for inviting my to Munich for my first injection experiments. Thanks to Astrid Velroyen, Sebastian Ehn, Marian Willner, Julia Herzen, and Martin Bech for your help and good company during my stays.

Carsten Gundlach (Imaging Industrial Portal, Technical University of Denmark). You have made a great effort with mounting the cooling chamber and making measurements until late in the evening. Bo Schødt (SP Sveriges Tekniska Forskningsinstitut A/S) for your creative design of the sample cooling chamber for the x-ray microscope.

Anders Bjorholm Dahl, Vedrana Dahl Andersen and Hildur Einarsdottir (DTU Compute, Technical University of Denmark) for your help and great collaboration about the imaging analysis tasks. Image analysis is an important aspect of the interpretation of x-ray imaging data, and I would not have been able to made it without your help.

An number of people from Novo Nordisk A/S have been involved in the project.

Hanne Refsgaard, for your valuable discussions of the clinical aspects and relevance of my work with the subcutaneous injections, and your continuing inputs for improvements to my

paper. Karen-Margrethe Pedersen, Sanne Gram-Nielsen, Trine Porsgaard, Helle Nygaard and Hanne Gamst-Andersen for providing the research animals for our injection studies and for help during the experiments. Rikke Kaae Kirk and Susanne Juul Rasmussen for providing histological images.

Christian Hove Rasmussen, who was a former employee in the Oral Biophysics & Preformulation tema (Novo Nordisk A/S). I am your deeply grateful for your commitment to my work. You have introduced my to a lot of people in Novo Nordisk A/S, and pushed my project forward. Morten Colling-Jørgensen for being the "devil's advocate" against my work. I should have gained a higher benefit of your knowledge.

Maj Pedersen for involving me in the implementation of the new preclinical μCT scanner in your departments.

I have enjoyed being part of the fantastic department Mechanical Engineering Support at the Device Research and Development Department, Novo Nordisk A/S. It have been a pleasure to be at a place of work with such a good spirits, and I am going to miss your all.

Ulrik Ullum, my team leader for providing me a great professional and personal support, specially at the hard times. Dorrit Eggert, you are always willing to help and I always became happy in our company. Lennert Berggen and Bo Bøgelund Pedersen for designing the motor driving injection device. Emil Vosmar Denning for proofreading several pages for this thesis. It is highly appreciated.

Not all experiments produced publishable results or could be carried through, but still effort was but into the experimental work.

Simon Bjerregaard (Novo Nordisk A/S) for preparation of the oral drug formulations. Anders Elias and Henrik El Ali (Faculty of Health, University of Copenhagen) for your help with *in vivo* CT-scan and MR-imaging of oral drug delivery in rodent.

Hassina Bilheux and Ian S. Anderson (Oak Ridge National Laboratory, Tennesee US) for offering me the opportunity to perform neutron imaging on tissue samples. Unfortunately the necessary visa could not be obtained and therefore the stay could not be realized.

At the University of Copenhagen I have enjoyed the company from my fellow students. Torsten Lauridsen, for your assistance during a number of experiments and help with many problems along the way, and Mikkel Schou Nielsen for great discussions and for establishing an imaging study group with valuable knowledge sharing.

Finally I will express my gratitude to my family for their lasting support. Specially Morten, for your indispensable support and love during the ups and downs along the way.

Maria Thomsen
Copenhagen, March 2015

Contents

Abstract **v**

Dansk resume **vii**

List of publications **ix**

Acknowledgement **xi**

1 Introduction **1**
1.1 General motivation 1
1.2 Problem statement 4
1.3 Background 5

2 Tissue pressure build-up **11**
2.1 Experimental design 13
2.2 Order of magnitude of tissue counterpressure 22
2.3 Presentation of Paper I 23
2.4 Summary 28
2.5 Outlook and applications 29

3 Visualization of subcutaneous injections **31**
3.1 Sample preparation 32
3.2 X-ray imaging 34
3.3 Summary 44

4 X-ray computed tomography **45**
4.1 Computed tomography 45
4.2 Presentation of Paper II 51
4.3 Presentation of Paper III 56
4.4 Results 58
4.5 Dual energy tomography 65

5 Drug distribution in subcutis **67**
5.1 Experimental procedure . . . 67
5.2 Segmentation and characterization . . . 71
5.3 Presentation of Paper IV . . . 78
5.4 Summary . . . 83
5.5 In vivo visualization . . . 84
5.6 Outlook and applications . . . 86

6 Bone morphology **89**
6.1 Experimental procedure . . . 90
6.2 Segmentation and classification . . . 91
6.3 Preliminary results to Paper V . . . 92
6.4 Further work . . . 94
6.5 Summary . . . 94

7 Summary **95**
7.1 Outlook . . . 97

A Image Analysis **113**
A.1 Markov Random Field Segmentation . . . 113
A.2 Learning Dictionaries of Discriminative Image Patches . . . 116

B Publications **121**

Chapter 1

Introduction

This thesis is based on an industrial PhD project, a collaboration between the Device Research and Development Department (DRD), Novo Nordisk A/S, and the Niels Bohr Institute, University of Copenhagen. Novo Nordisk A/S is a global healthcare company with innovation and leadership in diabetes care. Diabetics are treated by insulin drug formulations injected in the fat tissue under the skin, called subcutis. From there the drug is absorbed into the blood stream and distributed around the body. Novo Nordisk A/S produces and develops insulin drug formulations and injection devices.

The scientific target of this project is to characterize properties of subcutaneous injections as function of device parameters (e.g. dose size, delivery rate and needle dimensions). The commercial target is to develop a visual and quantitative analysis tool, which can be used to improve existing, and design new drug delivery systems. This thesis is written as a synopsis, giving an introduction to, and presenting the results from, the attached scientific papers. The necessary theoretical background for each topic is included, such that the content can be understood by a broad range of scientists in the pharmacy industry.

This first chapter provides a brief motivation for the project, leading to the problem statements and the outline of the thesis. The last section in this chapter gives an introduction to diabetes and a review of the existing methods used to evaluate the effect of new insulin drug formulations and visualize the injection bolus.

1.1 General motivation

Insulin was for the first time extracted from a dog's pancreas by Frederick Banting in 1921, and just a year after a 14 old boy was successfully treated with a subcutaneous insulin injection (Banting et al. 1922). Diabetics lack the ability to produce sufficient insulin, and therefore suffer from a chronic elevated blood glucose level (Poretsky et al. 2010, Skyler 2012). A chronic exposure to a high blood glucose level leads to damage to the blood vessels and can give long term complications such as cardiovascular disease, stroke, and peripheral vascular disease. In healthy people, insulin is secreted from the pancreas as a response to the elevated blood glucose level after a meal.

Figure 1.1 (A) shows the blood glucose concentration (top) and insulin concentration (bottom) during a day for a healthy subject (Owens 2002). Diabetics are treated by several insulin drug formulations, in order to obtain a good glycemic control. Today insulin is produced by recombinant DNA technology, and the insulin molecule has been modified to optimize the therapy (Owens et al. 2001, Heller et al. 2007). The drug formulations range from fast acting drugs taken in connection with meals, to long acting drugs taken once a day to keep a stable blood glucose level, shown in Figure 1.1 (B) (Hirsch 2005, Nolte 2009). Insulin taken orally is broken down by the gastric acid. To avoid this, the drug is injected into the subcutaneous fat tissue beneath the skin as shown in Figure 1.1 (C).

The absorption and action of many insulin formulations are associated with a considerable variability, both from patient to patient, but more importantly from injection to injection for the same patient (Heinemann 2002, Gin & Hanaire-Broutin 2005, Guerci & Sauvanet 2005). It means that patients cannot be certain to experience the same effect of similar injections. The effect of the insulin injection is known to depend on several factors, and some of those are related directly to the injection site and the injection process (Ogston-Tuck 2014). It has been shown that the absorption time depends on the injection site and depth (Frid & Linde 1992, Bantle et al. 1993, Rave et al. 1998, Karges et al. 2005, Gupta et al. 2011), the local subcutaneous blood flow and skin temperature (Vora et al. 1993, Cengiz et al. 2014, Pfützner et al. 2015). The variability is normally described in terms of the coefficient of variability ($CV = \frac{\text{std}}{\text{mean}}$) for different end-points, such as the maximum insulin blood concentration ($C_{\max}$), the time to reach $C_{\max}$ ($t_{\max}$) or the total insulin absorption, given by the area under the plasma insulin curve (AUC) (Heinemann 2008, Vora & Heise 2013). For fast acting insulin formulations CV of AUC is of the order 15-25% for the same patient, and 20-45% among patients (Heinemann 2008). This variability can lead to an unattended lowering of the blood glucose level, which can have severe consequences, such as cramp, paralysis, and unconsciousness (Holt et al. 2011).

A well controlled treatment starts with an accurate delivery of the drug, which was significantly improved by the introduction of the insulin pump in the 1970s and the insulin pen in 1985 (Selam 2010), as an alternative to the syringe. The insulin pen and pump have improved the convenience for the patient (Lajara et al. 2012), but still the patients deal with multiple daily injections, the fear of injection pain (Zambanini et al. 1999), and needle-phobia (Mollema et al. 2001). In worst case the trouble and fear can cause the patients to skip their injections (Peyrot et al. 2010, Farsaei et al. 2014). Therefore, some of the challenges in the design of injection devices include a reduced needle length, minimized injection pain during injection, and increased dose size to reduce the number of injections the patients need to take.

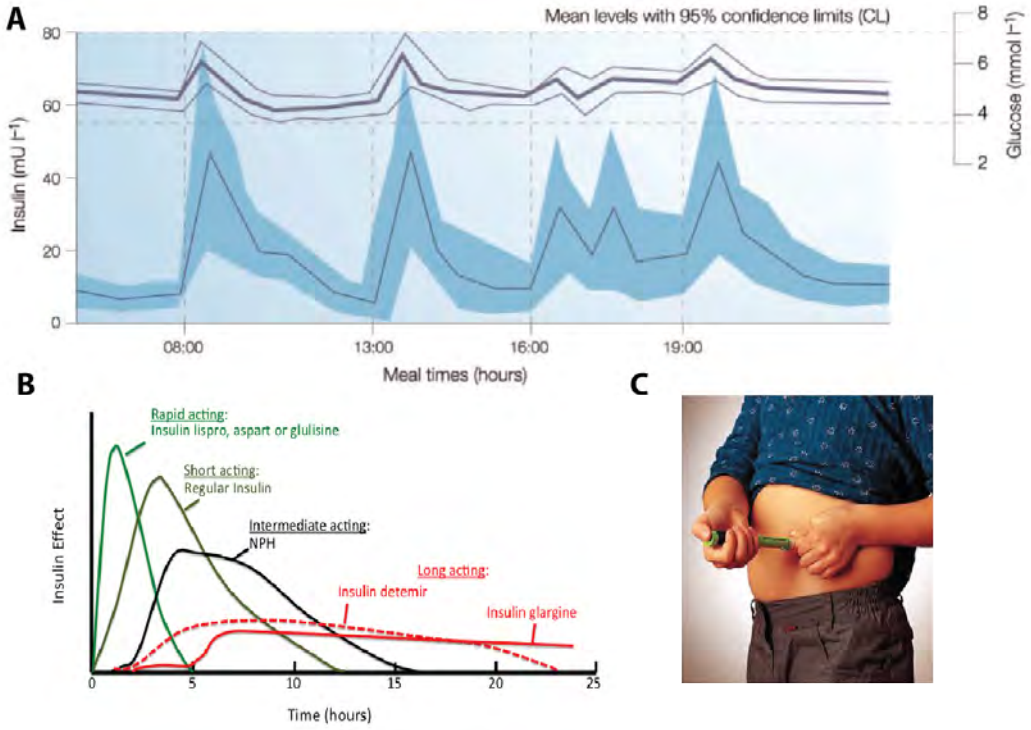

Figure 1.1: *(A) Daily variation in the plasma glucose (top) and insulin level (bottom). The figure is adapted from Owens (2002). (B) Illustration of the plasma insulin concentration as function of time for different insulin drug formulation. The figure is adapted from Nolte (2009). (C) Subcutaneous insulin injection by an insulin pen.*

1.2 Problem statement

Motivated by the challenges of insulin device development and importance of the injection technique in insulin therapy, this thesis will focus on the injection process and the drug distribution in subcutis for different injection parameters. The glucose lowering effect related to different injection techniques will not be considered. The project aims to develop methods to quantify the pressure build up during subcutaneous injections and the injection bolus formed in the tissue. The following three problems are considered:

Problem 1: Tissue Counterpressure

For injection devices, either pens or pump systems, the injection force delivered by the device must overcome both the resistance in the injection system and the resistance in the body tissue against deformations caused by the injected drug. High tissue resistance can have consequences for the treatment if e.g. the device is unable to deliver the full dose or leakage of drug from the needle insertion site is increased. The goal was to implement a non-invasive method to study the pressure build up in humans under standard injection conditions.

Problem 2: Visualization of subcutaneous injections

Preclinical tests of injection devices are performed in research animals, such as rodents and pigs. The goal was to develop a technique to visualize the injection bolus in subcutaneous pig tissue, in order to quantify the drug distribution and its variability. The visualization method was based on x-ray computed tomography (CT) using a commercial x-ray microscope, such that the method can be implemented in DRD.

Problem 3: Tissue-device interaction for different injection parameters

In device development the aim is to improve the drug absorption and patient convenience by adjusting the needle length, injecting larger volumes, and adjusting the injection speed. Here the goal was to quantify the drug distribution for injections performed in subcutaneous pig tissue for different injection parameters.

1.2.1 Thesis outline

The thesis is structured as follows: The remaining part of this chapter presents a description of the subcutaneous tissue, and gives a review of the existing methods used to evaluate both the injection bolus, the absorption from the injection site, and the glucose lowering effect of insulin drug formulations.

Chapter 2 presents a non-invasive method to evaluate the pressure build up during a subcutaneous injection. The measurements will be coupled to a model for the pressure build up, based on flow in a porous elastic media. The model is used to estimate the order of magnitude of the permeability and elasticity of adipose tissue in humans. The chapter is based on Paper I.

The first part of chapter 3 gives an overview of the structure of the skin and the subcutaneous fat tissue, for pigs and rats, which are the preclinical models used in the experiments presented in chapter 4 and 5. Furthermore, the injection procedure and preparation of the tissue biopsies is summarized. The second part of the chapter provides the theory behind x-ray absorption computed tomography, including a discussion of the use of contrast agents and limiting factors on the spatial resolution in x-ray radiography.

Chapter 4 presents the experimental considerations concerning visualization of subcutaneous injections using a commercial x-ray microscope. Polychromatic and monochromatic measurements will be compared in order to evaluate how the visualized drug distribution is effected by the spatial resolution, signal-to-noise ratio and beam hardening artefacts. The presented results are based on Paper II and III

Chapter 5 presents a segmentation and analysis protocol for quantification of subcutaneous insulin injections performed by different injection parameters, including flow rate, volume and needle length in pig subcutaneous tissue. In the end of the chapter analysis tools will be applied to injections performed in rat tissue, and visualized by a preclinical μCT for rodents. This heads toward an *in vivo* application where the observed drug distribution can be linked to the clinical effect of the drug. The results are based on Paper IV.

During the project the visualization method has found interest in other research areas in Novo Nordisk A/S. Chapter 6 presents a study of the morphology of the mouse tibia bone visualized by μCT, and its dependence on the scan resolution. The results are based on Paper V.

The thesis has resulted in five papers and a book chapter. Paper I-IV and the book chapter are included in their full length in Appendix A. The book chapter is a part of the book "Neutron Scattering: Theory, Instrumentation and Simulations" by Kim Lefmann and deals with neutron radiography and tomography, and its applications. The papers are referred to by roman numerals. Paper I-III have been published, while Paper IV have been submitted for internal review in Novo Nordisk A/S and Paper V is under preparation. The thesis contains most of the work presented in the publications.

1.3 Background

The following section is divided into three parts. The first part provides a brief introduction to diabetes mellitus. The second part gives an overview of the structure of subcutaneous tissue, the chemistry of the insulin in subcutis, and its influence on insulin absorption. The last section present a review of the existing methods used to evaluate the effect of insulin drugs, and visualization of the injection bolus. The benefits and limitations of each method will be discussed.

1.3.1 Insulin and diabetes mellitus

Insulin is a hormone produced in the β-cells in the pancreas and is released to the blood stream as a response to a high blood glucose level (Holt et al. 2011). The insulin is distributed around the body, where it binds to the insulin receptor on the surface of the cell membrane. The activation of the insulin receptor causes the glucose transporter protein to bind to the cell membrane and the glucose uptake is increased. Glucose is essential in the protein and fatty acid synthesis in the cells (Skyler 2012). In the liver glucose can be stored as glycogen. When the blood glucose level decreases the liver releases glucose and the fat cells release fatty acids, which are used in the protein synthesis.

Diabetes is a disease in continuous growth, estimated by WHO to affect about 350 million people worldwide in 2011 (Danaei et al. 2011). The diabetic patients can primarily be divided into two groups; type 1 and type 2 (Holt et al. 2011, Poretsky et al. 2010). Type 1 diabetic patients lack the ability to produce insulin due to an autoimmune disease, which destroys the β-cells in the pancreas. Type 2 diabetic patients have decreased insulin sensitivity (insulin resistance), sometimes combined with reduced insulin production. The insulin resistance can be caused by a persistent exposure to high insulin blood concentrations, which leads to a down-regulation in the number of insulin receptors.

Weight loss and dehydration are two symptoms of diabetes (Holt et al. 2011), because an insufficient production of insulin or insulin resistance causes a persistent breakdown of fatty acids. The level of glucose stays high in the blood and becomes excreted in the urine, which causes the production on urine to increase (Berg JM 2002).

Type 1 diabetes typically has its onset in the childhood, while type 2 diabetes is developed gradually, often related to obesity and has its typical onset in adult life. Type 2 diabetes accounts for about 90% of all cases of diabetes (Holt et al. 2011).

1.3.2 Subcutaneous injections

The subcutaneous compartment is used for the delivery of insulin drugs. The capillary absorption is delayed and thereby the dose is spread over a longer period of time, which resembles the normal situation in which insulin is gradually released from the pancreas. Furthermore the subcutaneous route is more convenient for self-administrated drugs, and does not demand the same high level of sterility as intravenous injections (Stoner et al. 2014).

Structure of subcutis

The subcutaneous fat layer is located beneath the skin. The skin comprises two layers; epidermis, and dermis, shown in Figure 1.2 by a schematic illustration (A) and in a histological image of subcutaneous pig tissue (B). The subcutaneous tissue is separated from dermis above and the muscle tissue below by layers of connective tissue, called fascias. At the neck of the pig and in some areas of the body in humans (e.g the upper arm and thigh), the subcutenaous layer is also divided by a fascia (B) (Nakajima et al. 2004). The subcutaneous fat layer is mainly composed of two components; adipose tissue and interstitial tissue, shown in Figure 1.2 (C) (Agache & Humbert 2004). The interstitial tissue is placed between the adipocytes and consists mainly

of a fibre framework made of collagen (Aukland & Reed 1993, Agache & Humbert 2004). The insulin drug distributes in the extracellular space between the fat cells, and is absorbed by the blood capillaries that run between the lobules.

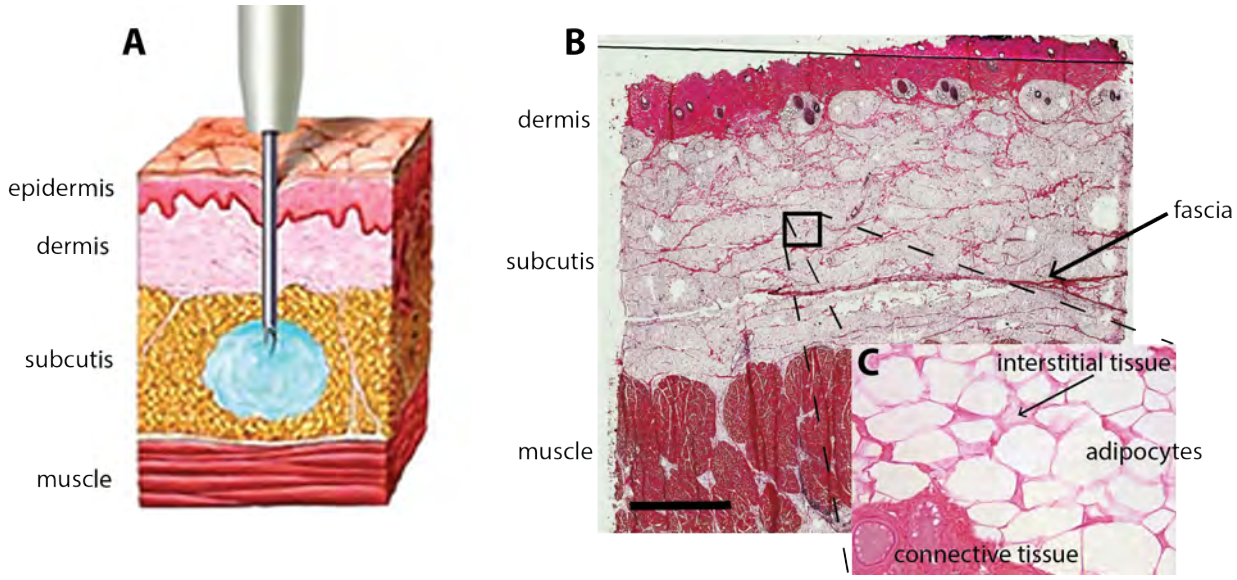

Figure 1.2: *(A) Schematic illustration of the human skin, subcutaneous fat layer and the muscle tissue. Insulin is injected into the subcutaneous fat layer. Figure is adapted from Ogston-Tuck (2014). (B) A histological cross section of the skin, adipose tissue and muscle tissue from the neck of the pig. The scale bar is 5 mm. (C) Zoom-in on the fat cells in the adipose tissue. The image is provided by Rikke Kaae Kirk from Histology & Imaging (Novo Nordisk A/S).*

Chemistry in subcutis

In solution, human insulin exists in a mutual equilibrium between the oligomers (hexamers, dimers and monomers)(Brange 1994, Søeborg et al. 2009), shown in Figure 1.3. Commercial insulin drug formulations contain zinc and phenol/metacresol to favour the hexameric form, since the hexamers are stable, and therefore appropriate for storage (Brange & Langkjaer 1992). In subcutis the auxiliary substances diffuses away from the injection site, and the hexamers self-associate and a chemical equilibrium between the oligomers is established.

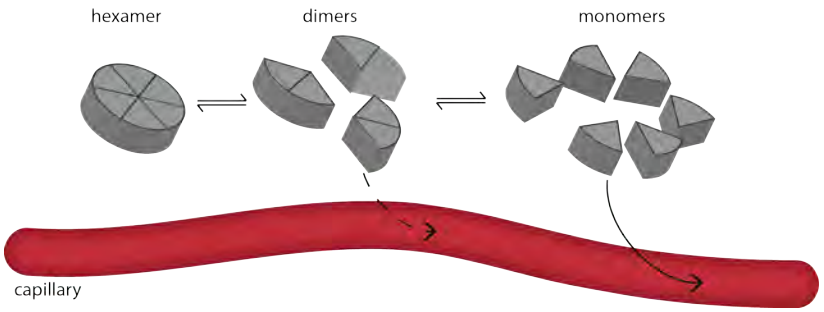

Figure 1.3: *Illustration of the insulin oligomers in mutual equilibrium and absorption of the dimers and monomers to the blood stream.*

From the subcutaneous injection site, small molecules (<15 kDa) can reach the systemic circulation through the blood capillaries, while larger molecules are expected to be absorbed by the lymphatic vessels (Porter & Charman 2000, Richter et al. 2012). Insulin hexamers, dimers, and monomers have a molecular weight of 36 kDa, 12 kDa and 6 kDa, respectively. This means that monomers and dimers are absorbed by the blood capillaries, while hexamers are thought to enter the systemic circulation primarily via the lymphatic vessels (Charman et al. 2001). Only limited absorption takes place via the lymphatic system (Kurtzhals & Ribel 1995), hence insulin absorption is controlled by the absorption rate of the insulin monomers and dimers. The higher the fraction of monomers and dimers at the injection site, the faster is the absorption (Kang et al. 1991). As the insulin concentration at the injection site decreases, the chemical equilibrium will be shifted towards monomers. Thus, lower the insulin concentration in the injected formulation will give rise to faster absorption. This has been confirmed experimentally by Hildebrandt et al. (1983). To give a faster absorption the insulin molecule has been modified in order to reduce its tendency to form dimers and the chemical equilibrium is shifted towards the monomers. One example of this is the fast acting insulin analogue insulin Aspart (IAsp). The insulin absorption for IAsp is compared to that of human insulin in Figure 1.1 (B).

1.3.3 Studies of insulin injections

Pharmacokinetic (PK) and pharmacodynamic (PD) studies are the standard way to evaluate the effect of new insulin drug formulations. In PK-studies the plasma insulin are measured in a time period after the injection is given and gives informations about the absorption of insulin drug from the injection site. In PD-studies are the blood glucose concentration measured, and gives information on the action of the drug. The advantages of these methods are that presence of insulin in plasma and the effect of insulin drug is measured directly. The limitation is that the measurements provide no information about the underlying mechanisms related to the observed effect.

The absorption process has been evaluated directly by radioactive labelling of the insulin molecule. The absorption rate is obtained by measuring the remaining radioactivity at the injection site as function of time. This method has been used to study the variabilities in the absorption process, and correlate the absorption rate with the subcutaneous blood flow (Moore et al. 1959, Lauritzen et al. 1980, Vora et al. 1992, 1993). The method requires that the absorption rate for labelled and non-labelled insulin correlates, which has been validated for human insulin in pigs (Deckert et al. 1982). However, for IAsp, the labelling of the insulin molecule changes the absorption kinetics in pigs (Sohoel et al. 2007). Therefore the method can be hard to implement for new insulin formulations.

Bio-mechanistic modelling

One way to achieve a better understanding of the processes involved in subcutaneous absorption, and distribution of drug to the body tissue, is a quantitative and mechanism-based approach. Several mathematical models have been proposed for the PK of insulin formulations (review by Nucci & Cobelli (2000) and Kagan (2014)). One example is a three compartment model for IAsp (Mosekilde et al. 1989, Rasmussen et al. 2013). The model consists of the extracellular

space in subcutis, the plasma, and fluid volume between the cells in the body tissue (interstitium), illustrated in Figure 1.4. The models are semi-mechanistic, meaning that they do not incorporate all mechanisms contribution to the pharmocokinetic effect. They are used to analyse preclinical and clinical data in the light of the physiological and chemical processes in the body, and enables systematic investigations the pharmacokinetic effect of e.g the self-association properties of the drug, subcutaneous blood flow, and the insulin receptor affinity (Rasmussen et al. 2013).

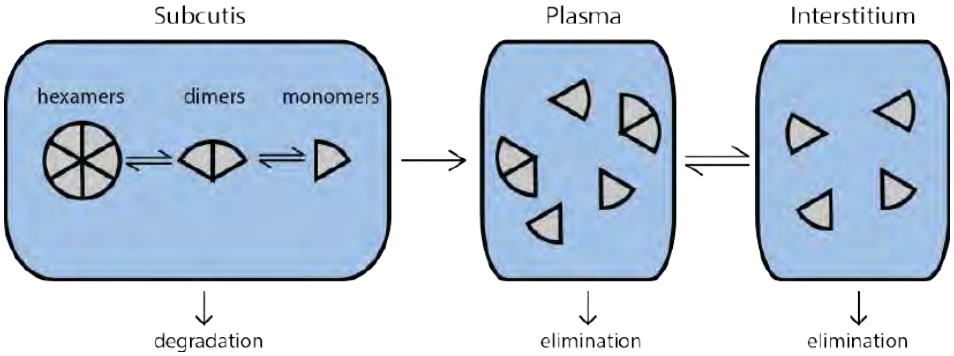

Figure 1.4: *Semi-mechanistic model for IAsp proposed by Rasmussen et al. (2013). The insulin hexamers self-associate to dimers and monomers, which are absorbed to plasma. In plasma the insulin monomers are either eliminated or absorbed by the interstitium.*

Visualization of the injection bolus

The injection bolus has been visualized for *ex vivo* injections of insulin mixed with a food colorant in adipose pig tissue. The tissue biopsies including the injection site was snap frozen, cut into thin slices and a digital image was taken of each slice (Jockel et al. 2013). The collection of the slices gives the overall shape of the injection bolus, an example is shown in Figure 1.5 (A). *In vivo* ultrasound measurements have been used to study the injection depth and evaluate if the injections were placed intradermally, subcutaneously or intramuscularly. In these studies the drug was either visualized directly (Polak et al. 1996), or the insulin injection was replaced by an air injections to improve contrast (Hofman et al. 2010, 2007).

Histology and light-sheet laser scanning microscopy can be used to visualize the drug distribution at micrometer resolution. In a histological study the tissue samples are sectioned into thin slices with a thickness of about 20 μm. The tissue is dried and the insulin is visualized directly with cellular resolution. Histology is mainly used to study inflammatory responses of insulin injections (Markussen et al. 1996). With a light-sheet microscope the insulin drug distribution can be visualized in 3 dimensions (3D). The insulin molecule is labelled with a fluorescence marker, and the tissue structures are cleared in chemical substances (Ertürk & Bradke 2013, Ertürk et al. 2012). An example of a 20 μL depot is shown in Figure 1.5 (B). The advantage is that both the insulin molecule and blood capillaries can be marked directly and visualized in 3D. A disadvantages is that the clearing alters the chemical composition of the tissue structure and the different tissue layers can not the distinguished. Another limitation is that the sample size can not be bigger than about $10\times10\times10$ mm^3. Since the insulin is distributed among the

fat cells, this sample size corresponds to an injected volume of about 20-30 µL. In humans the recommended dose depends on body weight, blood glucose level and insulin sensitivity, and can be up to 500-800 µL per injection.

This work aims to develop a visualization method based on x-ray computed tomography as a supplementary technique. The advantages and limitations of this method will be discussed in chapter 3-4.

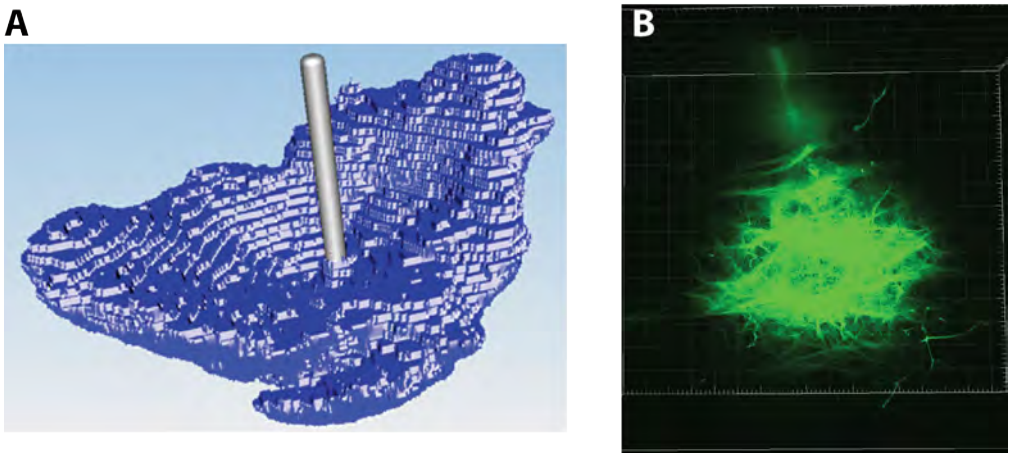

Figure 1.5: *(A) Digital images processed to visualize the 3D shape of the injection bolus. Figure adapted from Jockel et al. (2013). (B) Insulin monomer marked with the fluorophore Vivotag750S and injected in porcine fat tissue. The depot is visualized by a light-sheet microscope. The image is provided by Torben Seested Johansen from the Imaging Team (Novo Nordisk A/S). The scalebars were not provided for the images.*

Chapter 2

Tissue pressure build-up

This chapter presents the study of the pressure build-up during subcutaneous injections in humans. The chapter is divided into two parts. In the first part a non-invasive method is evaluated and used to given an order of magnitude of the pressure build-up in humans. The second part serves as an introduction to Paper I *"Model Study of the Pressure Build-Up during Subcutaneous Injection"* (Thomsen et al. 2014). In the paper we establish a model for the pressure build-up based on mass conservation and flow in a porous elastic media. The measurements from the human study are used to estimate the flow permeability and bulk modulus of the tissue.

The insulin infusion rate is driven by the mechanic components in the device for insulin pump systems and some insulin pens. To ensure that the full dose is injected, the force delivered by these injection devices must overcome both the resistance in the injection system and the resistance in the body tissue against the deformations caused by the injected drug. The second contribution is in the following referred to as the tissue counter pressure.

It has been shown previously that the counter pressure in subcutis increases from about 8 mbar to 60 mbar for infusion rates from 0.16 μL/s to 8.3 μL/s for saline water (Patte et al. 2013). This infusion rate is common for insulin pump systems, while insulin pens deliver the drug with an infusion rate of about 100 μL/s (Pearson 2010). A study performed on Götting minipigs (Allmendinger et al. 2014) showed that the injection force increases linearly with the infusion rate and drug viscosity for infusion rates between 2.5-200 μL/s and drug viscosities between 1-100 mPas.

Figure 2.1(A) shows an example of the injection force for an injection with a constant infusion rate of 100 µL/s in adipose pig tissue. The injection is performed right after the pig has been put down. The pressure was measured by a syringe pump mounted with a force sensor. After the needle has penetrated the tissue (green circle) the injection force is almost at a constant level (red arrow), which suggests a steady state situation, where the drug can diffuse away from the injection site fast enough to maintain a constant pressure level. After the needle is removed the injection force drops (yellow ellipse and green arrow). The histological cross section of a similar injection (B), shows that the insulin is distributed among the fat cells, and no bruising in the tissue structures is observed.

Conducting a study of the counter pressure in humans using a syringe pump requires a clinical study approval, which is hard to obtain and very expensive. Therefore we aim to develop a method that can be implemented without any clinical study approval. Section 2.1 provides a description of the injection device used for the study and the experimental method, followed by a discussion of the sensitivity of the method. Section 2.2 presents the measurements of the tissue counter pressure in humans, and in section 2.3 are the measurements coupled to the model for the pressure build-up.

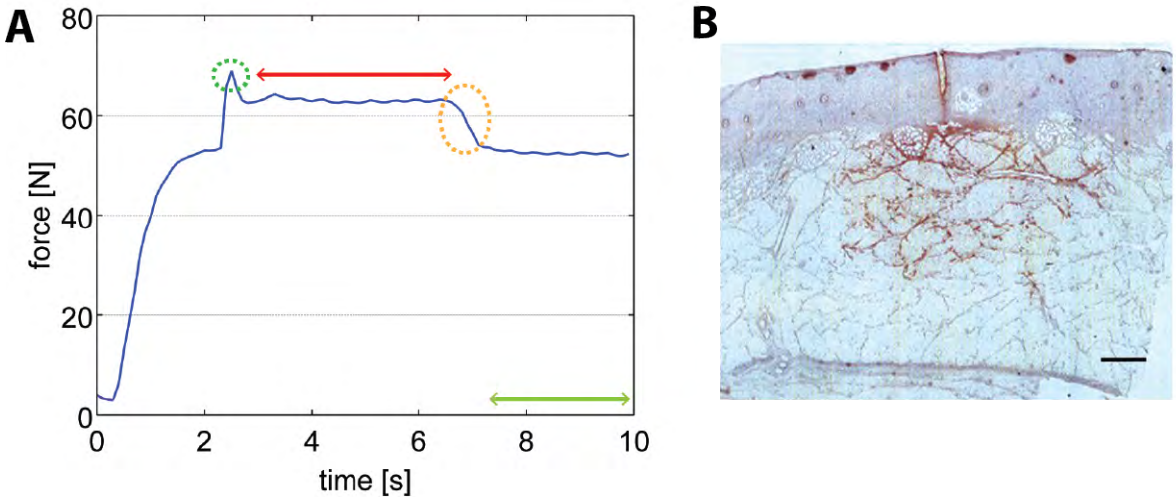

Figure 2.1: *(A) The infusion pressure measured in adipose pig tissue ex vivo for an injection speed at 100 µL. The injection is performed in the belly of the pig. The first and last part of the signal (green arrow) is the acceleration force of the device and injection force in air, respectively. After the penetration force (green circle) the injection force reaches an almost constant level (red arrow). After the needle is removed from the tissue the device components relax (orange ellipse). (B) Histological image of a similar injection of 100 µL of IAsp in adipose pig tissue, visualized by H& E staining. The scalebar is 2 mm. The histological image is adapted from Paper I.*

2.1 Experimental design

The method is based on the commercial injection device FlexTouch® (Novo Nordisk A/S), shown in Figure 2.2 (A). For this device the injection force is delivered by a torsion spring and an audio click signal is emitted for each 10 μL of injected drug, as shown in Figure 2.2 (B) (blue curve). This means that the flow rate can be estimated indirectly by recording the click signal (red curve). The flow rate for a given applied injection force is determined by three factors:

1. Device parameters: Needle dimensions, penfill dimensions, and internal friction forces.

2. Drug solution: Viscosity and density

3. Tissue counter pressure

By assuming that both (1) the device parameters, and (2) the drug solution is unchanged when performing an injection in air and subsequently performing an subcutaneous injection in humans, the tissue counter pressure can be deduced from the change in flow rate.

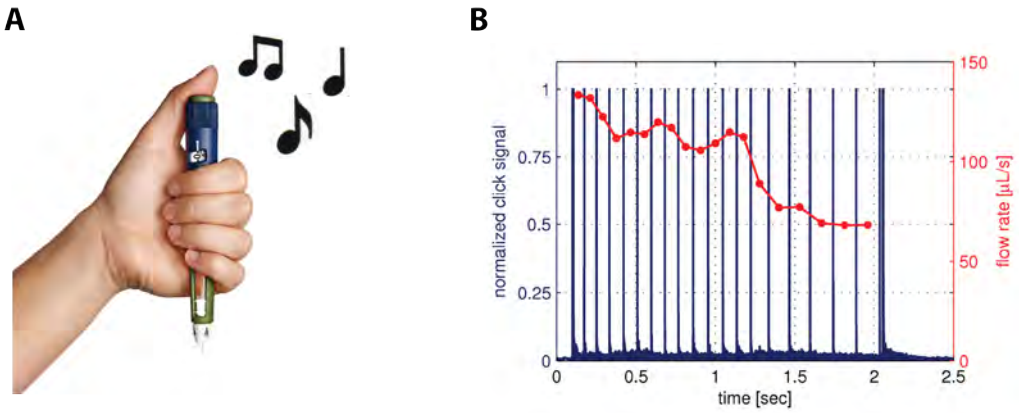

Figure 2.2: *(A) The insulin pen FlexTouch® (Novo Nordisk A/S). (B) Example of the audio click signal emitted when the drug is injected (blue curve). The device emits a click signal for each 10 μL of drug that have been injected, which means that the flow rate (red curve) can be estimated.*

By this technique the pressure build-up can be evaluated under normal injection conditions, without any modification of the injection device. The draw back is that the infusion rate can not be controlled and the spring force decreases during the injection, which means that the flow rate is not constant during the injection. Another limitation is that the pressure build-up is measured indirectly. This influences both the pressure sensitivity and the uncertainty of the measurement, which will be discussed in the following sections.

In Denmark FlexTouch® is currently marketed with the fast acting insulin analogue NovoRapid® (IAsp), and in other countries the device is on sale with other insulin formulations. An experimental method based on this device can be adapted as a tool in DRD to evaluate the device performance under clinical settings.

2.1.1 Mechanics of the injection device

In this section the relation between the measured flow rate and the tissue counter pressure is established. For clarity all variables and constants used are listed in Table 2.1, and defined when they are introduced in the text. The numerical values are given with the units used in the formulas. Variables not given by numerical values in the table are determined individually for each device and needle. Figure 2.3 shows a schematic drawing of the device. When the patient dials an insulin dose, a torsion spring is tightened. The spring is released by pressing a button, and the rubber piston in the penfill is moved from the initial position (d_0) to position the (d). The injection is driven by the pressure drop $P_{\text{in}} - P_{\text{out}}$ across the needle.

Needle radius	r_n	– [m]
Flow rate	Q	– [m^3/s]
Enhance flow velocity	U_0	• [m/s]
Kinematic viscosity	ν	$1.004 \cdot 10^{-6}$ m^2/s (20°C)
Dynamic viscosity	η	$1.002 \cdot 10^{-3}$ Pas (20°C)
Pressure at the needle inlet	P_{in}	– [Pa]
Pressure at the needle outlet	P_{out}	– [Pa]
Drug density	ρ_f	1000 kg/m^3
Needle length	L	0.0164 m

Table 2.1: *Variables introduced in the this section related to the injection device and injected drug. Numerical values not given are individual parameters for each insulin pen and needle.*

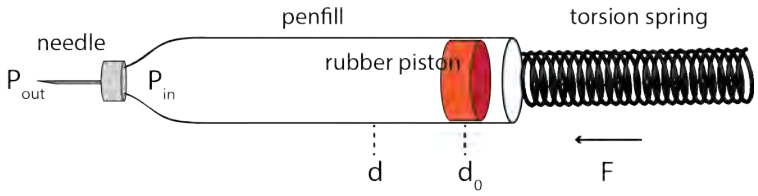

Figure 2.3: *Schematic representation of the injection device. During injection the rubber piston is moved by the spring force (F) from its initial position d_0 to d. A pressure drop is created across the needle. The figure is adapted from Paper II.*

For flow in cylindrical pipe the Reynolds number is given by

$$Re = \frac{2Q}{\nu r_n} \tag{2.1}$$

where Q is the flow rate, and ν is the kinematic viscosity. The insulin drug consist mainly of water, and the flow properties will be taken to be the same as for water. An insulin pen needle has a needle gauge between 30G-32G [1], which correspond to a nominal inner radius r_n $0.080 - 0.054$ mm. A flow rate 100 µL/s gives that $Re \approx 1000$, meaning that the flow in the needle can be considered laminar (Lautrup 2011).

[1] The outer diameters of hypodermic needles are described by gauge numbers. Smaller gauge numbers indicate larger outer diameters. The inner diameter depends on both gauge and wall thickness

The total pressure drop across the needle is given by (adapted from supplementary information to Paper I)

$$P_{\text{in}}(t) - P_{\text{out}}(t) = \frac{8\eta L}{\pi r_n^4} Q(t) + \frac{1.01\rho_f}{\pi^2 r_n^4} Q^2(t) \tag{2.2}$$

where ρ_f is the drug density, and $Q(t)$ is the flow rate as function of time. The first term at the right hand side corresponds to the pressure drop for a fully developed laminar flow in a pipe, given by the Hagen-Poiseuille law (Lautrup 2011). The second term arises because fluid inertia is not negligible in the entrance region of the needle. In the entrance region the fluid particles near the axis of the needle are accelerated, which is illustrated in Figure 2.4.

At the needle inlet the flow profile of the drug is constant with the velocity $U_0 = \frac{Q}{\pi r_n^2}$. Due to friction force exerted on the fluid particles from the needle wall, the particles near the wall will gradually slow down. Owing to mass conservation the velocity of the particles near the axis of the needle will increase and a parabolic flow profile will be established. The layer in which the velocity of the particles are reduced are called the boundary layer, denoted by δ in Figure Figure 2.4. The entrance length, L_e, is the distance down the needle at which $\delta(L_e) = r_n$ (Lautrup 2011). For the full derivation of the expression for L_e the reader is referred to the supplementary information to Paper I. The entrance length for the needle is given by

$$L_e \approx 0.228 \frac{U_0 r_n^2}{\eta} \tag{2.3}$$

where η is the dynamic viscosity. This expression is only valid for the high Reynolds number, and in good agreement with previous calculations (White 1991).

For a needle gauge of 31G ($r_n \sim 0.065$ mm) and flow rate of 100 µL/s the entrance length $L_e \sim 7$ mm. Since the full needle length $L = 16.4$ mm, the additional pressure drop must be taken into account.

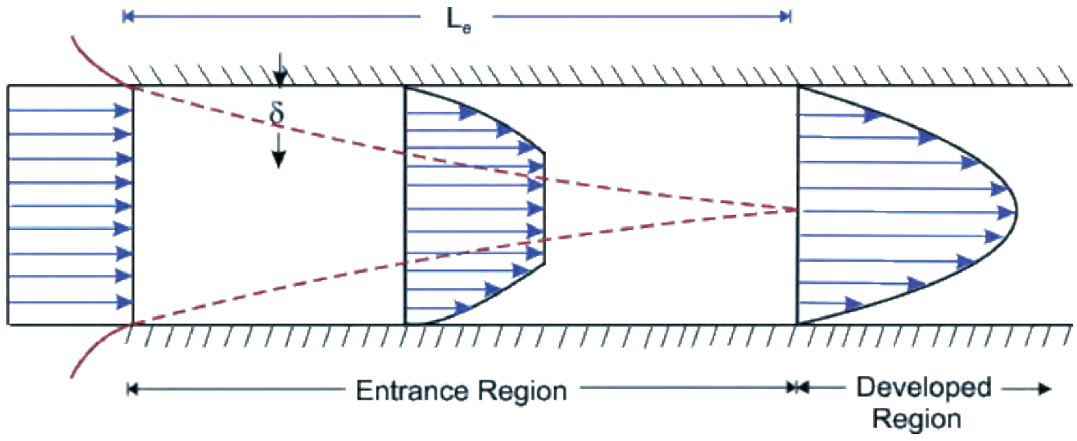

Figure 2.4: *Schematic illustration of the flow profile in a cylindrical tube. The drug enters the needle with a constant velocity U_0 and gradually develops to a parabolic flow profile, with a central velocity $2U_0$.*

The overpressure at the inlet of the needle (ΔP_{in}) is related to spring force by the Bernoulli equation

$$\Delta P_{in} \approx \frac{F(d)}{\pi r_s^2} - \frac{1}{2}\rho_f U_0^2 \tag{2.4}$$

where $F(d)$ is the effective force exerted on the fluid in the penfill by the rubber piston and r_s is the radius of the penfill. The kinetic energy of the fluid in the penfill has been neglected, since it is about a factor of 10^{-5} lower than the kinetic energy of the fluid in the needle.

Combining Eq. (2.2) and (2.4) the pressure drop over the needle is given by

$$\frac{F(t,d)}{\pi r_s^2} - CP(t) \;=\; \frac{8\eta L}{\pi r_n^4} Q(t) \left(1 + \frac{Q(t)}{5.29\pi\nu L}\right) \tag{2.5}$$

where $CP(t)$ is the tissue counter pressure. The second term on the right hand side accounts for the friction losses in the entrance region and is of the order 0.37 for a flow rate of 100 µL/s. This is a significant contribution to the pressure difference and is therefore included. By measuring the flow rate for injections in air the effective spring force, $F(t,d)$, can be predicted and used to calculate the tissue counter pressure from the flow rate estimated for the subcutaneous injection.

The pressure drop over the penfill is neglected. The inner radius of the penfill $r_s \sim 5$ mm, and the pressure drop is of the order $\sim 10^{-4}$ mbar. This is vanishing small compared to the pressure drop over the needle, which is of the order $\sim 10^3$ mbar ($r_n \sim 0.065$ mm).

2.1.2 Sensitivity of the method

This section presents the uncertainty and sensitivity of the method. The uncertainty is influenced by three factors; (1) how well the system is described by Eq. (2.5), (2) how well the flow rate and needle radius can be predicted, and (3) the variation in the flow rate from injection to injection.

In order to address factor (1), Eq. (2.5) was validated experimentally by measuring the needle flow for different pressure differences across the needle. In order to address factor (2), how well the flow rate can be predicted, it was examined how well the click signal corresponds to the needle flow.

To get an order of magnitude of the uncertainty in CP due to the uncertainty in the independent variables Q and r_n, δCP have been calculated by error propagation on Eq. (2.5), shown in Figure 2.5 for $Q = 100$ µL/s and $r_n = 0.065$ mm.

Because CP depends on r_n^{-4}, the needle radius was determined for each individual needle to reduce the uncertainty in r_n. The method is discussed in the following section.

To minimize the variations in the flow rate from injection to injection, both the spring force and the friction force between the rubber piston and the penfill glass have been examined experimentally.

Furthermore the measuring technique was tested by a number of test experiments. In these experiments a controlled counter pressure was applied on the needle tip, and the change in flow rate was calculated from the click signal.

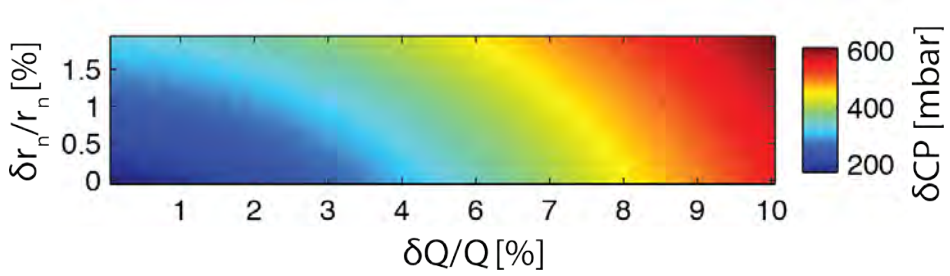

Figure 2.5: *The uncertainty in the counter pressure as function of relative uncertainty in the flow rate, $Q = 100$ $\mu L/s$, and inner needle radius, $r_n = 0.065$ mm.*

Needle flow

It was shown experimentally that the needle flow fulfils Eq. (2.5) by a series of flow tests at different pressure levels. The experimental setup is shown in Figure 2.6 (A). The needle inlet pressure was controlled by a water column and a pressure regulator, and the flow rate was calculated from the injected mass on a scale during a time interval. The flow rate was measured at seven different pressure levels between 500 mbar and 1400 mbar for two different 31G needles. Due to experimental limitations the pressure levels used were below the pressure difference across the needle for an injection, which was of the order 3000 mbar. Flow rates between 25-60 µL/s correspond to $Re \sim 250 - 600$. Since the flow is laminar at both the low and high pressure level, we expected Eq. (2.5) to be valid also for the higher flow rates in the human study.

The relation was fitted with the needle radius as the fit parameter, shown in Figure 2.6(B). The fit gives a inner diameter of 0.136 mm ($\chi^2 = 0.995$), with a deviation of 0.2% between the two needles. Therefore we expected Eq. (2.5) to describe the pressure drop well for the insulin needle used in our measurements and the theoretical expression was used for the measurements in the patients. The needle radius was predicted from Eq. (2.5) for each of the needle used, by measuring the flow rate at a single pressure level.

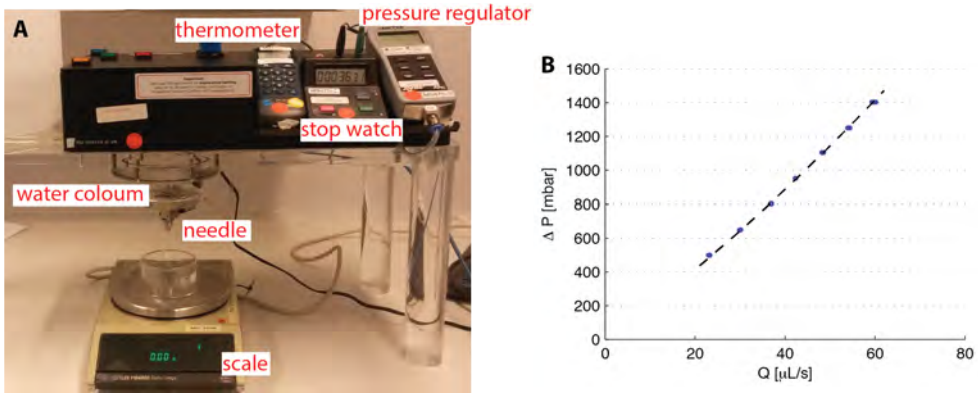

Figure 2.6: *(A) Experimental setup for determination of the needle radius from the flow capability of the needle. (B) Pressure drop across the needle for a 6 mm 31G needle. The data points are fitted to Eq. (2.5).*

Flow rate from click signal

In order to validate that the flow rate calculated from the click signal corresponds to the actual flow rate through the needle, the click signal was recorded and the injected mass measured on a scale simultaneously. Figure 2.7 (A) shows the flow rate calculated from the recorded audio click signal (red) and from the mass recorded on the scale (blue), for an injection of 0.40 mL of drug in air. It is seen that the flow rate have a kink after about 2 s (dashed line). This is due to an internal mechanism in the insulin pen that reduces the effective spring force on the rubber piston for the last seven clicks, shown in Figure 2.7 (B). The rubber piston will expands and more than 10 µL is injected between each click and the flow rate estimated from the click signal becomes lower than the actual flow rate. Therefore the last part of the signal has been omitted from the analysis. Also the first two clicks have been omitted from the signal, since during this phase the rubber piston is compressed and almost no drug is injected.

The average flow rate is calculated from the injected mass (Q_{scale}) and audio click signal (Q_{click}), and the deviations are shown in Table 2.2 for an injected dose of 150-400 µL. The table gives the average value of the relative difference between Q_{click} and Q_{scale} and the standard deviation. In total 54 injections were performed with 10 different insulin pen.

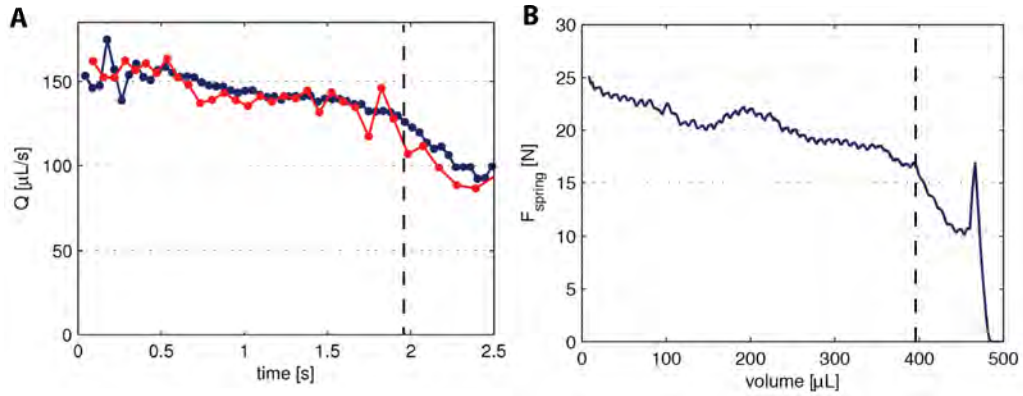

Figure 2.7: *(A) Needle flow rate calculated from the audio click signal (red curve) and from the mass recorded on a scale (blue). (B) The spring force from the torsion spring in the injection device for a 480 µL dialled dose. An internal mechanism in the device cause the effective spring force to drop in the last part of the curve (dashed line)*

On average the deviation is of the order 2.5%, and we therefore assume that average flow rate is reasonably well predicted from the click signal. Increased volume will give rise to a lower uncertainty for the estimated flow, because the number of clicks in the signal increases.

Injected volume [µL]	150	200	400
$\frac{Q_{click}-Q_{scale}}{Q_{scale}}$	(3.8± 2.3)%	(2.2 ± 1.5)%	(0.75 ± 0.39)%

Table 2.2: *Relative deviation between the injection flow rate estimated from the injected mass (Q_{scale}) and from the click signal (Q_{click})*

Torsion spring force and friction forces

This section presents experimental measurements of the torsion spring force and the penfill friction, both assumed to be unchanged from injection to injection. The torsion spring force during injection is shown in Figure 2.7(B). The spring force was measured for nine injection pens, and the spring was dialled five times for each pen. The dialling corresponded to a injection dose of 0.48 mL. The average force was calculated for each pen. Again the last part of the signal was omitted. The standard deviation over the mean for each pen was between 3-4%. It means that the injection rate is expected to be similar for equally performed injections.

The friction force was measured by mounting the penfill on a tensile testing machine with a 100 N load cell. A counter pressure was applied to the drug in the penfill to simulate the needle. The rubber piston was moved at a constant speed and the force was measured by the sensor. One example of the measured friction force is shown in Figure 2.8 for a penfill counter pressure at 2800 mbar and the injection speed changed from 125 µL/s to 75 µL/s after about 2 mL of drug had been injected (green ellipse). The friction force oscillates in the beginning of the penfill (red ellipse), due to the break-loose force between the rubber piston and the penfill. This effect is caused by the siliconization of the penfill, and therefore 1.5 mL of drug was injected into a bottle and discarded prior to each measurement of the tissue counter pressure.

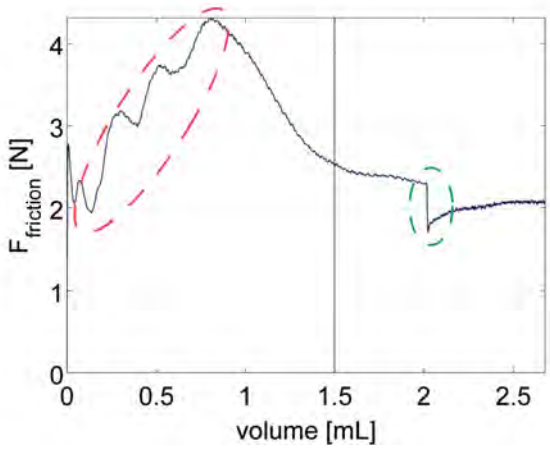

Figure 2.8: *Friction force between the rubber piston and the penfill glass. After about 2 mL of injected drug the injection rate is changed from 0.125 mL/s to 0.075 mL/s, seen as a drop in the penfill friction (green circle). In the beginning of the penfill the friction force oscillates due to the break-loose force between the rubber piston and the siliconization at the penfill walls (red circle)*

The friction force is seen to change with the injection speed (green ellipse). An extensive study of the friction force was performed in a bachelor project, where the dependency of both counter pressure in the penfill and rubber piston velocity were investigated in steady state. The report was claimed confidential, and therefore can details not be reported. The study showed that for an overpressure in the penfill of about 3000 mbar, the friction force is changes only with about 0.5-1% for a change in flow rate between 5-10%, and therefore the change is neglected in the calculations of the tissue counter pressure.

The friction force varies along the penfill for a constant flow rate. This variation, and the variation in the torsion spring force will be seen as a variation in the flow rate for equally performed injections. A number of air injections were performed both before and after the injection given to the patient. The variations between the air injections were used to estimate the uncertainty on the measured counter pressure.

2.1.3 Injections in controlled counter pressure

To estimate the sensitivity and uncertainty of the method a series of injections were performed in a counter pressure controlled by a pressure chamber. Six test pens were used, and four injections were made with each pen in the order $\{\text{pressure}, \text{air}, \text{pressure}, \text{air}\}$. The injected volume was 480 µL. Only 1.1 mL was injected into a bottle and discarded prior to the test, to be able to make five injection with a 3 mL penfill. In total 12 injections were performed in a controlled counter pressure. For half of the injections the applied pressure was 500 mbar, and for the other half, the applied pressure was 1000 mbar. Table 2.3 collects the calculated counter pressure, the deviation from the applied pressure and the estimated uncertainty calculated from the variation in Q_{air} and r_n. The measurements were performed with two different needles. The radius of each needles was determined by its flow capability, and the measurement was repeated twice for each needle. The uncertainty was taken as the difference between the measurements and the uncertainty in the flow rate was taken as the difference in the flow rate between the two reference measurements.

The deviations between the estimated and applied counter pressure were 10-30%. The uncertainty was 15-60%, except for the last device where there was a the large difference in the flow rate between the two air injections. Based on this experiment we expect that a tissue counter pressure of the order 500 mbar can be detected by this method, and the order of magnitude of the counter pressure can be estimated.

Device	CP (ref) [mbar]	CP (measured) [mbar]	Diff [%]	ΔQ [%]	Δr [%]	ΔCP [mbar]
1	500	420	16	3.9	0.32	258
1	500	437	13	3.9	0.32	258
2	500	611	22	1.8	0.32	122
2	1000	775	23	1.8	0.32	122
3	1000	881	12	6.0	0.32	355
3	1000	655	35	6.0	0.32	355
4	500	561	12	3.1	0.32	280
4	500	450	10	3.1	0.32	280
5	500	404	19	1.2	0.32	124
5	1000	695	31	1.2	0.32	124
6	1000	898	10	10.4	0.32	950
6	1000	759	24	10.4	0.32	950

Table 2.3: *Counter pressure calculated from the changed flow rate between a air injections and an injection into a controlled counter pressure.*

Summary

The needle flow test showed that the pressure drop across the needle was well described by Eq. (2.5), and the average flow rate could be reasonably well predicted from the click signal. Due to the break-loose force between the penfill and the rubber piston about 1.5 mL of drug was discarded prior to each measurements. The radius of each individual needle was determined by flow capability of the needle. A number of reference injections in air must be performed in order to estimate the uncertainty in the flow rate and check if the injection device performs equally from injection to injection. The change in friction force with changed flow rate has been neglected.

2.1.4 Injection procedure and patient inclusion criteria

The evaluation of the device parameters presented in the previous sections leads to the following injection procedure:

1. 1.5 mL of drug was injected into a bottle and discarded prior to the measurements.

2. A number of air injection were made and the click signal recorded. The injected volume fits the dose prescribed to the patient. These injections are used to calculate the effective spring force and estimate the uncertainty in the flow rate.

3. The patient received the subcutaneous injections and the click signal was recorded.

4. The air injections were repeated. The total number of air injections depends on the prescribed dose, since only 1.5 mL of drug was available for the whole injection series.

The study included 11 type 2 diabetic patients, all mid age men. All injection were given in the stomach, and no elevated skin fold was made. The subcutaneous injections and air injections were performed by the same nurse. The measurements were carried out at Steno Diabetes Center. The head of the Clinical Research Department, Lise Tarnow, who was responsible for the conduct of the study, approved the procedure, after acceptance from The Committee on Health Research Ethics from the Capital Region of Denmark. No institutional review process was necessary to take this decision.

In the analysis of the click signal the first two and last seven click were removed. As each click corresponds to a volume of 10 μL, an injected volume of 90 μL was not used in the analysis. Therefore the study required patients, who receive relative high doses of the fast acting insulin NovoRapid®. The inclusion criteria was set at a dose of 180 μL, which gave a click signal of 9 clicks for the analysis. This allows us to predict the flow rate with an uncertainty of about 4%, seen from Table 2.2. For this inclusion criteria the physicians from Steno Diabetic Center could recruit 11 patients during the six months, where the experiment was carried out. If we had required a higher dose, it would have been more difficult to recruit the patients.

2.2 Order of magnitude of tissue counterpressure

Figure 2.9 shows an example of the flow rate for a number of injections in air (grey), and for the subcutaneous injection given to the patient (red). Out of the 11 patients, 3 patients were omitted since no change in flow rate could be detected. The results are collected in Table 2.4. The estimated counter pressure range from about 150-1000 mbar, indicating a large variability between the patients.

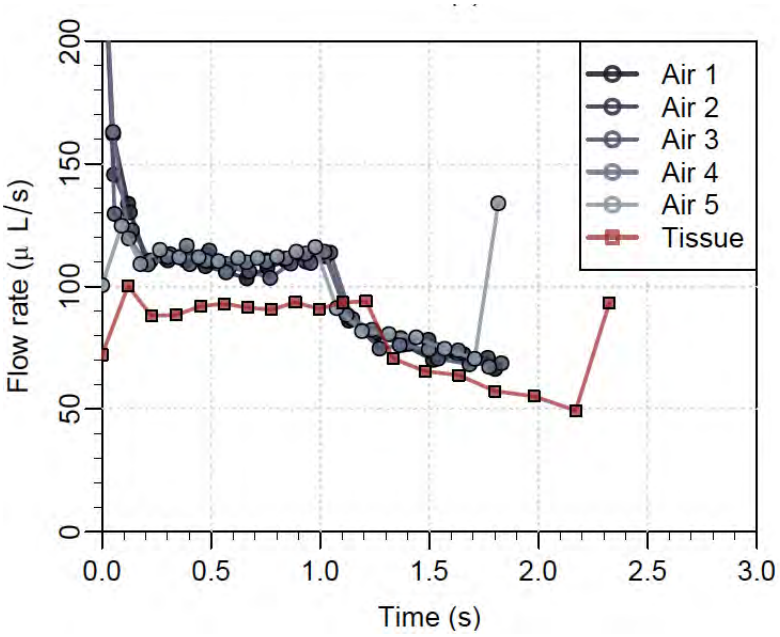

Figure 2.9: *Injection flow rate for patient no. 4. The flow rate is estimated from the audio click signal from the injection device for air injections (gray) and a subcutaneous injection in human tissue (red). The figure is adapted from Paper I.*

The uncertainty in the flow rate was taken as the standard deviation of the average flow rate measured for the air injections. The sensitivity was defined as the difference in pressure drop across the needle for the air injection with the highest and lowest flow rate. For patient no. 6 the counter pressure is very close to the sensitivity, and the uncertainty is about 60%, meaning that this method can hardly predict a counter pressure. For the remaining measurement the uncertainty is 6-27%, and the estimated counter pressure is 3-12 times the sensitivity. Again it should be emphasized that the flow rate estimated from the click signal not exactly matches the actual flow rate, and that the slight decrease in friction force with the decreased flow rate is neglected.

We believe that this relatively simple and non-invasive method can be used to estimate the order of magnitude of the tissue counter pressure in humans for standard insulin injections. The method can only be used to estimate the average counter pressure during the injection, and not the time evolution of the pressure build-up or relaxation time of the tissue after end injections.

Patient	Dose [µmL]	#inj.	Δr_n [%]	ΔQ [%]	CP [mbar]	ΔCP [mbar]	Sens. [mbar]
1	480	4	0.11	0.5	190	32	27
2	240	6	0.45	2.2	702	84	81
3	210	6	0.19	2.9	963	70	114
4	240	6	0.87	3.5	642	159	141
5	340	4	0.06	1.7	998	64	83
6	180	6	0.04	4.4	190	110	165
7	240	6	0.13	1.5	387	43	58
8	200	5	0.12	1.3	164	45	59
9	180	6	0.07	1.3	-	-	-
10	200	4	0.08	0.7	-	-	-
9	180	4	0.22	0.9	-	-	-

Table 2.4: *Estimated counter pressure during subcutaneous injections for 11 type 2 diabetic patients. For three patient no change in flow rate was detected. The uncertainty (ΔCP) is estimated from the variation in Q_{air}.*

2.3 Presentation of Paper I

In Paper I the measurements of the pressure build-up in humans were coupled to the tissue properties through a model for the tissue-drug interaction. The model is based on flow in porous media, and the tissue is characterized by its flow permeability and resistance to deformation, given by the bulk modulus. The experimental data gives the order of magnitude of these values.

2.3.1 Model for pressure build-up

This sections presents the deviation of the model. For clarity the variables introduced in the model are listed in Table 2.5, as well as introduced in the text when presented.

Tissue pressure during injection	$p(\mathbf{x}, t)$	[Pa]
Tissue pressure without distortion	p_0	[Pa]
Tissue porosity during injection	ϕ	•
Tissue porosity without distortion	ϕ_0	•
Bulk modulus of the tissue	β	[Pa]
Average drug velocity in a unit volume of pore space	$\mathbf{v}$	[m/s]
Tissue permeability	K	[m^2]
Local injection rate of mass	$q(\mathbf{x}, t)$	[kg/(m^3·s)]
Mass density of the infused fluid	ρ_f	1000 kg/m^3

Table 2.5: *Variables related to the model for the tissue-drug interaction. The values are individual parameters for each subject, except the drug mass density which is taken to be equal to the mass density of water.*

The porosity of the tissue in a point $\mathbf{x}$ at time t is given by

$$\phi(\mathbf{x}, t) = \frac{V_f}{V} \tag{2.6}$$

where V is a volume element centred around x and V_f is the volume of the pore space within V (e.g. the intestinal fluid volume).

The tissue is elastic and will be compressed when subjected to an external overpressure. Let V_t be the volume of the solid phase within V (e.g fat cells and fibres), such that $V = V_t + V_f$. The effective bulk modulus is defined as the pressure increase per fractional change in the volume of the solid phase and is in a discrete form given as

$$p(\mathbf{x}, t) - p_0 = \beta \left(\phi(\mathbf{x}, t) - \phi_0\right) \tag{2.7}$$

where p_0 is the tissue pressure and ϕ_0 is the porosity in undisturbed tissue. The effective bulk modulus is a measure of the incompressibility of the bulk material, meaning the higher the bulk modulus the higher is the pressure needed to distort the structures. In this case the deformation is assumed to be small and increase linear with the applied pressure. For larger deformations higher order elastic components can be included.

The velocity of the drug in the pore space, $\mathbf{v}$, is driven by the pressure gradient, ∇p, and given by Darcy's law

$$\mathbf{v} = -\frac{K}{\eta}\nabla p \tag{2.8}$$

where again η is the dynamic viscosity of the drug, and K is the tissue permeability. The tissue is considered homogeneous, so K is assumed to be a constant.

The model for the pressure build-up is established from mass conservation, which for a volume element at position $\mathbf{x}$ gives that

$$\frac{\partial \rho}{\partial t} + \nabla \cdot (\rho \mathbf{v}) = q(\mathbf{x}, t) \tag{2.9}$$

where ρ is the density of the drug in the volume element V, and $q(\mathbf{x}, t)$ is mass of drug being injected per unit volume per unit of time.

The density of drug in the volume V is given by

$$\rho = \rho_f \frac{V_f}{V} = \rho_f \phi \tag{2.10}$$

where ρ_f is the mass density of the injected drug, and ϕ is the porosity of the tissue.

Combining Eq. (2.9) with Eq. (2.7)-(2.8) the proposed model for the pressure evolution in the tissue is given by

$$\frac{\partial p}{\partial t} = \frac{K}{\eta}\nabla \cdot \left[\left(\beta\phi_0 + p - p_0\right)\nabla p\right] + \beta\frac{q(\mathbf{x}, t)}{\rho_f} \tag{2.11}$$

where p_0 is taken to be equal to atmospheric pressure. However, the tissue pressure have been measured to be slightly below atmospheric pressure (H. Wiig & Reed 2003).

Since it is assumed that the tissue is homogeneous and isotropic the equation can be rewritten in spherical coordinates where the angular components can be disregarded by symmetry. The

source is located at the tip of needle, taken as the center of the coordinate system, and the source term $q = q(r,t)\delta(r)$, where $\delta(r)$ is the Dirac delta function. This introduces a singularity, and the solution for the pressure evolution is found outside a small sphere with a radius equal to the radius of the needle. The source term is removed and replaced by the boundary condition

$$4\pi r_n^2 (\phi v_r) = Q(t) \tag{2.12}$$

where $Q(t) = \frac{4}{3}\pi r_n^3 \int \frac{q}{\rho_f} dV$ is the flow rate. Using Darcy's law the boundary for the pressure can be rewritten as

$$\frac{\partial p}{\partial r}|_{r=r_n} = -\frac{\eta}{4\pi r_n^2 \phi K} Q(t) \tag{2.13}$$

In the case where the deformations of the tissue structures are weak, the nonlinear terms in Eq. (2.11) can be neglected since $p - p_0 \ll \beta\phi_0$. In this case the pressure evolution reduces to the diffusion equation, with the diffusion coefficient $D = \frac{K}{\eta}\beta\phi_0$ and $\phi \sim \phi_0$. In the case of a constant infusion rate from the tip of the needle at $r = 0$, the pressure evolution in the tissue can be written as

$$\frac{\partial p}{\partial t} = D\nabla^2 p + \frac{\rho_f Q}{4\pi r^2}\delta(r) \tag{2.14}$$

This gives the analytical solution (Crank et al. 1975)

$$p(t,r) = p_0 + \frac{Q\eta}{4\pi K r}\mathrm{Erfc}\left(\frac{\mathrm{r}}{2\sqrt{\mathrm{Dt}}}\right) \tag{2.15}$$

where it have been used that $p(t, r = \mathrm{inf}) = p_0$ and $\mathrm{Erfc} = \frac{2}{\sqrt{\pi}}\int_{\mathrm{z}}^{\infty} \mathrm{e}^{-\mathrm{s}^2}\mathrm{ds}$ is the complementary error function.

The idealization of the infusion rate as the Dirac delta function, introduces a singularity of the pressure at $r = 0$. Physically the pressure the exerted on a small volume round the needle tip, meaning that the pressure at the needle tip can be defined as

$$\langle p(t,r)\rangle_{r_n} = \frac{1}{V_{r_n}}\int_{V_{r_n}} dV p(t,r) \tag{2.16}$$

where $V_{r_n} = \frac{4}{3}\pi r_n^3$.

Solving the integral the pressure in the tissue at the needle tip becomes

$$\langle p(t,r)\rangle_{r_n} = p_0 + \frac{1}{V_{r_n}}\frac{Q\eta}{4\pi K} H(r_n,t) \tag{2.17}$$

where

$$H(r_n,t) = -4r_n\sqrt{Dt\pi}\exp\left(\frac{r_n^2}{4Dt}\right) + 4Dt\pi\left(1 - \mathrm{Erfc}\left(\frac{\mathrm{r_n}}{2\sqrt{\mathrm{Dt}}}\right)\right) + 2\pi\cdot r_n^2 \mathrm{Erfc}\left(\frac{\mathrm{r_n}}{2\sqrt{\mathrm{Dt}}}\right) \tag{2.18}$$

In steady state ($t \to \infty$) $H(r_n,t) \to 1$ and the pressure at the needle tip increases linearly with the infusion rate. The lower the permeability, the higher is the steady state pressure, as expected. An increased value of β (the material becomes more stiff) means that the pressure increases with a higher rate.

This solution applies when the deformation is weak. In the following the experimental human data will be used to calculate the order of magnitude for the tissue permeability (K) and bulk modulus (β), and the model will be used estimate how drug viscosity and flow rate influences the tissue counterpressure.

2.3.2 Tissue permeability and bulk modulus for the human study

For each patient the average spring force as function of rubber piston displacement, $F(d)$, is estimated from the injections in air. This value, and the measured flow rate during the subcutaneous injection, is used to calculate the pressure in the tissue at the needle tip as function of time, using Eq. (2.5). The model parameters K, β and ϕ_0 are found by best fit (least square) to the model for $p(r_n, t)$ given by Eq. (2.11) and Eq. (2.13). Figure 2.10 (A) shows the experimental data (gray points) and the model fit (red curve) for patient no. 4.

The permeability, with 95% confidence interval, is found to be $K = (8.9 \pm 4.7) \cdot 10^{-11}$ m^2, shown in a box plot in Figure 2.10 (B) (top). These values are of the same order of magnitude as reported values for porcine tissue (Comley 2010). The bulk modulus is found to be $\beta = (0.89 \pm 0.13) \cdot 10^5$ Pa, shown in a boxplot in Figure 2.10 (B) (bottom). The background permeability was in general small $\phi_0 \sim 0$.

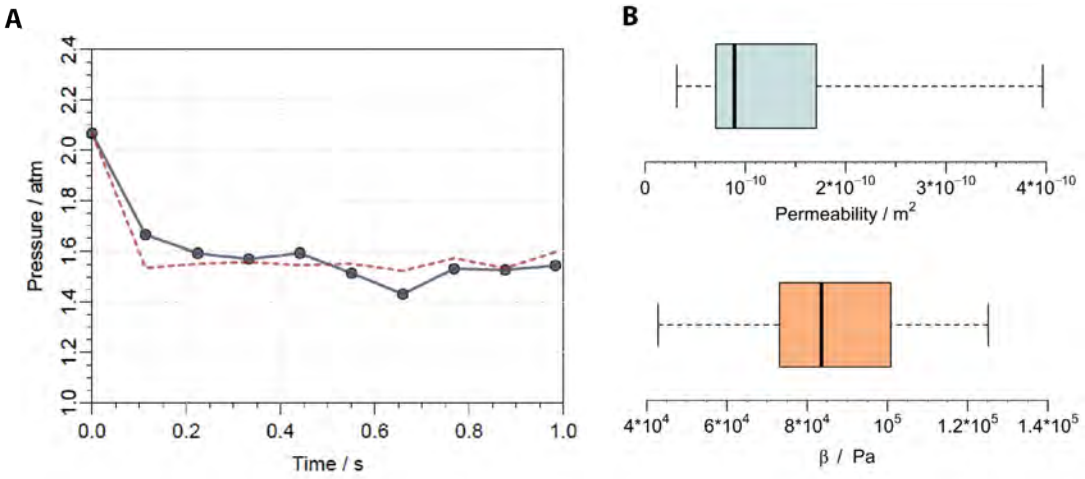

Figure 2.10: *(A) Pressure at the needle tip calculated from the flow rate (blue) and best fit to the model (red) for patient nr. 4. (B) The permeability (top) and bulk modulus (bottom) estimated from best fit to patient data. The middle line represents the median, the boarders of the box gives the lower and upper quartiles. The whiskers extend to the extreme values. The figures are adapted from Paper I.*

The measurement only provides an estimate of the tissue counter pressure at the needle tip. The overpressure as function of radial distance from the injection site can be calculated from the model. Figure 2.11 shows the relative pressure 0.01 sec, 0.01 sec, and 1 sec after the injection was started. for $K = 10^{-10}$ m^2 and $\beta = 10^5$ Pa. It is seen that the pressure quickly decreases away from the injection site. It should be noted that for a couple of patients the porosity, calculated from Eq. (2.7), becomes close to unity at the needle tip. This could be avoided by adding higher order elastic effects. Since the pressure decreases rapidly away from the needle tip, Eq. (2.7) is considered valid, when evaluated slightly away from the needle tip.

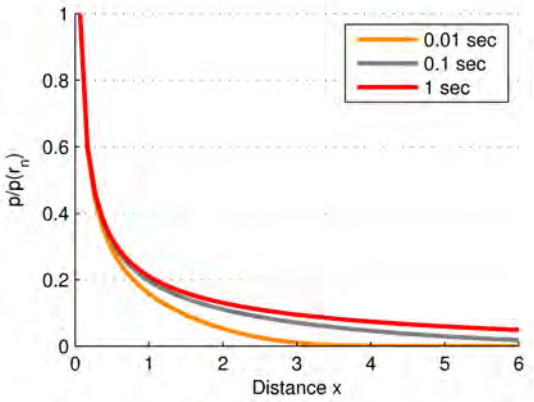

Figure 2.11: *Tissue pressure as function of radial distance from the needle tip for* 0.01 *sec,* 0.01 *sec, and* 1 *sec after the injection. The pressure is taken relative to* $p(r_n)$*. The permeability and elastic bulk modulus is taken as* $K = 10^{-10}$ m^2 *and* $\beta = 10^5$ *Pa, respectively*

The model provides an estimate of how the pressure build-up is changed when changing the device parameters. It is seen from the value $\beta \sim 10^5$ Pa, that the non-linear terms cannot be neglected, since $\beta\phi_0 \sim 10^3$ Pa, the same order of magnitude as the counter pressure, $p - p_0$.

Figure 2.12 shows the relative change in pressure for increasing viscosity (A), and flow rate (B). The pressure is evaluated in a distance $r = 2.5r_n$, and at a time $t = 0.01$ sec after beginning of the injection. The counter pressure is evaluated numerically from Eq. (2.11) with the tissue permeability $K = 10^{-10}$ m^2, the bulk modulus $\beta = 10^5$ Pa and inner needle radius $r_n = 65$ µm. Evaluating the pressure slightly away from the needle tip ensures that the porosity of the tissue is below unity and Eq. (2.7) stays valid. It is seen that the counter pressure does not increases linear with the flow rate due to the deformations of the tissue structures.

According to the model the tissue counter pressure can be expected to increase with about a factor of 5 when changing the injection flow rate from 25 μL/s to 300 μL/s. The pressure increases with about 50% when changing the viscosity by a factor of 2 for a 31G 6 mm needle. Thus, according to the model, the increased counter pressure caused by increased drug viscosity can be compensated for by a reduced injection speed.

For the FlexTouch® device the increased viscosity will cause the flow rate to decrease, due to a higher flow resistance in the needle. The additional pressure build-up in the tissue will further reduce the flow rate. This minimize the local tissue pressure and tissue expansion.

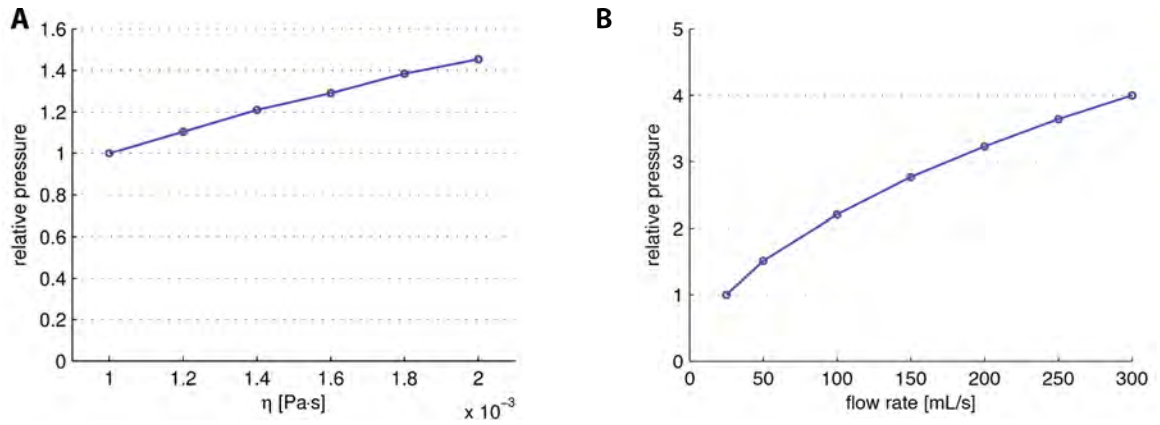

Figure 2.12: *(A) Relative change in tissue counter pressure with increasing viscosity at $Q = 100$ $\mu L/s$. The pressure is calculated relative to the pressure at $\eta = 10^{-3}$ Pas. (B) Relative change in pressure with increasing flow rate for $\eta = 10^{-3}$ Pas. The pressure is calculated relative to $Q = 25$ $\mu L/s$. For both graphs the pressure is evaluated at a distance $r = 2.5r_n$ from the injection center, and $K = 10^{-10}$ m^2 and $\beta = 10^5$ Pa.*

2.4 Summary

we have implemented a non-invasive method to obtain the order of magnitude of the pressure build-up during a subcutaneous injections. The measured counter pressure in the tissue is subject to a considerable uncertainty, since the flow rate is measured indirectly from the click signal. However, our test experiments showed that a counter pressure of the order 500-1000 mbar could estimated with an deviation of at most 35%. The method has sufficient sensitivity to measure a pressure build-up in the subcutaneous tissue for 8 out of 11 type 2 diabetics, with great variability among the patients. At the time of this study very few patients were prescribed sufficiently high doses (minimum 0.18 mL) in a period of 6 months. Higher doses would improves the sensitivity of the method, since the average flow rate is better estimated from a longer click signal.

The second part of this chapter presented a model for the pressure build-up during subcutaneous injection. The model is based on mass conservation and flow in porous media, and relay on the assumptions that the drug distributes isotropically around the injection site, and that the tissue deformation increases linear with the pressure.

The permeability estimated from the model is the tissue permeability during injection. Since the fat cells compress during injection, this permeability might be higher than the permeability in the undistorted tissue. It also means that the permeability might changes as a function of distance from the injection site, which is not taken into account in the model.

To further improve the model an accurate relation must be established between the tissue counter pressure and the injection speed and injected volume. Such experiments require an instrumented device and therefore a formal ethical approval, which is beyond the scope of this work. A clinical study for measuring the pain reception for healthy volunteers was carried out by Novo Nordisk A/S (Heise et al. 2014). The infusion rate was varied from 150-450 μL, and the injected volume was varied between 400-1600 μL. The study showed a significant increase

in injection pain with increased infused volume, but not with increased infusion rate. If the infusion pressure could be measured simultaneously in a similar setup, it would be possible to correlate the pain reception experienced by the patients with the pressure build-up, and to sophisticate the model.

2.5 Outlook and applications

The presented model can be implemented in DRD for optimization of new injection systems. Changing the injection rate, the needle dimensions or the viscosity of the drug changes both the resistance in the needle and the tissue counter pressure (according to the model). The tissue counter pressure can be estimated from the model, and the force delivered by the injection device can be designed to overcome the counter pressure. Today the functionally of the devices are tested for air injections, not taking the resistance of the tissue into account.

The estimated tissue parameters have great variability among patients. Repeated insulin injections in the same anatomical region can cause skin disorders (Vardar & Kızılcı 2007, Milan et al. 2010), and diabetics are instructed to change injection site from injection to injection. The click signal from the FlexTouch® can be recorded in the clinic without a formal clinical study approval, and the tissue pressure can be followed over time for the same patient and related to the insulin response for the individual.

Chapter 3

Visualization of subcutaneous injections

In the previous chapter it was shown that a tissue counter pressure is introduced during a subcutaneous injections. The pressure build-up varies among equally performed injections, both in the performed human study and for injections performed in adipose pig tissue (Allmendinger et al. 2014). After injected the drug distributes among the fat cells in the adipose tissue as shown in the histological image in Figure 3.1. The pharmacokinetics for insulin drugs have been shown to be different for subcutaneous and intramuscular injections (Vaag et al. 1990, Frid & Linde 1992, Karges et al. 2005), and dependent on the injection technique e.g. jet-injections (Engwerda et al. 2013), a dispersed injection strategy (Mader et al. 2012), and micro-needle injections (Pettis et al. 2011, Gupta et al. 2011, McVey et al. 2012).

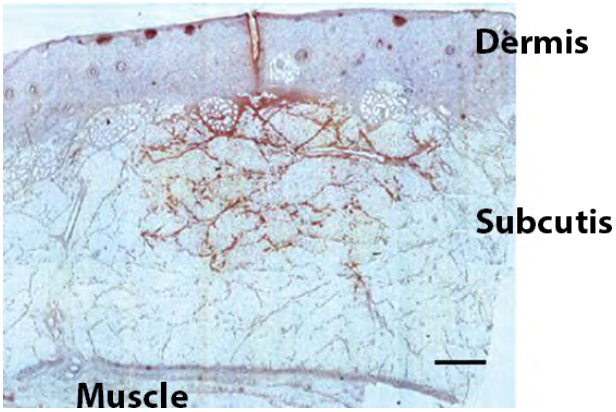

Figure 3.1: *Histological cross section of an 0.1 mL injection of IAsp performed in adipose pig tissue. The scalebar is 2 mm.*

New insulin drug formulations are tested preclinical first in rats and later in pigs. The aim of our studies was to implement a visualization technique that can be used to investigate how the injection procedure effects the spatial drug distribution, and to optimize the injection procedure in the animal test studies. The visualization method is based on x-ray computed tomography. Compared to histology and light sheet microscopy (Markussen et al. 1996, Jockel et al. 2013), x-ray computed tomography makes it possible to quantify the spatial drug distribution in 3D, and estimate the amount of drug in the dermal skin layer, subcutis, and the muscle (Jensen

et al. 2011). In x-ray computed tomography the injected fluid cannot be differentiated from the surrounding tissue, so the insulin drug is represented by a contrast agent.

This chapter begins with an overview of the skin structure of the pig and the rat in Section 3.1, followed by a discussion of the injection procedure. Section **??** provides the necessary theoretical background for x-ray radiography, and discuss our choose of x-ray contrast agent, and spatial resolution in the radiographic images.

3.1 Sample preparation

The injections visualized by x-ray computed tomography are preformed in tissue biopsies. The morphology of the skin and adipose tissue affects the distribution of the drug.

3.1.1 Preclinical models

The pig has a pharmacokinetic response to subcutaneous injected insulin, comparable to that of humans, and is used as a research animal in the development of new insulin drug formulations (Douglas 1972, Swindle et al. 2012). The injections are performed in the neck of the pig, since this region is easy to access, and the injections are well tolerated by the pigs. Compared to the skin and adipose tissue at the back of the pig, the tissue at the neck has a lower injection resistance, and is assumed to have a skin structure that represents human tissue better.

A histological cross section of the skin, adipose tissue and muscle tissue is shown in Figure 3.2 (A). At the neck of the pig the fat layer is divided into two by a fascia (black arrow). The studies presented in this thesis are performed on the crossbred Landrace & Yorkshire & Duroc pig (LYD). The thickness of the upper subcutaneous fat layer was measured by ultra sound in a previous internal study in Novo Nordisk A/S. The thickness was found to be (5.3 ± 0.9) mm (n=237), about the same thickness the subcutaneous fat layer in humans (Gibney et al. 2010, Hofman et al. 2007). The skin thickness (dermis and epidermis) is about 3 mm in humans and about 2-3 mm in pigs (Bronaugh et al. 1982).

The rat is used as research animal in the early tests of new drug formulations. The rats are injected in the neck, where the tissue is composed of five layers; edipermis, dermis, subcutis, panniculus muscle, and a connective tissue layer, shown in Figure 3.2 (B) for the rat species Sprague-Dawley (Wells et al. 2010). At the neck the subcutaneous layer is very thin with a sawtooth structure. The panniculus muscle is separated from subcutis by a thin layer of connective tissue. Because of the thin subcutaneous layer the insulin injections are most likely distributed partly intramuscular or intradermal. The injection experiment was performed in the rat species Zucker Obese, which has a a thicker subcutaneous fat layer compared to the Sprague-Dawley rats Wells et al. (2010).

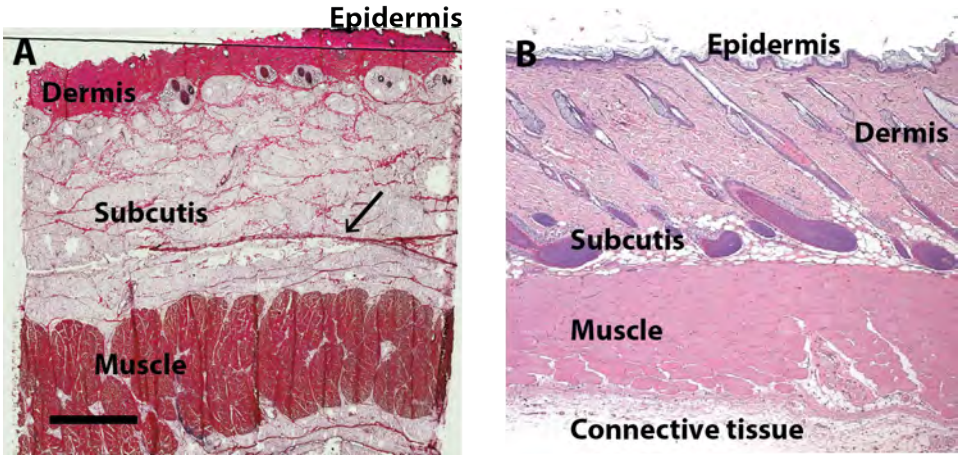

Figure 3.2: *Histological images of the skin (epidermis and dermis), subcutis, and the muscle tissue. (A) The neck of a LYD pig (H& E stain). Scalebar is 5 mm. The image is provided by Rikke Kirk, Novo Nordisk A/S Målæv. (B) The neck of Sprague-Dawley (H& E stain). The figure is adapted from Wells et al. (2010).*

3.1.2 Injection procedure

For the pig studies, the injections were performed with a 8 mm 30G needle, and the needle length was adjusted with a needle stop. The injection device was a motor driven injection device, where the injection speed and volume was digitally controlled, shown in Figure 3.3 (A). For the rats the injections were performed by a laboratory technician after in an elevated skin fold with a NovoPen Echo® (Novo Nordisk A/S) and a 8 mm 30G needle.

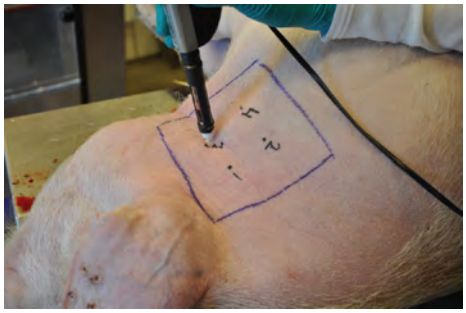

Figure 3.3: *Subcutaneous injections performed at the neck of a slaughtered LYD pig with a motor driven injection device.*

The animals were terminated, and the injections were performed within 1-10 min after termination. The destructions were performed by a veterinarian or laboratory technician for the pigs and rats, respectively. After injected the tissue samples were cut out, and instant frozen using dry ice and 2-methylbutane, within 15 min and 2 min after termination, for the pigs and rats, respectively. The tissue biopsies was cut out after the injections were performed, since the tissue subtracts, and the thickness of the skin and subcutaneous fat layer increase. The injection procedure was chosen as a trade-off between the need to maintain the injected liquid in place right after injected, and have *in vivo* conditions for the adipose tissue at the injection time.

The disadvantage of the procedure is that the interstitial fluid flow and blood flow in the adipose tissue are absent at the injection time. This might effect the drug distribution. By performing the injection within minutes after termination the changes in skin temperature and elasticity were brought to a minimum.

The advantage is that the visualized drug distribution would only be influenced by the injection technique and the morphology of the skin. The main absorption of the soluble insulin formulation, IAsp, happens within 10 minutes in pigs and even faster in rats. It means that if the injections were performed in the living animals, the drug will diffuse and be absorbed before the animals were terminated. Consequently, the observed drug distribution would not be related purely to the injection technique, but also to physiological factors such as the subcutaneous blood flow and the skin temperature.

3.2 X-ray imaging

This section outlines the theoretical background for x-ray radiography. For the radiographic images the contrast, noise, spatial resolution, and temporal resolution depend on the flux of the x-ray beam, the intrinsic detector resolution, and the efficiency of the detector. The advantages and limitation of different x-ray detector systems will be discussed in section 3.2.3.

X-rays imaging have been widely used since the discovery of x-rays by Wilhelm Röntgen in 1895 (Röntgen 1898). The technique is used for clinical and preclinical diagnostics, and in the industry for non-destructive inspection and testing. Today x-ray imaging is a well-established method in many RD facilities and manufacturing facilities. The standard x-ray imaging techniques are based on the attenuation of the x-ray beam. Sometimes the contrast available in absorption images is not sufficient for the intended purpose, which have lead to the implementation of refraction and scattering based x-ray imaging techniques (Davis et al. 373, Chapman et al. 1997, Bunk et al. 2009).

X-rays are electromagnetic waves with a wavelength (λ) of the order of Ångtrøm. The propagation of a monochromatic plane wave through a material is described by

$$\Phi(\mathbf{r}) = \Phi_0 \exp\left(-in\mathbf{k}\cdot\mathbf{r}\right) \tag{3.1}$$

where $\mathbf{r}$ is the position vector and $\mathbf{k}$ is the wave vector, with $k = \frac{2\pi}{\lambda}$, and n is the complex index of refraction. For x-rays the index of the refraction is given as (Als-Nielsen & McMorrow 2011)

$$n = 1 - \delta + i\beta \tag{3.2}$$

where the real part (δ) describes the phase shift and the imaginary part (β) describes the absorption of the x-ray beam.

The phase shift and absorption depend on the wavelength (λ), the atomic number (Z) and the atomic number density ρ_A

$$\beta = \frac{\lambda}{4\pi}\rho_A\sigma_a \tag{3.3}$$

$$\delta = \frac{\lambda}{4\pi}\rho_A\left(\lambda r_0 Z\right) \tag{3.4}$$

where $r_0 = 2.82 \cdot 10^{-15}$ m is the Thomson scattering length, and σ_a is the absorption cross section.

Figure 3.4 shows the transmission of the x-ray beam (T). The transmission measured by the detector pixel at position y is given by

$$T(y) = \frac{|\Phi(y)|^2}{|\Phi_0(y)|^2} \tag{3.5}$$

$$= \exp\left(-\int \mu(x,y)dx\right) \tag{3.6}$$

where $I = |\Phi|^2$ and $I_0 = |\Phi_0|^2$ are the transmitted and incoming beam intensity, respectively. The integral runs over the beam path, and the linear attenuation length (μ) is given by

$$\mu(x,y) = 2k\beta(x,y) \tag{3.7}$$

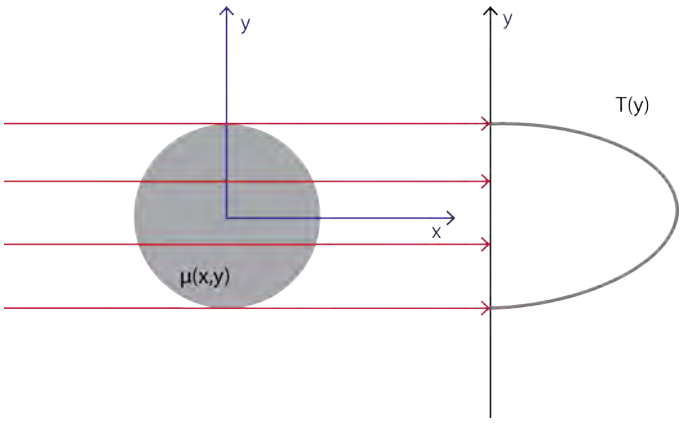

Figure 3.4: *Transmission of a parallel monochromatic x-ray beam. The attenuation length of the sample is given by $\mu(x,y)$.*

Figure 3.5 (A) shows the total attenuation length for water (blue), bone (green) and iodine (red) for a x-ray photon energy ($E = \frac{hc}{\lambda}$) from 1 keV to 100 keV. Soft tissue has an attenuation length very similar to that of water, since it is mainly composed of elements with low atomic numbers (H, O and C).

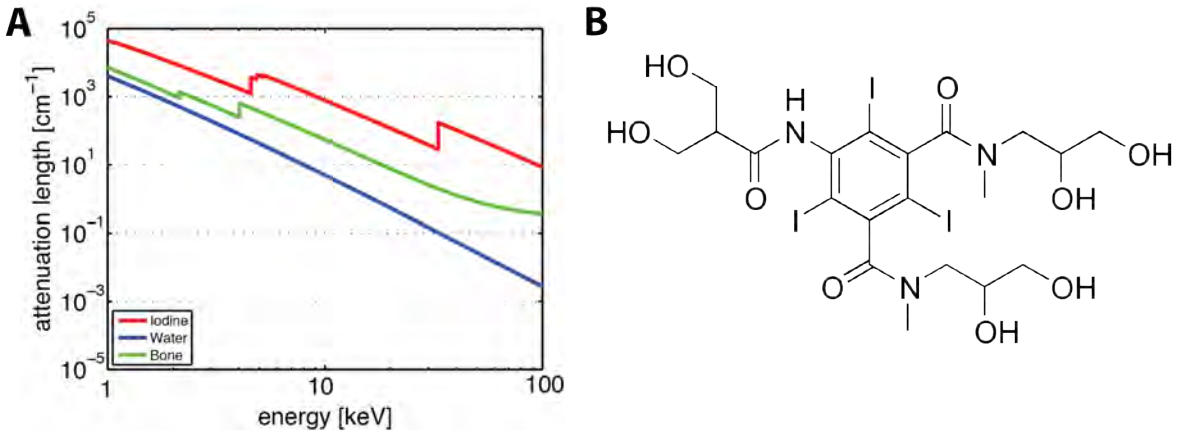

Figure 3.5: *(A) The attenuation length for iodine, water and bone plotted on double logarithmic scale. (B) Chemical structure of iobitridol.*

For imaging the x-ray photon energy is of the order 20 keV to 150 keV, where photoelectric absorption dominants over coherent and incoherent scattering. The x-ray photon energy is the same order of magnitude as the binding energy of the electrons to the atom. The binding energy defines the absorption edge, shown for iodine (33 keV) in Figure 3.5 (A) (red curve). It means that x-ray photons with an energy below the binding energy will not be absorbed by these electrons, while x-ray photons with an energy above will be absorbed by a finite probability. The probability is governed by the absorption cross section, σ_a. For energies above the absorption edges all electrons contribute to the absorption, and the absorption cross section has been to increase as Z^4 and decrease as E^{-3} (Als-Nielsen & McMorrow 2011). Thus, higher atomic number a the material and shorter wavelength of the x-ray beam will result in a stronger is the attenuation of the x-ray beam.

The phase shift of the x-ray beam gives a refraction angle

$$\alpha(y) = \frac{\partial}{\partial y} \int \delta(x, y) dy \tag{3.8}$$

The refraction angle is of the order $\sim 10^{-8}$ degree, and sophisticated experimental setups are needed in order to detect such a small refraction angle.

Phase contrast imaging is implemented at synchrotron radiation facilities, with a monochromatic, coherent x-ray beam, but also at laboratory x-ray sources by a grating interferometer (Pfeiffer et al. 2006). The grating interferometer also yields dark-field scatter images (Pfeiffer et al. 2008). The scattering reveals the distribution and orientation of nano-scale structures.

3.2.1 Contrast

The contrast in x-ray images are given by local differences in the atomic number (Z), the molar mass (M) and the mass density (ρ_M), for both attenuation based imaging ($\beta \propto Z^4 \frac{\rho_M}{M}$) and for phase contrast imaging ($\delta \propto Z \frac{\rho_M}{M}$). Absorption based x-ray imaging is very appropriate for imaging highly absorbing bone structures in a soft tissue matrix, while phase-contrast imaging have shown advantages for medical imaging with better contrast in biological samples (Pfeiffer et al. 2006).

An IAsp drug formulation contains 600 μM of IAsp ($C_{256}H_{381}N_{65}O_{79}S_6$), and the remaining part is primarily water. Since IAsp is made up of elements with low atomic number and the density of the drug is similar to the density of water, the insulin drug injected into adipose tissue cannot be visualized directly by either x-ray absorption or phase contrast radiography.

The insulin molecule can be labelled with up to four iodine atoms before altering the molecular structure. It gives an iodine concentration of 0.35 mg/mL of drug, and the density of the drug increases with 0.1 mg/mL. The linear attenuation length increases with about 3% at 34 keV (just above the K_α-edge for iodine). It was confirmed experimentally that the labelled insulin could not be visualized by K-edge imaging using synchrotron radiation (Thomsen 2011). The small change in density is not sufficient for phase-contrast imaging.

To our knowledge insulin has not been labelled with an atom with a higher atomic number than iodine.

Contrast agents

Since the subcutaneously injected insulin drug cannot be visualized directly we use an x-ray contrast agents to represent the drug, and use x-ray absorption based imaging for the visualizations. X-ray contrast agents are typically based on either barium (atomic number 56) or iodine (atomic number 53) (Webb & Flower 2012). The high atomic numbers mean that the x-ray attenuation length is higher than for soft tissue, shown for iodine in Figure 3.5 (A). Barium is insoluble in water and acid, and is neither absorbed or metabolised in patients (Widmark 2007). The iodinated contrast agents are water-soluble, and therefore selected for these studies.

Free iodine is toxic, so the iodine molecule is covalently bound to a stable organic functional group, like a benzene ring, shown for iobitridol in Figure 3.5 (B). The iodinated contrast agents can be divided into four groups; ionic monomers (one ring), ionic dimers (two rings), non-ionic monomers, and non-ionic dimers. The ionic contrast agents dissociate when injected, and therefore have a higher osmolarity than the non-ionic agents. This gives a water flux from the intra-cellular space to the extracellular space, and causes the cell to shrink. Furthermore the ions interact with the electrical potential of the cell membrane, making these contrast agents more toxic than the non-ionic contrast agents.

Tabel 3.1 lists some of the commercially available non-ionic iodine based contrast agents. The first five are monomers with an osmolarity of 600-700 mOsm/L, and a viscosity of 9-16 mPa·s at 20°C. The non-ionic dimer (iodixanol) have lower osmolarity, but higher viscosity due to the bigger particle size. The monomers were chosen due to the lower viscosity. The three contrast agents Ultravist, Omnipaque and Xenetix have similar osmolarity and viscosity.

Brand name (compound)	Iodine conc. [g/mL]	Visc. [mPa·s]	Osmolarity [mOsm/L]
Ultravist (iopromid)	300	9.2	607
Omnipaque (iohexol)	300	11.8	675
Xenetix (iobitridol)	300	11.8	695
Hexbrix (ioxaglate)	320	15.7	600
Visipaque (iodixanol)	320	26.6	290
Insulin drug	-	1.0	∼300

Table 3.1: *Brand name of iodinated contrast agent with the iodine compound in parenthesis. The compounds are sorted by viscosity.*

Xenetix where used in the presented studies. Both insulin and Xenetix distribute in the extracellular space (Bourrinet et al. 1995). A mixture of 70% IAsp and 30% Xenetix300 was selected as a trade-off between good contrast in the radiographic images, and increased viscosity. This mixture has a 7% higher density and about 50% higher viscosity than the pure drug.

The increased viscosity may effects the drug distribution. Allmendinger et al. (2014) found that the injection force in porcine tissue increases with the fluid viscosity, for viscosities in the range 1-100 mPa·s. According to our model for the pressure build up in humans, presented in section 2.3.1 (Eq. 2.5), an increased viscosity of 50% gives an increased tissue pressure of about 20%. The pressure is estimated for a 31G needle and calculated slightly away from the needle tip. The flow permeability of adipose pig tissue during injection was reported by Comley (2010) to be of the same order of magnitude, as in our measurements ($K \sim 10^{-11}$). This additional pressure should be taken into consideration when the drug distribution is evaluated.

To evaluate if the contrast media separates from the insulin drug during injection, 10 injections were performed in adipose pig tissue after the procedure described in Section 3.1.2. After freezing the samples, they were cut into 2 mm slices and a radiographic image was taken of each slice. Afterwards the slice containing the most drug was further sliced into 10 µm sections and the insulin visualized by *HU* staining [1]. Figure 3.6 shows an example of a radiographic image (A), and the corresponding histological image (B). The radiographic image shows the iodine distribution and the histological image shows the insulin distribution. The periphery of the insulin distribution found in (B) is shown as a red curve in the radiographic image (A). Apart from the small deformations due to the histological preparation, the distribution of the contrast agent is seen to represent the insulin distribution very well. Figure 3.6 (C) shows a zoom-in on the histological image in (B) (red box). The cracking of the tissue structures (red arrow) are an expected artefact related to the freezing and histological preparation and not related to the injection procedure. The structure of the adipose tissue is preserved after injection although the injected fluid is hyper-osmolar.

[1] A detailed description of the histological staining is given in the Material and Methods section in Paper IV.

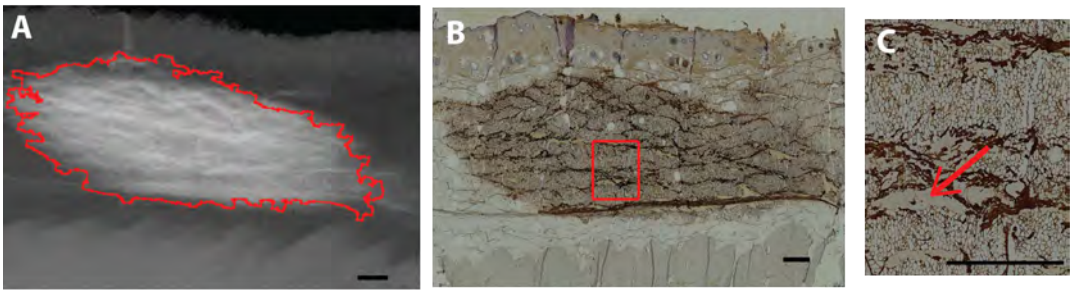

Figure 3.6: *Comparison between a radiography image of a slice of the tissue sample (A) and a histological image from the same slice (B). The radiographic image shows the distribution of the iodine contrast agent, and the in the histological image the insulin was stained by HUI18. The periphery of the insulin bolus obtained from (B) is shown as red curve in (A). (C) A zoom-in on the histological image (red box). Cracking of the tissue structures (red arrow) is an expected artefact due the freezing and histological preparation of the sample. The scalebar is 2 mm*

3.2.2 Polychromatic x-ray imaging

In Section 3.2 the theory for x-ray radiography was presented for a monochromatic x-ray beam. Commercial x-ray imaging systems operate with a polychromatic x-ray beam, where the x-ray beam is generated by the deceleration of electrons. The electrons are released from a heated filament and accelerated toward the target by an applied high voltage. The deceleration of electrons in the target gives a broad x-ray spectrum (bremsstrahlung). The target material is usually tungsten or molybdenum, which have a high melting point, and are able to resist the heat generated by the electron beam. The applied acceleration voltage sets the upper limit for the x-ray photon energy. Figure 3.7 shows the energy spectrum as emitted from a molybdenum target for four different acceleration voltages. The peaks are the characteristic K_α- and K_β-lines for molybdenum.

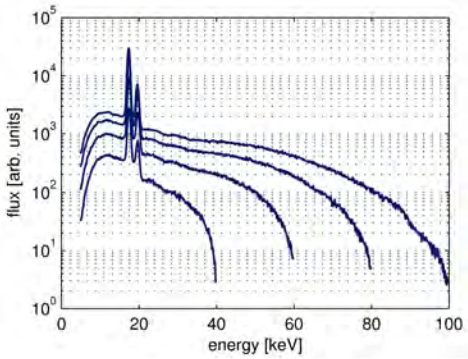

Figure 3.7: *Polychromatic x-ray spectrum from a molybdenum target at an acceleration voltage of 40 kV, 60 kV, 80 kV and 100 kV. The spectra were measured experimentally by a CdTe x-ray detector (*Amptek Inc. *2015).*

The transmitted intensity of a polychromatic beam is given by

$$I(y') = \int dE I_0(y', E) D(E) \exp\left(-\int \mu(E, x', y') dx'\right) \quad (3.9)$$

where E is the x-ray photon energy, $I_0(y', E)$ is the incoming beam intensity and $D(E)$ is the energy dependent detective quantum efficiency of the detector.

For a polychromatic beam the image contrast depends not only on the material composition in the sample, but also on the energy dependent detector efficiency. The next section discuss how the detector design effects the image noise and spatial resolution.

3.2.3 Detector systems

This section presents the key concepts of the three different detector systems that have been used for the experiments presented in this thesis. The three systems used are: A scintillator screen in conjunction with a charged coupled device (CCD), a hybrid photon counting detector, and an energy sensitive detector. The optimal detector has high spatial resolution, high detector efficiency, high signal-to-noise ratio, and spectral resolution.

The detector systems are compared in Table 3.2. It have not been possible to obtain product information about the CCD detector in the x-ray microscope used (XRadia Versa 410, ZEISS) (*ZEISS* 2015). The listed values are based on examples from the literature (Crystals 2008, Nikl 2006, Zhao et al. 2004).

Detector	Scintiallator/CCD	PILATUS 100 K	LAMBDA
Pixel size	∼10 μm	172 μm	55 μm
Sice of detector screen	$\sim$ 2000 $\times$ 2000 pixels^2	487 $\times$ 195 pixels^2	256 $\times$ 256 pixels^2
Absorbing layer material	CsI:TI	silicon	silicon
Absorbing layer thickness	∼200 µm	350-1000 μm	300 μm
Absorption efficiency (50 keV)	∼45%	$\sim 3 - 10\%$	∼3%

Table 3.2: *Characteristics of a scintillator screen in conjunction with a charged coupled device (CCD)(Crystals 2008, Nikl 2006, Zhao et al. 2004), a hybrid photon counting detector (PILATUS 100 K) (Kraft et al. 2009a), and an energy sensitive detector (LAMBDA) (Pennicard et al. 2013). The efficiency is given as the absorption in the detector layer.*

Figure 3.8 (A) shows the detection principle for a scintillator screen coupled to a CCD detector. A scintillator screen stops the x-ray photons and convert these into visible light that is subsequently detected by the CCD. The scintillator screen can be made of e.g. caesium iodine doped with titanium (CsI:TI) (Nikl 2006, Zhao et al. 2004), which is used in commercial flat panel detectors (*Hamamatsu Photonics K.K.* 2015).

Figure 3.8 (B) shows the detection principle for hybrid photon counting solid state detector. One example is the PILATUS 100K detector, developed for x-ray diffraction experiments at the Paul Scherrer Institut (Broennimann et al. 2006, Hülsen-Bollier 2005). In the PILATUS detector, the active layer is a biased silicon layer. The incident x-ray photons generate a charge cloud, which is directly transferred to a read-out chip (Kraft et al. 2009a,b).

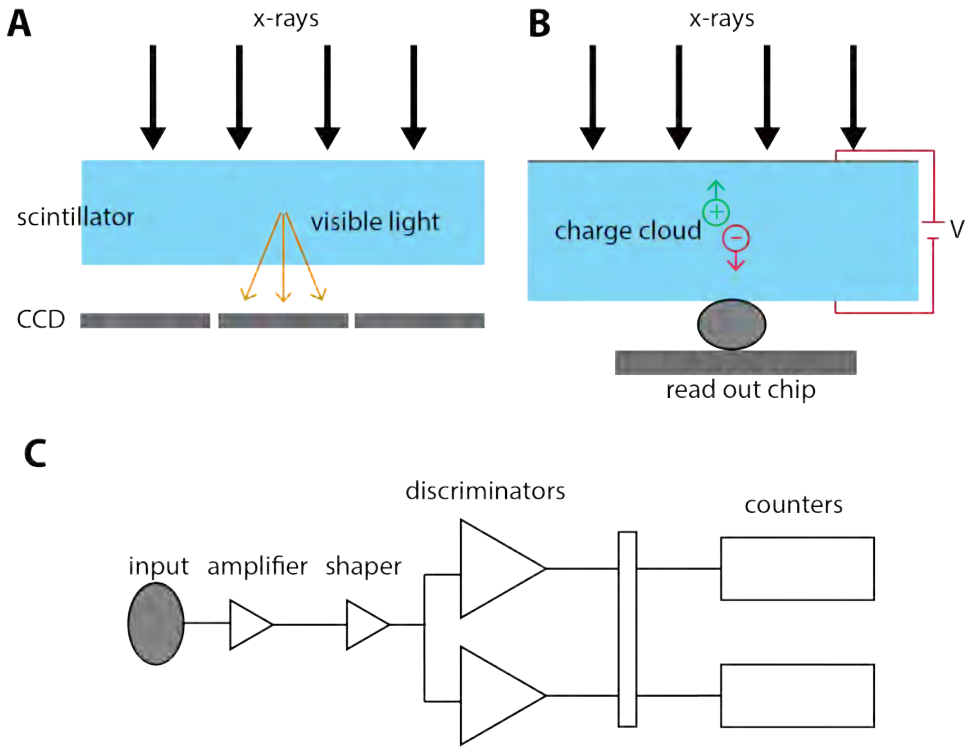

Figure 3.8: *Schematic presentation of the scintillator coupled to a CCD detector (A), a hybrid photon counting detector (B), and the read out chip, Medipix3, in the LAMBDA detector (C).*

The advantages of the scintillator screen coupled to the CCD detector is higher efficiency for high energy photons and higher spatial resolution (smaller pixel size) compared to the PILATUS. The spatial resolution is not only determined by the pixel size, but is also effected by the physical precision by which the photons are detected. For both detector systems are the design a trade-of between the detection efficiency and spatial resolution. A thin detection layer improves the spatial resolution, but reduce the detection efficiency (Stampanoni et al. 2002). For the PILATUS the detection efficiency is improved in the newly develop PILATUS3 X detector (*DECTRIS* 2015). In this detector the active layer is made of cadmium telluride, which improves the efficiency for a 1 mm layer to 90% at 60 keV.

The disadvantages of the scintillator screen coupled to the CCD detector is that the x-ray photons are detected indirectly. This process causes the image quality to be degraded from several sources of noise, e.g shot noise (statistical fluctuation in the light output from the scintillator screen), and dark current (thermal generated electrons in the CCD pixel). In the PILATUS 100K detector an energy threshold can be set to discriminate low energy photons, and thereby remove dark current and improve the signal-to-noise ratio. Furthermore this detector have a fast read out time, and high count rate, which allows for fast measurements with a high x-ray flux (Bech et al. 2008).

The spectral resolution can be obtained by the energy sensitive LAMBDA detector (Large Area Medipix3 Based Detector Array) (Pennicard et al. 2013). As for the PILATUS detector the active layer is a biased silicon layer. The special feature of the LAMBDA detector is the

Medipix3 read-out chip. A simplified illustration of the read-out chip is shown in Figure 3.8 (C). The discriminators receive a current signal proportional to the incoming amount of charge. A logical signal is sent to the counters, depending on whether the signal is above or below the predefined threshold for the discriminators. This gives two images as output. By subtracting the images, only x-ray photons with an energy between the thresholds contribute to the final image and nearly monochromatic images can be obtained. This can improve the image contrast. The energy resolution is about 3 keV (Ballabriga et al. 2006, 2011).

In summary the scintillator detector in conjunction with a CCD gives a higher spatial resolution than the PILATUS detector and higher efficiency for high energy x-ray photons. The improved resolution comes with a cost of a lower signal to noise ratio. The energy dispersive LAMBDA detector allows to discriminate between the x-ray photon energies, which can be used to improve the image contrast. These measurements require a long acquisition time since only a small fraction of x-ray photons contribute to the image. The next section will discuss the trade-off between spatial resolution, acquisition time and field of view (FOV).

3.2.4 Spatial resolution

The spatial resolutions limits on the size of the structures that can be distinguished.

The resolution is limited by two factors; the intrinsic detector resolution and the geometry of the setup. The intrinsic detector resolution is determined by the pixel size and by the spatial precision in the physical and digital detection process. The effective pixel size in the image is $\frac{x_D}{M}$, where x_D is the width of the detector pixels and M is the magnification. The magnification is given by the ratio of the source-detector (x_{sd}), and source-sample distance (x_{ss}). A higher magnification is obtained by either moving the sample closer to the source or moving the detector away from the source. A higher resolution gives a smaller field of view, and the flux is reduced at the detector screen, if the source to detector distance is increased.

The geometrical resolution is given by

$$\sigma_f = \frac{x_{sd} - x_{ss}}{x_{ss}} \cdot f \tag{3.10}$$

where f is the focal spot size, x_{sd} is the source to detector distance and x_{ss} is the source to sample distance, shown in Figure 3.9. The geometric resolution can be improved by decreasing the focal spot size or increasing the source to detector distance, which both gives an decreased flux. Furthermore a very narrow beam spot or a longer source to detector distance cause diffraction effects at the sample edges.

The image resolution is determined experimentally as the full width half max (FWHM) of the line spread function obtained from the projection or tomography image of a sharp edge.

In the case of adipose tissue samples the insulin distributes in the extracellular space between the fat cells, shown in Figure 3.10 (A). The size of the extracellular structures are of the order 3 μm, estimated from the FWHM of the intensity peaks along the red line (B). In order to resolve these structures an image resolution of the order 1-2 µm is needed, and even better in order to quantify the drug content in each pore. For a flat panel detector with about 2000×2000 pixels,

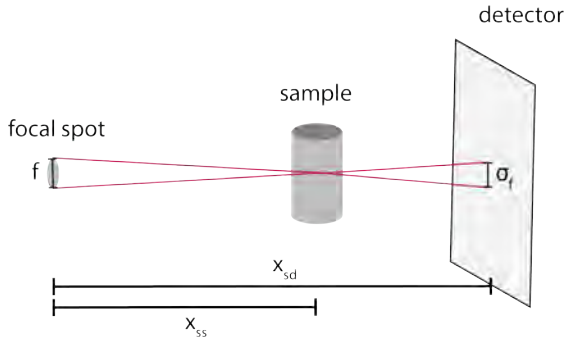

Figure 3.9: *The geometric resolution in a tomography setup is defined by the focal spot size (f), the source to sample (x_{ss}) and source to detector distance (x_{sd}).*

this resolution will results in a field of view of about 2×2 mm. This is considerably smaller than an insulin injection of 0.1 mL of drug, which has a diameter of about 10 mm.

In a tomographic reconstruction each volume element (voxel) represents the local x-ray attenuation length. Making a reconstruction with a bigger voxel size than the adipose structure means that the reconstructed gray scale (g) for each voxel reflects both the tissue porosity (ϕ) and the concentration (c) of the contrast agent.

$$g = (1 - c\phi)g_{\text{tissue}} + c\phi g_{\text{fluid}} \tag{3.11}$$

where g_{tissue} and g_{fluid} are the reconstructed gray scale values for the tissue, and the injected fluid (30% Xenetix), respectively.

Local variation in the tissue porosity will be seen as variation in the reconstructed grey scale for the insulin bolus injection. This means that if the injection of the drug causes local damage of the tissue structures (increase ϕ) it will be seen as an increase in the reconstructed grey scale value g.

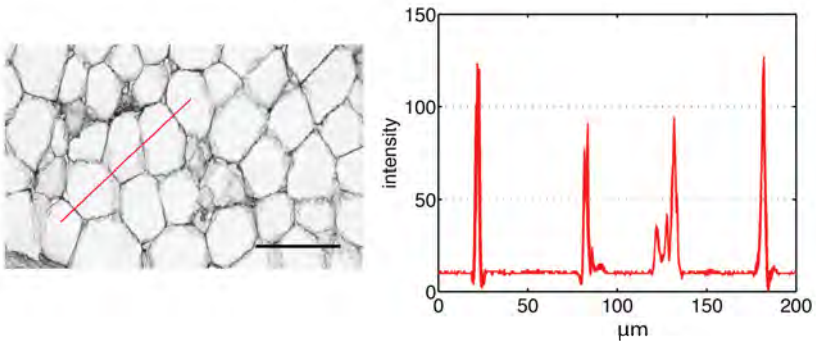

Figure 3.10: *(A) Histological image of subcutaneous pig tissue with IAsp distributed in the extracellular space. The scalebar is 0.1 mm. (B) Image intensity profile along the red line in (A). The size of the pore structures are estimated from FWHM of the peaks.*

3.3 Summary

This chapter has presented and discussed the injection procedure used in the injection studies presented in Chapter 5. The injection procedure was selected such that it could be evaluated how the injection technique influences the injection bolus, with a minimal influence of physiological effects. At the same time the procedure ensures that tissue layer thickness and elasticity are as close to the *in vivo* situation as possible.

In the x-ray radiography and tomography images the insulin drug is represented by an iodine based contrast agent. Like the insulin drug the contrast agent distributes in the intracellular space. From a comparison with histology the distribution of the contrast agent was seen to be similar to the insulin distribution. To visualize the shape and overall distribution of the drug, the image pixel size must be larger than the size of the intracellular pore structures. Consequently the visualized density distribution reflects variations in both the local tissue porosity and drug concentration.

In Chapter 4 the visualizations will be extended to 3D by making x-ray computed tomography.

Chapter 4

X-ray computed tomography

In the previous chapter it was shown that subcutaneous injections of soluble insulin formulations could be represented by an iodine contrast agent and visualized by x-ray absorption radiography. This chapter shows the 3D visualization and quantification of the drug distribution in subcutaneous pig tissue by x-ray computed tomography. The presented results are based on Paper II (Thomsen et al. 2015a) and Paper III (Thomsen et al. 2012).

This chapter starts with a presentation of the tomographic reconstruction algorithm and a discussion of the image artefacts seen for polychromatic x-ray computed tomography. One of these artefacts are beam hardening, which gives artificial density variations in the tomographic images and influences quantitative measurements. Beam hardening artefacts depend on several factors, e.g. the energy dependent intensity distribution of the x-ray spectrum, the energy dependent quantum efficiency of the detector, the sample geometry and density, and the geometry of the experimental setup.

Paper II presents a virtual x-ray tomography experiment in McXtrace (Knudsen et al. 2013) with implementation of cone beam geometry and the energy dependent detector efficiency. The simulation tool is used to study how beam hardening artefacts influences the estimated spatial drug distribution for the subcutaneous injections.

Paper III presents the visualization and quantification of the subcutaneous injections by x-ray computed tomography. The experimental protocol was implemented at conventional x-ray system to be appropriate for studies in RD. The spatial drug distribution calculated from the polychromatic data will be compared to monochromatic measurements, and the effect of beam hardening and image contrast evaluated.

4.1 Computed tomography

This section is based on the book chapter ***"Neutron Imaging"*** *from* ***Neutron Scattering: Theory, Instrumentation and Simulation*** *by K. Lefmann. (Paper VI) (Thomsen & Strobl 2014b)*

In Chapter 3 the image contrast and spatial resolution were discussed for 2D radiographic images. This section presents the reconstruction algorithm for x-ray computed tomography

(CT). X-ray CT was invented by Godfrey Hounsfield (Hounsfield 1973) and Allan McLeord Cormack (Cormack 1963) during the 1960s, and the first clinical scan was performed in 1971.

The basic idea in x-ray CT is to combine radiographic images obtained from different view angles to make a 3D reconstruction of the interior of the sample. The grey scale values in the reconstructed images (the tomograms) are given by the local x-ray attenuation length, $\mu(x, y, z)$. It means that the grey scale value is related to the material composition (Z) and the mass density (ρ_M). The technique is widely used for non-invasive morphological and quantitative studies. One example is studies of bone morphology and mineral density in rodent using either synchrotron radiation (Nuzzo et al. 2002, Ito et al. 2003) or a conventional x-ray tube (Kazakia et al. 2008, Nazarian et al. 2008).

For simplicity the reconstruction algorithm will be presented for a 2D sample illuminated by a monochromatic x-ray beam in a parallel beam geometry, as illustrated in Figure 4.1. The figure shows the 1D projection of a 2D object. The object is described by its x-ray attenuation length $\mu(x, y)$, and illuminated from an angle θ. The transmission of the beam (T_θ) is measured along the line $x' = x\cos\theta + y\sin\theta$. The projection is defined as (Slaney & Kak 1988)

$$P_\Theta(x') = -\log\left(T_\theta(x')\right) \tag{4.1}$$

$$= \int_{-\infty}^{\infty} dx \int_{-\infty}^{\infty} dy \mu(x, y)\delta(x\cos\theta + y\sin\theta - x') \tag{4.2}$$

where $P_\Theta(x')$ is called the Radon transformation of $\mu(x, y)$ (Radon 2005). The task for the reconstruction algorithm is to obtain the function $\mu(x, y)$, when the projection, $P_\Theta(x')$ is known for a limited number of angle steps and x'-values.

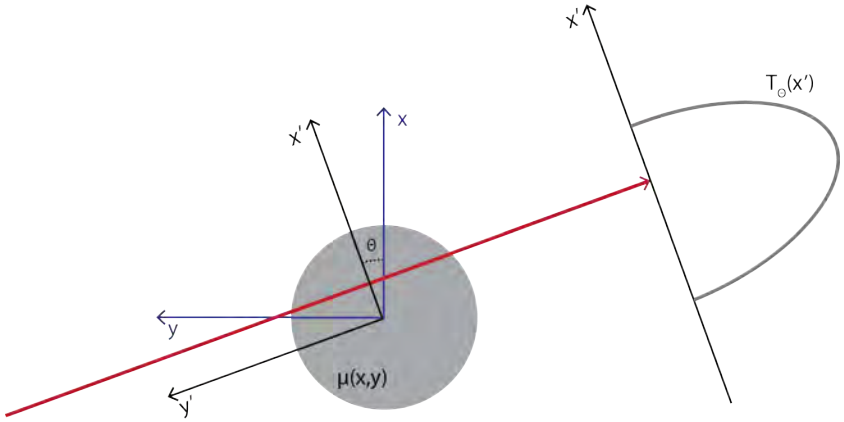

Figure 4.1: *Transmission of a monochromatic x-ray beam measured in a detector pixel at position x'. The sample is illuminated from an angle θ. The sample can have a spatial variation in the absorption length given by $\mu(x, y)$.*

Two major categories of reconstruction algorithms exit; analytical reconstructions and iterative reconstructions. The reconstruction used throughout this thesis is the filtered backprojection algorithm (FBP), which is an analytical reconstruction algorithm (Slaney & Kak 1988).

This algorithm can be implemented to run very efficiently, and the reconstruction of even large data sets can be obtained within minutes. A major disadvantage of this algorithm is that areas with high attenuation length in the sample may produce streak artefacts in the reconstruction due to the backprojection procedure.

For the iterative reconstruction algorithms, the solution to $\mu(x, y)$ is iteratively optimized to the measured projections (Beister et al. 2012, Willemink et al. 2013). The algorithms are more flexible, and e.g. an irregular sampling scheme, noise models, and the detector geometry can be incorporated. In that way the image quality can be improved, and the algorithm has shown advantages for low dose CT (Liu 2014). The improvements come with a cost of higher computation time than the FBP.

The FBP algorithm is based on the Fourier Slice Theorem, which states that the Fourier transformation of the projection, $\tilde{P}_\theta$, is equal to the 2-dimensional Fourier transformation of the object function, $\tilde{\mu}$, along a line in the Fourier domain (Slaney & Kak 1988). The line goes through the origin and subtends the angle θ with respect to the u-axis, shown in Figure 4.2 (A) for a discrete sampling of data points. The Fourier Slice Theorem is directly proven from Eq. (4.2)

$$\begin{aligned} \tilde{P}_\theta(w) &= \int_{-\infty}^{\infty} dx' P_\Theta(x') \exp\left(-i2\pi w x'\right) && (4.3) \\ &= \int_{-\infty}^{\infty} dx \int_{-\infty}^{\infty} dy \mu(x, y) \exp\left(-i2\pi(xu + yv)\right) \\ &= \tilde{\mu}(u, v) && (4.4) \end{aligned}$$

with the spatial frequency $w = u\cos(\theta) + v\sin(\theta)$.
The Fourier transformation of the object function becomes known along more lines in the Fourier domain, when measuring the projections from several angles, shown in Figure 4.2 (B).

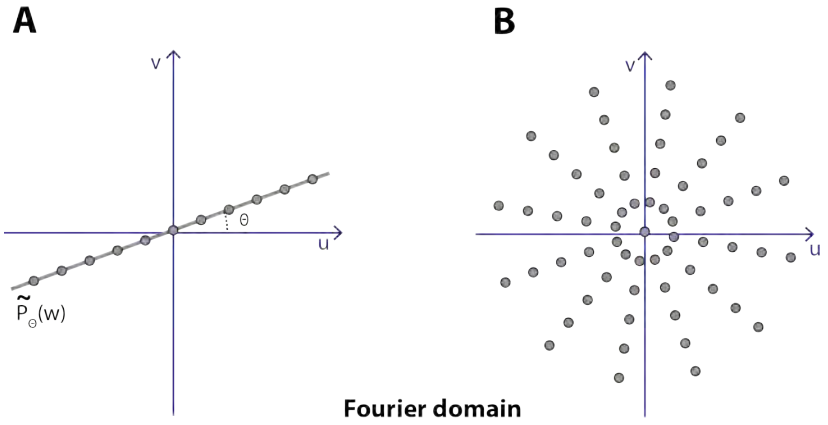

Figure 4.2: *(A) Fourier transformation of a single projection measured in discrete points. (B) Projections from multiple angles.*

For the projections to cover the whole Fourier domain equally, each projection should ideally cover a pie shape in the Fourier domain, as shown in Figure 4.3 (A). Since information is only obtained along a single line (B), the points near the rotational axis are much closer sampled than those further away. To compensate for that, a linear ramp filter, $|w|$, is applied (C) before the inverse Fourier transformation is performed.

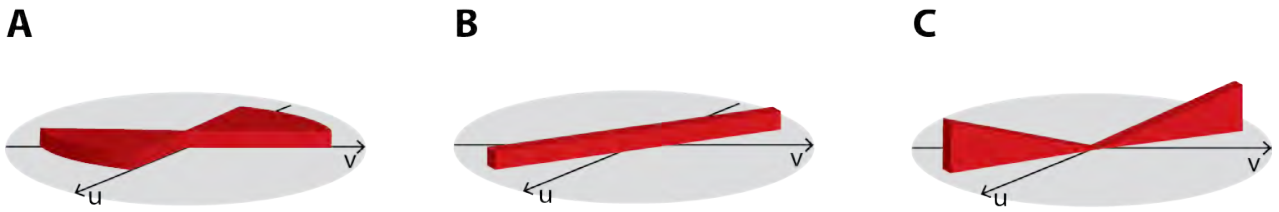

Figure 4.3: *(A) Ideal situation where the Fourier transform of the projection covers a pie shape in the Fourier domain. (B) Fourier transformation of a single projection before, and (C) after applying the spatial filter $|w|$.*

The filter function is introduced as the Jacobian when changing from Cartesian to polar coordinates in the Fourier transformation

$$\mu(x,y) = \int_{-\infty}^{\infty} du \int_{-\infty}^{\infty} dv \tilde{\mu}(u,v) \exp\left(i2\pi(xu+yv)\right) \tag{4.5}$$

$$= \int_{0}^{\pi} d\theta \int_{-\infty}^{\infty} dw |w| \tilde{\mu}(w,\theta) \exp\left(i2\pi w(x\cos\theta + y\sin\theta)\right) \tag{4.6}$$

where it has been used that $\mathcal{FT}(\mu(w,\theta)) = \mathcal{FT}(\mu(-w,\theta+\pi))$. This restricts the domain for θ to $[0,\pi[$ and introduces the numerical sign in the filter function $|w|$.

By using the Fourier Slice Theorem in Eq. (4.6), the FBP algorithm is given by (Slaney & Kak 1988)

$$\mu(x,y) = \int_{0}^{\pi} d\theta \mathcal{FT}^{-1}(\tilde{P}_\theta(w)|w|) \tag{4.7}$$

where $\mathcal{FT}^{-1}(\tilde{P}_\theta(w))$ is the inverse Fourier transform of $\tilde{P}_\theta(w)$. As the name implies the algorithm consists of two parts: (1) A filtering in the Fourier domain with the filter function $|w|$, called the Ram-Lak filter. (2) A backprojection of the filtered data over the image plane.

In actual experiments the projections are known in discrete values of x' (the detector pixels), and from a finite number of angles, θ, and the FBP is implemented using the discrete Fourier Transform (DFT).

Data collected by a 1D detector with N pixels from M different angles are collected in a $N \times M$ matrix, called a sinogram. The reconstruction of the object goes in the following four steps: (1) The 1D DFT is performed along the N detector pixels in the sinogram. (2) The sinogram is filtered by the Ram-Lak filter. (3) The 1D inverse DFT along the N detector pixel is performed. These operations do not change the dimension of the matrix. (4) Each point, (x,y), in the object is reconstructed. The reconstructed slice has $N \times N$ points. The point (x,y) is reconstructed by making a sum of the corresponding data points (x') for all θ. Since

only discrete values for x' are given in the data set, the value $x' = x\cos\theta + y\sin\theta$ does not necessary exist, but is then estimated by interpolation from the neighbouring points.

The FBP algorithm is illustrated in Figure 4.4, where a 2D phantom is reconstructed from 8 projections (A), 32 projections (B) and 64 projections (C). The figure shows how the reconstruction improves as the number of projections increases.

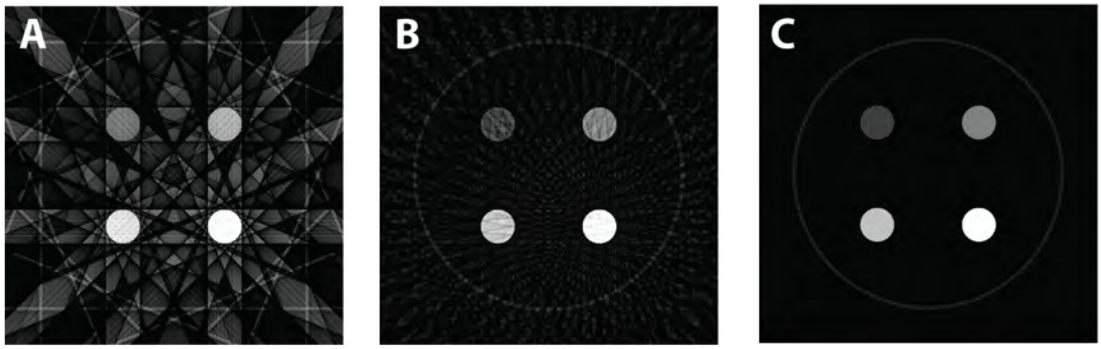

Figure 4.4: *Reconstruction of a synthetic sample by the FBP from (A) 8 projections, (B) 16 projections, and (C) 32 projections.*

The reconstruction algorithm is extended to 3D by repeating the algorithm for different height steps in the case of parallel beam geometry or by implementation of cone-beam geometry. For the full derivation of FBP algorithm with cone beam geometry, the reader is referred to Slaney & Kak (1988) and Feldkamp et al. (1984). The tomography setup with cone beam geometry is illustrated in Figure 4.5.

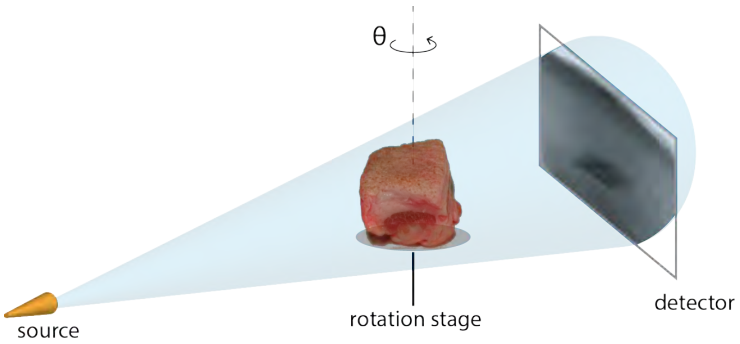

Figure 4.5: *Experimental setup for x-ray CT with cone beam geometry.*

4.1.1 Artefacts in tomographic reconstructions

The FBP algorithm was derived for a monochromatic x-ray beam, where the projection is a line integral over the attenuation length given by Eq. (4.2). In the case of a polychromatic x-ray beam the transmitted intensity is given by Eq. (3.9) and the projection is calculated as

$$P_\theta(x') = -\ln\left(\frac{\int dE I_0(x', E) D(E) \exp\left(-\int \mu(E, x', y') dy'\right)}{\int dE I_0(x', E) D(E)}\right) \tag{4.8}$$

The x-ray attenuation length decreases strongly with increasing photon energy (except at the absorption edges), meaning that low energy photons will be absorbed more efficiently than high energy photons. Figure 4.6 (A) illustrates the energy dependent intensity distribution of the x-ray spectrum emitted from a molybdenum target (dark blue), and how the distribution is changed after penetrating a 2 mm aluminium (Al) filter (dashed light blue). The weighted average energy of the spectrum, $\langle E \rangle = \frac{\int dE E I(E)}{\int dE I(E)}$, increases from 18 keV, when emitted from the source, to 29 keV after penetrating the Al filter. This effect is called beam hardening (Brooks & Di Chiro 1976).

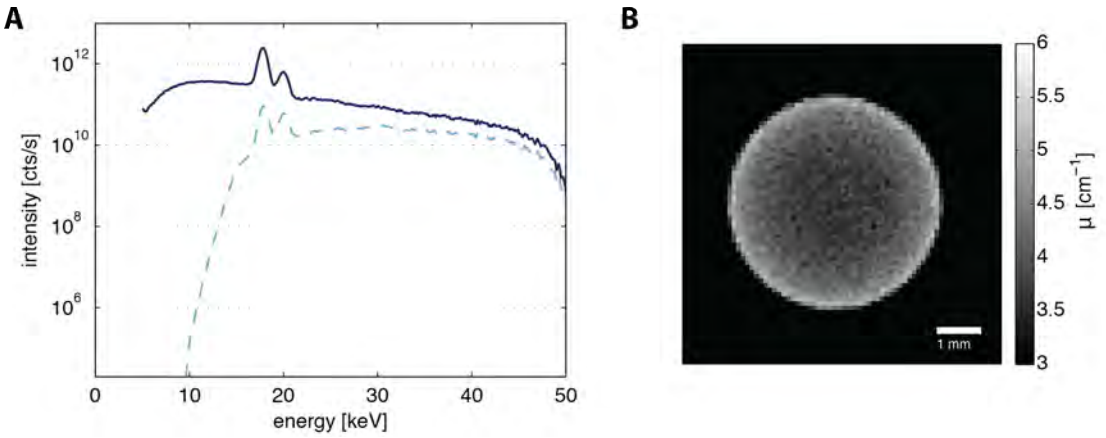

Figure 4.6: *(A) Bremsstrahlung spectrum from a molybdenum target at an acceleration voltage of 50 kV, as emitted from the source (dark solid blue) and after penetrating a 2 mm aluminium filter (light dashed blue). The spectrum is simulated by McXtrace. (B) Cupping artefacts in a aluminium cylinder with a diameter of 5 mm. Experimental data adapted from Paper II*

In the case of a low absorbing material and a short penetration length the projection can be approximated by (Chabior et al. 2011).

$$P_\theta(x') \approx -\int dy' \left(\frac{\int dE I_0(x', E) D(E) \mu(E, x', y')}{\int dE I_0(x', E) D(E)}\right) \tag{4.9}$$

The reconstructed attenuation length becomes a weighted average over all energies in the spectrum, and depends on the energy dependent detector efficiency ($D(E)$). Beyond the regime where this approximation is valid, the grey scale value decreases artificially toward the center of the sample. This effect is known as the cupping effect (Brooks & Di Chiro 1976), illustrated for an Al cylinder in Figure 4.6 (B). The cupping effect increases with increasing material density

and sample thickness (Meganck et al. 2009). The grey scale values become dependent on the sample geometry and the surrounding materials.

The cupping effect can be reduced by a physical filtering of the x-ray beam to attenuate the low energy photons (Jennings 1988, Lopes et al. 2000) or by dual energy methods (Petersilka et al. 2008, Coleman & Sinclair 1985, Alvarez & Macovski 1976). Another approach is to use a linearisation procedure (Herman 1979, Hammersberg & Mangard 1998). From Eq. (4.8) it is seen that, for a polychromatic x-ray beam, $P_\theta(x')$ does not decrease linearly with the sample thickness, as it is the case for a monochromatic beam. When making a linearisation, the attenuation, as a function of object thickness, is predicted from calibration measurements or the reconstruction of from the sample itself (Van de Casteele & Raman 2002, Krumm et al. 2008, Van Gompel et al. 2011). The projection images measured for the sample is adjusted to depend linearly on the thickness before the final reconstruction is performed.

Other artefacts include streaks, ring artefacts and partial volume effects (Schulze et al. 2014). Streak artefacts appear from strongly absorbing materials, such as metal parts and are caused by beam hardening, scattering, and the backprojection procedure in the reconstruction algorithm. Ring artefacts are often related to variations in the response of individual detector pixels. Partial volume artefacts are due to interpolation in the image plane from the finite number of projections and pixel elements in each projection. This causes a blurring of the edge structures, which degrades the image resolution.

4.2 Presentation of Paper II

This section summarizes the results from Paper II, *"Prediction of beam hardening artefacts in computed tomography using Monte Carlo simulations"* (Thomsen et al. 2015a). A virtual x-ray tomography experiment was designed in McXtrace, and the simulated data was compared to experimental data. It was demonstrated how the cupping artefacts in tomograms could be well reproduced by Monte Carlo simulations.

4.2.1 Monte Carlo simulations

McXtrace does not simulate individual photons but ensembles of photons, called rays. In each ray the photons have common direction, energy, polarisation, momentum and phase. The number of photons in each ray is, by convention, called the weight factor. The initial weight factor is determined by the spectral density of the energy spectrum as emitted from the source (Knudsen et al. 2013). When a photon penetrates an absorbing material, it will be absorbed by a probability given by the absorption cross section. To optimise the simulation no rays are removed but the weight factor for each ray is multiplied by the transmission probability $\exp\left(-\int \mu(E,\mathbf{r})dl\right)$, where $\mathbf{r}$ is the position and the integral runs over the path of the ray.

As input McXtrace takes the x-ray spectrum emitted from the target, the energy dependent x-ray attenuation coefficient, the sample geometry, and the energy dependent detector efficiency.

For the presented experiments the x-ray spectrum for the molybdenum target was measured experimentally using an XR-100T-CdTe detector from AmpTek (*Amptek Inc.* 2015). The spectrum was measured at the CT-scanner system Phoenix Nanotom S (*GE Measurements & Control* 2013). McXtrace also offers source components that generate the spectrum from a theoretical approximation (Kramers 1923) and tabulated values for the energy distribution (Bearden 1967). The simulations were optimized by only considering rays, that had a direction into the solid angle covered by the detector window. The detector module was 201×195 pixels, with a pixel size of 172×172 μm^2.

The energy dependent x-ray attenuation lengths were taken from the XCOM database administrated by the National Institute of Standards and Technology (NIST) (Berger et al. 1998).

The detector used in the real experiment was the PILATUS 100K detector (Broennimann et al. 2006), where the absorbing silicon layer is 1 mm thick. In the simulations the energy dependent detector efficiency was assumed to be purely determined by the absorption in the silicon layer. The 50 µm aluminium filter placed in front of the detector window was included in the simulations (Kraft et al. 2009a). Air absorption was taken into account, but scattering and refraction of the X-ray photons had not been included in the simulations. The simulated experimental setup is illustrated in Figure 4.7. Each simulated tomography scan has 401 projections over 360° with 10^8 simulated rays for each projection.

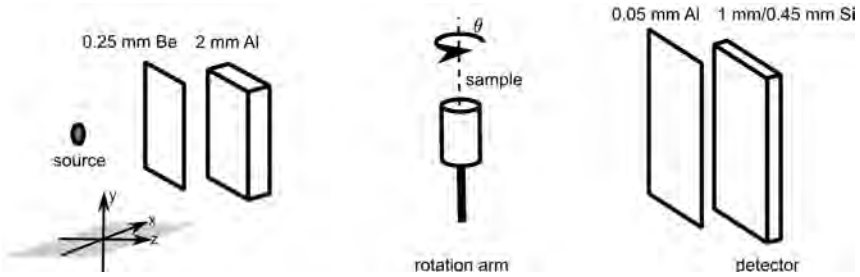

Figure 4.7: *Experimental setup as simulated in McXtrace. The setup is constructed to match the experimental setup at the laboratory x-ray source. The figure is adapted from Paper II*

4.2.2 Experimental design

The experiments were performed at the Technische Universität München. The x-ray source was a rotating anode with a molybdenum target. The acceleration voltage and current were set at 50 keV and 70 mA, respectively. A 2 mm aluminium filter was placed in front of the beam to avoid saturation of the detector. The filter also reduces beam hardening artefacts. Each tomography scan has 410 projections over 360°, and an exposure time of 150 ms per projection. The magnification was ×1.58, which gave an effective voxel size of 102×102× 102 μm^3 in the reconstructions.

The phantom samples were cubes ($10\times10\times10$ mm^3) with a cylinder in the center (diameter 5 mm), shown in Figure 4.8 (A). For one phantom the cube was made of polymethyl methacrylate (PMMA) and the cylinder made of Al, and for the other phantom it was opposite.

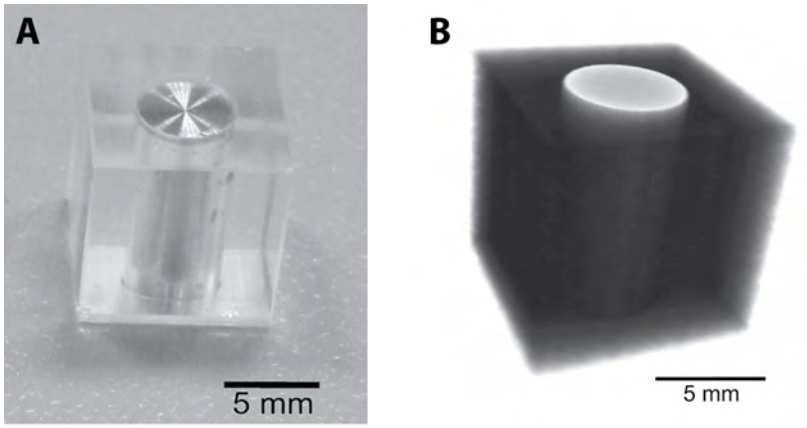

Figure 4.8: *(A) Image of one of the two phantom samples. The $10\times10\times10$ mm^3 cube is made of PMMA and the cylinder is made of aluminium and has a diameter of 5 mm. (B) 3D rendering of the phantom obtained from simulated projection images. The figures are adapted from Paper II*

4.2.3 Results

Figure 4.8 (B) shows a 3D rendering of the reconstructed PMMA cube with the aluminium cylinder embedded in the center. The reconstruction is calculated from simulated data.

Figure 4.9 (A) shows a horizontal cross section of the reconstruction. The reconstructed attenuation length along the red horizontal line is shown in Figure 4.9 (B) for the experimental data (blue) and the simulated data (green). Cupping is seen in the Al cylinder, but not in the PMMA cube, due to the 2 mm Al filter. The simulations reproduce the cupping artefact in the tomograms very well, and there is a good numerical agreement between the simulated and experimental data. For each of the samples the average reconstructed attenuation length and the standard deviation was calculated for PMMA and Al, collected in Table 4.1.

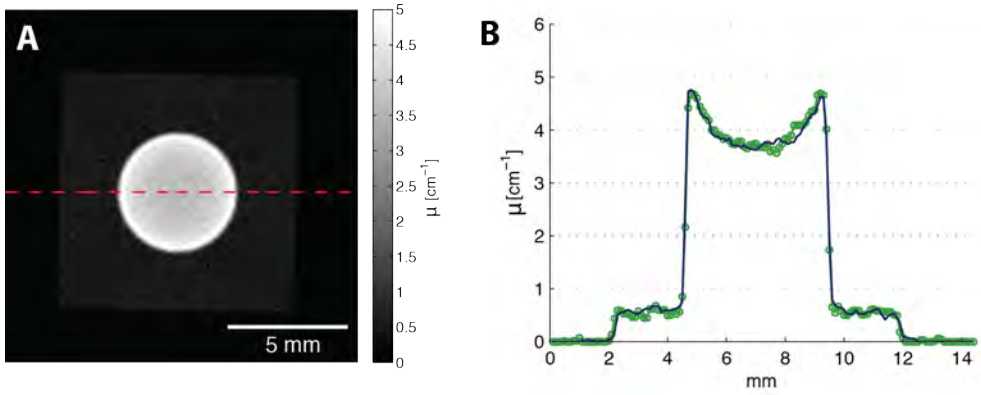

Figure 4.9: *(A) Horizontal slice of the reconstruction of the PMMA cube with the Al cylinder in the center. The reconstructed attenuation length along the horizontal red line is plotted in (B) for experimental data (blue) and simulated data (green). The figures are adapted from Paper II*

Average attenuation lenght (standard deviation) [cm^{-1}]			
		PMMA	Al
PMMA cube	exp	0.54 (0.15)	4.03 (0.56)
10×10×10 mm^3	sim	0.55 (0.24)	4.17 (0.62)
Al cube	exp	1.06 (0.27)	3.10 (0.38)
10×10×10 mm^3	sim	0.98 (0.28)	3.26 (0.43)
Signal-to-noise ratio			
		PMMA	Al
PMMA cube	exp	3.56	7.14
10×10×10 mm^3	sim	2.31	6.71
Al cube	exp	3.93	8.21
10×10×10 mm^3	sim	3.48	7.58

Table 4.1: *Average attenuation coefficient (standard deviation) and signal-to-noise ratio of the voxels values for PMMA and Al for experimental data (first row) and simulated data (second row). The values are calculated for each of the phantom samples; PMMA cube with a Al cylinder in the center, and Al cube with a PMMA cylinder in the center. The average is taken over the total volume of the cylinder and the cube. This corresponds to about $12{\cdot}10^4$ and $50{\cdot}10^4$ voxels for the cylinder and cube, respectively. The standard deviation of the mean attenuation coefficient is less than 0.1% for all materials.*

The deviation between the average reconstructed attenuation coefficients for all materials was between 2-8%. The largest deviation was found for the PMMA cylinder embedded in the Al cube, where the beam has been strongly attenuated by the Al cube before hitting the cylinder.

This suggests that stronger attenuation leads to larger differences between experimental data and simulated data. To further improve the quantitative agreement between the simulated and experimental data the quantum efficiency of the detector must be more accurately known, including, e.g. charge sharing effects (Schubert et al. 2010) and the read-out performance (Kraft et al. 2009a,b).

The signal-to-noise ratio $\left(\frac{\text{mean}}{\text{std}}\right)$ in the reconstructions were higher for the measurements than for the simulations when simulating 10^8 rays. In the simulations the signal-to-noise ratio can be improved by simulating more rays.

Further, Paper II continuous to demonstrate how the simulated projection images can be used as calibration measurements for a standard linearisation procedure (Hammersberg & Mangard 1998), and reduce the cupping artefacts in the phantoms by almost a factor of 5. The simulations can be used to predict beam hardening artefacts in samples with a complex geometry, illustrated in the paper by a simulation of a chess king.

4.2.4 Summary of Paper II

In Paper II we demonstrate how a tomography setup can be implemented in McXtrace. Good numerical agreement could be obtained by implementing the source spectrum and the energy dependent quantum efficiency of the detector. Since McXtrace is based on ray tracing this software package is not appropriate for simulating phase contrast or scattering based imaging, which both rely on the wave properties of the x-ray beam.

Monte Carlo simulations have the advantages of being flexible regarding beam geometry, sample composition and detector efficiency. The simulation tool can be used to optimize the imaging setup with respect to e.g. filters and energy settings, and in that way improve the image contrast and reduce beam hardening artefacts.

4.3 Presentation of Paper III

This section presents and discusses the results from Paper III *"Visualization of subcutaneous injections by x-ray computed tomography"*(Thomsen et al. 2012). The paper deals with the visualization and quantification of the subcutaneous injections by polychromatic x-ray CT.

The tomograms of the tissue samples provides; (1) a 3D visualization of the injection bolus and tissue morphology and (2) a quantitative representation of the drug concentration distribution in subcutis.

The experiments were performed at a laboratory x-ray setup with a rotating anode. The tomograms could be obtained within 72 sec, by combining the high flux from the rotating anode with the fast read out for the PILATUS 100K detector. Using this setup we could investigate if the volumetric drug distribution was influenced by the deformation of the tissue samples caused by the snap freezing.

The quantitative measurements of the spatial drug distribution will be effected by beam hardening artefacts. The McXtrace simulations were used to study how the reconstructed image grey scale values depends on the drug concentration and shape of the injection bolus. Two samples were visualized, both with monochromatic and polychromatic radiation. The monochromatic measurements are free of beam hardening, and have higher signal to noise ratio compared to the polychromatic data. To evaluate how well the spatial drug distribution could be evaluated from polychromatic measurements, the segmented injection bolus provided by the polychromatic measurement and the monochromatic data were compared.

4.3.1 Experimental procedure

Sample preparation

The injections were performed *ex vivo* in pieces of adipose pig tissue, with a NovoPen® 3 (Novo Nordisk A/S) and a 6 mm 30G needle. The injected volumes were 0.1, 0.4 and 0.7 mL of the mixture of IAsp (70%) and Xenetix (30%). The volume of 0.7 mL of drug corresponds to the maximum possible dose that can be injected with a NovoPen® 3. In total 20 injections were visualized at the laboratory x-ray source, and two of the 0.1 mL injections were visualized at a synchrotron radiation facility.

Laboratory x-ray source

The polychromatic x-ray CT measurements were performed at the laboratory setup at the Techniche Universität München. The setup operates with a rotating anode with a molybdenum target. The acceleration voltage and current were set at 50 kV and 75 mA, respectively, which were the maximum possible at this setup. A 2 mm aluminium filter was placed in front of the beam to avoid detector saturation and reduce beam hardening. The flux was approximately 10^5 counts/s in each pixel of the detector. The experimental settings are listed in Tabel 4.2, and the experimental setup is shown in Figure 4.10. After the first tomography scan the samples were snap frozen, and the scan was repeated.

Laboratory setup	
Target	Molybdenum
Accleration voltage	50 kV
Current	75 mA
Number of projections	401 over 360°
Rotation step	0.9°
Total measuring time	1 min
Detector size	487 × 195 pixels^2
Detector pixel size	172 µm
Magnification	×1.58
Effective voxel size in reconstruction	109 µm

Table 4.2: *Experimental settings at the laboratory setup at the Technische Universität München.*

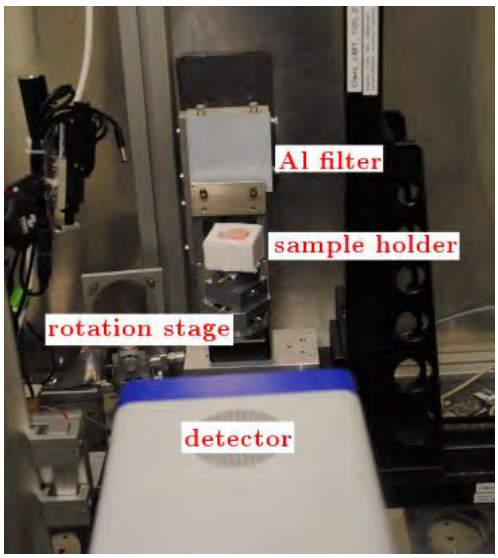

Figure 4.10: *Picture of the experimental setup for absorption tomography at the laboratory x-ray source. The experiment was carried out at the Technische Universität München.*

Synchrotron radiation

The synchrotron radiation measurements were carried out at the W2 (HARWII-II) beamline at DESY, Hamburg. The energy was set at 34.2 keV, an energy just above the K_α-edge for iodine. The effective field of view for the Cadmium Tungstate scintillator detector was 21× 4 mm^2 in the horizontal and vertical direction, respectively. To cover the full sample the scans were performed as off axis tomography scans in three height steps. The total measuring time was 2.5 hours per scan. Prior to reconstruction a 4×4 binning was applied to the projection images to reduce image noise and the effective voxel size in the reconstructions was 27×27 μm^2. All parameters for the tomography scans are collected in Table 4.3.

HARWII II beam line	
Energy	34.4 keV
Number of projections	720 over 360°
Rotation step	0.5°
Total measuring time	2.5 hours
Detector size	3056 × 3056 pixels^2
Detector pixel size	12 μm
Magnification	×1.75
Effective voxel size in reconstruction	27.3 μm

Table 4.3: *Experimental settings at the HARWII II beamline at the synchrotron radiation facility DESY, Hamburg.*

4.4 Results

4.4.1 Visualization of the injection bolus

The 20 injections visualized at the laboratory x-ray source showed large variability in the shape of the injection bolus for similar injections. Two examples of 0.4 mL injections are shown in Figure 4.11, with a vertical cross section of the tomogram shown in (1A+1B) and the 3D rendering of the segmented bolus injections shown in (2A+2B). Figure 4.11 (1A) shows that the injection bolus is placed in subcutis, and the fluid is pressed back through the injection channel, forming a droplet on top of the skin, which will be referred to as the back flow. The different skin layers, dermis, subcutis and the muscles, are visually distinguishable in the tomographic reconstructions due to the density differences between the layers.

The injection bolus could not be segmented by a simple threshold segmentation. Therefore a slightly modified Chan-Vese algorithm was used for the segmentation (Chan & Vese 2001). The Chan-Vese algorithm is a geometric active contour model, where an initial curve evolves according to an evolution equation. A detailed derivation of the model is given in Thomsen (2011).

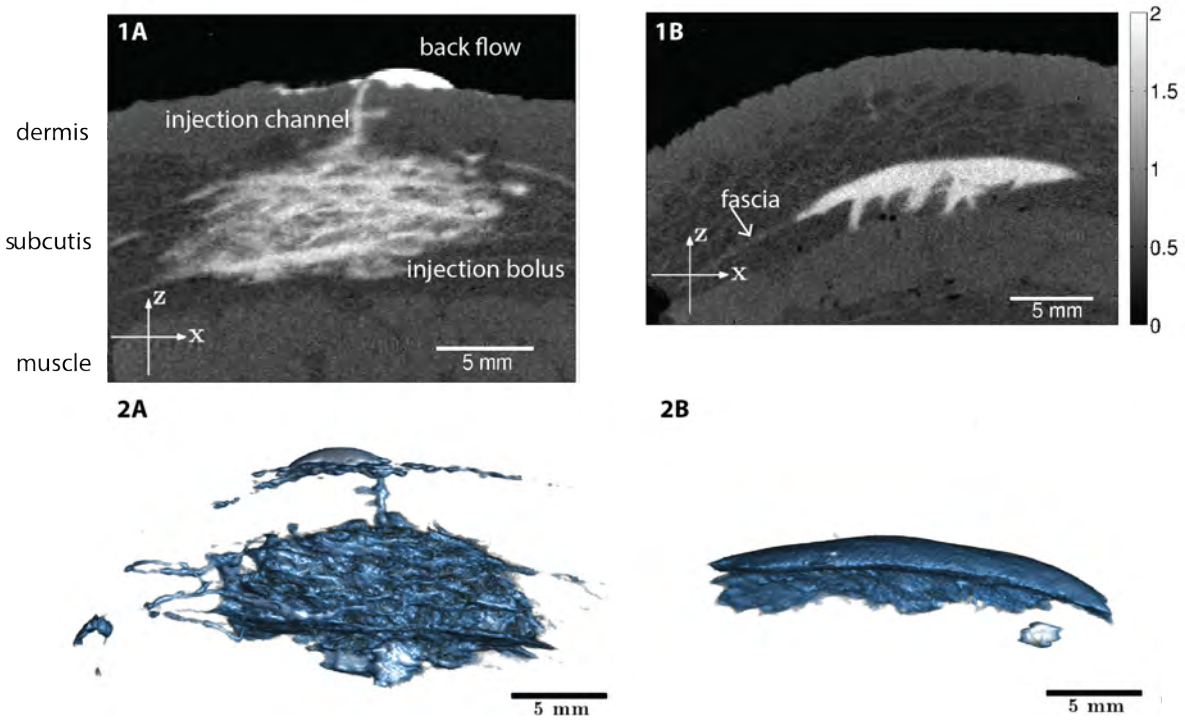

Figure 4.11: *(Top) Vertical cross sections of the tomographic reconstructions of the adipose tissue samples including a 0.4 mL injection of IAsp (70%) and Xenetix (30%). Dermis, subcutis and the muscle tissue are distinguishable. The grey scale is proportional to the x-ray attenuation length. (1A) The injection bolus is placed in the subcutaneous fat layer. Fluid is pressed back through the injection channel and forms a droplet at the top of the skin (back flow). (1B) The injection bolus is place in the fascia in the subcutaneous fat layer. (Bottom) 3D rendering of the segmented injecton bolus. (2A) Corresponds to the injection in (1A), and (2B) corresponds to the injection in (1B). The figure is adapted from Paper III (Thomsen et al. 2012).*

To quantify the variability in the shape of the injection bolus, the surfaces were fitted to ellipsoidal shapes, the simplest geometrical shape that represents the shape of the bolus relatively well. The shape is fitted by a minimum volume enclosing ellipsoid algorithm by an existing fitting routine (Moshtagh 2005). One example of the fit is shown in Figure 4.12 (A). The extension is taken as the principal axes of the ellipsoid, two in the plane parallel to the skin (xy-plane) and one perpendicular to the skin surface (z-direction). The $CV = \frac{\text{std}}{\text{mean}}$ for the extension is of the order 15-30% in each direction, independent of the volume. Figure 4.12 (B) shows the length of the principal axis of the ellipsoids in the z-direction as function of injected volume. On average the size in the z-direction does not increase when increasing the volume from 0.4 to 0.7 mL. This suggests that the extension of the injection bolus in adipose pig tissue becomes limited by the connective tissue layer between dermis, subcutis and the muscle. The extension in the xy-plane increases with the injected volume. Since the different tissue layers are distinguishable the tomograms can provide information about how the tissue morphology influences the drug distribution at the injection site.

Freezing the tissue samples were seen to deform the injection bolus. An example of a 0.1 mL injection is shown in Figure 4.13 (A), where the surface of the segmented injection bolus is shown for an unfrozen (grey) and a frozen sample (blue). Figure 4.13 (B) shows the histogram of the segmented injection bolus (solid line) and the surrounding adipose tissue (dashed line) for the frozen (blue) and unfrozen sample (grey). At an effective voxel size of 109 μm, the reconstructed grey scale values were almost unaffected by the freezing. The deformation follows the skin structures, illustrated in Figure 4.13 (C+D). Therefore we assume that the volumetric distribution among the different tissue layers can be deduced from the frozen biopsies.

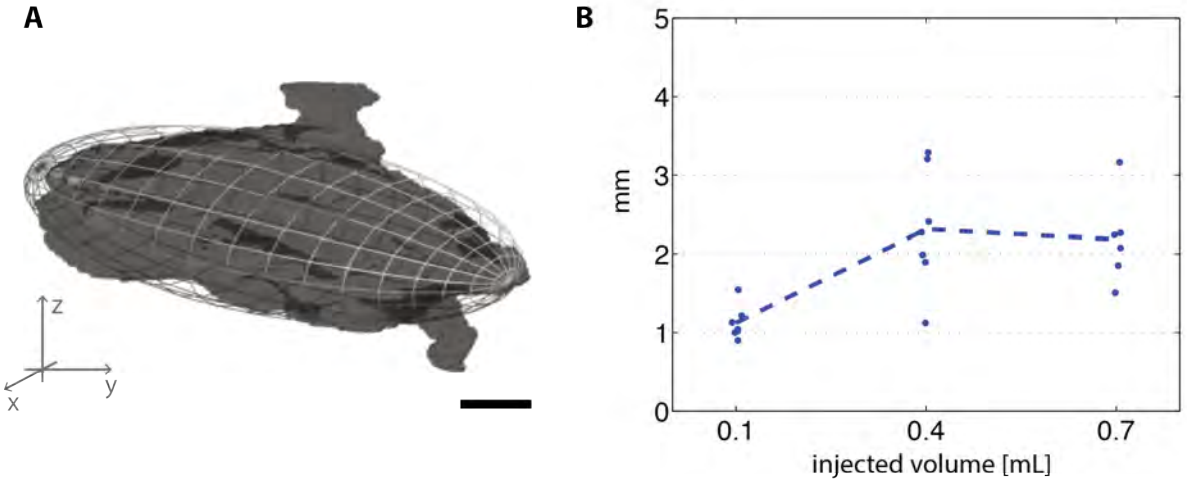

Figure 4.12: *(A) 3D rendering of a 0.1 mL injection bolus. The surface is fitted to an ellipsoidal shape. (B) Length of the axis of the fitted ellipsoid in the z-direction as function of injected dose.*

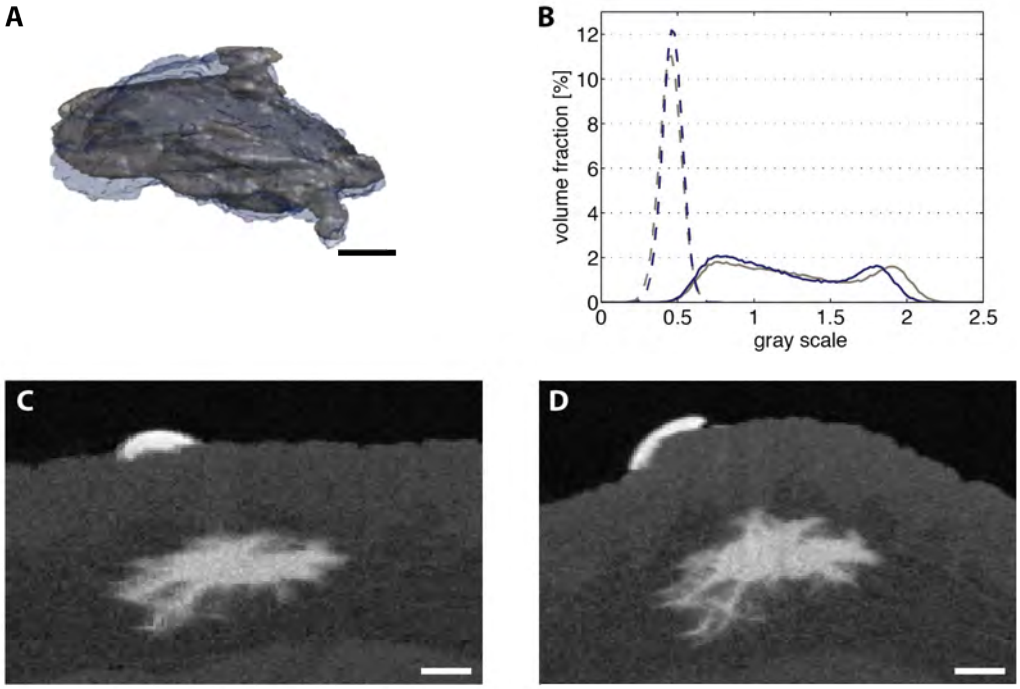

Figure 4.13: *(A) 3D rendering of the segmented injection bolus for a 0.1 mL injection when measured unfrozen (grey) and frozen (transparent blue) (B) Histogram of the grey scale values of the segmented depot (solid line) and tissue (dashed line), before (grey) and after freezing (blue). (Bottom) Vertical slice of the tomographic reconstruction of the tissue sample before freezing (C) and after freezing (D). The deformation of the depot is seen to follow the morphology of the tissue. The scalebar is 2 mm.*

4.4.2 Spatial drug distribution

The McXtrace simulation tool was used to study how the cupping artefacts in the reconstructed injection bolus depends on the shape. The ellipsoidal shapes representing the bolus injections were used as input for the simulations. The ellipsoids were embedded in blocks of adipose tissue. All simulations have a 2 mm aluminium filter in front of the beam and the energy dependent detector efficiency equals the efficiency of the PILATUS detector.

Figure 4.14 (1A-3A) shows a horizontal cross section of three different ellipsoidal shapes. The first two depots (1A+2A) correspond to an injection of 0.1 mL of drug, and the last depot (3A) corresponds to an injection of 0.4 mL of drug. The reconstructed attenuation lengths along the black dashed lines are shown Figure 4.14 (B) for a concentration of 20% Xenetix and 10% Xenetix. Cupping is seen for the both solutions. For the 20% Xenetix solutions the standard deviation is about 5-8%, and for the largest ellipsoid (dark green) the average grey scale value is about 4-5% lower compared to the smaller ellipsoids (red and blue).

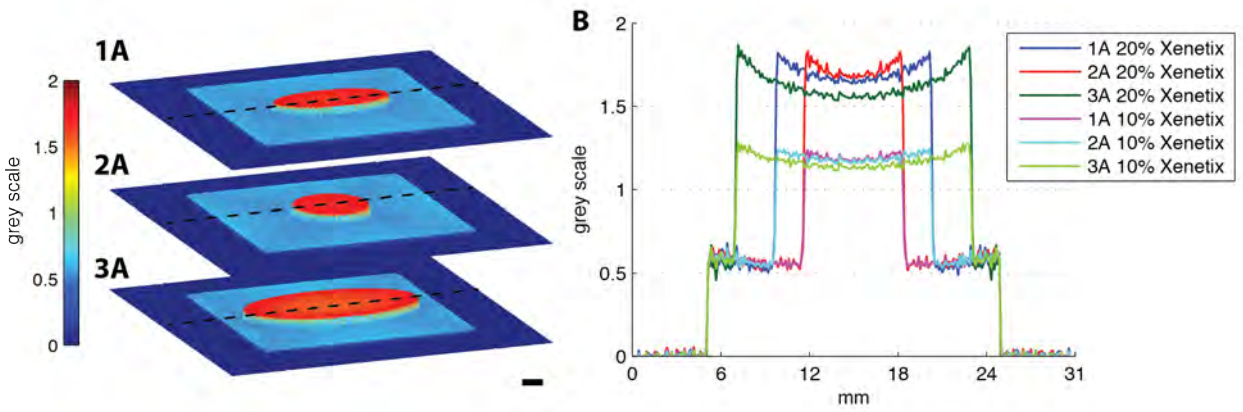

Figure 4.14: *(A) Horizontal cross section of the tomographic reconstruction of three different ellipsoidal shapes. The tomography scans are simulated in McXtrace. The ellipsoids contain a homogeneous distribution of a solution of water (80%) and Xenetix (20%). The color scale represent the reconstructed grey scale value. The scalebar is 2 mm. (B) Reconstructed grey scale value along black dashed line in (A) for the ellipsoids with mixtures of water and Xenetix, with a Xenetix concentration of 10% or 20%.*

These artefacts influences the density calibration. This was seen for the polychromatic measurements, where the density was calibrated against two calibration phantoms; a plastic tube with a diameter of 4 mm and a plastic tube with a diameter of 10 mm filled. Both were filled with mixtures of IAsp and Xenetix at varying concentrations, and scanned at the same settings as the tissue samples. The slopes of the calculated calibration curves were different due to beam hardening.

Figure 4.15 (1A-1B) shows two horizontal cross sections from one of the 0.1 mL injections. Monochromatic data (top grey) is compared to the polychromatic data calibrated against the large tube (red) and small tube (green). Monochromatic measurements are free of beam hardening artefacts and the density was calibrated against a series of reference measurements of mixtures of IAsp and Xenetix at varying concentrations.

For both the monochromatic and polychromatic data the reconstructed grey scale value in each voxel where calibrated to the average drug concentration (c_i) using the calibration curves, such that $c_i = \frac{g_i - g_{tissue}}{\alpha}$, where g_{tissue} is the average grey scale value for the adipose tissue, and α is the slope of the calibration curve.

Figure 4.15 (2A-2B) shows the average drug concentration along the red line dashed line. The shape of the bolus is irregular and the drug concentration varies across the bolus, so even though the average drug concentration is high (1A+2A), no cupping artefacts are not seen for

the 0.1 mL injection. Compared to the 4 mm tube, the 10 mm tube provides a better correlation between the monochromatic and polychromatic data. The 10 mm tube fits the dimensions of the injection bolus better than the 4 mm tube, and the beam hardening artefacts for this tube are more similar to the beam hardening artefacts expected in the injection bolus.

In Figure 4.15(1B) (black arrow) it is seen that a part of the injected drug cannot be recovered from the polychromatic measurements, because of a lower signal-to-noise ratio and lower spatial resolution.

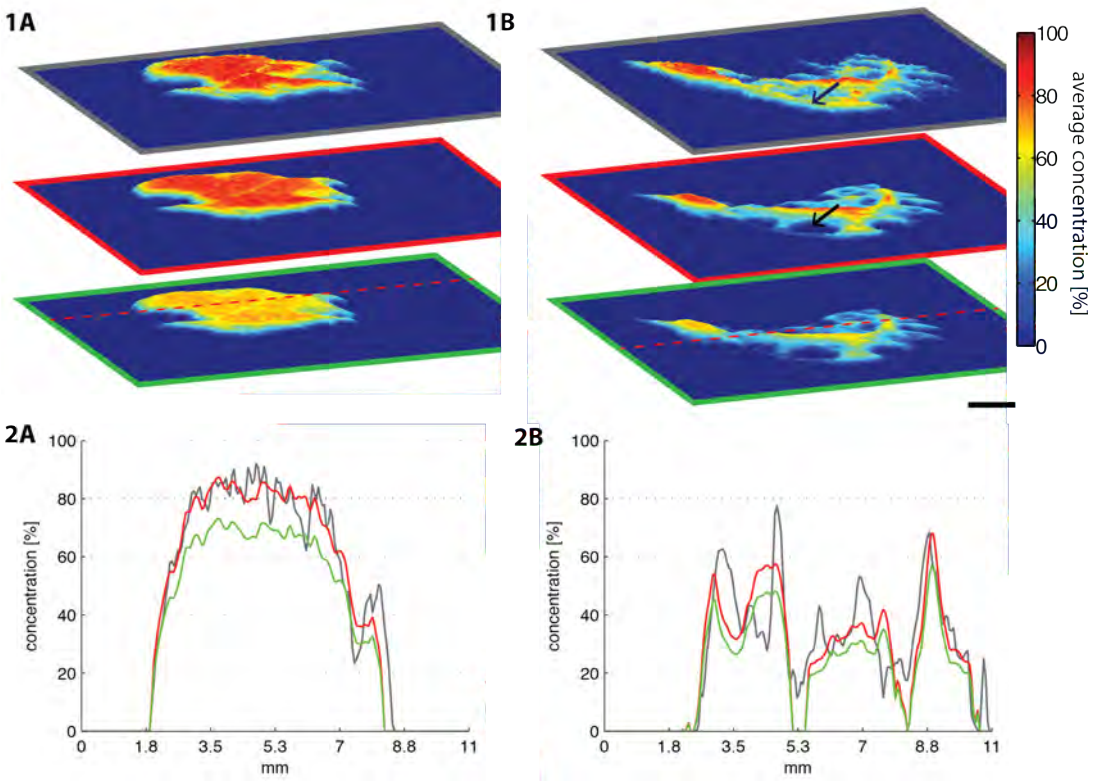

Figure 4.15: *(1A+1B) Horizontal slices of the segmented 0.1 mL injection. The color scale represents the average drug concentration, where 100% corresponds to a 30% Xenetix concentration. The top slices (grey) is the monochromatic data, and the middle (red) and bottom (green) slice are the corresponding slice from the polychromatic tomogram. For the polychromatic data the grey scale values are calibrated using two different calibration phantoms. The calibration phantoms were plastic tubes with different diameter. For the middle slice (red) the plastic tube have a diameter of 10 mm. For the slice at the bottom (green) the plastic tube have a diameter of 4 mm. A smaller fraction of the injected volume could be recovered from the polychromatic data, compared to the monochromatic data (black arrow). The scale bar is 2 mm. (2A+2B) Average drug concentration along the red dashed line in (1A) and (1B). The colors corresponds to the boarders of the slices in (1A) and (1B).*

Figure 4.16 shows the 3D rendering of the segmented injection bolus for the monochromatic data (grey) and polychromatic data (blue). The shape is seen to be very similar for the two measurements. For the voxels at the periphery of the injection bolus the drug concentration is low, and these are lost for the polychromatic measurements.

From the monochromatic data about 85% of the injected volume could be recovered from the segmentation (excluding the back-flow). Using the 10 mm tube 75% of the volume could be recovered from the polychromatic data. For second injection bolus visualized by synchrotron radiation the drug was more diluted in the tissue, and only 60% of the injected volue could be recovered from the monochromatic data, and 50% from the polychromatic data.

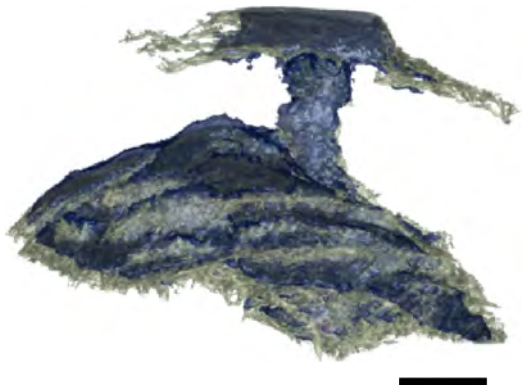

Figure 4.16: *3D rendering of the segmented 0.1 mL injection bolus from synchrotron data (grey) and polychromatic data (blue). Scalbar is 2 mm.*

4.4.3 Summary of Paper III

Paper III showed that subcutaneous injections can be visualized by x-ray computed tomography using a polychromatic x-ray source. The dermal layer, subcutis and the muscle are distinguishable in the tomograms. This means that it is possible to estimate the volumetric distribution of the drug among the different layers from the tomograms. The large variability in the shape of the injection bolus showed that the spatial drug distribution depends on the morphology of the tissue at the injection site. The distribution of drug around the needle tip is effected by the connective tissue in subcutis and between the tissue layers.

The density calibration is affected by beam hardening artefacts, which means that the average drug concentration distribution calculated from the tomograms depends on the size and shape of the injection bolus.

A good correlation was found in the spatial distribution between the monochromatic and polychromatic data when using a calibration phantom that matches the dimensions of the bolus, and no cupping was observed in the reconstructions for the 0.1 mL injections.

Chapter 5 presents a study were x-ray computed tomographic reconstructions were used to evaluate how the spatial drug distribution was influenced by different injections parameters. For the study we modify the experimental setup to reduce beam hardening and improve the image contrast in the tissue.

4.5 Dual energy tomography

One way to reduce beam hardening and improve the image contrast between the injected fluid and the tissue is by K-edge imaging. It have been demonstrated that the contrast for the iodine injection could be improved by K-edge imaging using synchrotron radiation (Thomsen 2011). An improved contrast may reduce the concentration of the contrast agent in the injected drug, and thereby reduces the drug viscosity. Furthermore K-edge imaging allows to distinguish between more injections and explore the distribution of multiply dose formulations.

It was tested if the method could be implemented at a conventional x-ray system. One test experiment was performed using the energy dispersive LAMBDA detector (see Section 3.2.3) (Pennicard et al. 2013). As proof of principle this preliminary study was made with silver nitrogen oxide with an K_α-edge at 25.5 keV. Iodine could not be used since the thin silicon layer of the detector has a very low sensitivity at the K_α-edge for iodine (33 keV). Silver nitrogen is toxic for the skin, and not appropriate for studying injections performed *in vivo*.

Four energy thresholds were needed to conduct K-edge imaging with the LAMBDA detector; two above and two below the K_α-edge. Therefore four detector pixels were binned to work as a single unit. This gives a pixel size of 110 μm and eight energy thresholds, so the two counters in each pixel were set at the same threshold. The two thresholds below the K_α-edge were 21 keV and 24 keV, and the two above were 27 keV and 30 keV. The magnification was $\times 1.14$ and the effective pixel size was 96 μm. The detector window was 12×12 mm^2.

The four images are subtracted pairwise, such that one image results from the x-ray photons with an energy between 21 keV and 24 keV, and the other image results from x-ray photons between 27 keV and 30 keV, shown in Figure 4.17 (A) and (B), respectively. The images have been filtered by a median filter. The absorption length for the surrounding tissue is almost unaltered, and the injection is therefore enhanced by subtracting these two images, as shown in Figure 4.17 (C).

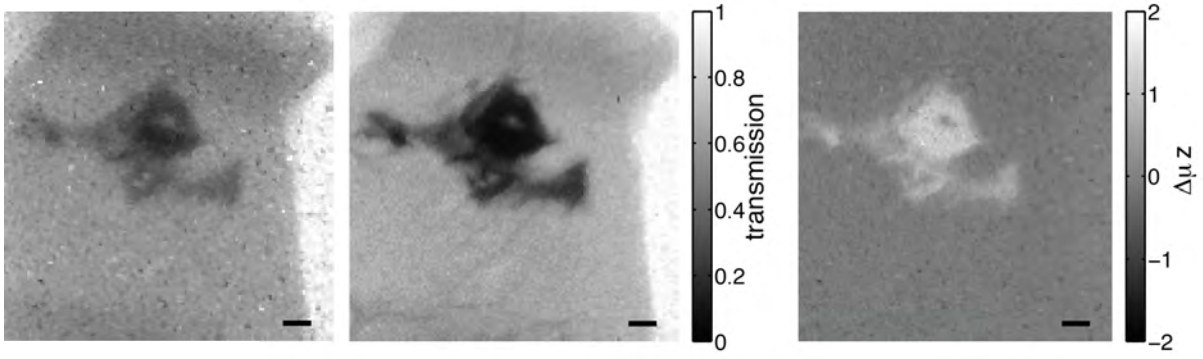

Figure 4.17: *Dual energy imaging of an 0.05 mL $AgNO_3$ in a piece of adipose tissue. The radiographic images resulting from subtracting the two threshold images, 21 keV and 24 keV (A), and 27 keV and 30 keV (B). These images are subtracted to enhance the injection bolus (C). The scalebar is 1 mm.*

The measurements required a long acquisition time, since a 300 μm silicon sensor has a quantum efficiency about 10-20% for x-ray photons with an energy between 20-30 keV. Furthermore only a small fraction of the total flux contributes to the nearly monochromatic images. It was not possible to keep the injection sample frozen for more than 4 hours, and at that point the signal-to-noise ratio in the images were too low to provide a proper 3D reconstruction.

This test experiment shows that for this method to be useful for studying subcutaneous injections, the quantum efficiency for the detector must be improved. A higher quantum efficiency between 20-40 keV will make it possible to used iodine as contrast agent. An improved efficiency will also reduce the acquisition time and make it easier to keep the sample stable during the measurement.

To separate two injections a second contrast agent is needed. Gadolinium is commonly used as a contrast agent in MR-imaging and have also been demonstrated useful for x-ray CT (Gierada & Bae 1999, Elleaume et al. 2002, Le Duc et al. 2004). Similar to the iodine based contrast agent, gadolinium distributes in the extracellular space (Bellin & Van Der Molen 2008). Gadolinium have a K_α-edge at 50 keV, and therefore demands a high quantum efficiency of the detector at these high x-ray energies.

Chapter 5

Drug distribution in subcutis

This chapter presents the results from Paper IV *"Spatial distribution of soluble insulin in pig subcutaneous tissue: Effect of needle length, injection speed and injected volume"* (Thomsen et al. 2015b). The aim of the study was to implement a robust analysis method that can be applied to multiple injections, and study how the injection parameters effect the drug distributions at the injection site.

Section 5.1 describes the design of the study and the experimental procedure, followed by an outline of the image analysis tools in section 5.2. Section 5.3 presents the results from Paper IV and in section 5.5 it is demonstrated how the injection protocol and the image analysis tools can be directly implemented for *in vivo* injections in rodents.

5.1 Experimental procedure

5.1.1 Study groups

The injections were performed in the subcutaneous tissue at the neck of the pig after the procedure described in section 3.1.2. Before being used for this study the pigs had been included in investigations approved by the Danish Animal Experiment Inspectorate. The study was divided in two parts and the study groups are listed in Table 5.1. In total 72 injections were performed in 14 pigs.

Group	Number of injections	Needle length [mm]	Volume [mL]	Speed [µL/s]
1	16	8	0.1	100
2	16	5	0.1	100
3	8	6	0.1	25
4	8	6	0.1	100
5	7	6	0.1	300
6	7	6	1	25
7	8	6	1	100

Table 5.1: *Study parameters for the seven study groups. All injections were performed at the neck of slaughtered LYD pigs.*

In the first part of the study the effect of injection depth on the drug distribution was evaluated. From PK-studies on pigs it had been shown that the variability in the plasma insulin could be reduced in the pig studies by using a 5 mm needle instead of a 8 mm needle (internal studies at Novo Nordisk A/S). For the first study group the injections were performed with a 5 mm needle (group 1), and for the second study group the injections were performed with a 8 mm needle (group 2). For both groups the injection speed was 100 μL/s and the injected volume was 0.1 mL. Each study group contained 16 injections.

In the second part of the study the effect of injection speed and injected volume on the drug distribution was evaluated. The study was divided into five groups; three groups with an injection volume of 0.1 mL, at varying injection speed from 25 μL/s to 300 μL/s (group 3-5), and two groups where the injected volume was 1 mL and the injection speed was either 25 μL/s or 100 μL/s (group 6-7). One 0.1 mL injection (group 5) and one 1 mL injections (group 6) were excluded from the study because a part of the injection bolus was missing after cutting out the tissue biopsy.
A 6 mm needle was used for these injections. For the injections done with the 5 mm needle, the injection bolus was seen to be placed close to the dermal layer, and to avoid that the 1 mL injections would be placed intradermally, we chose a slightly longer needle for this study. For each group 8 injections were performed. This is the standard group size for PK-studies for fast acting insulin analogues. The study was designed in collaboration with pharmacologists from Novo Nordisk A/S, to reproduce the normal injection procedure as closely as possible.

For these studies an injection flow rate at 100 μL/s presents the standard injection flow rate, with that in mind that the viscosity of the injected fluid is increased compared to the pure insulin formulation. For the FlexTouch® device the injection flow rate was of the order 120 μL/s in air with a 31G needle.

An injection volume of 0.1 mL of drug is the standard volume injected in PK studies on pigs. The large volume of 1 mL was selected as an upper limit, above the maximum volume of 0.6-0.8 mL that can be delivered by an insulin pen (NovoPen® and FlexTouch®).

5.1.2 CT acquisition

The tomography scans were carried out at the Imaging Industrial Portal at the Technical University of Denmark, using the 3D X-ray microscope XRadia Versa 410 (*ZEISS* 2015).

The x-ray source had a tungsten target and the acceleration voltage and current were set at 80 kV and 75 μA, respectively. A polymer filter was placed in front of the beam slit, as this was shown to improve contrast and reduce beam hardening. The effective voxel size in the reconstructions was 50 μm, and the resolution was experimentally determined to be 120 μm. The scan time was 45 min for a full tomography scan with 401 projections over 360°. All the experimental parameters for the tomography scans are listed in Table 5.2.

A cooling chamber was mounted in the CT-scanner, to keep the samples frozen during the scan, as shown in Figure 5.1.

XRadia Versa410	
Target	Tungsten
Accleration voltage	80 kV
Current	75 µA
Number of projections	401 over 360°
Rotation step	0.9°
Total measuring time	45 min
Detector size	2048 × 2048 pixels^2
Detector pixel size	13.5 µm
Pixel-binning	2×2
Detector objective	x0.4
Magnification	x1.37
Effective voxel size in reconstruction	50 µm

Table 5.2: *Experimental settings at the 3D x-ray microscope (XRadia Versa410).*

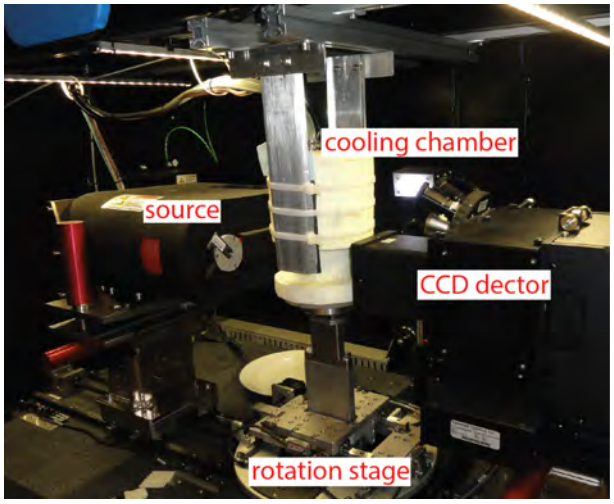

Figure 5.1: *The 3D X-ray microscope Versa-410 (XRadia). A cooling chamber was mounted at the rotation stage. The experiments were preformed at the Imaging Industrial Portal at the Technical University of Denmark.*

Beam hardening artefacts

The analysis in chapter 4 showed that beam hardening artefacts influence the reconstructed grey scale value for polychromatic x-ray computed tomography.

To compare the spatial drug distribution for injections with varying shape, we aimed at minimizing these artefacts. For the 3D x-ray microscope XRadia Versa 410, the energy dependent detector efficiency is unknown, so the beam hardening artefacts were predicted experimentally. A calibration phantom was made of polymethyl methacrylate (PMMA), with steps drilled in the center, illustrated in Figure 5.2 (A). PMMA has an x-ray attenuation length similar to attenuation length for soft tissue (Zou et al. 2011, Chantler 2000). The step hole was filled with a solution of IAsp and Xenetix at varying concentrations, and scanned at the same settings as the tissue samples.

Figure 5.2 (B) shows the reconstructed grey scale values along a horizontal line across a step where the diameter is 12 mm or 4 mm for solutions with a Xenetix concentration of 30% (dark blue), 25% (light blue), 15% (green), and 5% (red). Cupping artefacts were primarily seen for the undiluted fluid (dark blue). Since the drug distributes between the fat cell, it was assumed that beam hardening artefacts were limited in the tomograms, and that the reconstructed grey scale values could be compared across the samples.

The grey scale values for the different solutions were used to relate the grey scale value in each voxel in the segmented injection bolus, to the average concentration of the injected fluid.

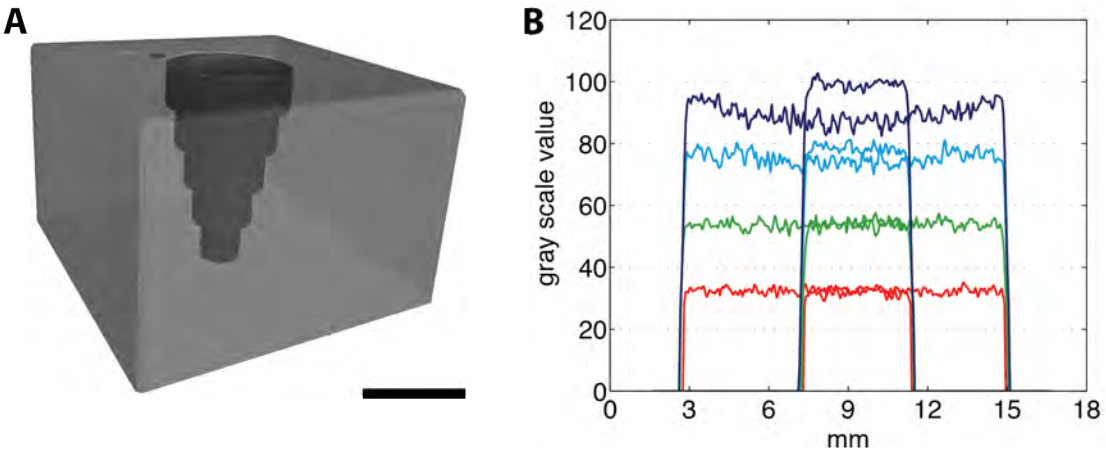

Figure 5.2: *(A) Calibration phantom of PMMA (30×30×30 mm^3) with steps drilled in the center. (B) Reconstructed grey scale value long a horizontal line through a step where the diameter is 12 mm or 4 mm. The phantom was scanned with mixtures of IAsp and Xenetix, where the Xenetix concentration was 30% (dark blue), 25% (light blue), 15% (green), or 5% (red). The scale bar is 5 mm.*

5.2 Segmentation and characterization

Figure 5.3 shows three examples of the reconstructed tissue samples, including the injection bolus. The injections were performed with different injection parameters. The color scale gives the average drug concentration [%], and the grey scale relates to x-ray attenuation length, where a lighter color translates to a higher attenuation length.

Figure 5.3 (A) shows a 0.1 mL injection performed with a 5 mm needle, which is placed close to the dermal/subcutis interface. The 0.1 mL injection performed with a 6 mm needle (B) is distributed partly in the muscle layer. For the 1 mL injections (C) a fraction of the drug is accumulated in the fascia that divides subcutis in two layers (black arrow). The observation of these features leads to the following analysis; (1) segmentation of the injection bolus and tissue layer, (2) layer detection to quantify the intradermal, subcutaneous and intramuscular volume fraction, and (3) a texture classification of the spatial distribution to quantify the amount of drug placed in the connective tissue layer. The different steps in the analysis are outlined in Figure 5.4 and discussed in details in the following sections.

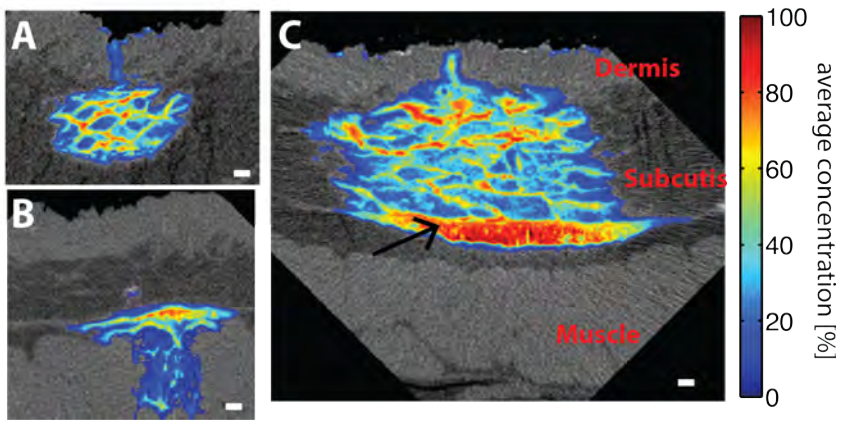

Figure 5.3: *Vertical slices of three reconstructed tissue sample. (A) 0.1 mL injection performed with a 5 mm needle placed close to the dermal-subcutis interface. (B) 0.1 mL injection performed with a 6 mm needle placed partly intramuscular. (C) 1 mL injections, where a part of the injected volume is placed in the fascia between the two layers in subcutis (black arrow). The color scale represents the average drug concentration [%], and the grey scale relates to x-ray attenuation length, where a lighter color translates to a higher attenuation length. The scale bar is 1 mm.*

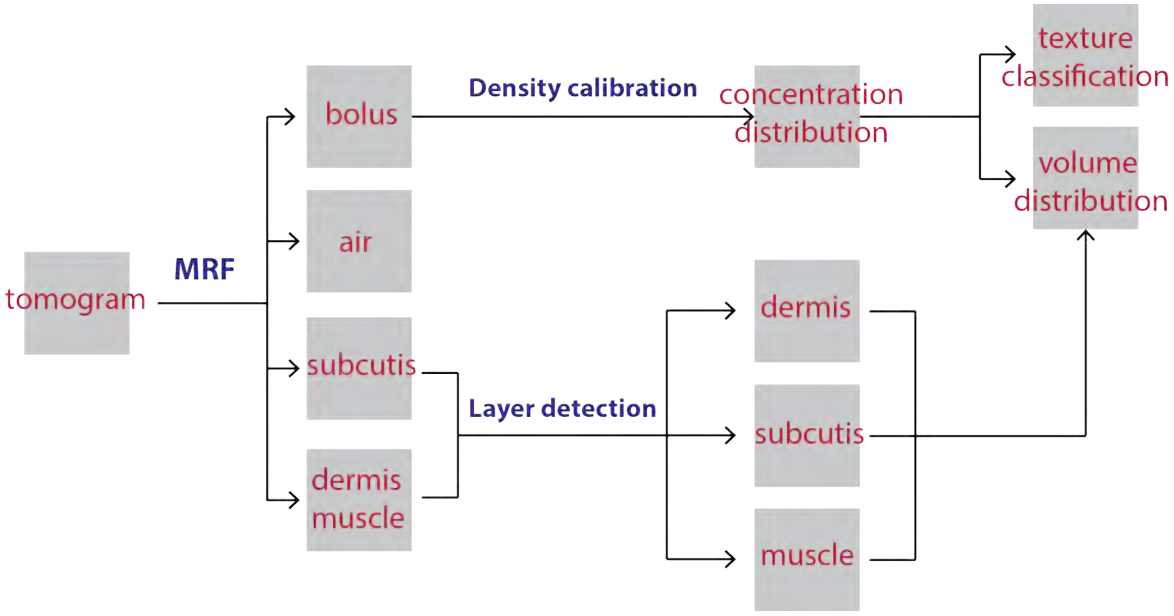

Figure 5.4: *Overview of the steps in the analysis of the tissue samples. The tissue samples were segmented by the Markov Random Field (MRF) segmentation algorithm (Li 2009). The tissue classes were separated by layer detection of the boundary between the classes, and used to estimate the volumetric drug distribution among the layers. The spatial distribution was classified by a texture segmentation algorithm (Dahl & Larsen 2011, Emerson et al. 2015).*

5.2.1 Markov Random Field Segmentation

Figure 5.5 shows a horizontal cross section of an injection bolus (A) and the corresponding histogram (B). The dermal/muscle layer and the subcutaneous fat layer are seen as two overlapping Gaussian distributions, and the injection is seen as a tail at high grey scale values. A simple threshold segmentation was not sufficient to give a proper segmentation.

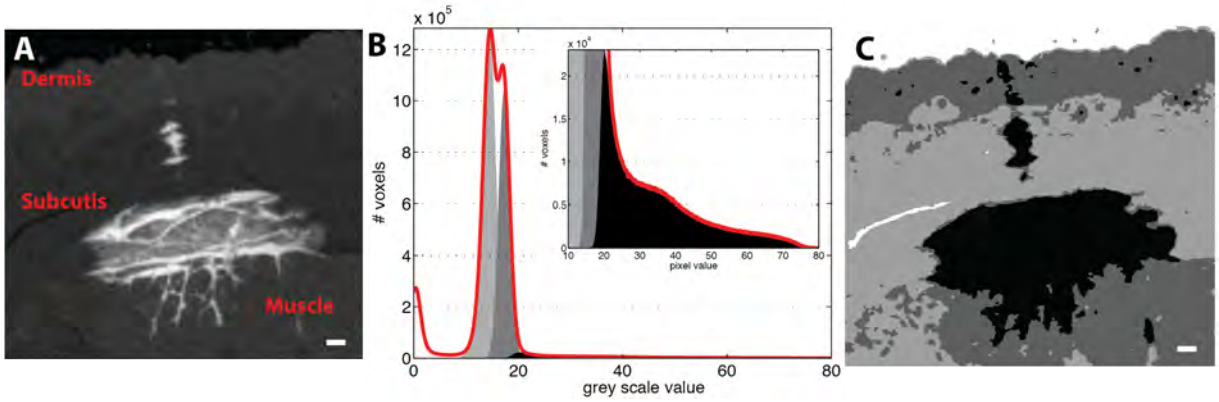

Figure 5.5: *(A) Vertical slice of a reconstructed tissue sample with an injection bolus. (B) Image histogram of the reconstruction (red curve). The grey scale distribution for each class is extracted after segmented; air (white), subcutis (light grey), the dermal and muscular layer (dark grey) and the injection bolus (black). A zoom-in on the histogram of the injection bolus is shown at the top right corner. (C) Result of the MRF segmentation algorithm where the image is divided into four classes. The scale bar is 1 mm.*

The tomograms were segmented by the Markov Random Fields (MRF) segmentation (Li 2009), which takes the grey scale value of the neighbouring pixels into account, and includes a smoothing factor, to reduce the influence of image noise. This section presents the concept of the algorithm, while a more detailed description is given in Appendix A in Section A.1. Parts of the algorithm were pre-implemented.

Let $\mathcal{S}$ be the set of pixels in the image and $\mathcal{L}$ be the set of labels in the segmentation. In this case $\mathcal{L} = \{\text{air}, \text{dermis/muscle}, \text{subcutis}, \text{injected drug}\}$. The MRF segmentation takes a probabilistic approach, where each site in the image, $i \in \mathcal{S}$, is considered as a random variable, which can take a value $f_i \in \mathcal{L}$. The Markov property gives that the information about the label of site i from all other sites in the image is contained only in the labels of the sites in the neighbourhood of i. It means that the probability for a pixel in the image to have the label f_i is given by

$$p(f_i|f_j, j \in \{\mathcal{S} \setminus i\}) = p(f_i|f_j, j \in \mathcal{N}_i) \tag{5.1}$$

where $\mathcal{N}_i$ is the neighbourhood of the pixel i. All configurations ($f = \cup_i f_i$) are possible, meaning that $p(f) > 0, \forall f$.

To find the label configuration, f, with the highest probability it is used that a MRF is equivalent to a Gibbs Random Field (Clifford 1990). A Gibbs Random Field is a random field, where the probability for the configuration of labels f is given by

$$p(f) \quad \propto \quad e^{-U(f)} \tag{5.2}$$

where $U(f)$ is the potential function. Finding the maximum likelihood for the configuration of labels corresponds to minimizing the potential function $U(f)$.

The potential function, $U(f)$, is defined in terms of cliques, $\mathcal{C}$, such that

$$U(f) = \sum_{c \in \mathcal{C}} V_c(f) \tag{5.3}$$

where $V_c(f)$ are the clique potential.

The set of one cliques, $\mathcal{C}_1$, is equal to the set of all sites, $\mathcal{S}$. The set of two clique is the set of pair of site, (i, j), where $i \in \mathcal{S}$ and $j \in \mathcal{N}_i$, etc.

For the tissue samples, only the one clique and two clique potentials are considered. As an example consider the subcutaneous fat layer, where the one clique potential, $V_i(f_i)$, and the two clique potential, $V_{(i,j)}(f_i, f_j)$, are given by

$$V_i(f_i) \quad = \quad \ln(2\pi\sigma_{\text{sub}}) + \frac{1}{2}\left(\frac{g_i - \tilde{g}_{\text{sub}}}{\sigma_{\text{sub}}}\right)^2 \tag{5.4}$$

$$V_{(i,j)}(f_i, f_j) \quad = \quad \beta(1 - \delta_k(f_i - f_j)) \tag{5.5}$$

where $\tilde{g}_{\text{sub}}$ and σ_{sub} are the average and standard deviation of the grey scale value for the subcutaneous tissue, respectively. δ_k is the kronecker delta function, and β is the smoothness term.

The smoothness term controls the weight of the neighbouring pixel labels in the segmentation. Higher values of β lead to a more homogeneous segmentation

The potential is minimized by minimum graph cut (Kolmogorov & Zabin 2004), outlined in Section A.1.2 in Appendix A. The algorithm was applied in 3D on 8 bit images. The smoothness factor was selected to be $\beta = 0.5$, from a visual inspection of the results of the segmentation. Figure 5.5 (C) shows the result of the MRF segmentation, where the four classes are found as homogeneous regions in the image.

5.2.2 Layer detection

The MRF algorithm provides a segmentation of the tissue structures surrounding the injection bolus. To estimate the amount of drug in each layer the border of the interfaces between the layers must be extrapolated into the region covered by the bolus. Different methods were tested, including image inpainting (Bertalmio et al. 2000, Schönlieb & Bertozzi 2011) and a surface layer detection algorithm (Li et al. 2006), but the irregular structure of the tissue complicated a robust segmentation by these methods.

Due to problems involved in the implementation of an full automatic layer detection a simple, semi-automatic method was implemented, where a plane was defined from three manually selected points at the interface. A grid of $N \times N$ points in 3D was constructed, illustrated in a 2D slice in Figure 5.6 (red line). The points at the grid where moved iteratively to find the interface.

Let $\mathbf{x_j} = (x_j, y_j, z_j)$ be the coordinates at site j on the grid and $\mathbf{n} = (n_x, n_y, n_z)$ be the normal vector of the plane, illustrated in Figure 5.6. The grid points were moved iteratively with the z-coordinates being fixed. For iteration $k+1$ the grid point j has the coordinates

$$\mathbf{x_j^{k+1}} = \begin{cases} (x_j^k + \Delta_k n_x, y_j^k + \Delta_k n_y, x_z^k) & \text{if } f_j^k = f_M \\ (x_j^k - \Delta_k n_x, y_j^k + \Delta_k n_y, x_z^k) & \text{if } f_j^k = f_S \end{cases} \tag{5.6}$$

where f_S and f_M are the labels for subcutis and the muscle, respectively and f_j^k is the label value at the point j. Δ_k is the shift of the points at iteration k, which was set to decrease exponential with k. Only the grid points with labels f_S and f_M were considered, meaning that grid points in the region covered by the injection bolus were removed. The grid points were not moved if the move was opposite to the last iteration. The first iteration step is illustrated in Figure 5.6 (blue curve).

The points missing, in the region covered by the injection bolus, were interpolated by fitting the points at the boundary to a smooth surface. Having identified the boundary the voxels in the injection bolus were assigned as being either above or below the interface.

Let $\mathcal{I}$ be the set of all points in the injection bolus, $\mathcal{S}_M$ be the set of points at the boundary between subcutis and the muscle. Let $d(\mathbf{x}_i)$ be the shortest Euclidean distance between the point $\mathbf{x}_i \in \mathcal{I}$ and the points in $\mathcal{S}_M$. The points at the boundary, $\mathcal{S}_M$, were fitted to a plane with normal vectors $\hat{n}_M$, where $\hat{n}_M$ points from the muscle tissue to subcutis.

For $\mathbf{x}_i \in \mathcal{I}$, the set of points (M) placed beneath the boundary is given as

$$M = \{\mathbf{x}_i \mid \forall \mathbf{x}_i \in \mathcal{I} : d(\mathbf{x}_i) < d(\mathbf{x}_i + \hat{n}_M)\} \tag{5.7}$$

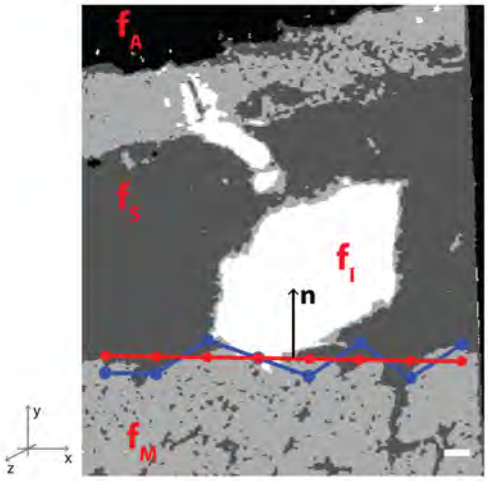

Figure 5.6: *Vertical slice of a tomogram segmented into four classes; air (f_A), dermis/muscle (f_M), subcutis (f_S) and the injection bolus (f_I). A plane is placed manually at the interface between subcutis and the muscle (red line). The points at the plane are moved iteratively in the direction normal to the plane according to Eq. (5.6) (blue line). The scale bar is 1 mm*

The points in the injection bolus placed in the dermal layer was found in a similar way, and the remaining points were assigned to belong to subcutis.

An example of a layer segmentation is shown in Figure 5.7 in 3D (A) and in a 2D vertical cross section (B). The points in the injection bolus are coloured according to the tissue class, they are estimated to belong to; the dermal layer (grey), subcutis (yellow), or the muscle tissue (purple).

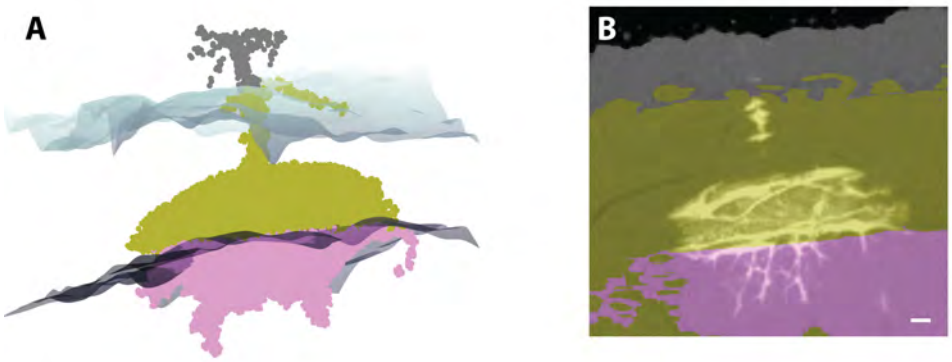

Figure 5.7: *The injection depot shown as a point cloud (A) and a 2D slice of the sample (B), with the individual voxels assigned to dermis (grey), subcutis (yellow) and the muscle (purple). The scale bar is 1 mm*

5.2.3 Texture classification

The injection bolus was further segmented according to the local distribution of the drug. Figure 5.8 shows a vertical slice of the reconstructed tissue samples (A+C) and the histological images of a single slice from the same samples (B+D). For the injection bolus in (A+B) the drug is seen to be homogeneously distributed between the fat cells. The bands of connective tissue are seen as regions with a higher average drug concentration (black arrow). Only minor cracking of the tissue structures are seen, due to the freezing and histological preparation (red arrow). For the injection bolus seen in (C+D) the drug is partly placed in the fascia, and the expansion of the drug in the freezing process is seen to cause severe cracking of the tissue structures. These different regions are identified using learning dictionaries (Dahl & Larsen 2011, Emerson et al. 2015).

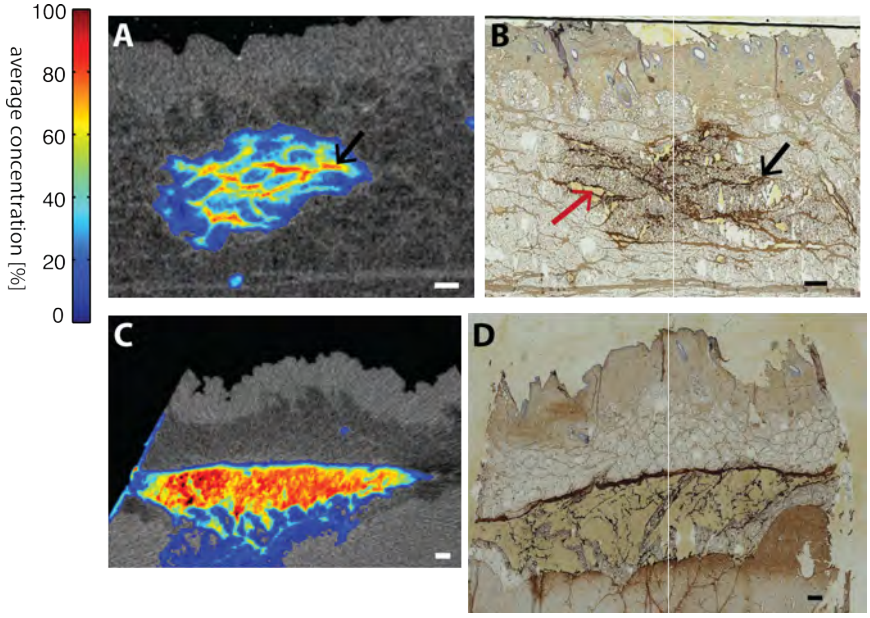

Figure 5.8: *Vertical slices of the tomographic reconstruction (A and C), compared to histological images from the same injections (B and D). For the injection shown in (A) the drug is distributed regular in the adipose tissue. The regions with high concentration is seen as the connective tissue layers in (B) (red arrow). The bruising of the tissue structures are an expected artefact from the histological preparation of frozen samples (B) (blue arrow). The regions with high concentration of drug (C) is seen in the histological images to be caused by either tissue expansion or bruising (D). Scale bar is 1 mm*

One example of an injection bolus, where a part of the injection, is placed in the fascia is shown in Figure 5.9 (A). For this slice the injection bolus was manually divided into two classes; a subcutaneous part (white), and a region with drug accumulation (grey). The algorithm used is based on an implementation made by Anders Dahl (DTU Compute) (Dahl & Larsen 2011), and optimized for this problem.

The algorithm has three steps; (1) annotation of training images, (2) construction of the intensity directory and label directory, (3) labelling of the remaining slices. The output is a probability image for each of the classes defined in the training image. The algorithm was in this case implemented for 2D images, which means that information between slices was not taken into account. However, the segmentation was found to be satisfactory from a visual inspection. A detailed description of the algorithm is given in Section A.2 in Appendix A, and in the original paper (Dahl & Larsen 2011).

Examples of the probability images for the two texture classes are shown in Figure 5.9 (D-E), compared to the original image (C). The textures were segmented by selecting the texture with the highest probability for each voxel. In order to conserve memory capacity and speed up the algorithm, the images are down scaled by a factor of 2 before segmented.

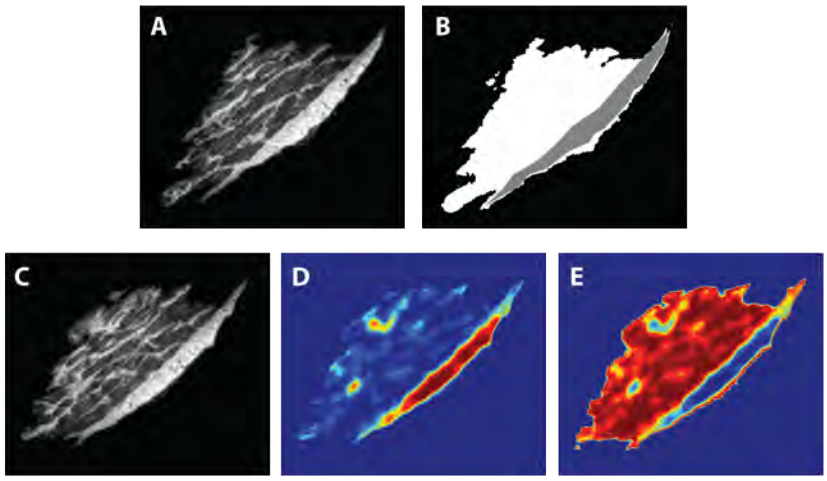

Figure 5.9: *Vertical slice of a 1 mL injection (A) and the corresponding manual annotation in two classes (B). Another slice from the same sample (C) and the probability map for the drug distributed between the fat cells (D) and for the drug accumulated in the fascia layer (E).*

5.2.4 Spatial distribution

The variability in the spatial distribution for each group was quantified in terms of the χ^2 difference of the image histograms

$$\chi^2 = \sum_{i=1}^{M} \frac{2(H_i - \tilde{H}_i)^2}{H_i + \tilde{H}_i} \tag{5.8}$$

where H_i is the histogram with M-bins for one injection, and $\tilde{H}_i$ is the mean histogram for the study group with the same number of bins.

To compare the injection depth, the boundary between dermis and subcutis was taken as the reference plane. The injection depth was defined as the distance between this plane, and a

parallel plane, that divides the injection bolus in half. The injection depths calculated cannot be translated directly to the injection depth *in vivo*, since the tissue biopsies were cut out after the injections were performed. This caused the tissue to subtract, while also the freezing expands the sample.

5.3 Presentation of Paper IV

The paper presents a quantitative comparison of the study groups, based on the analysis presented in the previous sections. Figure 5.10 shows the 3D rendering (left column) and a vertical cross section (right column) of injections performed with a 8 mm needle (A-B), and 1 mL injections (C-D). The skin surface, dermal/subcutis interface, and the subcutis/muscular interface are shown as a grey transparent layers in the 3D rendering (left column).

A large variability is observed in the shape of the depot from injection to injection, as in the *ex vivo* study, presented in section 4.3. The shapes were quantified by a number of parameters; the elongation in the plane parallel to the skin (xz-plane), the deviation from a circular shape, and volume fraction spread as smaller injection channels (red arrow in the Figure 5.10 (C)). All parameters where shown to have a $CV = \frac{\text{std}}{\text{mean}}$ of the order 20-50%. The shape parameters were analysed by analysis of variance (ANOVA) with injection depth, injection speed, injected volume and the individual animal as factors. No significant difference was found for any of the parameters.

The needle stick channel and the drug at the skin surface (the backflow) were removed digitally and only the injection bolus was analysed. With the applied density calibration 70-95% of the injected drug volume could be recovered from the segmentation. The remaining part of the injection drug is lost as backflow or has become to diluted to be resolved in the tomograms. The calculated volume depends on the density calibration and the tissue density. The reconstructed grey scale value for the tissue was on average vary equal from sample to sample, with a variation of less than 2%.

The segmented volume was, like the shape parameters, analysed by ANOVA, and no significant difference was found for any of the parameters. Thus, none of the injection parameters affect the segmentation.

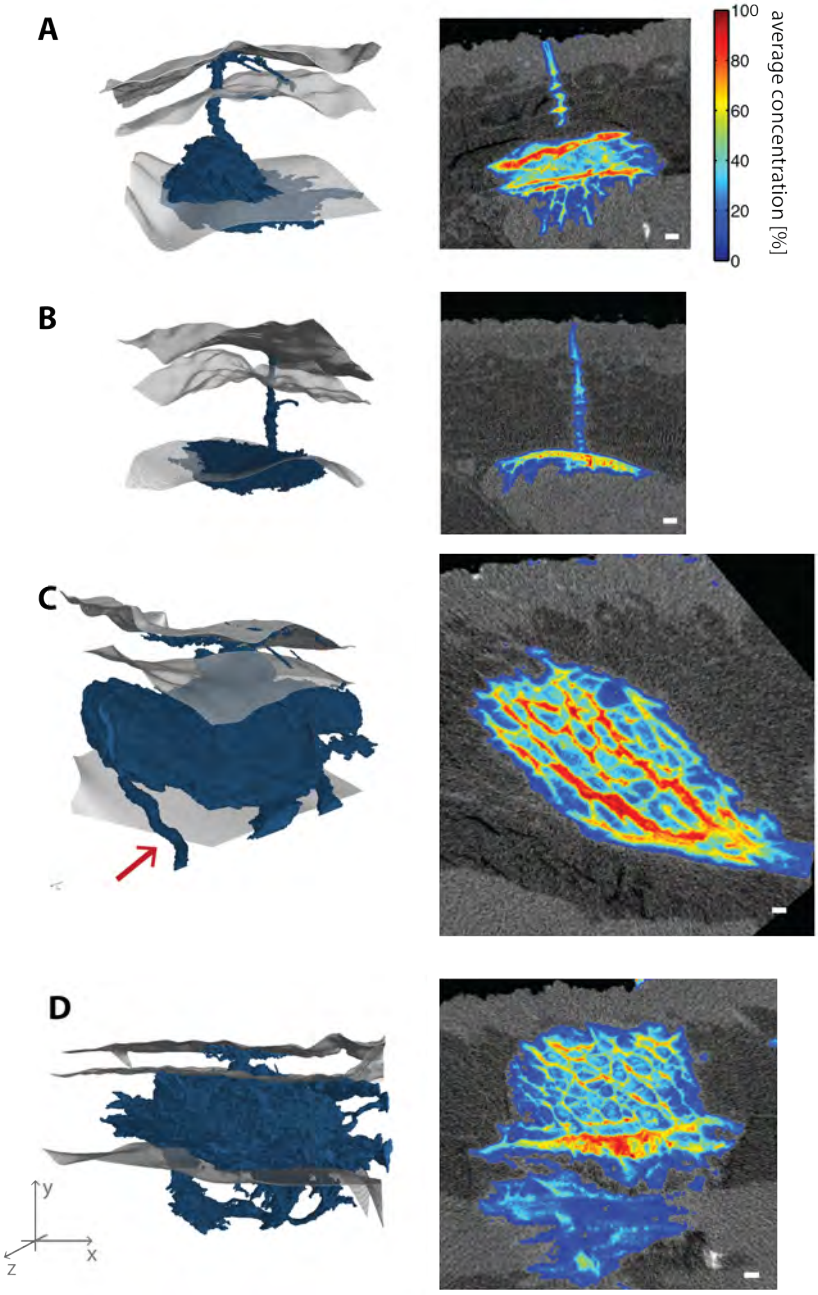

Figure 5.10: *3D rendering of four depots (left column). The skin surfaces, the dermal/subcutis interfaces and the muscle/subcutis interfaces are shown as semitransparent grey layers. Vertical slices of the corresponding tissue samples (right colomn). The color scale gives the average drug concentration and the grey scale is proportional to the x-ray attenuation length, where a higher attenuation length translates to a lighter grey scale value. Scale bar is 1 mm. (A-B) Injections performed with an 8 mm needle; one placed partly intramuscular (A), and one placed in the facia between subcutis and the muscle (B). (C-D) 1 mL injections. One placed subcutaneously (C) and one placed partly intramuscular and in the fascia layer (D).*

5.3.1 Injection depth

In this section are the injections performed with a 5 mm (group 1) and an 8 mm needle (group 2) compared. Table 5.3 lists the injection depth, and histogram difference (χ^2). CV is given in parentheses. The injection depth is measured from the interface between dermis and subcutis. *In vivo* is the thickness of the dermal layer for pigs about 2 mm, measured by ultrasound in a previous study (data not shown).

Group	Depth [mm]	Histogram difference (χ^2)
1 (0.1 mL, 5 mm)	1.54 (0.38)	0.059 (0.68)
2 (0.1 mL, 8 mm)	7.74 (0.18)	0.35 (0.80)

Table 5.3: *Mean value and* $CV = \frac{\text{std}}{\text{mean}}$ *the injection depth and histogram difference for group 1 and 2. For clarity is the injected volume and needle length given in parentages.*

The injection depths were about 5 times higher for the injections performed with the 8 mm needle compared to the injections performed with the 5 mm needle. Even though this not reflects the injection depth *in vivo* it shows that the injection depth is not only determined by the needle length, but is also affected by the morphology of the tissue. Using an 8 mm needle the fascia between subcutis and the muscle might be penetrated by the needle tip, and the injection becomes intramuscular.

This is also seen in the histogram of the intramuscular volume fraction, shown in Figure 5.11(A) for the 5 mm needle (blue) and the 8 mm needle (red). For the 8 mm needle half of the injections were placed partly intramuscular. The injections performed with a 5 mm needle were purely subcutaneously, as no injections were seen to be placed intradermally (data not shown).

Figure 5.11 (B) shows the image histogram of the average concentration distribution. For the injections performed with the 5 mm needle, the histograms are very similar, which is reflected in the χ^2 difference in Table 5.3. For group 2 (8 mm needle) a number of injections have a peak at low concentrations and two injections have a peak at an average drug concentration about 80%. The peak at low drug concentrations corresponds to the intramuscular injections, since the muscle tissue has a lower porosity. One example is shown in Figure 5.11 (C). Both injections with the peak at high concentrations were placed in the lower subcutaneous fat layer, shown in Figure 5.11 (D). The drug did not accumulate around the injection site for all injection placed in this layer. The accumulation of drug was observed for three out of the 16 injections performed with the 8 mm needle, and not observed for any of the injections performed with the 5 mm needle. The regions with drug accumulation were segmented by the texture segmentation algorithm, and the volume fraction is listed in Table 5.4.

Group	♯ samples	volume fraction
1 (0.1 mL, 5 mm)	0	•
2 (0.1 mL, 8 mm)	3	$\{0.14, 0.57, 0.95\}$

Table 5.4: *The number of injections where drug accumulation was observed and the relative volume segmented by the texture segmentation algorithm.*

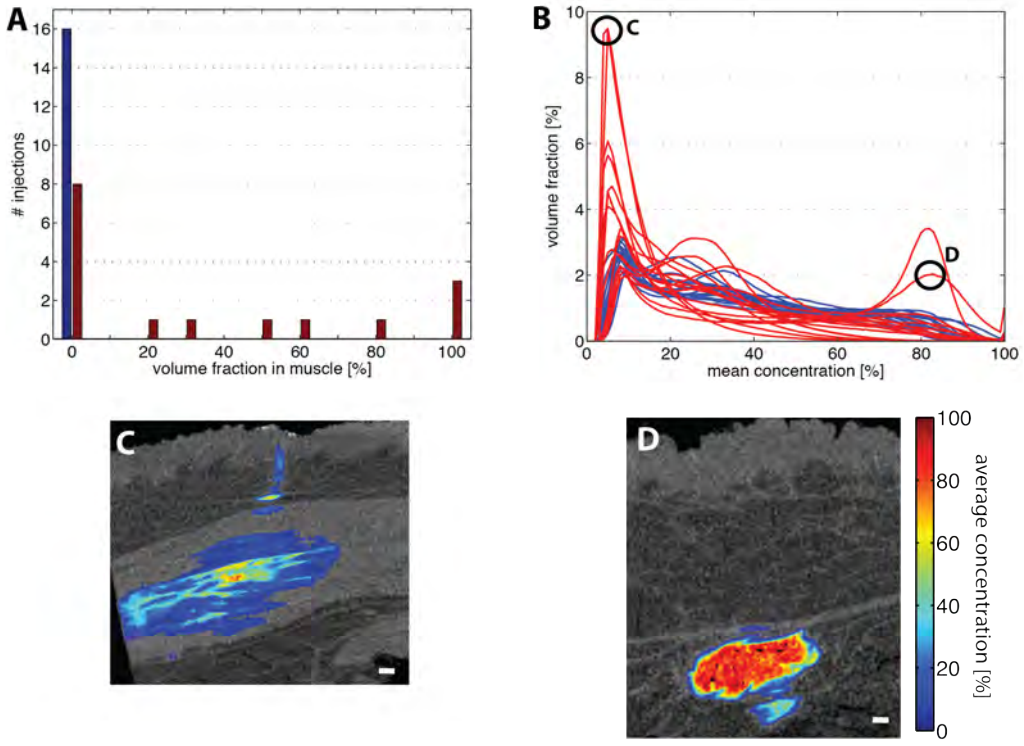

Figure 5.11: *(A) Histogram of the intramuscular volume fraction for injections performed with a 5 mm needle (group 1) (blue), and an 8 mm needle (group 2) (red). (B) Image histogram of the average concentration distribution for injections performed with a 5 mm needle (group 1) (blue), and an 8 mm needle (group 2) (red). (C+B) Vertical cross section of two tissue sample with injections performed with an 8 mm needle. (C) The injection is placed in the lower subcutaneous fat layer. (D) Intramuscular injections. The color scale presents the average concentration of the injected fluid. The grey scale is proportional to the x-ray attenuation length, where a lighter color corresponds to a higher attenuation length. The scale bar is 1 mm.*

5.3.2 Injection speed and injected volume

In this section are the 0.1 mL (group 3-5) and 1 mL (group 6-7) injections performed at varying injection speeds compared. Table 5.5 lists the injection depth, and average drug concentration. As expected, the average concentration is higher for the 1 mL injections due to a lower surface to volume fraction for the bolus.

Group (volume, speed)	Depth [mm]	Average concentration
3 (0.1 mL, 0.025 mL/s)	5.23 (0.21)	0.25 (0.18)
4 (0.1 mL, 0.1 mL/s)	5.37 (0.18)	0.26 (0.23)
5 (0.1 mL, 0.3 mL/s)	5.54 (0.19)	0.27 (0.16)
6 (1 mL, 0.025 mL/s)	7.01 (0.18)	0.41 (0.22)
7 (1 mL, 0.3 mL/s)	6.28 (0.14)	0.34 (0.18)

Table 5.5: *Mean value and CV* $= \frac{\text{std}}{\text{mean}}$ *the injection depth and average concentration the 0.1 mL injections (group 3-5) and 1 mL injections (group 6-7).*

For the injections performed with different injections speed (group 3-5 and group 6-7), there was no significant difference in either the injection depth or average concentration (ANOVA). It means that a high injection speed was not seen to cause damage on the tissue structures, since tissue damage will cause a higher average drug concentration due to the changed tissue porosity.

The injections were pooled, and the volumetric and concentration distributions compared for 0.1 mL injections (group 3-4) and 1 mL injections (group 6-7). Only the injections performed with an injection speed of 0.025 mL/s and 0.1 mL/s were included, resulting in 15 injections in each group.

Figure 5.12 (A) shows the histogram of the intramuscular volume fraction for the 0.1 mL injections (green), and the 1 mL injections (purple). It is seen that a larger injection volume not increases the relative amount of drug in the muscle layer. The 1 mL injections were neither placed partly intradermally (data not shown).

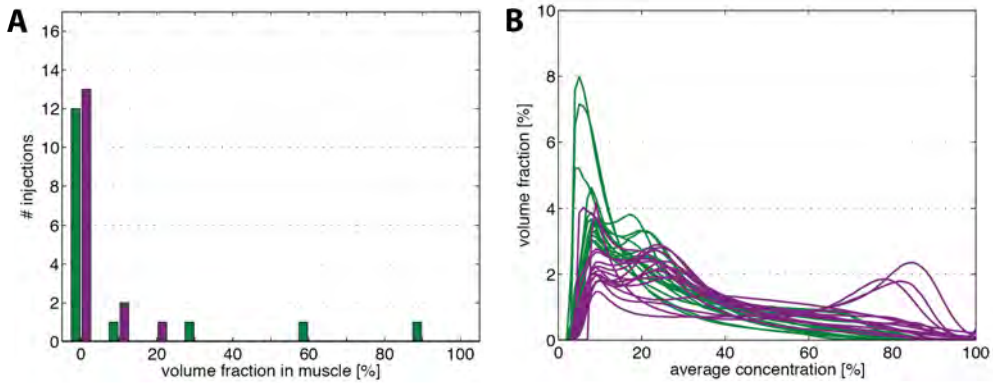

Figure 5.12: *(A) Histogram over the intramuscular volume fraction for the 0.1 mL injections (group 3-4) (green), and the 1 mL injections (group 6-7) (purple). (B) Image histogram of the average concentration distribution for the 0.1 mL injections (group 3-4) (green), and the 1 mL injections (group 6-7) (purple).*

Figure 5.12 (B) shows the image histogram for the 0.1 mL injections (green) and 1 mL injections (purple). The two partly intramuscular injections are seen as peaks in the histograms for the 0.1 mL injections. The histogram difference (χ^2) is given in Table 5.6, and both groups show increased variability compared to the injections performed with the 5 mm needle.

For ten of the 1 mL injections it was observed that a part of the injected volume was placed in the fascia layer. The same was only observed for two of the 0.1 mL injections in group 3-4, and for two injections in group 5. This effect was not related to the injection speed. These injections were segmented by the texture segmentation. For the 1 mL injections the volume fractions were between 10-90%. To our knowledge, it is not known how this will affect the absorption kinetics of subcutaneous injections in pigs.

The study groups were randomized among the different animals, and for all the analysed parameters, no significant difference was seen between the individual animal (ANOVA).

Group	Histogram difference (χ^2)	♯ samples	Volume fractions
3-4 (0.1 mL, 6 mm)	0.11 (0.89)	2	$\{0.40, 0.70\}$
6-7 (1 mL, 6 mm)	0.18 (0.89)	10	0.47 (0.66)

Table 5.6: *Histogram difference (χ^2), the number of injections where drug accumulation was observed and the relative volume segmented by the texture segmentation algorithm. For group 6-7 the mean volume fraction and CV is given.*

5.4 Summary

In Paper IV the visualization technique based on x-ray computed tomography was used to quantify the drug distribution for different injection parameters; needle length, injection speed and injected volume. A semi-automatic analysis method has been presented. The segmentation algorithm and texture classification have been shown to be robust, and with a few user inputs the full 3D volume could be quantified across the device parameters for all 70 tissue samples.

Using a 5 mm needle when performing injections in LYD pigs gave purely subcutaneous injections. From the image histogram the drug concentration distributions were observed to be similar from injection to injection. All injections were placed in the upper subcutaneous layer. The injections performed with a 5 mm needle have in previous study been shown to give the smallest variation in PK-studies. This suggests that an *ex vivo* analysis of the drug distribution, can be used to optimize the injection technique and reduce the variability in preclinical studies.

In this study no effect of the injection speed on the spatial concentration distribution was seen. Increasing the injected volume to 1 mL did not causes the injections to be intramuscular, but drug accumulation in the subcutaneous fascia layer was more frequently present for the 1 mL injections compared to the 0.1 mL injections. The layered structure in subcutis is not only seen in pigs, but also for humans in some regions of the body (Nakajima et al. 2004). It should be emphasized that the drug distribution might be different from the *in vivo* situation where vascular flow is present.

Because the experiment were performed *ex vivo*, the results cannot be coupled directly to the pharmacokinetics of the drug. High resolution x-ray CT has become a standard analysis tool for diagnostic and quantitative analysis in preclinical studies of rodents (Bouxsein et al. 2010, Campbell & Sophocleous 2014). This technique enables visualization of injections performed *in vivo* in rats, and thus linking drug distribution to the pharmacokinetics of the drug.

5.5 In vivo visualization

For *in vivo* scans, the scan time and resolution is limited by the radiation dose (Ford et al. 2003). Further, is the scan time restricted by the absorption kinetics of the insulin drug for the injection studies. For rats the insulin is present in plasma after a few minutes.

This section presents a test experiment with two injections visualized using both the 3D x-ray microscope (XRadia Versa410, ZEISS), and the preclinical μCT-scanner (QuantumFX, PerkinElmer) (*PerkinElmer* 2015). The injections were performed *ex vivo* after the procedure described in section 3.1.2. For the scans performed at the 3D x-ray microscope, the effective voxel size was 37.5 μm and scan time was 45 min. For the scans performed at the preclinical μCT-scanner, the effective voxel size was 39 μm. The scan was repeated twice; one scan with a scan time of 26 sec and one scan with a scan time of 4.5 min. The segmentation was performed by the MRF algorithm, and the smoothness factor was set at $\beta = 0.5$ for 8 bit images.

Figure 5.13 shows a vertical slice of the tomograms, obtained with a scan time of 45 min (1A), 26 sec (2A) and 4.5 min (3A). The segmentation is shown in Figure 5.13 (1B-3B). Similar to the injections in adipose pig tissue, the drug accumulates in a connective tissue layer.

Figure 5.14 (A) shows the 3D rendering of the segmented depot, from the tomographic reconstruction obtained by the 3D x-ray microscope (grey) and by the preclinical scanner (blue) for a scan time of 4.5 min. Figure 5.14 (B) shows the segmented injection bolus from the tomography scan with a scan time of 4.5 min (blue) compared to the scan with a scan time of 26 sec (grey). Good correlation in the shape is seen for the scans. For the scan with an acquisition time of 26 sec, noise is seen at the periphery of the injection bolus.

The good correlation is also seen from the total segmented volume, calculated for each scan, collected in Table 5.7. The volume is given relative to the volume recovered from the tomograms obtained by the 3D x-ray microscope (scan time 45 min). The images grey scale values were calibrated against water and air (Hounsfield scale)(Webb & Flower 2012), and each voxel was weighted by its grey scale value. The difference in the calculated volume is about 2% between the scans.

The texture segmentation was used to segment the region where the drug is distributed in the connective tissue layer (black arrow), shown in Figure 5.13 (1C-3C) and the volume fractions are listed in Table 5.7. Again we see good correlation between the *ex vivo* and *in vivo* scans.

This small test experiment suggest that the segmentation algorithms are robust, and can be directly applied to *in vivo* µCT-images.

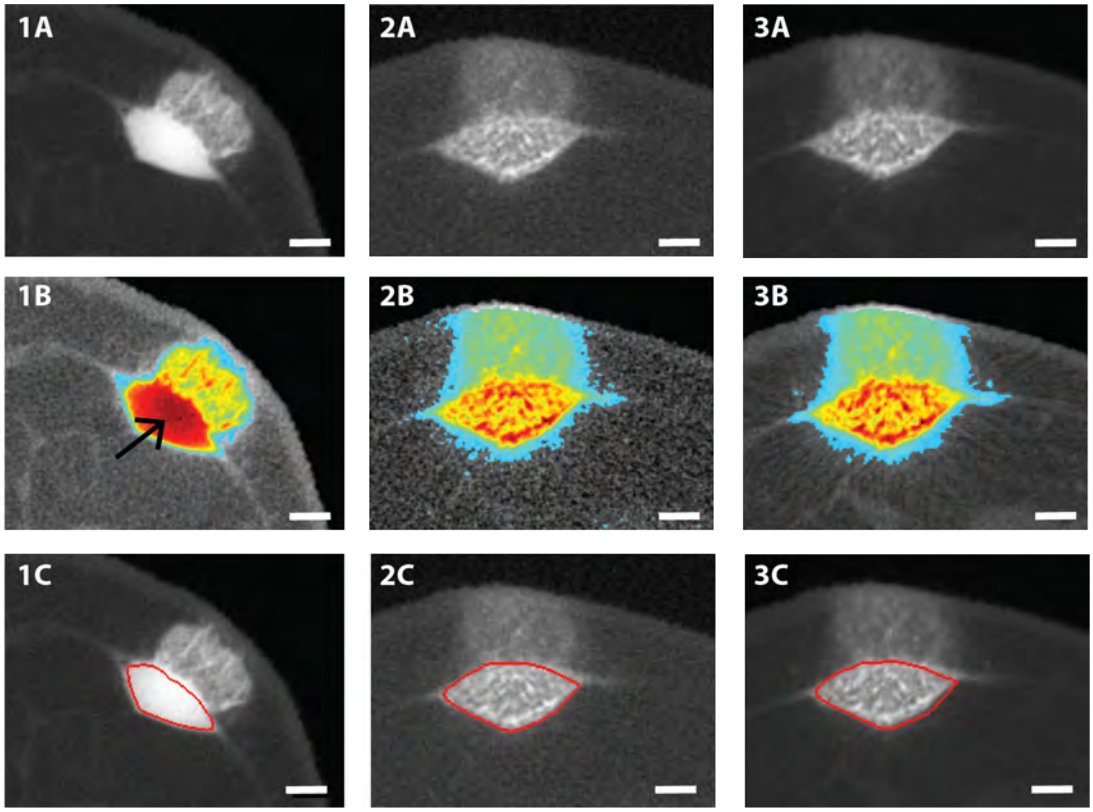

Figure 5.13: *Vertical slice of tomograms obtained by the 3D X-ray microscope (ZEISS XRadia 410 Versa) (1A-C), and a preclinical μCT (QuantumFX, PerkinElmer) with a scan time of 26 sec (2A-C) and 4.5 min (3A-C). The injection bolus is segmented by the MRF algorithm (B), and the high intensity regions are segmented by the texture segmentation algorithm (C). The color scale is related to the iodine concentration (not calibrated). Scale bar is 1 mm.*

Rat	*Ex vivo* scan (45 min)	*In vivo* scan (26 sec)	*In vivo* (4.5 min)
Relative volume			
1	1	1.02	0.98
2	1	1.01	0.98
Volume fraction by texture segmentation			
1	0.45	0.42	0.44
2	0.37	0.34	0.37

Table 5.7: *Total segmented voxel volume relative to the ex vivo scan (scan time 45 min), and the volume fraction segmented by the texture segmentation for the ex vivo scan and two in vivo scans with different scan time. The scan time is given in parentheses.*

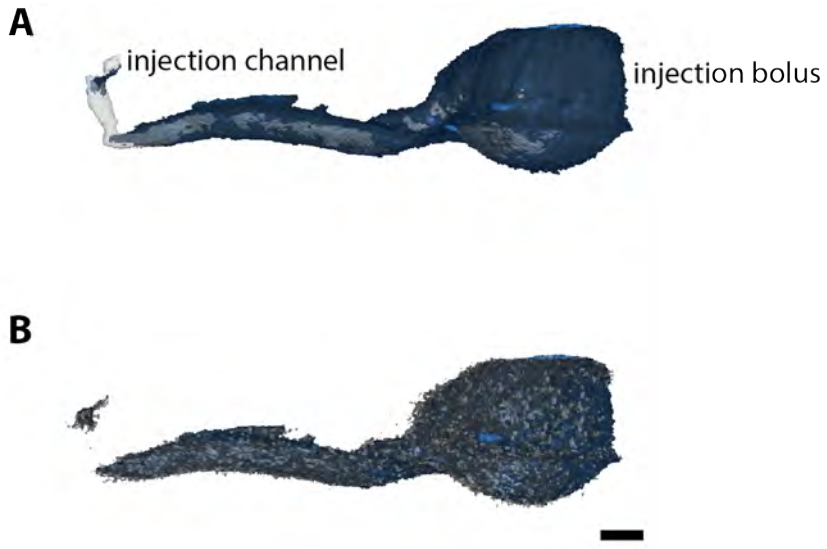

Figure 5.14: *3D rendering of the segmented injection bolus for a 0.03 mL injection in the neck of the rat. (A) The reconstruction obtained from the scan performed at XRadia Versa410, ZEISS with a scan time of 45 min (grey) is compared to reconstruction obtained from the scan performed with QuantumFX, PerkinElmer with a scan time of 4.5 min (blue). (B) The reconstruction obtained from the the scan with a scan time of 4.5 min (blue) is compared to the scan with a scan time of 26 (sec) (grey). Scale bar is 1 mm.*

5.6 Outlook and applications

In this chapter and in Paper IV it has been demonstrated how the spatial distribution of subcutaneously injected drug is influenced by the morphology of the tissue structure and the injection technique. Because the visualization technique is based on x-ray computed tomography it can be implemented for *in vivo* μCT, and the distribution can be linked to the pharmacokinetics of the drug.

Mechanistical modelling can be used to reveal how the different drug distributions seen in the tomograms are related to the absorption kinetics of the drug.

The subcutaneous absorption of soluble insulin has been described by a simplified mechanistic model, initially proposed by Mosekilde et al. (1989). The model is a three compartment model; the subcutaneous tissue, plasma and the interstitium. Several models for both latent

(long acting) and monomeric (fast acting) insulin have later been proposed based on the same basic ideas (Trajanoski et al. 1993, Wach et al. 1995, Tarin et al. 2005, Søeborg et al. 2009).

A semi-mechanistical model for the absorption kinetics for IAsp is presented in Paper VIII (Rasmussen et al. 2013). To illustrate how partly intramuscular injections influences the PK-profile, the model was extended by a muscular compartment. The absorption rate of soluble insulin formulations is higher for intramuscular injections, than for subcutaneous injections, which has been shown in a study of the disappearance rate of radioactive labelled insulin from injections performed with a 3 mm needle (subcutaneous injections) and a 12 mm needle (intramuscular injections) (Hildebrandt et al. 1985).

Figure 5.15 shows the simulated mean PK-profile with a 68% confidence interval (standard deviation) for the injections performed with a 8 mm needle in the pig study, where the intramuscular volume fraction is taken into account (blue curve), compared the purely subcutaneous injections performed with a 5 mm needle (red curve). According to the model CV on $C_{\max}$ (maximum insulin plasma concentration) is increased by about 15%, which illustrates how the accidental intramuscular injections influence the time action profile of the injected drug.

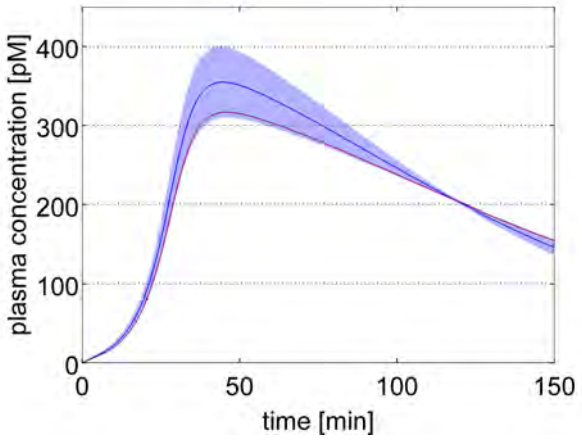

Figure 5.15: *Modelling of the pharmacokinetics of 0.1 mL IAsp injection placed purely subcutaneously (red) or partly intramuscular (blue). The model parameters are adapted from Rasmussen et al. (2013).*

The model parameters were adapted from Paper VIII (Rasmussen et al. 2013), and are based on PK-data from type 1 diabetics (Thorisdottir et al. 2009, Ma et al. 2012). The intramuscular absorption rate was estimated to be 40% higher than the subcutaneous absorption rate from the human study presented by Hildebrandt et al. (1985). For the studies presented in Paper VIII CV for $C_{\max}$ is of the order 35%. In pig studies CV for $C_{\max}$ is of the order 45% for the optimal injection setup (internal study at Novo Nordisk A/S), which emphasizes that the variability is not only related to the injection technique, but also influenced by physiological factors, e.g. differences in the local blood flow, diffusion capacity of the drug, and level of physical activity of the pig.

The model parameters differ among different species, and must be evaluated to have an accurate model description. Furthermore the model can be refined to give a more detailed analysis of how the tissue morphology influences the absorption kinetics.

Chapter 6

Bone morphology

During the project the image analysis tools used for the injection studies found interest in another department in Novo Nordisk A/S, working with hormone therapy for treatment of e.g. osteoporosis and growth hormone deficiencies. These diseases are characterized by low bone mineral density, low bone mineral content, and altered bone morphology (Jee & Yao 2001, Lelovas et al. 2008, Fritton et al. 2010). The mouse and the rat are used as research animals in these studies. The bone morphology in rodents have been characterized both *ex vivo* and *in vivo* by μCT (Bouxsein et al. 2010).

This chapter presents the primarily results from a study of the morphology of the tibia mouse bone quantified by μCT. Figure 6.1 shows the 3D rendering of a tomographic reconstruction of the tibia mouse bone. The study was focused on the region around the epiphyseal growth plate (red arrow). The morphology of the epiphyseal growth plate is of critical importance in the formation of bones (Kronenberg 2003, Blumer et al. 2008).

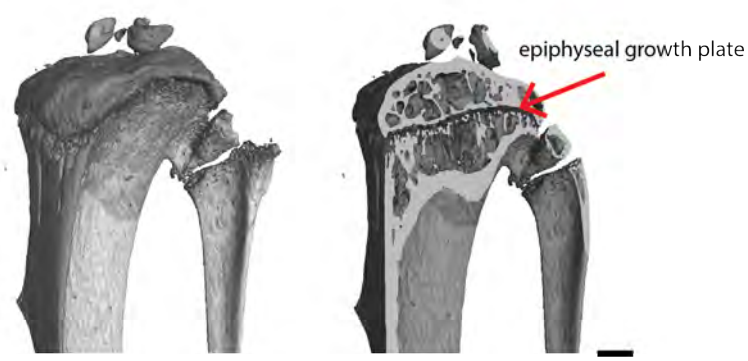

Figure 6.1: *3D rendering of tomographic reconstruction of the tibia mouse. The epiphyseal growth plate is seen in the vertical planer cut (right). The effective voxel size is 9.3* μm*. The scale bar is 500* μm*.*

In the analysis of the tomographic reconstruction of the tibia mouse bone the volume of interest is typically defined from vertical planes extended either proximally or distally from a given plane of interest, e.g. the in the epiphyseal growth plate (Hanson & Bagi 2004, Campbell & Sophocleous 2014). A disadvantages of using a planar cut in the volume is that it does not necessarily follow the anatomy of the bone, and thereby become the volume of interest different

among animals and for the same animal from scan to scan.

Furthermore, the morphological measurements are influenced by the scan resolution (Palacio-Mancheno et al. 2014). *In vivo* μCT investigations are severely limited compared to *ex vivo* investigations, because of the lower radiation dose that can be given to the animals (Ford et al. 2003).

The aim of this study was two fold; (1) to implement an automatic image analysis method that enables direct comparison between different scans, and (2) segment morphological structures from tomograms obtained at different scan resolutions. The results are planned to be submitted to "Journal of Bone Mineral Research", and listed as Paper V *"A volumetric and morphological method for quantification of the growth plate in mice using high resolution μCT"*.

6.1 Experimental procedure

6.1.1 Sample preparation

The mice were euthanized by cervical dislocation. The right and left hind legs were collected by dissection at the head of the femur. The bone samples were fixed in freshly prepared 4% paraformaldehyde for two days and then changed to 70% ethanol. The bones were stored in ethanol between the scans. The study included three tibia mouse bones.

6.1.2 CT acquisition

The bone samples were scanned three times at the 3D X-ray microscope (ZEISS XRadia 410 Versa). A 2×2 binning was applied to the projection images before reconstruction. The effective voxel sizes for the scans were 1.5, 3.7 and 9.3 μm, respectively. No physical filtering of the x-ray beam or beam hardening correction in the reconstruction were applied. The scan parameters are listed in Table 6.1. For clarity the different scans are denoted by their resolution in the following way; HR (high resolution), MR (medium resolution), and LR (low resolution).

ZEISS XRadia 410 Versa			
Target	Tungsten		
Accleration voltage	40 kV		
Current	125 μA		
Detector size	2048 × 2048 pixels^2		
Detector pixel size	13.5 μm		
Pixel-binning	2×2		
Abbreviation	HR	MR	LR
Number of projections over 360°	2601	1601	1601
Total measuring time	15.5 hours	3 hours	5 hours
Detector objective	x10	x4	x0.4
Effective voxel size in reconstruction [μm]	1.5	3.7	9.3

Table 6.1: *Experimental settings for the 3D x-ray microscope (ZEISS XRadia 410 Versa) for the three different scan resolutions.*

6.2 Segmentation and classification

Figure 6.2 shows a vertical (A) and horizontal slice (B) of the tomographic reconstruction with an effective voxel size of 1.5 µm. The tomographic reconstruction can be divided into three classes; bone, cartilage and air. The classes were segmented by the MRF algorithm (Li 2009) (see Section A.1 in Appendix A).

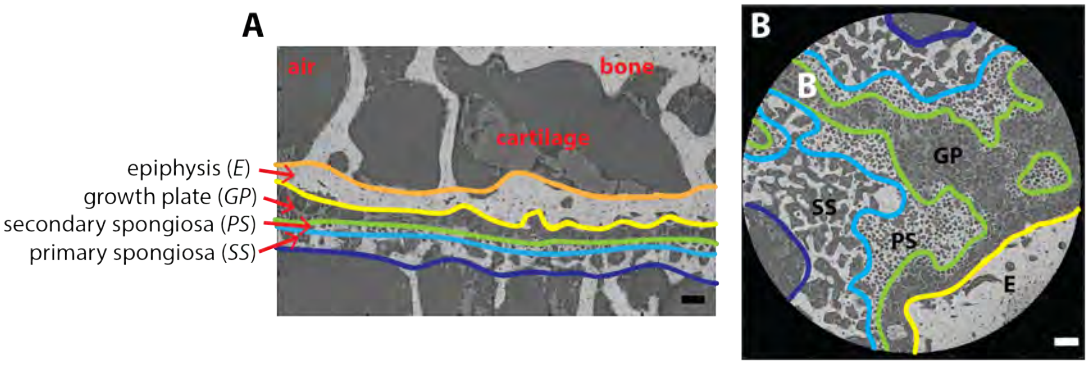

Figure 6.2: *(A) Vertical slice of the tomographic reconstruction with an effective voxel size of 1.5 µm. The sample can be divided into three classes; bone, cartilage and air. The region around the growth plate can be divided into four layers. (B) Horizontal slice of the same tomographic reconstruction, which shows the different textures in each of the layers. The scale bar is 100 µm.*

Four different layers were identified in the region around the epiphyseal growth plate; the epiphysis (E), the growth plate (GP), primary spongiosa (PS), and secondary spongiosa (SS). Each layer can be distinguished by the structure of the bone, shown in Figure 6.2 (B). GP consists of a cartilage layer between the compact bone structure (E), and the porous bone structure (PS). The structures in SS are less compact than the structures in E.

The layers were segmented using learning dictionaries (Dahl & Larsen 2011, Emerson et al. 2015) (see Section A.2 in Appendix A), by the same procedure as used for the injection bolus. The probability maps, obtained for each of the layers, were used as input to a layer surface detection algorithm (Li et al. 2006). The algorithm used was implementation by Vedrana Andersen Dahl (DTU Compute)

6.3 Preliminary results to Paper V

Figure 6.3 shows horizontal slices of the tomographic reconstruction of the tibia bone at an effective voxel size of 1.5 µm (A), 3.7 µm (B) and 9.3 µm (C). It is seen that for HR (A) and MR (B) the four different textures are clearly identified, while for LR the textures become blurred. The texture classification has so far been implemented for HR and MR. Due to the differences in the textures further modification is needed for LR.

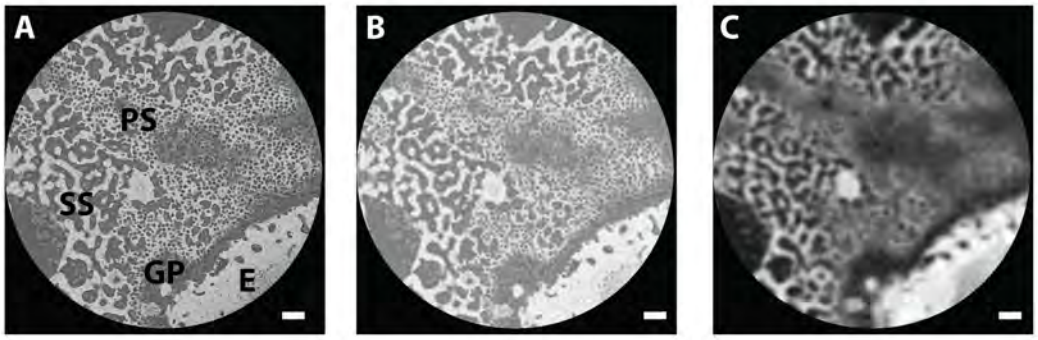

Figure 6.3: *Horizontal slice of the tomographic reconstructions with an effective voxel size of 1.5 µm (A), 3.7 µm (B) and 9.3 µm (C). The scale bar is 100 µm.*

Figure 6.4 shows a vertical and horizontal slice of the HR reconstruction (A), the result of the texture segmentation (B) and the layer surface detection algorithm (C). The algorithms were able to identity the layers for all three samples for HR and MR.

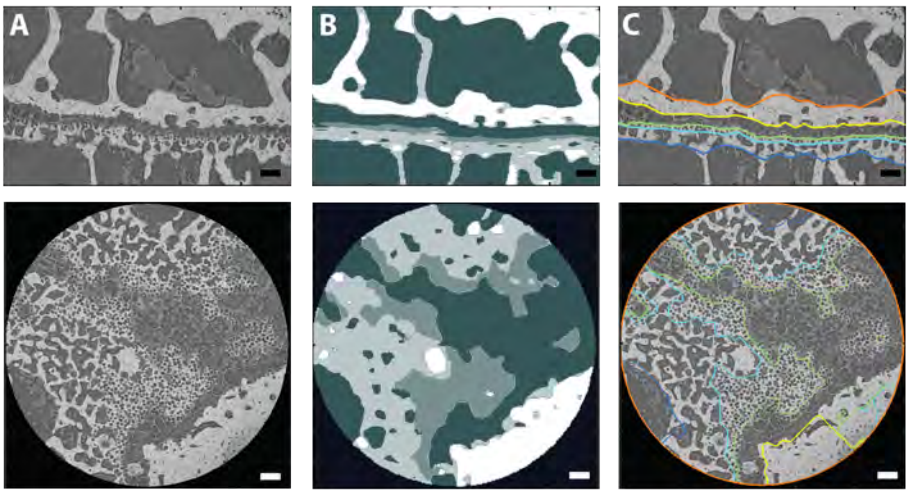

Figure 6.4: *(A) Vertical (top) and horizontal slice (bottom) of the tomographic reconstructions with an effective voxel size of 1.5 µm. (B) Result of the texture segmentation. (C) Result of the layer surface detection algorithm. The scale bar is 100 µm.*

6.3.1 Layer thickness

For each layer the thickness was calculated. The bones were aligned with the long axis in the vertical direction, and the thickness of the layers was calculated as the distance in the vertical direction between the interfaces (coloured lines in Figure 6.4).

The FOV was smaller for HR than for MR, so to compare the thickness calculated at each resolution the two scan were registered manually. The thicknesses for each of the layers were calculated in the region covered by both scans. The results are listed in Table 6.2.

Sample 1

	GP [µm]	PS [µm]	SS [µm]
HR	62.9 (19.1)	22.5 (6.2)	90.7 (35.8)
MR	61.6 (16.1)	31.5 (6.6)	95.8 (31.1)

Sample 2

	GP [µm]	PS [µm]	SS [µm]
HR	41.4 (13.5)	21.3 (4.8)	69.7 (27.1)
MR	38.8 (10.5)	29.2 (0.7)	68.2 (29.8)

Sample 3

	GP [µm]	PS [µm]	SS [µm]
HR	50.7 (11.1)	23.4 (5.4)	78.9 (25.3)
MR	46.9 (9.6)	31.9 (5.1)	83.0 (28.2)

Table 6.2: *Mean layer thickness and standard deviation for the two scans with a resolution of 1.5 µm (HR) and 3.7 µm (MR).*

The standard deviation is given in parentheses and is of the order 20-35% for most of the layers. This shows that measurements in single 2D histological slices may not represent the bone morphology well. Only the PS layer for MR in sample 2 have a vary low variation. The low variation could suggest an error in the segmentation, but from a visual inspection of the segmentation results the layers were segmented well. This is illustrated in Figure 6.5, where (A) shows the layer segmentation in MR, compared to the HR segmentation (B). The PS layer is between the green curve and light blue curve.

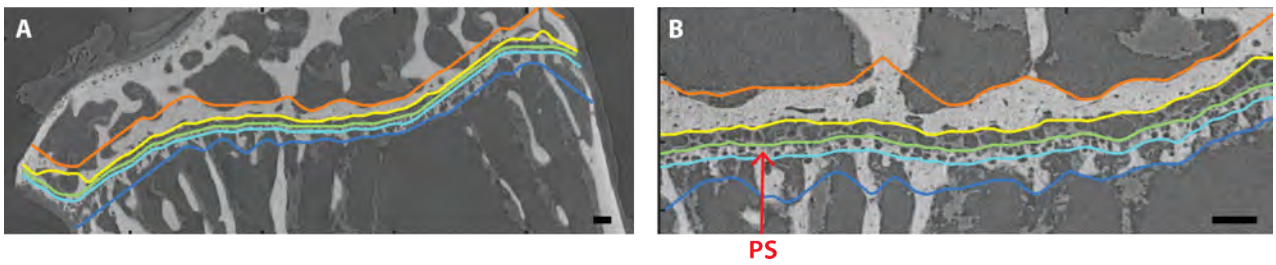

Figure 6.5: *Layer segmentation for sample 2. (A) MR. (B). HR. The PS layer is seen to have a low variability for MR. The scale bar is 100 µm.*

For both GP and SS a good agreement was found in the layer thickness between the two scan resolutions, both for the average value and the standard deviation. The difference between the resolutions are of the order 1-1.5 times the voxel sizes in MR (3.7 μm). The thin PS layers are measured to be thicker from the MR resolution compared to the HR resolution. The measured difference corresponds to about 2-2.5 times the voxel size in MR. This shows that the segmentation algorithm have been able to segment identical structures across the scan resolutions for this sample set.

6.4 Further work

Other measurements of the bone morphology are planned to be implemented, e.g. the bone thickness, total bone volume, and the pore size distribution (Bouxsein et al. 2010). The comparison across scan resolutions requires a rigid registration of the samples to perform the analysis in the same region for each scan resolution. Difference in the morphology seen between the different scans of the same bone can be due either (1) the spatial resolution, or (2) the segmentation algorithms. The aim is to evaluate how both factors affect the quantitative measurements for the individual bones and the comparison between the bones, as presented for the layer thickness.

The sample set also includes scans performed at the preclinical μCT scanner (QuantumFX, PerkinElmer). These scans have about the same effective voxel size (9.8 μm) as LR, but the scanner operates with a larger focal spot size and a much shorter scan time (3 min). Thus, the spatial resolution and the signal to noise ratio are reduced. The aim is identify the structures that can be distinguished in the tomograms, and evaluate how the quantitative analysis of the bone morphology is affected.

6.5 Summary

This chapter presented the primarily results from a quantitative study of the bone morphology using μCT. The segmentation and texture classification algorithm used were the same as used for the adipose tissue samples and insulin injections. The texture segmentation algorithm was able to extract the same textures for the HR and MR scan. By the layer surface detection algorithm four different layers could be extracted.

Studies of bone morphology are often made as comparative studies between the study group and a control group. In these studies it is important to have a robust identification of the volume of interest. For *in vivo* studies the same volume of interest must be identified between scans in order to evaluate the progression of e.g. a bone disorder over time. The layer surface detection algorithm can be used to identify the growth plate, which is suitable as a reference plane.

Ex vivo μCT with a resolution of the order 1-4 μm is a supplementary technique to histology, where the bone morphology is evaluated from 2D slices. From μCT the morphological measurements are obtained in 3D, and thereby better represent the variations in each sample.

Chapter 7

Summary

The absorption of insulin followed subcutaneous injection is a complex processes depending on several factors, e.g. the drug formulation, the injection technique and physiological conditions.

The aim of this PhD project was to investigate the interaction between the injection parameters and the drug distribution at the injection site. This section will summarize and conclude on both the scientific and commercial target for the project.

Scientific target

The scientific target was to characterize the subcutaneous injection process as function of device parameters. The pressure build-up was measured in humans during standard insulin injections, and a model was established for the pressure evaluation at the injection site. From the model the tissue permeability during injection and the bulk modulus was estimated.

A soluble insulin drug formulation was represented by an iodine based x-ray contrast agent, and the spatial distribution in subcutaneous pig tissue was visualized by x-ray computed tomography. The technique provides the spatial drug distribution in 3D for dose sizes in the clinical relevant regime between 0.1-1 mL. The technique is supplementary to the two established methods, histology and laser sheet microscopy, to study the spatial drug distribution. Using this technique it was studied how the spatial drug distribution was effect by the needle length, the injection speed and injected volume. From the tomograms the variability among equally performed injections was quantified. The drug distribution was shown to depend on the injection depth for a needle length between 5-8 mm, and the injected volume for a dose size between 0.1-1 mL. The spatial distribution was not effected by the injection speed in the range from 25-300 μL/s, and no damage of the tissue structures was seen in relation to an increased injection speed. The lowest variability between subcutaneous injections was achieved with a 5 mm needle, which is in agreement with previously PK-studies. This suggest that the presented technique based on *ex vivo* injections can be used to optimize the injection procedure for preclinical testing.

Commercial target

The commercial target was to develop a visual and quantitative analyse tool, which can be used to improve existing and development new delivery system for diabetes care.

A non-invasive method to evaluated the tissue counter pressure, based on a commercial insulin pen, was established. This method can be used to study the performance of existing insulin pens under clinical settings. Furthermore, the experimental measurements were coupled to a model for the pressure evolution in the tissue at the injection site. The model can be implemented in the design phase for new injection systems to simulated the pressure build-up in human tissue.

A visualization tool based on x-ray computed tomography have been established and optimized. Most of the presented experiments were performed using a commercial x-ray imaging systems, and the experimental method has been directly implemented in DRD and used in studies of the drug distribution in subcutaneous pig tissue for different needle designs. The characterization of the drug distribution from the tomograms was applied on both *ex vivo* μCT-tomograms, and low dose *in vivo* μCT tomograms. The technique is appropriate to study a large number of injections and has a direct preclinical application.

As proof of principle we have demonstrated that an energy dispersive x-ray detector can be used to improve the contrast for the injected fluid. Potential this can be used to study the drug distribution for two adjacent injections. At this point in time the technique is limited by the detector performance.

Besides the work with the subcutaneous injections, the project have contributed to the implementation of x-ray computed in other researched areas in Novo Nordisk A/S. During the time of this project a preclinical μCT-scanner for rodents was purchased to study the bone morphology in rodents. The bone morphology visualized by the *in vivo* μCT was compared to high resolution *ex vivo* μCT. The high resolution μCT with an effective voxel size of 1.5 μm was supplementary to histology. The bone structures for the high resolution scans have been segmented and classified. The work are still under progress to finally conclude on how the quantitative measurements of the bone morphology are affected by the spatial resolution in the textitin vivo μCT scan.

A number of studies have not been included in this thesis. The spatial drug distribution of subcutaneous injections in beagle dogs have been visualized by μCT to investigate the variability among species. *In vivo* μCT have been used to study the disintegration of oral tablet formulations and transport of small pellets in the gut and intestine in rodents.

Aortic plaque in the Göttingen Minipig has been visualized by the use of different staining agents, and the technique is now under development as an supplementary technique to histological examinations. This have opened for a new collaboration opportunity between academia and Novo Nordisk A/S.

7.1 Outlook

An optimized insulin injection therapy includes both a convenient injection technique and a controlled absorption rate from the injection site.

Further investigations of the tissue counter pressure in humans requires a clinical study, where the pressure build-up is studied for different device parameters. Monitoring of the tissue pressure not only at the needle tip, but also in the surrounding tissue, with a link to the pain experienced by the patient, can provide DRD with an improved quantitative optimization tool for designing new injection devices.

Obesity is one of the risk factors for developing type 2 diabetes, and for these patients the prescribed insulin dose can be high, due to both a high level of insulin resistance and the weight of the patient. The absorption rate of the insulin from the injection site depends on the insulin concentration, and therefore, it is not trivial to increase the insulin concentration of the formulation. This demands injection devices that are able to deliver a large volume in a single injection not associated with increased pain, not resulting in damage of the tissue structures at the injection site, or causes the injected drug to be partly intramuscular or intradermal.

Human studies cannot be conducted in the design phase of new injection systems, and therefore are the subcutaneous pig tissue used as a model for the human tissue. Today a correlation between the drug distribution in adipose pig tissue and humans tissue, have not been established. The first step in establishing such a link could be a visualization of *ex vivo* injections in fresh cadavers, and secondly to investigate the opportunities and limitations of clinical CT for *in vivo* evaluations.

Understanding the factors effecting the absorption process is important for further optimization of the subcutaneous insulin drug formulations and injection systems. Novel insight in the absorption kinetics for insulin formulation can be obtained by linking the PK and PD of the drug to the drug distribution and the physiological conditions at the injection site, e.g. drug concentration, pH level, zinc concentration and blood flow. This will require measurements with multiply different techniques which is challenging to combine in a single experiment.

Alternatives to the subcutaneous injections are extensively studied, including inhaled insulin and oral drug formulation. For the oral formulations the insulin must be absorbed either from the gut or from the intestine. Oral insulin formulations still stuffer from a lower bioavailability and larger variability than the subcutaneous injections. Different imaging modalities such as magnetic resonance imaging can provide insight into the *in vivo* tablet disintegration or PET imaging can be to study the absorption.

See how things look and behave *in vivo* is a direct and intuitive way to understand the challenges involved in the design of new drug formulations, and new imaging modalities must be developed in that direction.

Bibliography

Agache, P. & Humbert, P. (2004), *Measuring the skin*, Springer.

Allmendinger, A., Mueller, R., Schwarb, E., Chipperfield, M., Huwyler, J., Mahler, H.-C. & Fischer, S. (2014), 'Measuring tissue back-pressure-in vivo injection forces during subcutaneous injection', *Pharmaceutical research* pp. 1–12.

Als-Nielsen, J. & McMorrow, D. (2011), *Elements of modern X-ray physics*, Wiley.

Alvarez, R. & Macovski, A. (1976), 'Energy-selective reconstructions in x-ray computerised tomography', *Physics in Medicine and Biology* **21**(5), 733.

Amptek Inc. (2015), http://amptek.com/.
URL: *http://amptek.com/*

Aukland, K. & Reed, R. (1993), 'Interstitial-lymphatic mechanisms in the control of extracellular fluid volume', *Physiological reviews* **73**(1), 1–78.

Ballabriga, R., Campbell, M., Heijne, E., Llopart, X. & Tlustos, L. (2006), 'The Medipix3 prototype, a pixel readout chip working in single photon counting mode with improved spectrometric performance', *Nuclear Science Symposium Conference Record, 2006. IEEE* **6**, 3557–3561.

Ballabriga, R., Campbell, M., Heijne, E., Llopart, X., Tlustos, L. & Wong, W. (2011), 'Medipix3: A 64k pixel detector readout chip working in single photon counting mode with improved spectrometric performance', *Nuclear Instruments and Methods in Physics Research Section A: Accelerators, Spectrometers, Detectors and Associated Equipment* **633**, S15–S18.

Banting, F., Best, C. H., Collip, J. B., Campbell, W. R. & Fletcher, A. A. (1922), 'Pancreatic extracts in the treatment of diabetes mellitus', *Canadian Medical Association Journal* **12**(3), 141.

Bantle, J., Neal, L. & Frankamp, L. (1993), 'Effects of the anatomical region used for insulin injections on glycemia in type i diabetes subjects', *Diabetes Care* **16**(12), 1592–1597.

Bearden, J. A. (1967), 'X-ray wavelengths', *Reviews of Modern Physics* **39**(1), 78.

Bech, M., Bunk, O., David, C., Kraft, P., Brönnimann, C., Eikenberry, E. & Pfeiffer, F. (2008), 'X-ray imaging with the PILATUS 100k detector', *Applied Radiation and Isotopes* **66**(4), 474–478.

Beister, M., Kolditz, D. & Kalender, W. A. (2012), 'Iterative reconstruction methods in X-ray CT', *Physica medica* **28**(2), 94–108.

Bellin, M.-F. & Van Der Molen, A. J. (2008), 'Extracellular gadolinium-based contrast media: an overview', *European journal of radiology* **66**(2), 160–167.

Berg JM, Tymoczko JL, S. L. (2002), *Biochemistry*, 5th edition edn, New York: W H Freeman.

Berger, M., Hubbell, J., Seltzer, S., Chang, J., Coursey, J., Sukumar, R., Zucker, D. & Olsen, K. (1998), 'XCOM: photon cross sections database', *NIST Standard reference database* **8**, 87–3597.

Bertalmio, M., Sapiro, G., Caselles, V. & Ballester, C. (2000), Image inpainting, *in* 'Proceedings of the 27th annual conference on Computer graphics and interactive techniques', ACM Press/Addison-Wesley Publishing Co., pp. 417–424.

Blumer, M. J., Longato, S. & Fritsch, H. (2008), 'Structure, formation and role of cartilage canals in the developing bone', *Annals of Anatomy-Anatomischer Anzeiger* **190**(4), 305–315.

Bourrinet, P., Dencausse, A., Havard, P., Violas, X. & Bonnemain, B. (1995), 'Transplacental passage and milk excretion of iobitridol', *Investigative radiology* **30**(3), 156–158.

Bouxsein, M. L., Boyd, S. K., Christiansen, B. A., Guldberg, R. E., Jepsen, K. J. & Müller, R. (2010), 'Guidelines for assessment of bone microstructure in rodents using micro–computed tomography', *Journal of Bone and Mineral Research* **25**(7), 1468–1486.

Brange, J. (1994), *Stability of insulin: Studies on the physical and chemical stability of insulin in pharmaceutical formulation*, Kluwer Academic Publishers.

Brange, J. & Langkjaer, L. (1992), 'Chemical stability of insulin. 3. Influence of excipients, formulation, and pH.', *Acta pharmaceutica nordica* **4**(3), 149.

Broennimann, C., Eikenberry, E., Henrich, B., Horisberger, R., Huelsen, G., Pohl, E., Schmitt, B., Schulze-Briese, C., Suzuki, M., Tomizaki, T. et al. (2006), 'The PILATUS 1M detector', *Journal of synchrotron radiation* **13**(2), 120–130.

Bronaugh, R. L., Stewart, R. F. & Congdon, E. R. (1982), 'Methods for in vitro percutaneous absorption studies II. Animal models for human skin', *Toxicology and applied pharmacology* **62**(3), 481–488.

Brooks, R. & Di Chiro, G. (1976), 'Beam hardening in x-ray reconstructive tomography', *Physics in Medicine and Biology* **21**(3), 390.

Bunk, O., Bech, M., Jensen, T. H., Feidenhans, R., Binderup, T., Menzel, A. & Pfeiffer, F. (2009), 'Multimodal x-ray scatter imaging', *New Journal of Physics* **11**(12), 123016.

Campbell, G. M. & Sophocleous, A. (2014), 'Quantitative analysis of bone and soft tissue by micro-computed tomography: applications to ex vivo and in vivo studies', *BoneKEy reports* **3**.

Cengiz, E., Weinzimer, S. A., Sherr, J. L., Tichy, E. M., Carria, L., Cappiello, D., Steffen, A. & Tamborlane, W. V. (2014), 'Faster in and faster out: accelerating insulin absorption and action by insulin infusion site warming', *Diabetes technology & therapeutics* **16**(1), 20–25.

Chabior, M., Donath, T., David, C., Bunk, O., Schuster, M., Schroer, C. & Pfeiffer, F. (2011), 'Beam hardening effects in grating-based x-ray phase-contrast imaging', *Med. Phys* **38**(3), 1189–1195.

Chan, T. & Vese, L. (2001), 'Active contours without edges', *Image Processing, IEEE Transactions on* **10**(2), 266–277.

Chantler, C. (2000), 'Detailed tabulation of atomic form factors, photoelectric absorption and scattering cross section, and mass attenuation coefficients in the vicinity of absorption edges in the soft x-ray (z= 30-36, z= 60-89, e= 0.1 kev-10 kev), addressing convergence issues of earlier work detailed tabulation of atomic form factors, photoelectric absorption and scattering cross section, and mass attenuation coefficients in the vicinity of absorption edges in the soft x-ray (z= 30-36, z= 60-89, e= 0.1 kev-10 kev), addressing convergence issues of earlier work', *Journal of Physical and Chemical Reference Data* **29**(4), 597.

Chapman, D., Thomlinson, W., Johnston, R., Washburn, D., Pisano, E., Gmür, N., Zhong, Z., Menk, R., Arfelli, F. & Sayers, D. (1997), 'Diffraction enhanced x-ray imaging', *Physics in medicine and biology* **42**(11), 2015.

Charman, S. A., McLennan, D. N., Edwards, G. A. & Porter, C. J. (2001), 'Lymphatic absorption is a significant contributor to the subcutaneous bioavailability of insulin in a sheep model', *Pharmaceutical research* **18**(11), 1620–1626.

Clifford, P. (1990), 'Markov random fields in statistics', *Disorder in physical systems: A volume in honour of John M. Hammersley* pp. 19–32.

Coleman, A. & Sinclair, M. (1985), 'A beam-hardening correction using dual-energy computed tomography', *Physics in Medicine and Biology* **30**(11), 1251.

Comley, K. S. C. (2010), The mechanical properties of adipose tissue, PhD thesis, University of Cambridge, Emmanuel Collage.

Cormack, A. M. (1963), 'Representation of a function by its line integrals, with some radiological applications', *Journal of Applied Physics* **34**(9), 2722–2727.

Crank, J. et al. (1975), *The mathematics of diffusion*, Vol. 2, Clarendon press Oxford.

Crystals, S.-G. (2008), 'Efficiency calculations for selected scintillators'.

Dahl, A. L. & Larsen, R. (2011), Learning dictionaries of discriminative image patches, *in* '22nd British Machine Vision Conference'.

Danaei, G., Finucane, M. M., Lu, Y., Singh, G. M., Cowan, M. J., Paciorek, C. J., Lin, J. K., Farzadfar, F., Khang, Y.-H., Stevens, G. A., Rao, M., Ali, M. K., Riley, L. M., Robinson, C. A. & Ezzati, M. (2011), 'National, regional, and global trends in fasting plasma glucose and diabetes prevalence since 1980: systematic analysis of health examination surveys and epidemiological studies with 370 country-years and 2.7 million participants', *The Lancet* **378**(9785), 31 – 40.

Davis, T., Gao, D., Gureyev, T., Stevenson, A. & Wilkins, S. (373), 'Phase-contrast imaging of weakly absorbing materials using hard x-rays', *Nature* **6515**(595–598), 1995.

Deckert, T., Hansen, B., Kølendorf, K., Poulsen, J. & Smith, M. (1982), 'Absorption of NPH-insulin from subcutaneous tissue: A methodological study in pigs', *Acta pharmacologica et toxicologica* **51**(1), 30–37.

DECTRIS (2015), https://www.dectris.com.

Douglas, W. R. (1972), 'Of pigs and men and research', *Origins of Life and Evolution of Biospheres* **3**(3), 226–234.

Elleaume, H., Charvet, A., Corde, S., Esteve, F. & Le Bas, J. (2002), 'Performance of computed tomography for contrast agent concentration measurements with monochromatic x-ray beams: comparison of k-edge versus temporal subtraction', *Physics in medicine and biology* **47**(18), 3369.

Emerson, M. J., Jespersen, K. M., Jørgensen, P. S., Larsen, R. & Dahl, A. L. (2015), Dictionary based segmentation in volumes. (unpublished).

Engwerda, E. E., Tack, C. J. & de Galan, B. E. (2013), 'Needle-free jet injection of rapid-acting insulin improves early postprandial glucose control in patients with diabetes', *Diabetes care* **36**(11), 3436–3441.

Ertürk, A., Becker, K., Jährling, N., Mauch, C. P., Hojer, C. D., Egen, J. G., Hellal, F., Bradke, F., Sheng, M. & Dodt, H.-U. (2012), 'Three-dimensional imaging of solvent-cleared organs using 3DISCO', *Nature protocols* **7**(11), 1983–1995.

Ertürk, A. & Bradke, F. (2013), 'High-resolution imaging of entire organs by 3-dimensional imaging of solvent cleared organs (3DISCO)', *Experimental neurology* **242**, 57–64.

Farsaei, S., Radfar, M., Heydari, Z., Abbasi, F. & Qorbani, M. (2014), 'Insulin adherence in patients with diabetes: Risk factors for injection omission', *Primary care diabetes* **8**(4), 338–345.

Feldkamp, L., Davis, L. & Kress, J. (1984), 'Practical cone-beam algorithm', *JOSA A* **1**(6), 612–619.

Ford, N., Thornton, M. & Holdsworth, D. (2003), 'Fundamental image quality limits for microcomputed tomography in small animals', *Medical physics* **30**(11), 2869–2877.

Frid, A. & Linde, B. (1992), 'Intraregional differences in the absorption of unmodified insulin from the abdominal wall', *Diabetic medicine* **9**(3), 236–239.

Fritton, J. C., Emerton, K. B., Sun, H., Kawashima, Y., Mejia, W., Wu, Y., Rosen, C. J., Panus, D., Bouxsein, M., Majeska, R. J. et al. (2010), 'Growth hormone protects against ovariectomy-induced bone loss in states of low circulating insulin-like growth factor (igf-1)', *Journal of Bone and Mineral Research* **25**(2), 235–246.

GE Measurements & Control (2013), http://www.ge-mcs.com/en/.
URL: *http://www.ge-mcs.com/en/*

Gibney, M. A., Arce, C. H., Byron, K. J. & Hirsch, L. J. (2010), 'Skin and subcutaneous adipose layer thickness in adults with diabetes at sites used for insulin injections: implications for needle length recommendations', *Current Medical Research & Opinion* **26**(6), 1519–1530.

Gierada, D. S. & Bae, K. T. (1999), 'Gadolinium as a ct contrast agent: assessment in a porcine model', *Radiology* **210**(3), 829–834.

Gin, H. & Hanaire-Broutin, H. (2005), 'Reproducibility and variability in the action of injected insulin', *Diabetes & metabolism* **31**(1), 7–13.

Guerci, B. & Sauvanet, J. (2005), 'Subcutaneous insulin: pharmacokinetic variability and glycemic variability', *Diabetes & metabolism* **31**(4), 4S7–4S24.

Gupta, J., Felner, E. I. & Prausnitz, M. R. (2011), 'Rapid pharmacokinetics of intradermal insulin administered using microneedles in type 1 diabetes subjects', *Diabetes technology & therapeutics* **13**(4), 451–456.

H. Wiig, K. R. & Reed, R. K. (2003), 'New and active role of the interstitium in control of interstitial fluid pressure: potential therapeutic consequences', *Acta Anaesthesiological Scandinavica* **47**, 111–121.

Hamamatsu Photonics K.K. (2015), https://www.hamamatsu.com.

Hammersberg, P. & Mangard, M. (1998), 'Correction for beam hardening artefacts in computerised tomography', *Journal of X-ray Science and Technology* **8**(1), 75.

Hanson, N. A. & Bagi, C. M. (2004), 'Alternative approach to assessment of bone quality using micro-computed tomography', *Bone* **35**(1), 326–333.

Heinemann, L. (2002), 'Variability of insulin absorption and insulin action', *Diabetes technology & therapeutics* **4**(5), 673–682.

Heinemann, L. (2008), 'Variability of insulin action: Does it matter?', *Insulin* **3**(1), 37–45.

Heise, T., Nosek, L., Dellweg, S., Zijlstra, E., Præstmark, K. A., Kildegaard, J., Nielsen, G. & Sparre, T. (2014), 'Impact of injection speed and volume on perceived pain during subcutaneous injections into the abdomen and thigh: a single-centre, randomized controlled trial', *Diabetes, Obesity and Metabolism* **16**(10), 971–976.

Heller, S., Kozlovski, P. & Kurtzhals, P. (2007), 'Insulin's 85th anniversary: An enduring medical miracle', *Diabetes research and clinical practice* **78**(2), 149–158.

Herman, G. (1979), 'Correction for beam hardening in computed tomography', *Physics in Medicine and Biology* **24**(1), 81–106.

Hildebrandt, P., Sejrsen, P., Nielsen, S., Birch, K. & Sestoft, L. (1985), 'Diffusion and polymerization determines the insulin absorption from subcutaneous tissue in diabetic patients', *Scandinavian Journal of Clinical and Laboratory Investigation* **45**(8), 685–690.

Hildebrandt, P., Sestoft, L. & Nielsen, S. L. (1983), 'The absorption of subcutaneously injected short-acting soluble insulin: influence of injection technique and concentration', *Diabetes Care* **6**(5), 459–462.

Hirsch, I. B. (2005), 'Insulin analogues', *New England Journal of Medicine* **352**(2), 174–183.

Hofman, P. L., Derraik, J. G. B., Pinto, T. E., Tregurtha, S., Faherty, A., Peart, J. M., Drury, P. L., Robinson, E., Tehranchi, R., Donsmark, M. et al. (2010), 'Defining the ideal injection techniques when using 5-mm needles in children and adults', *Diabetes Care* **33**(9), 1940–1944.

Hofman, P., Lawton, S., Peart, J., Holt, J., Jefferies, C., Robinson, E. & Cutfield, W. (2007), 'An angled insertion technique using 6-mm needles markedly reduces the risk of intramuscular injections in children and adolescents', *Diabetic Medicine* **24**(12), 1400–1405.

Holt, R. I., Cockram, C., Flyvbjerg, A. & Goldstein, B. J. (2011), *Textbook of diabetes*, John Wiley & Sons.

Hounsfield, G. N. (1973), 'Computerized transverse axial scanning (tomography): Part 1. description of system', *British Journal of Radiology* **46**(552), 1016–1022.

Hülsen-Bollier, G. (2005), The PILATUS 1M detector a novel large area pixel detector, PhD thesis, Swiss Federal Institute of Technology Zurich.

Ito, M., Ejiri, S., Jinnai, H., Kono, J., Ikeda, S., Nishida, A., Uesugi, K., Yagi, N., Tanaka, M. & Hayashi, K. (2003), 'Bone structure and mineralization demonstrated using synchrotron radiation computed tomography (SR-CT) in animal models: preliminary findings', *Journal of Bone and Mineral Metabolism* **21**(5), 287–293.

Jee, W. & Yao, W. (2001), 'Overview: animal models of osteopenia and osteoporosis', *J Musculoskelet Neuronal Interact* **1**(3), 193–207.

Jennings, R. (1988), 'A method for comparing beam-hardening filter materials for diagnostic radiology', *Medical Physics* **15**(4), 588–599.

Jensen, T. H., Böttiger, A., Bech, M., Zanette, I., Weitkamp, T., Rutishauser, S., David, C., Reznikova, E., Mohr, J., Christensen, L. B. et al. (2011), 'X-ray phase-contrast tomography of porcine fat and rind', *Meat science* **88**(3), 379–383.

Jockel, J. P. L., Roebrock, P., Shergold, O. A. & Huwiler, C. (2013), 'Insulin depot formation in subcutaneous tissue', *Journal of diabetes science and technology* **7**(1), 227–237.

Kagan, L. (2014), 'Pharmacokinetic modeling of the subcutaneous absorption of therapeutic proteins', *Drug Metabolism and Disposition* **42**(11), 1890–1905.

Kang, S., Brange, J., Burch, A., Vølund, A. & Owens, D. R. (1991), 'Subcutaneous insulin absorption explained by insulin's physicochemical properties: evidence from absorption studies of soluble human insulin and insulin analogues in humans', *Diabetes care* **14**(11), 942–948.

Karges, B., Boehm, B. & Karges, W. (2005), 'Early hypoglycaemia after accidental intramuscular injection of insulin glargine', *Diabetic Medicine* **22**(10), 1444–1445.

Kazakia, G., Burghardt, A., Cheung, S. & Majumdar, S. (2008), 'Assessment of bone tissue mineralization by conventional x-ray microcomputed tomography: comparison with synchrotron radiation microcomputed tomography and ash measurements', *Medical physics* **35**, 3170.

Knudsen, E., Prodi, A., Baltser, J., Thomsen, M., Willendrup, P., Sanchez del Rio, M., Ferrero, C., Farhi, E., Haldrup, K., Vickery, A. et al. (2013), 'Mcxtrace: a Monte Carlo software package for simulating x-ray optics, beamlines and experiments', *Journal of Applied Crystallography* **46**(3), 679–696.

Kolmogorov, V. & Zabin, R. (2004), 'What energy functions can be minimized via graph cuts?', *Pattern Analysis and Machine Intelligence, IEEE Transactions on* **26**(2), 147–159.

Kraft, P., Bergamaschi, A., Broennimann, C., Dinapoli, R., Eikenberry, E., Henrich, B., Johnson, I., Mozzanica, A., Schlepütz, C., Willmott, P. et al. (2009b), 'Performance of single-photon-counting pilatus detector modules', *Journal of synchrotron radiation* **16**(3), 368–375.

Kraft, P., Bergamaschi, A., Bronnimann, C., Dinapoli, R., Eikenberry, E., Graafsma, H., Henrich, B., Johnson, I., Kobas, M. & Mozzanica, A. (2009a), 'Characterization and calibration of pilatus detectors', *Nuclear Science, IEEE Transactions on* **56**(3), 758–764.

Kramers, H. A. (1923), 'Xciii. on the theory of x-ray absorption and of the continuous x-ray spectrum', *The London, Edinburgh, and Dublin Philosophical Magazine and Journal of Science* **46**(275), 836–871.

Kronenberg, H. M. (2003), 'Developmental regulation of the growth plate', *Nature* **423**(6937), 332–336.

Krumm, M., Kasperl, S. & Franz, M. (2008), 'Reducing non-linear artifacts of multi-material objects in industrial 3d computed tomography', *NDT & E International* **41**(4), 242–251.

Kurtzhals, P. & Ribel, U. (1995), 'Action profile of cobalt (III)-insulin: a novel principle of protraction of potential use for basal insulin delivery', *Diabetes* **44**(12), 1381–1385.

Lajara, R., Guerrero, G. & Thurman, J. (2012), 'Healthcare professional and patient perceptions of a new prefilled insulin pen versus vial and syringe', *Expert Opinion on Drug Delivery* **9**(10), 1181–1196.

Lauritzen, T., Binder, C. & Faber, O. (1980), 'Importance of insulin absorption, subcutaneous blood flow, and residual beta-cell function in insulin therapy', *Acta Paediatrica* **69**, 81–84.

Lautrup, B. (2011), *Physics of Continuous Matter*, Taylor& Francis, Second Edition.

Le Duc, G., Corde, S., Charvet, A.-M., Elleaume, H., Farion, R., Le Bas, J.-F. & Esteve, F. (2004), 'In vivo measurement of gadolinium concentration in a rat glioma model by monochromatic quantitative computed tomography: comparison between gadopentetate dimeglumine and gadobutrol', *Investigative radiology* **39**(7), 385–393.

Lelovas, P. P., Xanthos, T. T., Thoma, S. E., Lyritis, G. P. & Dontas, I. A. (2008), 'The laboratory rat as an animal model for osteoporosis research', *Comparative medicine* **58**(5), 424.

Li, K., Wu, X., Chen, D. Z. & Sonka, M. (2006), 'Optimal surface segmentation in volumetric images-a graph-theoretic approach', *Pattern Analysis and Machine Intelligence, IEEE Transactions on* **28**(1), 119–134.

Li, S. Z. (2009), *Markov random field modeling in image analysis*, Springer.

Liu, L. (2014), 'Model-based iterative reconstruction: A promising algorithm for today's computed tomography imaging', *Journal of Medical Imaging and Radiation Sciences* **45**(2), 131–136.

Lopes, R., Costa, E. & de Jesus, E. (2000), 'Computed tomography with monochromatic bremsstrahlung radiation', *Applied Radiation and Isotopes* **53**(4), 665–671.

Ma, Z., Parkner, T., Frystyk, J., Laursen, T., Lauritzen, T. & Christiansen, J. S. (2012), 'A comparison of pharmacokinetics and pharmacodynamics of insulin aspart, biphasic insulin aspart 70, biphasic insulin aspart 50, and human insulin: a randomized, quadruple crossover study', *Diabetes technology & therapeutics* **14**(7), 589–595.

Mader, J. K., Birngruber, T., Korsatko, S., Deller, S., Köhler, G., Boysen, S., Augustin, T., Mautner, S. I., Sinner, F., Pieber, T. R. et al. (2012), 'Enhanced absorption of insulin aspart as the result of a dispersed injection strategy tested in a randomized trial in type 1 diabetic patients', *Diabetes care* .

Markussen, J., Havelund, S., Kurtzhals, P., Andersen, A., Halstrøm, J., Hasselager, E., Larsen, U., Ribel, U., Schäffer, L., Vad, K. et al. (1996), 'Soluble, fatty acid acylated insulins bind to albumin and show protracted action in pigs', *Diabetologia* **39**(3), 281–288.

McVey, E., Hirsch, L., Sutter, D. E., Kapitza, C., Dellweg, S., Clair, J., Rebrin, K., Judge, K. & Pettis, R. J. (2012), 'Pharmacokinetics and postprandial glycemic excursions following insulin lispro delivered by intradermal microneedle or subcutaneous infusion', *Journal of diabetes science and technology* **6**(4), 743–754.

Meganck, J., Kozloff, K., Thornton, M., Broski, S. & Goldstein, S. (2009), 'Beam hardening artifacts in micro-computed tomography scanning can be reduced by x-ray beam filtration and the resulting images can be used to accurately measure BMD', *Bone* **45**(6), 1104–1116.

Milan, G., Murano, I., Costa, S., Pianta, A., Tiengo, C., Zulato, E., Centobene, C., Bruttomesso, D., Cinti, S. & Vettor, R. (2010), 'Lipoatrophy induced by subcutaneous insulin infusion: ultrastructural analysis and gene expression profiling', *Journal of Clinical Endocrinology & Metabolism* **95**(7), 3126–3132.

Mollema, E., Snoek, F., Heine, R. & Van der Ploeg, H. (2001), 'Phobia of self-injecting and self-testing in insulin-treated diabetes patients: opportunities for screening', *Diabetic medicine* **18**(8), 671–674.

Moore, E., Mitchell, M. & Chalmers, T. (1959), 'Variability in absorption of insulin-I131 in normal and diabetic subjects after subcutaneous and intramuscular injection', *Journal of Clinical Investigation* **38**(7), 1222.

Mosekilde, E., Jensen, K. S., Binder, C., Pramming, S. & Thorsteinsson, B. (1989), 'Modeling absorption kinetics of subcutaneous injected soluble insulin', *Journal of pharmacokinetics and biopharmaceutics* **17**(1), 67–87.

Moshtagh, N. (2005), 'Minimum volume enclosing ellipsoid', *Convex Optimization* .

Nakajima, H., Imanishi, N., Minabe, T., Kishi, K. & Aiso, S. (2004), 'Anatomical study of subcutaneous adipofascial tissue: a concept of the protective adipofascial system (pafs) and lubricant adipofascial system (lafs)', *Scandinavian journal of plastic and reconstructive surgery and hand surgery* **38**(5), 261–266.

Nazarian, A., Snyder, B., Zurakowski, D. & Müller, R. (2008), 'Quantitative micro-computed tomography: a non-invasive method to assess equivalent bone mineral density', *Bone* **43**(2), 302–311.

Nikl, M. (2006), 'Scintillator detectors for x-rays', *Measurement Science and Technology* **17**, R37–R54.

Nolte, M. (2009), 'Pancreatic hormones and antidiabetic drugs', *In: Katzund BG, Masters SB, Trevor AJ. Eds. Basic and Clinical Pharmacology. USA: McGrew-Hill* pp. 737–747.

Nucci, G. & Cobelli, C. (2000), 'Models of subcutaneous insulin kinetics. a critical review', *Computer methods and programs in biomedicine* **62**(3), 249–257.

Nuzzo, S., Peyrin, F., Cloetens, P., Baruchel, J. & Boivin, G. (2002), 'Quantification of the degree of mineralization of bone in three dimensions using synchrotron radiation microtomography', *Medical Physics* **29**, 2672.

Ogston-Tuck, S. (2014), 'Subcutaneous injection technique: an evidence-based approach', *Nursing Standard* **29**(3), 53–58.

Owens, D. R. (2002), 'New horizonsalternative routes for insulin therapy', *Nature Reviews Drug Discovery* **1**(7), 529–540.

Owens, D. R., Zinman, B. & Bolli, G. B. (2001), 'Insulins today and beyond', *The lancet* **358**(9283), 739–746.

Palacio-Mancheno, P., Larriera, A., Doty, S., Cardoso, L. & Fritton, S. (2014), '3d assessment of cortical bone porosity and tissue mineral density using high-resolution μct: effects of resolution and threshold method.', *J Bone Miner Res* **29**(1), 142–150.

Patte, C., Pleus, S., Wiegel, C., Schiltges, G., Jendrike, N., Haug, C. & Freckmann, G. (2013), 'Effect on infusion rate and indwelling time on tissue resistance pressure in small-volume subcutaneous infusion like in continuous subcutaneous insulin infusion', *Diabetes Technology & Therapeutics* **15**(4), 289–294.

Pearson, T. L. (2010), 'Practical aspects of insulin pen devices', *Journal of diabetes science and technology* **4**(3), 522–531.

Pennicard, D., Lange, S., Smoljanin, S., Hirsemann, H., Graafsma, H., Epple, M., Zuvic, M., Lampert, M., Fritzsch, T. & Rothermund, M. (2013), The LAMBDA photon-counting pixel detector, *in* 'Journal of Physics: Conference Series', Vol. 425, IOP Publishing, p. 062010.

PerkinElmer (2015), http://www.perkinelmer.com.

Petersilka, M., Bruder, H., Krauss, B., Stierstorfer, K. & Flohr, T. G. (2008), 'Technical principles of dual source CT', *European Journal of Radiology* **68**(3), 362–368.

Pettis, R. J., Ginsberg, B., Hirsch, L., Sutter, D., Keith, S., McVey, E., Harvey, N. G., Hompesch, M., Nosek, L., Kapitza, C. et al. (2011), 'Intradermal microneedle delivery of insulin lispro achieves faster insulin absorption and insulin action than subcutaneous injection', *Diabetes Technology & Therapeutics* **13**(4), 435–442.

Peyrot, M., Rubin, R. R., Kruger, D. F. & Travis, L. B. (2010), 'Correlates of insulin injection omission', *Diabetes care* **33**(2), 240–245.

Pfeiffer, F., Bech, M., Bunk, O., Kraft, P., Eikenberry, E. F., Brönnimann, C., Grünzweig, C. & David, C. (2008), 'Hard-x-ray dark-field imaging using a grating interferometer', *Nature materials* **7**(2), 134–137.

Pfeiffer, F., Weitkamp, T., Bunk, O. & David, C. (2006), 'Phase retrieval and differential phase-contrast imaging with low-brilliance x-ray sources', *Nature physics* **2**(4), 258–261.

Pfützner, A., Raz, I., Bitton, G., Klonoff, D., Nagar, R., Hermanns, N. & Haak, T. (2015), 'Improved insulin absorption by means of standardized injection site modulation results in a safer and more efficient prandial insulin treatmenta review of the existing clinical data', *Journal of diabetes science and technology* **9**(1), 116–122.

Polak, M., Beregszaszi, M., Belarbi, N., Benali, K., Hassan, M., Czernichow, P. & Tubiana-Rufi, N. (1996), 'Subcutaneous or intramuscular injections of insulin in children: Are we injecting where we think we are?', *Diabetes Care* **19**(12), 1434–1436.

Poretsky, L. et al. (2010), *Principles of diabetes mellitus*, Springer.

Porter, C. J. & Charman, S. A. (2000), 'Lymphatic transport of proteins after subcutaneous administration', *Journal of pharmaceutical sciences* **89**(3), 297–310.

Radon, J. (2005), '1.1 über die Bestimmung von Funktionen durch ihre Integralwerte längs gewisser Mannigfaltigkeiten', *Classic papers in modern diagnostic radiology* p. 5.

Rasmussen, C., Røge, R., Ma, Z., Thomsen, M., Thorisdottir, R., Chen, J., Mosekilde, E. & Colding-Jørgensen, M. (2013), 'Insulin aspart pharmacokinetics: an assessment of its variability and underlying mechanisms.', *European Journal of Pharmaceutical Sciences. Submitted* .

Rave, K., Heise, T., Weyer, C., Herrnberger, J., Bender, R., Hirschberger, S. & Heinemann, L. (1998), 'Intramuscular versus subcutaneous injection of soluble and lispro insulin: comparison of metabolic effects in healthy subjects', *Diabetic medicine* **15**(9), 747–751.

Richter, W. F., Bhansali, S. G. & Morris, M. E. (2012), 'Mechanistic determinants of biotherapeutics absorption following sc administration', *The AAPS journal* **14**(3), 559–570.

Röntgen, W. C. (1898), 'Über eine neue art von strahlen', *Annalen der Physik* **300**(1), 1–11.

Schönlieb, C.-b. & Bertozzi, A. (2011), 'Unconditionally stable schemes for higher order inpainting', *Communications in Mathematical Sciences* **9**(2), 413–457.

Schubert, A., OKeefe, G., Sobott, B., Kirby, N. & Rassool, R. (2010), 'Characterisation of individual pixel efficiency in the PILATUS II sensor', *Radiation Physics and Chemistry* **79**(11), 1111–1114.

Schulze, R., Heil, U., Groβ, D., Bruellmann, D., Dranischnikow, E., Schwanecke, U. & Schoemer, E. (2014), 'Artefacts in CBCT: a review'.

Selam, J.-L. (2010), 'Evolution of diabetes insulin delivery devices', *Journal of diabetes science and technology* **4**(3), 505–513.

Skyler, J. (2012), *Atlas of diabetes*, Springer Science & Business Media.

Slaney, M. & Kak, A. (1988), 'Principles of computerized tomographic imaging', *SIAM, Philadelphia* .

Søeborg, T., Rasmussen, C., Mosekilde, E. & Colding-Jørgensen, M. (2009), 'Absorption kinetics of insulin after subcutaneous administration', *European Journal of Pharmaceutical Sciences* **36**(1), 78–90.

Sohoel, A., Plum, A., Frokjaer, S. & Thygesen, P. (2007), '^{125}i used for labelling of proteins in an absorption model changes the absorption rate of insulin aspart', *International journal of pharmaceutics* **330**(1), 114–120.

Stampanoni, M., Borchert, G., Wyss, P., Abela, R., Patterson, B., Hunt, S., Vermeulen, D. & Rüegsegger, P. (2002), 'High resolution x-ray detector for synchrotron-based microtomography', *Nuclear Instruments and Methods in Physics Research Section A: Accelerators, Spectrometers, Detectors and Associated Equipment* **491**(1), 291–301.

Stoner, K. L., Harder, H., Fallowfield, L. J. & Jenkins, V. A. (2014), 'Intravenous versus subcutaneous drug administration. which do patients prefer? a systematic review', *The Patient-Patient-Centered Outcomes Research* pp. 1–9.

Swindle, M., Makin, A., Herron, A., Clubb, F. & Frazier, K. (2012), 'Swine as models in biomedical research and toxicology testing', *Veterinary Pathology Online* **49**(2), 344–356.

Tarin, C., Teufel, E., Picó, J., Bondia, J. & Pfleiderer, H.-J. (2005), 'Comprehensive pharmacokinetic model of insulin glargine and other insulin formulations', *Biomedical Engineering, IEEE Transactions on* **52**(12), 1994–2005.

Thomsen, M. (2011), Inspection of subcutaneous injections by x-ray computed tomography, Master's thesis, Niels Bohr Institute.

Thomsen, M., Hernandez-Garcia, A., Mathiesen, J., Poulsen, M., Sørensen, D. N., Tarnow, L. & Feidenhans'l, R. (2014), 'Model study of the pressure build-up during subcutaneous injection', *PLoS ONE* **9**(8), e104054.

Thomsen, M., Knudsen, E., Willendrup, P., Bech, M., Willner, M., Pfeiffer, F., Poulsen, M., K., L. & Feidenhans'l, R. (2015a), 'Prediction of beam hardening artefacts in computed tomography using monte carlo simulations', *Nuclear Instruments and Methods in Physics Research Section B: Beam Interactions with Materials and Atoms* **342**(0), 314 – 320.

Thomsen, M., Poulsen, M., Bech, M., Velroyen, A., Herzen, J., Beckmann, F., Feidenhans'l, R. & Pfeiffer, F. (2012), 'Visualization of subcutaneous insulin injections by x-ray computed tomography', *Phys. Med. Biol.* **57**, 7191–7203.

Thomsen, M., Rasmussen, C., Refsgaard, H., Pedersen, K., Kirk, R., M, P. & R, F. (2015b), 'Spatial distribution of soluble insulin in pig subcutaneous tissue: Effect of needle length, injection speed and injected volume', *(submitted for internal review in Novo Nordisk A/S) To be submitted to European Journal of Pharmaceutical Science* .

Thomsen, M. & Strobl, M. (2014b), Neutron imaging, *in* 'Neutron Scattering: Theory, Instrumentation, and Neutron Scattering: Theory, Instrumentation and Simulation', University of Copenhagen.

Thorisdottir, R. L., Parkner, T., Chen, J.-W., Ejskjær, N. & Christiansen, J. S. (2009), 'A comparison of pharmacokinetics and pharmacodynamics of biphasic insulin aspart 30, 50, 70 and pure insulin aspart: a randomized, quadruple crossover study', *Basic & clinical pharmacology & toxicology* **104**(3), 216–221.

Trajanoski, Z., Wach, P., Kotanko, P., Ott, A. & Skraba, F. (1993), 'Pharmacokinetic model for the absorption of subcutaneously injected soluble insulin and monomeric insulin-analogues-pharmakokinetisches modell für die absorption von subkutan injiziertem löslichem insulin und monomeren insulinanaloga', *Biomedizinische Technik/Biomedical Engineering* **38**(9), 224–231.

Vaag, A., Pedersen, K. D., Lauritzen, M., Hildebrandt, P. & Beck-Nielsen, H. (1990), 'Intramuscular versus subcutaneous injection of unmodified insulin: consequences for blood glucose control in patients with type 1 diabetes mellitus', *Diabetic Medicine* **7**(4), 335–342.

Van de Casteele, E., V. D. D. S. J. & Raman, E. (2002), 'An energy-based beam hardening model in computed tomography', *Physics in Medicine and Biology* **47**, 4181–4190.

Van Gompel, G., Van Slambrouck, K., Defrise, M., Batenburg, K., de Mey, J., Sijbers, J. & Nuyts, J. (2011), 'Iterative correction of beam hardening artifacts in ct', *Medical Physics* **38**, S36.

Vardar, B. & Kızılcı, S. (2007), 'Incidence of lipohypertrophy in diabetic patients and a study of influencing factors', *Diabetes research and clinical practice* **77**(2), 231–236.

Vora, J., Burch, A., Peters, J. & Owens, D. (1993), 'Absorption of radiolabeled soluble insulin in type 1 (insulin-dependent) diabetes: Influence of subcutaneous blood flow and anthropometry', *Diabetic medicine* **10**(8), 736–743.

Vora, J. & Heise, T. (2013), 'Variability of glucose-lowering effect as a limiting factor in optimizing basal insulin therapy: a review', *Diabetes, Obesity and Metabolism* **15**(8), 701–712.

Vora, J. P., Burch, A., Peters, J. R. & Owens, D. R. (1992), 'Relationship between absorption of radiolabeled soluble insulin, subcutaneous blood flow, and anthropometry', *Diabetes Care* **15**(11), 1484–1493.

Wach, P., Trajanoski, Z., Kotanko, P. & Skrabal, F. (1995), 'Numerical approximation of mathematical model for absorption of subcutaneously injected insulin', *Medical and Biological Engineering and Computing* **33**(1), 18–23.

Webb, S. & Flower, M. A. (2012), *Webb's physics of medical imaging*, second edition edn, CRC Press.

Wells, M. Y., Voute, H., Bellingard, V., Fisch, C., Boulifard, V., George, C. & Picaut, P. (2010), 'Histomorphology and vascular lesions in dorsal rat skin used as injection sites for a subcutaneous toxicity study', *Toxicologic pathology* **38**(2), 258–266.

White, F. M. (1991), 'Viscous fluid flow, 1974'.

Widmark, J. M. (2007), 'Imaging-related medications: a class overview', *Proceedings (Baylor University. Medical Center)* **20**(4), 408.

Willemink, M. J., de Jong, P. A., Leiner, T., de Heer, L. M., Nievelstein, R. A., Budde, R. P. & Schilham, A. M. (2013), 'Iterative reconstruction techniques for computed tomography part 1: technical principles', *European radiology* **23**(6), 1623–1631.

Zambanini, A., Newson, R. B., Maisey, M. & Feher, M. D. (1999), 'Injection related anxiety in insulin-treated diabetes', *Diabetes Research and Clinical Practice* **46**(3), 239–246.

ZEISS (2015), http://www.xradia.com/versaxrm-410/.
URL: *http://www.xradia.com/versaxrm-410/*

Zhao, W., Ristic, G. & Rowlands, J. (2004), 'X-ray imaging performance of structured cesium iodide scintillators', *Medical physics* **31**(9), 2594–2605.

Zou, W., Hunter, N. & Swain, M. (2011), 'Application of polychromatic μCT for mineral density determination', *Journal of Dental Research* **90**(1), 18–30.

Appendix A

Image Analysis

A.1 Markov Random Field Segmentation

The Markov Random Field (MRF) segmentation combines MRF with minimum graph cut (Kolmogorov & Zabin 2004), and have been used to segment the tissue samples.

A.1.1 Markow Random Fields

The concept of MRF can be illustrated from the 2D image with three classes shown in Figure A.1 (A).

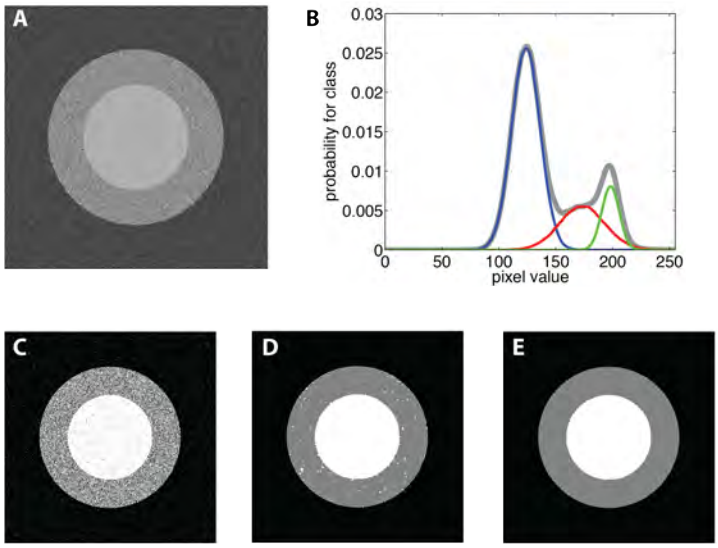

Figure A.1: *2D image with three regions where the pixel values in each region is Gaussian distributed (A). Histogram for the image (B). Segmentation by normal threshold (C) and MRF with $\beta = 2.5$ (D) and $\beta = 10$ (E).*

Let $\mathcal{S}$ be the set of pixels in the image and $\mathcal{L}$ be the set of labels. Each class do not have a single pixel grey scale value, but the grey scale values belongs to a distribution, shown in Figure A.1 (B). The pixel values can be considered as a random variable $\mathcal{F}_i$, where $i \in \mathcal{S}$. A set of random variables is called a random field, $\mathcal{F} = \cup_i \mathcal{F}_i$ (Li 2009). In the segmentation problem each random variable have the realization $f_i \in \mathcal{L}$, giving a specific assignment of labels $f = \cup_i f_i$. For the image shown in Figure A.1 (A), the probability for the pixel with grey scale value g_i, to belong to the red class is given by

$$p(f_i = red) = \frac{1}{\sqrt{2\pi\sigma_{\text{red}}^2}} \exp\left(\frac{1}{2}\left(\frac{g_i - \tilde{g}_{\text{red}}}{\sigma_{\text{red}}}\right)\right)^2 \tag{A.1}$$

where $\tilde{g}_{\text{red}}$ is the mean gray scale value, and σ_{red} is the standard deviation for the red class. The configuration of labels with the highest probability, $\max_{\text{f}}(\text{p}(\mathcal{F} = \text{f}))$, gives a normal threshold segmentation, shown in Figure A.1 (C).

The MRF segmentation also takes the grey scale values of the neighbouring pixels into account. MRF is a random field were the information on the label assigned to the image element i, from all other site labels is contained only in the labels of its neighbours $\mathcal{N}_i$, formally written as

$$p(f_i | f_j, j \in \mathcal{S} \setminus i) = p(f_i | f_j, j \in \mathcal{N}_i) \tag{A.2}$$

where $\mathcal{N}_i$ is the neighbourhood of pixels to pixel i. All configurations, f, are possible, meaning that $p(\mathcal{F} = f) > 0, \forall f$.

To find the label configuration with the highest probability it is used that a MRF is equivalent to a Gibbs Random Field (Clifford 1990). A Gibbs Random Field is a random field, where the probability for the configuration of labels f is given by

$$p(\mathcal{F} = f) \quad \propto \quad e^{-U(f)} \tag{A.3}$$

where $U(f)$ is the potential. Finding the maximum likelihood for the configuration of labels corresponds to a minimizing the potential function $U(f)$.

This is illustration for the 2D image in Figure A.1 (A), where we want to include the four nearest neighbours in the segmentation of the red class. Let the potential for the pixel it self ($V_i(f_i)$), and for the four nearest ($V_i(f_i, f_j)$) be given as

$$V_i(f_i) \quad = \quad \ln(2\pi\sigma_{\text{red}}) + \frac{1}{2}\left(\frac{g_i - \tilde{g}_{\text{red}}}{\sigma_{\text{red}}}\right)^2 \tag{A.4}$$

$$V_{(i,j)}(f_i, f_j) \quad = \quad \beta\left(1 - \delta_k(f_i - f_j)\right) \tag{A.5}$$

where δ_k is the kronecker delta function, and β is the smoothness term. The potential is given by

$$U(f) = \sum_i V_i(f_i) + \sum_{(i,j)\in\mathcal{N}_i} V_{(i,j)}(f_i) \tag{A.6}$$

The segmentation that minimize the potential for $\beta = 2.5$ and $\beta = 10$ is shown in Figure A.1 D-E). The potential is minimized by using minimum graph cut, explained in the following section.

A.1.2 Minimum graph cut

The basic concept of the minimum graph cut algorithm can be illustrated by looking at the 1D image shown in Figure A.2 (A), with pixel values between 0 and 1. The image should be segmented into two classes with labels $\mathcal{L} = \{0, 1\}$. The segmentation can be formulated as a minimum graph cut problem, by adding a source (s) and a sink (t) term to the image, and connecting each pixel to the source and the sink.

Let $f_i \in \mathcal{L}$ be the label for pixel i and define a potential as

$$V_i(f_i) = \begin{cases} \text{pixel value} & \text{for } f_i = 0 \\ \text{1-pixel value} & \text{for } f_i = 1 \end{cases} \tag{A.7}$$

The edges between the source and the pixel have a weight of $V(f_i = 0)$ and the edges between the pixel and the sink have weights $V_i(f_i = 1)$. A graph cut is a cut that divide the pixels into two groups; one connected to the source and one connected to the sink. The capacity of a cut is the sum of edge weights included in the cut. The minimum graph cut is the cut with the lowest capacity, shown in Figure A.2(B). This corresponds to a normal threshold segmentation with a threshold at 0.5.

The relation between neighbouring pixels (i, j) is taking into account by including edges between pixels with the potential given by Eq. (A.6). The minimum cut depends on the values of β, shown in Figure A.2 (C-D) for $\beta = 0.1$ and $\beta = 0.5$. The higher the value of β the more homogeneous the segmentation.

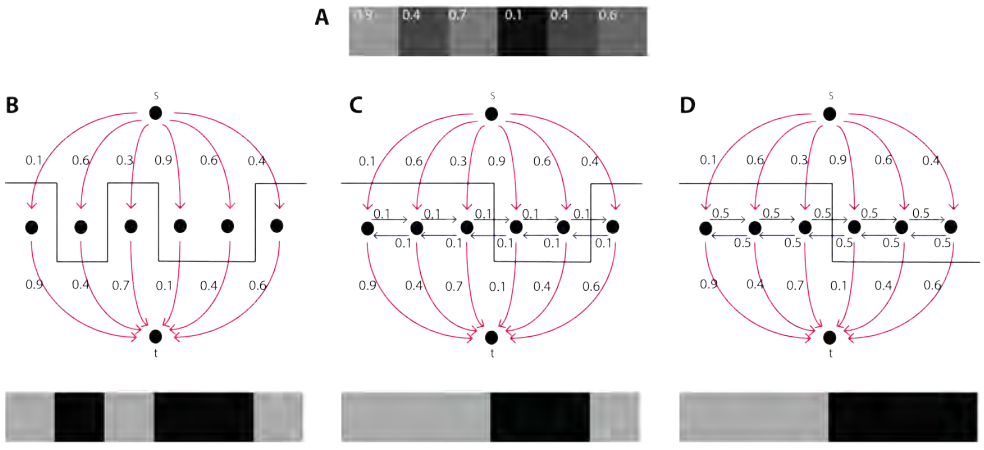

Figure A.2: *1D image with pixel values between 0 and 1. Minimum graph cut using only the potential for each pixel (B), and with the smoothing term $\beta = 0.1$ (C) and $\beta = 0.5$ (D).*

A.1.3 Image with more than two labels

The case where the image have more than two classes, will be illustrated for the 2D image in Figure A.1, which consist of three classes $q \in \mathcal{L} = \{\text{black}, \text{gray}, \text{white}\}$.

The algorithm than goes through the following steps

1. The image is segmented by threshold segmentation (C), and the mean and standard deviation of the gray scale values are calculated. The labelling is given by $k = \cup_i k_i$.

2. Run through the labels q. Define the image g with all sites having the label q. Use graph cut to find the binary segmentation f^*, where the potential is given as

$$V_i(f_i) = \begin{cases} V_i(q) & \text{for } f_i = 0 \\ V_i(k_i) & \text{for } f_i = 1 \end{cases} \tag{A.8}$$

   and the potential for the neighbourhood is defined by Eq. (A.5)

   The original labelling k is updated by

$$k = k \bullet f^* + g \bullet (1 - f^*) \tag{A.9}$$

   where $\bullet$ is the element wise product. Step (2) is continued until no labels are changed.

A.1.4 Selecting thresholds and smoothness factor

For the initial thresholds segmentation for the tissue samples, the thresholds were selected by extracting a region of interest (ROI) in subcutis (s), a ROI in dermis (d), and a ROI in air (a). The average gray scale value, $\tilde{\mu}$, and standard deviation, σ, was calculated, and the thresholds was chosen as $(\tilde{\mu}_s + \tilde{\mu}_d))/2$ between dermis/subcuts, $\tilde{\mu}_d + 2\sigma_d$ between dermis/iodine, and $(\tilde{\mu}_s + \tilde{\mu}_a))/2$ between subcutis/air.

To optimize computer performance the dimensions of the reconstructed volumes were down-scaled by a factor of 2 before segmented. The result of the MRF segmentation is a image mask with four classes. The mask was scaled to the original size, before applied to reconstructed volume to extract each class.

A.2 Learning Dictionaries of Discriminative Image Patches

In the following the main steps of the texture segmentation algorithm will be presented. The texture segmentation were used to divided the segmented injection bolus and bone samples into different regions.

The algorithm is adapted from Dahl & Larsen (2011), and for a detailed description the reader are referred to the original paper. The algorithm is applied on 2D slices of the 3D reconstructed volume, and the segmentation are afterwards stacked together. It means that information between slices is not included in the segmentation.

The algorithm consist of three steps; (1) manually annotation of training images, (2) construction of the intensity directory and label directory, (3) labelling of the remaining images.

In step (1) a single image from the tomogram is annotated manually, illustrated in Figure A.3 (A) for an image with two classes.

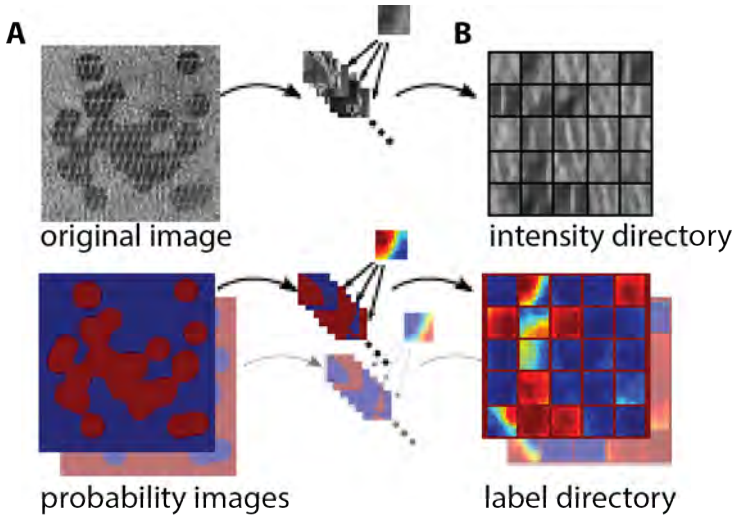

Figure A.3: *(A) 2D grey scale image (top) manually annotated with two classes (bottom). (B) Image patches are extracted from the grey scale image and the labelled image to form a intensity directory (top) and a label directory (bottom). The figure is adapted from Dahl & Larsen (2011).*

In step (2) a set ξ of associated image patches are randomly selected from the intensity image, $\hat{\mathbf{d}}_\mathbf{j}$, and from the labelled image, $\hat{\mathbf{l}}_\mathbf{j}$, with $j = 1, .., \xi$. The patches have dimensions $\sqrt{n} \times \sqrt{n}$, and $\sqrt{n} \times \sqrt{n} \times l$, for the intensity and labelled image, respectively. l is the number of classes in the labelled image.

The set of patches are used as a training set to construct the intensity directory $\mathbf{D} \in \mathbb{R}^{n \times m}$ and the label directory $\mathbf{L} \in [0; 1]^{ln \times m}$, shown in Figure A.3 (B).

In order to segment the remaining 2D slices by using the directories, the directories must have good discrimination and clustering properties. This can be achieved by choosing $\mathbf{D}$ such that

$$\mathbf{D} = \arg\max_{\mathbf{D}} \sum_{j=0}^{\xi} \|\mathbf{d}_{i(\eta)} - \hat{\mathbf{d}}_\eta\|_2^2 \tag{A.10}$$

where $i(\eta)$ is the index of the intensity directory element with the shortest Euclidian distance to the image patch $\hat{\mathbf{d}}_\eta$ in the training set.

Simultaneously the label directory, $\mathbf{L}$, must be chosen such that

$$\mathbf{L} = \arg\max_{\mathbf{L}} \sum_{j=0}^{\xi} \|\mathbf{l}_{i(\eta)} - \hat{\mathbf{l}}_\eta\|_2^2 \tag{A.11}$$

This can not be solved analytically, and therefore are the directories constructed iteratively by a $k-$means clustering algorithm. A subset of m of the ξ patches are randomly selected and used as the initial intensity directory $\mathbf{D}^0$, and an initial label directory $\mathbf{L}^0$. Each element in $\mathbf{D}$

and $\mathbf{L}$ are iteratively updated such that

$$\mathbf{d}_i^{t+1} = \frac{1}{v_i} \sum_{\kappa \in S_i} (1 - \lambda \|\mathbf{l}_i^t - \hat{\mathbf{l}}_\kappa\|_2) \hat{\mathbf{d}}_\kappa \tag{A.12}$$

where $i = 1, .., m$ and S_i is the set of indices from the set ξ where the intensity patches have the closest Euclidean distance from the dictionary element i.

The normalization v_i is given by

$$v_i = \sum_{\kappa \in S_i} (1 - \lambda \|\mathbf{l}_i^t - \hat{\mathbf{l}}_\kappa\|_2) \tag{A.13}$$

This ensures that the images patches with labels similar to the directory elements have a higher weight.

The label directory elements are updated by

$$\mathbf{l}_i^{t+1} = \frac{1}{|S_i|_0} \sum_{\kappa \in S_i} \hat{\mathbf{l}}_\kappa \tag{A.14}$$

where $|S_i|_0$ are the number of elements in S_i.

The number of iteration was chosen from Emerson et al. (2015) to be 10. For the tissue and bone samples the number of training image patches were set at $\xi = 10000$ and the subset $m = 2000$.

In step (3) image patches are extracted from the original image, $\mathbf{u}_h$, where $h = 1, ..(x - \sqrt{n} + 1)(y - \sqrt{n} + 1)$. The nearest element in the intensity directory is given as

$$i(h) = \text{argmin} \|\mathbf{d}_\text{i} - \mathbf{u}_\text{h}\|_2^2 \tag{A.15}$$

The corresponding element $\mathbf{l}_{i(h)}$ is taken from the label directory and added to the label probability image. The segmentation procedure is illustrated in Figure A.4 for an image with two classes.

The patches are overlapping, so at the end the labelled probability image is normalized. The labelled image can than be found by selecting the class with the highest probability for each voxel.

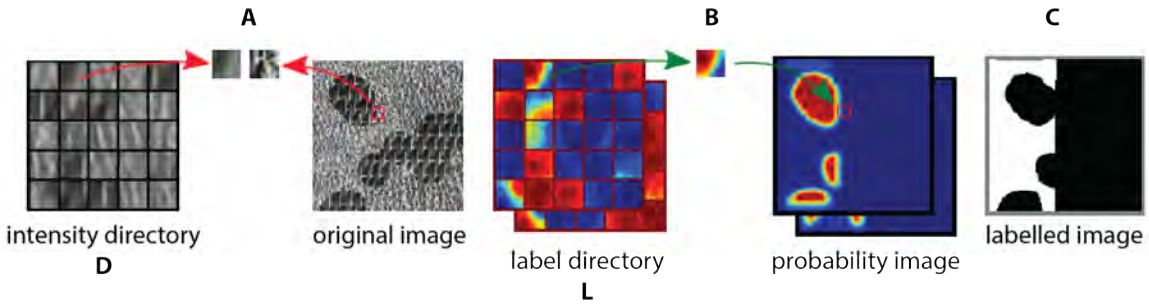

Figure A.4: *(A) For each of the image patches from the original image is the image patch from intensity directory with shortest Euclidian distance identified. (B) The corresponding element in the label directory is extracted and added to the probability image. (C) The labelled image are found by selecting the class with the highest probability in each voxel. The figure is adapted from Dahl & Larsen (2011).*

Appendix B

Publications

Papers I-IV and VI are attached.

Paper I

M. Thomsen, A. Hernandez-Garcia, J. Mathiesen, M. Poulsen, D.N. Sørensen, L. Tarnow, R. Feidenhans'l.
Model Study of the Pressure Build-Up during Subcutaneous Injection.
PLoS ONE (2014) 9(8): e104054. doi:10.1371/journal.pone.0104054

OPEN ACCESS Freely available online

PLOS ONE

Model Study of the Pressure Build-Up during Subcutaneous Injection

Maria Thomsen[1,2]*, Anier Hernandez-Garcia[1], Joachim Mathiesen[1], Mette Poulsen[2], Dan N. Sørensen[2], Lise Tarnow[3,4,5], Robert Feidenhans'l[1]

1 Niels Bohr Institute, University of Copenhagen, Copenhagen, Denmark, **2** Novo Nordisk A/S, Hillerød, Denmark, **3** Nordsjæ llands Hospital, Hillerød, Denmark, **4** Klinisk Epidemiologisk Afdeling, Aarhus Universitetshospital, Aarhus, Denmark, **5** Steno Diabetes Center A/S, Gentofte, Denmark

Abstract

In this study we estimate the subcutaneous tissue counter pressure during drug infusion from a series of injections of insulin in type 2 diabetic patients using a non-invasive method. We construct a model for the pressure evolution in subcutaneous tissue based on mass continuity and the flow laws of a porous medium. For equivalent injection forces we measure the change in the infusion rate between injections in air at atmospheric pressure and in tissue. From a best fit with our model, we then determine the flow permeability as well as the bulk modulus of the tissue, estimated to be of the order 10^{-11}–10^{-10} m^2 and 10^5 Pa, respectively. The permeability is in good agreement with reported values for adipose porcine tissue. We suggest our model as a general way to estimate the pressure build-up in tissue during subcutaneous injection.

Citation: Thomsen M, Hernandez-Garcia A, Mathiesen J, Poulsen M, Sørensen DN, et al. (2014) Model Study of the Pressure Build-Up during Subcutaneous Injection. PLoS ONE 9(8): e104054. doi:10.1371/journal.pone.0104054

Editor: Juan Carlos del Alamo, University of California San Diego, United States of America

Received March 21, 2014; **Accepted** July 4, 2014; **Published** August 14, 2014

Data Availability: The authors confirm that all data underlying the findings are fully available without restriction. All relevant data are within the paper and its Supporting Information files.

Funding: The authors have no support or funding to report.

Competing Interests: The authors Maria Thomsen, Mette Poulsen, and Dan N. Sørensen are employees of Novo Nordisk A/S. The authors confirm that the company has no competing interests or financial disclosures and declare that the affiliation to Novo Nordisk A/S does not alter the authors' adherence to PLOS ONE policies on sharing data and materials.

* Email: mariath@fys.ku.dk

Introduction

Diabetics are treated by several daily injections of insulin, most commonly delivered subcutaneously from where the insulin gets absorbed by the blood vessels. The injections are typically performed using an insulin pen or normal syringe. Due to the high frequency of injections for diabetics, increased patient convenience is of great importance and devices are therefore continuously improved to simplify treatment.

The force delivered by injection devices, either injection pumps or auto-injection devices, must overcome both the resistance in the injection system and the resistance in the body tissue to make room for the insulin bolus. The second part we refer to as the tissue counter pressure. The subcutaneous compartment is decomposed mainly of two components; adipose tissue and interstitial tissue. Adipose tissue consists of adipocytes assembled in lobules separated by a thin layer of connective tissue and nerves and blood vessels running between the lobules. The interstitial tissue is placed between the adipocytes and consists mainly of a fibre framework made of collagen embedded in a mucopolysaccharide gel [1,2]. Insulin therapy may lead to skin disorders, where the most common is lipohypertrophy, where extra adipose tissue is accumulated under the skin. The risk of developing lipohypertrophy increases with the time the patients have been treated, the frequency of changing the needle and injection site [3–6]. Lipoatrophy is a rarer condition, mostly related to impurities in insulin formulations. In lipoatrophy the size of the adipocytes in subcutis decreases around the injection site [7–9]. These kind of skin disorders impair in some cases the insulin absorption [5,10,11], but as the skin structure is changed it might also change the tissue counter pressure and affect the way the drug is delivered by the injection device.

The interstitial fluid pressure in subcutis has been measured by the wick clamp technique to be of the order −1.3 mbar, when not subjected to mechanical stress [13,14] and it has been shown that the tissue counter pressure in subcutis increases with increasing infusion rate for continuous saline infusion from about 8 mbar to 60 mbar for infusion rates from 0.16 μL/s to 8.3 μL/s [15], in a study targeting insulin infusion pumps. To our knowledge the infusion pressure has not been measured for subcutaneous injections at injection speeds of the order 100 μL/s, which is the common infusion rate using an insulin pen [16].

In this study we present a non-invasive technique for measuring the tissue counter pressure during a normal insulin injection. We use an auto-injection device, where a click signal gives information on the flow rate. By comparing the infusion rate for subcutaneous injections and reference injections in air, we calculate the tissue counter pressure. We propose a model for the pressure evolution in subcutaneous tissue and from that we estimate the flow permeability and bulk modulus of the tissue.

Materials and Methods

Ethical approval

The study involving human subjects was conducted in collaboration with Steno Diabetes Center A/S. While a nurse

administered insulin to the patient, the audible clicks, emitted from the injection device, were recorded by microphone. Prior to the investigation The Committee on Health Research Ethics from the Capital Region of Denmark reviewed the project. The conclusion from the committee was that the project could be conducted without further ethical approval because of its limited intervention. The participating patients all had type 2 diabetes and received regular control of their diabetes at Steno Diabetes Center. The responsible nurse contacted the patients prior to their control visit and questioned them about participation in the study. The head of the Clinical Research Department, who was responsible for the conduct of the study, approved the inclusion of patients without written informed consent, after acceptance of this procedure by The Committee on Health Research Ethics from the Capital Region of Denmark. No institutional review process was necessary to take this decision. The only restriction to the selection of subjects was that their insulin dose should be above 18 units to have a sufficiently long sound file for the subsequent analysis. All patients that were asked to participate gave their consent.

Experimental design

To measure the pressure build-up in human tissue, we use the insulin pen FlexTouch from Novo Nordisk A/S, which is an auto injecting device, where the drug is injected by the force from a torsion spring. The spring is twisted when the patient dials the dose and as the spring is untwisted during the injection the device emits a click for each 10 μL of drug which has been delivered. By recording the click signal with a microphone we predict the flow rate. One example of a click signal and the calculated flow rate is shown in Figure 1 for an injection of 240 μL of insulin in air. It is seen that the flow rate decreases throughout the injection as the spring is untwisted and due to a special feature inside the pen the spring force is reduced for the last part of the click signal, seen as a drop in the flow rate after about 1.2 s. Therefore the last part of the click signal has been omitted in our analysis.

In order to confirm that the flow rate calculated from the click signal match the actual flow rate a series of injections were performed in air where the click signal was recorded by a microphone and the injected mass was measured on a scale, simultaneously. Figure 2 shows an example of the flow rate as calculated from the click signal (red curve) and from the injected mass (blue curve). In total the flow rate was measured for 70 injections, using 10 different pens, and the injected dose was varied from 150–800 μL. On average the deviation between the flow calculated from the click signal and the injected mass was about 2%. This uncertainty is related to the flow rate prediction and not to the total dose delivered, which has been shown to be very accurate for this device [17,18].

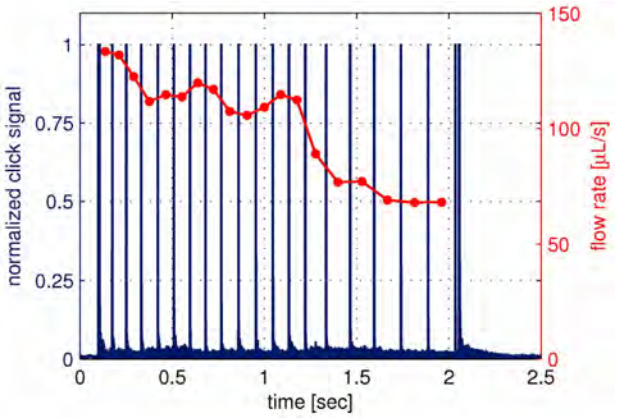

Figure 1. Click signal as emitted from the device and the flow rate. The click signal (blue curve) is measured by a microphone and the flow rate (red curve) is calculated from the time steps between the click signal. This example is for an injection of 240 μL in air.
doi:10.1371/journal.pone.0104054.g001

Data collection

This study includes 11 men with type 2 diabetes. All the injections were given subcutaneously in the abdomen using a 6 mm 31G needle and performed by the same nurse. The patients were treated with NovoRapid U100 from Novo Nordisk A/S and the dose injected was set by the treatment scheme of the individual. Therefore the dose varies from 180 μL up to 480 μL. Both before and after the subcutaneous injection given to the patient, we record the click signal from a series of similar injections in air. The difference in the flow rate between the injections in air and in tissue relates to the counter pressure. After the injections the radius of each of the needles was calculated from Eq. (4) (see the Results section), by measuring the flow rate through the needle for a known pressure.

Results

Insulin injected subcutaneously distributes between the fat lobulus and forms a depot, as seen from the histological cross section of a 100 μL insulin injection shown in Figure 3 (left). The insulin has been dyed to appear red and it is seen how the needle has penetrated dermis (blue skin layer). For the model of the tissue mechanics we consider the tissue as a porous elastic medium. Figure 3 (right) shows the 3 dimensional structure of a similar injection depot visualized by X-ray computed tomography, where the insulin drug has been diluted with an iodine based contrast agent in order to distinguish the fluid from the tissue, as described in a previous study [19]. The extension of the depot is about 1 cm and we have observed that the shape of the depot vary from injection to injection. For simplicity we assume, that the tissue is homogeneous and that the drug is distributed spherical symmetrically around the injection site.

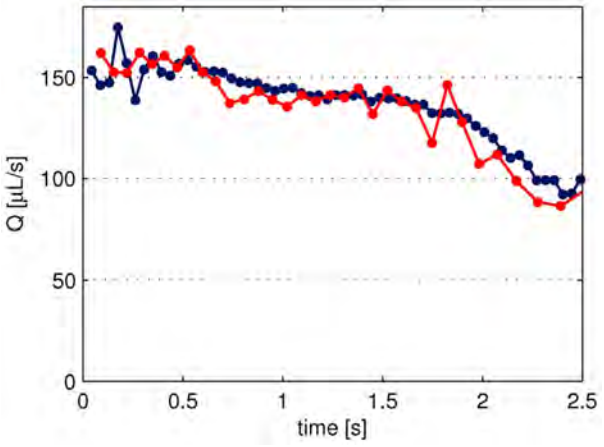

Figure 2. Comparison of flow rate calculated from the click signal and measured on a scale. The click signal and the injected mass are measured simultaneously, to give the flow rate calculated from the time steps between the click signals (red curve) and from the injected mass between equal time steps (blue curve). The injected volume was 400 μL.
doi:10.1371/journal.pone.0104054.g002

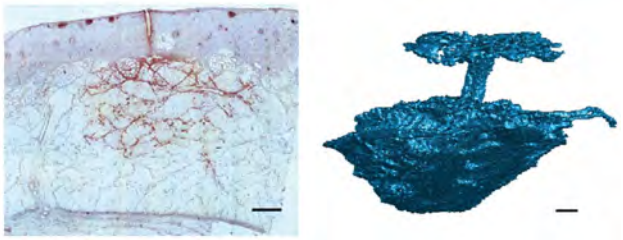

Figure 3. Histological cross section (left) and X-ray computed tomography scan (right) of similar subcutaneous injections. The injections were performed in adipose pig tissue and the injected volume was 100 μL. For histology the insulin has been dyed to appear red in the light microscopy image. The segmented tomographic reconstruction shows the 3 dimensional extension of the injection depot together with the injection channel and the backflow at the skin surface. The contrast between the tissue and the injected fluid is obtained by mixing the insulin drug with an iodine based contrast agent. The scale bar is 1 mm.
doi:10.1371/journal.pone.0104054.g003

In the description of the model we introduce a number of variables and constants, which we for clarity have listed in Table 1.

Mechanics of the injection device

The mechanical characteristics of the injection device is analysed through a series of test experiments where the drug is injected in air at atmospheric pressure. A simple schematic illustration of the injection device is shown in Figure 4.

The pressure drop in the syringe due to viscous forces (ΔP_v^s) is vanishingly small when compared with the pressure drop in the needle (ΔP_v^n). The pressure drop in the needle consists of a transient part, the entry length, over which the flow evolves to a steady state parabolic Poiseuille flow and a final part where the flow attains its parabolic shape (see Supporting Information S1). In the syringe the flow does not reach the full parabolic form during the short injections times considered here, however, an upper estimate of the pressure drop is achieved by assuming that the flow has reached a fully developed Poiseuille flow, which leads to $\Delta P_v^s \approx 10^{-2}$Pa. The pressure drop in the needle is estimated from the following expression derived in the Supporting Information S1, Eq. (S30),

$$P_s - P_o = \frac{8\eta\ell}{\pi r_n^4} Q(t) + \frac{1.01\rho_f}{\pi^2 r_n^4} Q^2(t), \tag{1}$$

where η is the dynamic viscosity of the insulin drug, $Q(t)$ is the injection flow rate, ρ_f is the mass density of the drug and ℓ and r_n denote the length and radius of the needle, respectively. We get for typical injection flow rates $Q(t) \approx 100$ μL/s a pressure drop in the needle $\Delta P_v^n \approx 10^5$ Pa. The pressure drop in the needle is therefore of the order 10^7 times larger than that in the syringe. Therefore, we shall neglect the viscous forces inside the syringe in our calculations below.

From the Bernoulli Equation we obtain that the pressure at the inlet of the needle is approximately given by

$$P_s \approx \frac{F(d)}{\pi R_o^2} - \frac{1}{2}\rho_f v_s^2, \tag{2}$$

where $F(d)$ is the force delivered by the spring, R_0 is the radius of the syringe and v_s denotes the average velocity over the cross section at the needle inlet, which can be determined as

$$v_s = \frac{Q(t)}{\pi r_n^2}, \tag{3}$$

Inserting Eq. (2) and (3) in Eq. (1), we obtain

$$\frac{F(d)}{\pi R_o^2} - P_o = \frac{8\eta\ell}{\pi r_n^4} Q(t)\left(1 + \frac{Q(t)}{5.29\pi\, v\, \ell}\right). \tag{4}$$

We now estimate the typical values of the second term inside the parentheses in Eq. (4). In Figure 5, we observe that the largest flow rates during the injection in air are approximately 150 μL/s. Using the value of the kinematic viscosity of water $v = 1.004 \cdot 10^{-6} \frac{m^2}{s}$ and that the length of the needle is $\ell = 16.4$ mm, we have that

$$\frac{Q(t)}{5.29\pi\, v\, \ell} \approx 0.55. \tag{5}$$

As for the case of the fluid injection in the tissue, we also observe in Figure 5 that the largest flow rates are approximately 100 μL/s, which leads to

$$\frac{Q(t)}{5.29\pi\, v\, \ell} \approx 0.37. \tag{6}$$

The second term in Eq. (4) therefore contributes significantly to the the pressure drop between the syringe and the tissue/air and is included in our model.

Pressure in the tissue

In the derivation of an equation for the pressure evolution in tissue during injection we start from mass-conservation,

$$\frac{\partial \rho}{\partial t} + \nabla\cdot(\rho \mathbf{v}) = q(\mathbf{x},t), \tag{7}$$

where ρ is the mass of the injected drug per unit volume V, $\mathbf{v}$ is the pore flow velocity in a unit volume and the local source term $q(\mathbf{x},t)$ is the mass of drug being injected per volume per time. A unit volume in the tissue is assumed to comprises of the tissue (V_t) and the injected drug (V_f), i.e.

$$1 = V_t/V + V_f/V.$$

The drug density in a unit volume of tissue can be written in terms of the mass density of the drug (ρ_f) as $\rho = \rho_f V_f/V$, where V_f/V is the local volume fraction of the drug. We introduce a field for the local volume fraction of injected fluid $\phi(\mathbf{x},t) = V_f/V$ in Eq. (7) and end up with the equation:

$$\frac{\partial \phi}{\partial t} + \nabla\cdot(\phi\tilde{\mathbf{v}}) = \frac{q(\mathbf{x},t)}{\rho_f}, \tag{8}$$

Table 1. Table of constants and variables introduced in the text.

$P_s(t)$	pressure at the inlet of the needle attached to the syringe [Pa]
P_0	pressure at the outlet of the needle [Pa]
$F(d)$	force delivered by the torsion spring [N]
d	position of the piston head [m]
R_o	inner radius of the syringe [m]
r_n	inner radius of the needle [m]
ℓ	length of the needle [m]
ρ_f	mass density of infused fluid in the tissue [kg/m^3]
v_s	average velocity over the cross section of the needle inlet [m/s]
$Q(t)$	total injection rate in the tissue [m^3/s]
v	kinematic viscosity of the drug being infused [m^2/s]
η	dynamic viscosity of the drug being infused [Pa·s]
$\rho(\mathbf{x},t)$	density of infused fluid in the tissue [kg/m^3]
$\mathbf{v}$	average velocity of the injected fluid in a unit volume of pore space [m/s]
$q(\mathbf{x},t)$	local injection rate of mass [kg/(m^3·s)]
$\phi(\mathbf{x},t)$	local volume fraction of infused fluid in the tissue [-]
ϕ_0	porosity of the tissue [-]
$p(\mathbf{x},t)$	pressure in the tissue [Pa]
p_0	tissue pressure without distortion [Pa]
β	bulk modulus of the tissue [Pa]
K	permeability of the tissue [m^2]

doi:10.1371/journal.pone.0104054.t001

where $\tilde{\mathbf{v}}$ is the pore averaged flow velocity of the injected fluid in a unit volume. Below we shall only consider the averaged velocity and therefore for convenience omit the tilde over $\tilde{\mathbf{v}}$.

The flow velocity is assumed to be given by the pressure gradient through Darcy's Law [12]

$$\mathbf{v} = -\frac{K}{\eta}\nabla p, \tag{9}$$

in which K is the permeability, η the dynamic viscosity of the fluid and p is the pressure.

Moreover we assume that displacement of the tissue by the injected fluid gives rise to a counter pressure, which will act to restore the tissue structure. This pressure is in the most simple approximation and for small deformations assumed to be linearly proportional to the difference in local tissue porosity before (ϕ_0) and after (ϕ) displacement by the injected fluid

$$p(\mathbf{x},t) - p_0 = \beta(\phi(\mathbf{x},t) - \phi_0), \tag{10}$$

where β is an effective bulk modulus describing the force needed to locally displace the tissue. Note that this form of the pressure-porosity relation is only valid for relatively small pressures, since for a very large pressure this relation might even lead to a porosity larger than unity, which would be highly non-physical. From Eq. (8)–(10), we can now derive the following equation for the pressure evolution in the tissue.

$$\frac{\partial p}{\partial t} = \frac{K}{\eta}[(\beta\phi_0 + p - p_0)\nabla^2 p + |\nabla p|^2] + \beta\frac{q}{\rho_f}, \tag{11}$$

A similar equation is frequently encountered in studies on flows in poro-elastic media [20,21] and in pattern formation studies of air injection in granular media [22], where we here have assumed that both the relative variation of volume and the advective contribution from the tissue motion are negligible.

We shall here take the tip of the needle as our center of coordinates. For simplicity, the tissue surrounding the needle tip is assumed to be homogeneous and isotropic and the injected fluid will therefore be distributed in the tissue in a spherical symmetric way. The equation for the pressure evolution is most conveniently solved in spherical coordinates where the angular components by symmetry can be disregarded. Since the source term is located at the tip of the needle, we remove this term from the equation by considering the pressure evolution outside a small sphere surrounding the tip. The radius of this sphere is taken to be equal to the radius of the needle r_n and is therefore assumed to be infinitesimal relative to the scales on which the fluid are distributed. From Eq. (8) we then get from Gauss theorem, and from the fact that mass cannot accumulate in an infinitesimal volume, a boundary condition on the form,

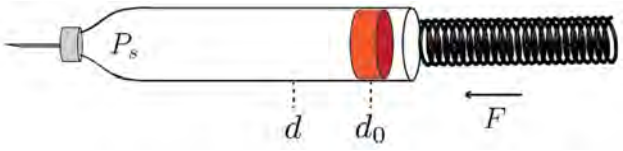

Figure 4. Schematic illustration of the insulin injection device. The force, *F*, acting on the piston from the torsion spring is a function of position, *d*, of the piston.
doi:10.1371/journal.pone.0104054.g004

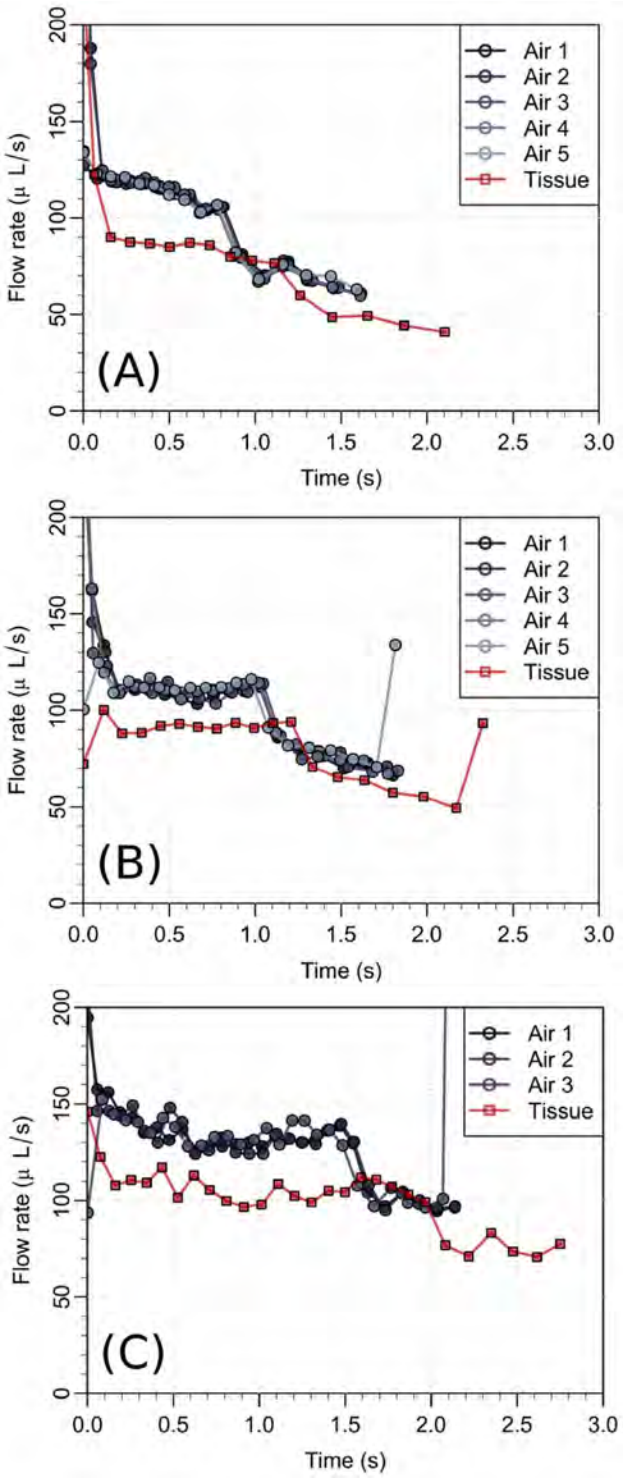

Figure 5. Flow rate during injection in air and in subcutis on three different patients. A significant drop in the flow rate is seen when the drug is injected in the tissue. The final and sudden jump in the flow rate in the panels (B) and (C) is due to an intended change in the mechanics of the syringe at end of the injection.
doi:10.1371/journal.pone.0104054.g005

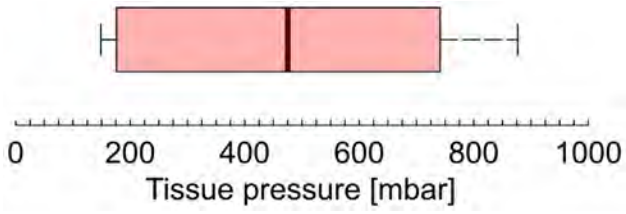

Figure 6. Average tissue counter pressure for eight patients. The boarder of the box is from the first to the third quartiles, with the median value marked as a black line. The whisker extend to the extreme values. The pressure is estimated from Eq. (4) using $F(d)$ estimated from the reference measurements in air and the flow rate $Q(t)$ in tissue.
doi:10.1371/journal.pone.0104054.g006

$$4\pi r_n^2(\phi v_r)|_{r=r_n} = Q(t) \tag{12}$$

where v_r is the radial component of the fluid velocity and the flow rate $Q(t) = (4/3)\pi r_n^3 \int q/\rho_f dV$. If we now make use of Darcy's law, we end with the following boundary condition for the pressure

$$\left.\frac{\partial p}{\partial r}\right|_{r=r_n} = -\frac{\eta Q(t)}{4\pi r_n^2 \phi K}, \tag{13}$$

where the porosity ϕ is calculated from the pressure through Eq. (10).

Experimental data on subcutaneous injection

As examples of the flow data, Figure 5 shows the measurements from 3 of the 11 patients. From Eq. (4), we can directly estimate the function $F(d)$ from the injections in air, since the atmospheric pressure, P_0, is known (note that variations in the atmospheric pressure have a negligible impact on our calculations and it is assumed that the friction force between the rubber piston and the syringe is independent on the flow rate). From our estimate of $F(d)$, the drug injection rate and from Eq. (11) and (12), we can calculate the pressure evolution in the tissue once we know the model parameters K, β and ϕ_0. The other parameters like the viscosity of water (η) and atmospheric pressure (p_0) are known. The far field pressure in the tissue (away from the needle) is assumed to be equal to atmospheric pressure. In general, however, the pressure in subcutaneous tissue might be slightly below atmospheric pressure [13]. The pressure at the outlet of the needle tip is calculated from the function $F(d)$ and the injection rate by using Eq. 4, where P_0 now is the pressure in the tissue and is a function of time. The average tissue counter pressure is shown in a box plot in Figure 6. Three patients has been omitted, as no change in the flow rate was observed indicating a low tissue resistance. We then compare the pressure $P_0(t)$ in the tissue with that predicted by the model at the needle tip, $p(r_n,t)$, in order to find the free model parameters through a best fit (least squares). Note that in our calculation of $p(r_n,t)$, we use the flow rate as a boundary condition, given by Eq. (12). In Figure 7 we show $P_0(t)$ together with the model estimate $p(r_n,t)$ achieved by a best fit. The pressure evolution in radial distance from the needle tip and over time is presented in Figure 8. We see that the over-pressure is more or less localized in a sphere with a radius less than 5 mm, which is consistent with the distribution shown in Figure 3 (right).

In Figure 9A we show a box plot of the permeability computed from a best fit with the model to the patient data, again where three patients have been omitted. The typical permeability is from

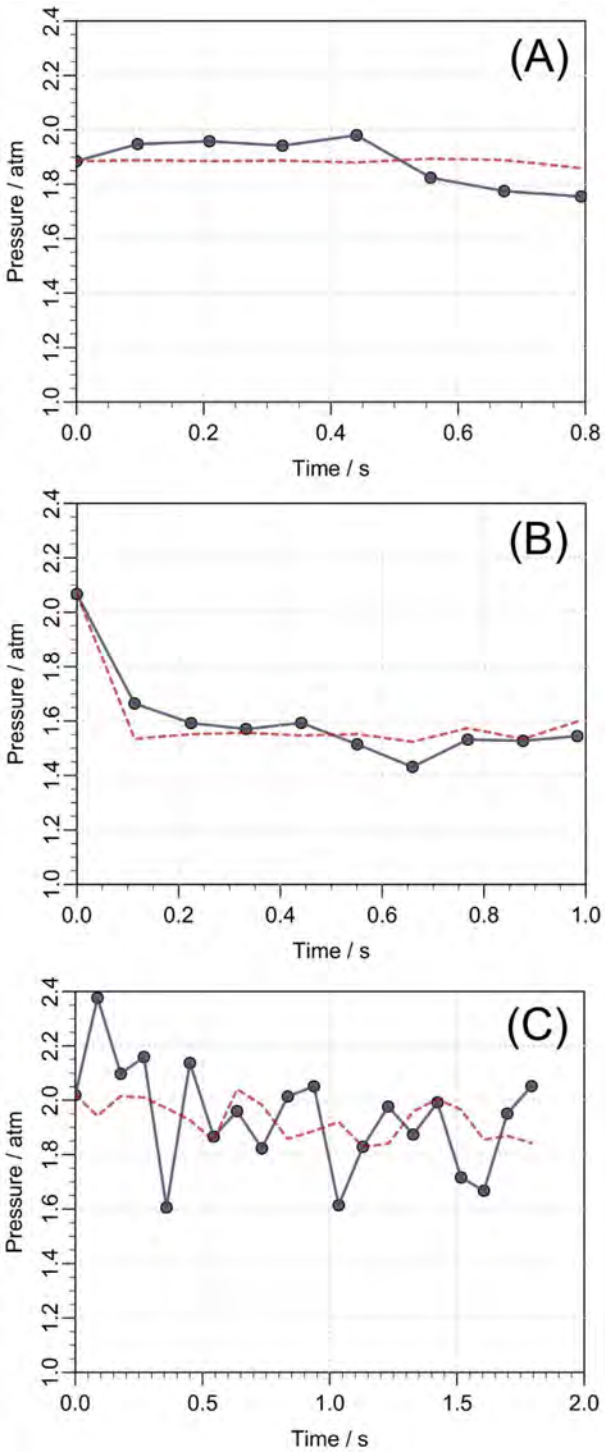

Figure 7. Pressure in the tissue during drug injection for three different patients. The pressure at the outlet of the needle (full line) is estimated from the spring force on the piston using the data on injection in air in Figure 5. The model prediction (dashed line) of the same pressure is computed from Eq. (11) and (12) by using the measured flow rate $Q(t)$ as a boundary condition. The pressure curves (A–C) corresponds to the flow rates shown in Figure 5 (A–C).
doi:10.1371/journal.pone.0104054.g007

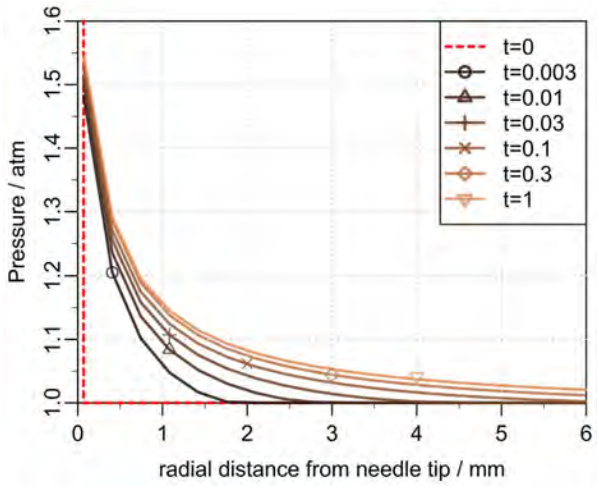

Figure 8. Pressure evolution in the tissue. The pressure in the tissue as function of the radial distance from the needle tip at different times (in seconds). Initially the over-pressure is localized around the tip of the needle and then quickly becomes distributed in the surrounding tissue.
doi:10.1371/journal.pone.0104054.g008

the model estimated to be of the order $10^{-11}-10^{-10}$ m^2. From the interquartile range, we estimate the 95% confidence interval (the notch [23]) to be between $K=(8.9\pm4.7)\cdot10^{-11}$ m^2. Measurements of the permeability in porcine adipose tissue [24] gave values of the same order of magnitudes as reported in this article. The estimated values of the bulk modulus are shown in Figure 9B with a 95% confidence interval between the values $\beta=(0.89\pm0.13)\cdot10^5$ Pa. Note that at the outlet of the needle, the

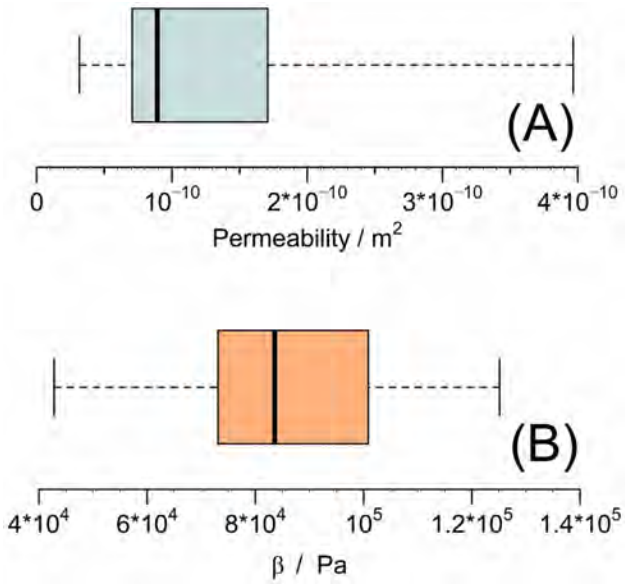

Figure 9. Box plots of the tissue permeability and bulk modulus. The values are estimated from best fits to the patient data. The permeability estimates are presented in panel (A) and the bulk modulus in panel (B). The middle line of the plot represents the value of the median and the outer edges of the box represent lower and upper quartiles, respectively. The whiskers extend to the extreme values.
doi:10.1371/journal.pone.0104054.g009

pressure in the tissue does for a few patients reach levels which are not fully consistent with a constitutive equation on the form of Eq. (10), i.e. the tissue porosity reaches values close to unity or might slightly exceed it. One way to remedy this is to change the constitutive equation and include higher order elastic or plastic effects. That being said, the pressure in the tissue does immediately drop slightly away from the needle tip (see Figure 8) and Eq. (10) becomes a valid description. Finally the background porosity ϕ_0 is in general very small and of the order ~ 0.01.

Discussion

Using a simple experimental setup we have been able to estimate the average tissue counter pressure during a subcutaneous injection with an insulin pen. The major advantages of this setup it that we do not modify the injection device and therefore are able to evaluate the pressure built up under normal injection conditions. We observe large variations in the counter pressure from a very low pressure, not detectable with this method, and up to pressures of about 800 mbar. All injections where performed with out complications, meaning that no skin reactions or pain during or after the injections were observed.

We have derived a model for the pressure evolution during injection in subcutaneous tissue, based on mass continuity as well as the basic laws of viscous flow in a poro-elastic medium. From application of the model to data on the insulin injections in diabetic patients, we have been able to determine flow permeability and bulk modulus of the tissue. Our model makes it possible to estimate how changes in the flow permeability and bulk modulus effect the pressure build-up in subcutaneous tissue during drug infusion, which is an important part of designing injection devices for insulin treatment. Control ensures that the device can deliver the full dose, that the back-flow through the injection channel is minimized and that injection pain or even tissue damage is reduced. Furthermore, our model, using the fitted parameters, is useful in general predictions of tissue pressure changes when mechanics of the injection device or the size of the needle is changed. Using the non-invasive method presented here the changes in counter pressure can easily be evaluated during clinical trails.

Supporting Information

Supporting Information S1 Total pressure drop along the needle.
(PDF)

Acknowledgments

We acknowledge nurse Bente Blaaholm, from Steno Diabetes Center A/S, for help with performing the insulin injections and Dorrit Eggert, from Device R&D, Novo Nordisk A/S Hillerød, for help with collecting the data. Susanne Primdahl, Maibritt C. Pedersen and Jonas Kildegård, from Insulin Pharmacology, Histology & Imaging, Novo Nordisk A/S Måløv, for providing the histology image in Figure 3.

Author Contributions

Conceived and designed the experiments: MT MP DNS LT RF. Performed the experiments: MT MP. Analyzed the data: MT AHG JM. Contributed to the writing of the manuscript: MT AHG JM.

References

1. Aukland K, Reed R (1993) Interstitial-lymphatic mechanisms in the control of extracellular fluid volume. Physiological reviews 73: 1–78.
2. Agache P, Humbert P (2004) Measuring the skin. Springer.
3. Vardar B, Kızılcı S (2007) Incidence of lipohypertrophy in diabetic patients and a study of influencing factors. Diabetes research and clinical practice 77: 231–236.
4. Strauss K, Gols HD, Hannet I, Partanen TM, Frid A (2002) A pan-european epidemiologic study of insulin injection technique in patients with diabetes. Practical Diabetes International 19: 71–76.
5. Omar MA, El-Kafoury AA, El-Araby RI (2011) Lipohypertrophy in children and adolescents with type 1 diabetes and the associated factors. BMC research notes 4: 290.
6. De Coninck C, Frid A, Gaspar R, Hicks D, Hirsch L, et al. (2010) Results and analysis of the 2008–2009 insulin injection technique questionnaire survey. Journal of Diabetes 2: 168–179.
7. Milan G, Murano I, Costa S, Pianta A, Tiengo C, et al. (2010) Lipoatrophy induced by subcutaneous insulin infusion: ultrastructural analysis and gene expression profiling. Journal of Clinical Endocrinology & Metabolism 95: 3126–3132.
8. Peteiro-González D, Fernández-Rodríguez B, Araújo-Vilar D, et al. (2011) Severe localized lipoatrophy related to therapy with insulin analogs in type 1a diabetes mellitus. Diabetes research and clinical practice 91: e61–e63.
9. Holstein A, Stege H, Kovacs P (2010) Lipoatrophy associated with the use of insulin analogues: a new case associated with the use of insulin glargine and review of the literature. Expert Opinion on Drug Safety 9: 225–231.
10. Johansson UB, Amsberg S, Hannerz L, Wredling R, Adamson U, et al. (2005) Impaired absorption of insulin aspart from lipohypertrophic injection sites. Diabetes Care 28: 2025–2027.
11. Gentile S, Agrusta M, Guarino G, Carbone L, Cavallaro V, et al. (2011) Metabolic consequences of incorrect insulin administration techniques in aging subjects with diabetes. Acta diabetologica 48: 121–125.
12. Darcy H (1856) Les fontaines publiques de la ville de Dijon: exposition et application. Victor Dalmont.
13. Wiig H, Rubin K, Reed RK (2003) New and active role of the interstitium in control of interstitial fluid pressure: potential therapeutic consequences. Acta Anaesthesiological Scandinavica 47: 111–121.
14. Stranden E, Myhre H (1982) Pressure-volume recordings of human subcutaneous tissue: a study in patients with edema following arterial reconstruction for lower limb atherosclerosis. Microvascular research 24: 241–248.
15. Patte C, Pleus S, Wiegel C, Schiltges G, Jendrike N, et al. (2013) Effect on infusion rate and indwelling time on tissue resistance pressure in small-volume subcutaneous infusion like in continuous subcutaneous insulin infusion. Diabetes Technology & Therapeutics 15: 289–294.
16. Pearson TL (2010) Practical aspects of insulin pen devices. Journal of diabetes science and technology 4: 522–531.
17. Wielandt JO, Niemeyer M, Hansen MR, Bucher D, Thomsen NB (2011) An assessment of dose accuracy and injection force of a novel prefilled insulin pen: comparison with a widely used prefilled insulin pen. Expert opinion on drug delivery 8: 1271–1276.
18. Heinemann L (2013) Insulin pens and new ways of insulin delivery. Diabetes Technology & Therapeutics 15: S–48.
19. Thomsen M, Poulsen M, Bech M, Velroyen A, Herzen J, et al. (2012) Visualization of subcutaneous insulin injections by x-ray computed tomography. Phys Med Biol 57: 7191–7203.
20. Spiegelman M (1993) Flow in deformable porous media. part 1 simple analysis. J Fluid Mech 247: 17–38.
21. Wang H (2000) Theory of linear poroelasticity with applications to geomechanics and hydrogeology. Princeton University Press.
22. Johnsen Ø, Toussaint R, Måløy KJ, Flekkøy EG (2006) Pattern formation during air injection into granular materials confined in a circular Hele-Shaw cell. Physical Review E, 74(1), 011301.
23. McGill R, Tukey JW, Larsen WA (1978) Variations of box plots. The American Statistician, 32(1), 12–16.
24. Comley KSC (2010) The mechanical properties of adipose tissue. Ph.D. thesis, University of Cambridge, Emmanuel Collage.

Paper II

M. Thomsen, E.B. Knudsen, P.K. Willendrup, M. Bech, M. Willner, F. Pfeiffer, M. Poulsen, K. Lefmann, R. Feidenhans'l.
Prediction of beam hardening artefacts in computed tomography using Monte Carlo simulations.
Nuclear Inst. and Methods in Physics Research, B (2014) 342, pp. 314-320. doi:10.1016/j.nimb.2014.10.015

Nuclear Instruments and Methods in Physics Research B 342 (2015) 314–320

Contents lists available at ScienceDirect

Nuclear Instruments and Methods in Physics Research B

journal homepage: www.elsevier.com/locate/nimb

Prediction of beam hardening artefacts in computed tomography using Monte Carlo simulations

M. Thomsen [a,b,*], E.B. Knudsen [c], P.K. Willendrup [c], M. Bech [d,e], M. Willner [d], F. Pfeiffer [d], M. Poulsen [b], K. Lefmann [a], R. Feidenhans'l [a]

[a] University of Copenhagen, Universitetsparken 5, DK-2100 Copenhagen, Denmark
[b] Novo Nordisk A/S, Brennum Park 20, DK-3400 Hillerød, Denmark
[c] Department of Physics, Technical University of Denmark, Building 307, DK-2800 Kgs. Lyngby, Denmark
[d] Technical University Munich, James-Franck-Straße 1, D-85748 Garching, Germany
[e] Medical Radiation Physics, Lund University, Barngatan 2:1, SE-22185 Lund, Sweden

ARTICLE INFO

Article history:
Received 7 January 2014
Received in revised form 21 September 2014
Accepted 21 October 2014

Keywords:
Monte Carlo simulations
X-ray computed tomography
Beam hardening artefacts

ABSTRACT

We show how radiological images of both single and multi material samples can be simulated using the Monte Carlo simulation tool McXtrace and how these images can be used to make a three dimensional reconstruction. Good numerical agreement between the X-ray attenuation coefficient in experimental and simulated data can be obtained, which allows us to use simulated projections in the linearisation procedure for single material samples and in that way reduce beam hardening artefacts. The simulations can be used to predict beam hardening artefacts in multi material samples with complex geometry, illustrated with an example. Linearisation requires knowledge about the X-ray transmission at varying sample thickness, but in some cases homogeneous calibration phantoms are hard to manufacture, which affects the accuracy of the calibration. Using simulated data overcomes the manufacturing problems and in that way improves the calibration.

1. Introduction

Computed tomography (CT) is extensively used for characterisation of the geometry and material composition of multi material components. The contrast in tomographic reconstructions is given by the X-ray attenuation coefficients and can be used to calculate the 3-dimensional (3D) micro-structure and material distribution, which has been demonstrated for e.g. bones using monochromatic radiation [1–3]. Beamtime at synchrotron radiation facilities is scarce, and such measurements are therefore relatively inaccessible. Therefore, most CT experiments are performed using either a laboratory X-ray source or a conventional CT-scanner system, which both have a polychromatic X-ray source. Tomographic reconstructions calculated from projections measured using a polychromatic X-ray source will be influenced by artificial density variations and streak artefacts. These artefacts appear because the X-ray attenuation coefficients in most cases decrease strongly with increasing X-ray photon energy, meaning that low energy photons will be absorbed more efficiently than photons with high energy. This effect is known as beam hardening. When making a 3D reconstruction of a homogeneous sample the attenuation coefficient inside the sample is supposed to be constant, but due to beam hardening the reconstructed attenuation coefficient will be lower in the centre of the sample than at the edges, called the cupping effect [4]. The cupping effect increases with increasing sample thickness and density and makes it hard to predict variations in the material density from the tomographic reconstructions [5].

Beam hardening artefacts in tomographic reconstructions have been extensively studied and the most common methods for reducing the artefacts include: Physical filtration of the beam, dual-energy tomography, or algorithmic corrections either of the projections or the reconstruction [6,7]. When making a filtration with e.g. an aluminium or copper filter the low energy X-ray photons are attenuated and the effect of beam hardening is reduced, but not completely removed [8,9]. The disadvantage is that the flux is reduced too, so the acquisition time must be extended or hence the noise level will increase. Furthermore, the filtering reduces the contrast between low absorbing materials [8]. In the dual-energy method a CT-scan is performed at two different tube voltages, typically about 140 kV and 80 kV [10], and from these scans the photoelectric interaction and the Compton

* Corresponding author at: University of Copenhagen, Universitetsparken 5, DK-2100 Copenhagen, Denmark. Tel.: +45 30285261.
E-mail address: mariath@fys.ku.dk (M. Thomsen).

http://dx.doi.org/10.1016/j.nimb.2014.10.015
0168-583X/

scattering are reconstructed separately or the measured attenuation is linearised for the two energies [11,12]. This technique requires either a special setup with two sources and detectors or that the sample is scanned at two different energies, which is very time consuming and increases the radiation dose. Another way to reduce beam hardening artefacts is by using a linearisation method [13,14]. Using a polychromatic X-ray source the logarithm to the normalised intensity no longer decreases linearly with the sample thickness, as is the case for a monochromatic beam. When making a linearisation, the attenuation as a function of object thickness is predicted from a prior reconstruction of the sample or calibration measurements and the attenuation measured is adjusted to depend linearly on the thickness before the final reconstruction is performed. The technique works for samples consisting of a limited number of materials and with a simple geometry [15].

We have approached the problem about predicting and correcting beam hardening artefacts using the Monte Carlo simulation tool McXtrace [16], developed from the well established simulation tool for neutron experiments McStas, which has proven useful for both instrumentation [17,18] and data analysis [19]. One advantage of using simulations as, e.g. Monte Carlo, is that they are very flexible regarding changes in the beam geometry and sample composition and objects with different geometry and densities can easily be combined to form new samples. However the simulations require knowledge about the detector efficiency and about the energy spectrum of the X-ray beam as emitted from source.

The aim of this study is to evaluate how well simulations can predict beam hardening artefacts and to show how the simulations can be implemented in a linearisation procedure and in that way correct the artefacts in single material samples. We have simulated projections of simple phantom samples, compared the resulting reconstructions to similar experimental data and used simulations to correct the cupping effect in the reconstructions. Furthermore we have simulated a geometric figure both as a single and multi material samples to demonstrate the flexibility of McXtrace.

2. Materials and methods

For polychromatic X-ray radiation the transmitted intensity measured by the detector is given by

$$I = \int dE I_0(E) D(E) \exp\left(-\int dl \mu(E, \mathbf{r}(l))\right) \quad (1)$$

where $I_0(E)$ is the incoming X-ray intensity at energy E, $D(E)$ is the energy dependent efficiency of the detector and $\int dl \mu(E, \mathbf{r}(l))$ is the line integral of the X-ray attenuation coefficient along the path of the beam. The attenuation coefficient depends on the photon energy, E, and position in sample, $\mathbf{r}$.

Radiographic images of the sample are obtained from different angles and the 3D structure is reconstructed using the filtered backprojection algorithm [20]. The experimental setup as simulated in McXtrace is illustrated in Fig. 1.

In order to investigate the ability to reproduce tomographic reconstructions by simulations we have measured two simple phantom samples. The phantoms were $10 \times 10 \times 10\ \mathrm{mm}^3$ cubes with a cylinder with a radius of 2.5 mm in the centre. For one of the samples the cube was made of polymethyl methacrylate (PMMA) and the cylinder was made of aluminium and for the other sample it was opposite.

2.1. X-ray computed tomography

The measurements were performed at a laboratory X-ray source at the Technische Universität München. The X-ray beam was generated by a molybdenum target and the acceleration voltage and filament current were set to 50 kV and 75 mA, respectively. A 2 mm aluminium filter was placed in front of the source to avoid the detector being saturated and to reduce the effect of beam hardening on the tomographic reconstructions. The detector used for the experiments was the photon counting detector, Pilatus 100K, with a pixel size of $172 \times 172\ \mu\mathrm{m}^2$ [21]. With a magnification of 1.58 the effective voxel size in the reconstructions was $102 \times 102 \times 102\ \mu\mathrm{m}^3$. The exposure time was 150 ms for each projection and a full tomography scan had 401 projections over 360°.

2.2. Monte Carlo simulations

McXtrace does not simulate individual photons but ensembles of photons, called rays. In each ray the photons have common direction, energy, polarisation, momentum and phase. The number of photons in each ray is by convention called the weight factor. The initial weight factor is determined by the spectral density of the energy spectrum as emitted from the source [16]. When a photon penetrates an absorbing material it will be absorbed by a probability given by the absorption cross section. To optimise the simulation no rays are removed but the weight factor for each ray is multiplied by the transmission probability $\exp(-\int dl \mu(E, \mathbf{r}(l)))$, as given by Eq. (1). The energy distribution from the molybdenum target has been measured experimentally using a XR-100T-CdTe detector from AmpTek [22]. The spectrum was measured at the CT-scanner system Phoenix Nanotom®S [23]. The simulated source is a point source emitting photons in all directions. In order to make the simulations more efficient only the rays having a direction into the solid angle, Ω, covered by the detector window, are simulated. The initial weight factor of the ray, p_0, is reduced by a factor $\Omega/(4\pi)$.

For each tomography scan we simulated 401 projection over 360° with 10^8 rays for each projection. Since the rays may be considered independent the simulations can easily be run in parallel. In this case a 32 core GNU/Linux based machine was used and

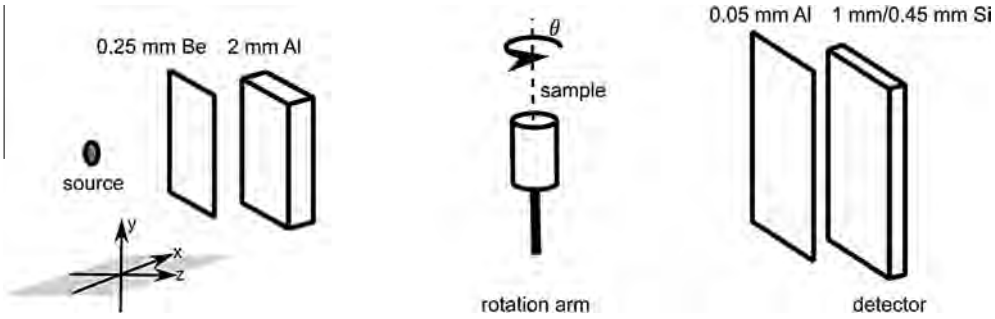

Fig. 1. Experimental setup for X-ray computed tomography as simulated in McXtrace. The setup is constructed to match the experimental setup at the laboratory X-ray source.

the run time for a full tomography scan was about 5 h, depending on sample geometry.

The Pilatus 100K detector used for the experiment is a semiconductor detector where the effective layer is made of silicon, with a thickness of 1 mm. A 50 μm aluminium foil was placed in front of the detector window to protect the silicon layer [21]. In the simulations it is assumed that the detector efficiency is purely determined by the absorption in the silicon layer. The energy dependent X-ray absorption coefficients used in the simulations are all taken from a database administrated by the National Institute of Standards and Technology (NIST) [24]. Air absorption is taken into account, but scattering and refraction of the X-ray photons have not been included in the simulations.

3. Results

The PMMA cube with the aluminium cylinder in the centre and a simulated projection image is shown in Fig. 2.

As the beam propagates from the source to the detector the energy distribution of the beam changes, because of the energy dependence of the X-ray attenuation coefficients, illustrated for aluminium in Fig. 3. In the absence of any absorption edges the attenuation coefficient decreases almost as E^{-3}. To reduce read out noise the lower detection limit of the detector was set to 5 keV and the acceleration voltage of 50 kV put an upper limit for the X-ray photon energy, indicated with black dashed lines in the figure. To illustrate how the energy distribution of the X-ray spectrum changes through the setup, we implemented energy-sensitive monitors in the simulation. The monitors were 4.4×4.2 mm^2, covering the central part of the 33.5×33.4 mm^2 detector area. Fig. 4 shows the energy spectrum emitted from the source (blue solid line) and after the aluminium filter (light blue dashed line), showing how the filter removes the low energy photons. The average energy of the spectrum increases from 18 keV to 29 keV. After penetrating the aluminium cylinder the average energy further increases to 36 keV (green solid circles), while the energy distribution is almost unchanged when passing though the PMMA cube (light green dashed circles). The energy distribution of the photons passing through the detector, shows that the low energy photons are detected more efficiently than the high energy photons (black crosses).

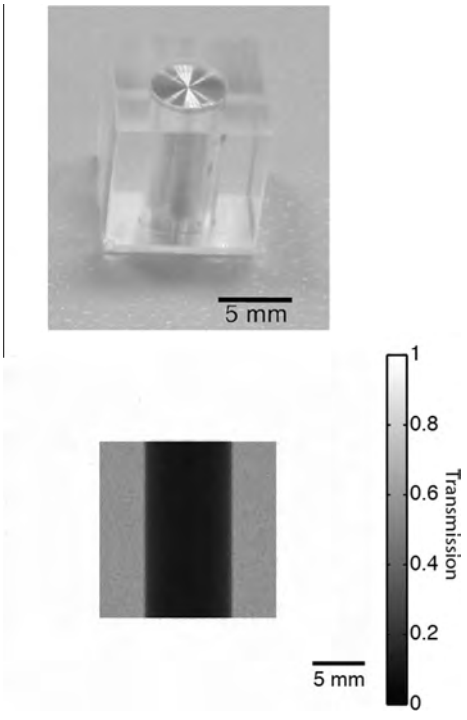

Fig. 2. Top: A $10 \times 10 \times 10$ mm^3 cube of PMMA with a cylinder of aluminium with a diameter of 5 mm. Bottom: Simulated projection image with 10^8 rays per projections. Magnification is 1.58.

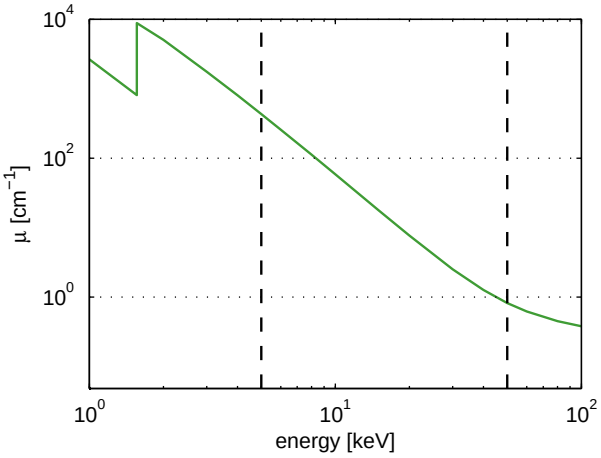

Fig. 3. X-ray attenuation coefficient for aluminium with a density of 2.70 g/cm^3. The black dashed lines indicate the detector threshold at 5 keV and the maximum photon energy at 50 keV, set by the acceleration voltage.

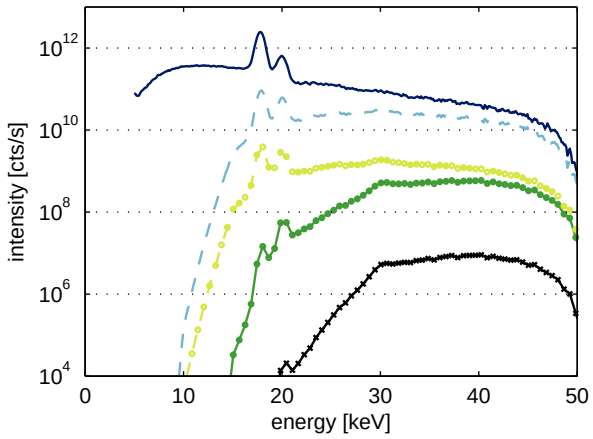

Fig. 4. Energy spectrum for the X-ray photons as emitted from the source (blue solid line), after the 2 mm Al-filter (light blue dashed line), after the aluminium cylinder (green solid circles), PMMA cube (light green dashed circles) and after the detector (black crosses). The characteristic K_α- and K_β-lines for molybdenum are at 17.5 keV and 19.6 keV, respectively. (For interpretation of the references to colour in this figure legend, the reader is referred to the web version of this article.)

3.1. Accuracy of the Monte Carlo simulations

Fig. 5 shows the 3D rendering (top) and a single slice of tomographic reconstruction (bottom) of the PMMA cube with the aluminium cylinder. The reconstructed attenuation coefficient along the red line in Fig. 5 (bottom), is shown in Fig. 6 for the PMMA cube (top) and aluminium cube (bottom), for experimental (blue solid line) as well as simulated data (green circles). The lines shown, represent an average over three neighbour voxels to reduce the noise. We find good agreement between simulated and experimental data and the simulations nicely reproduce the cupping effect.

To compare the experimental and simulated data the average attenuation coefficient for the different materials are calculated from the reconstructions and collected in Table 1, where the top

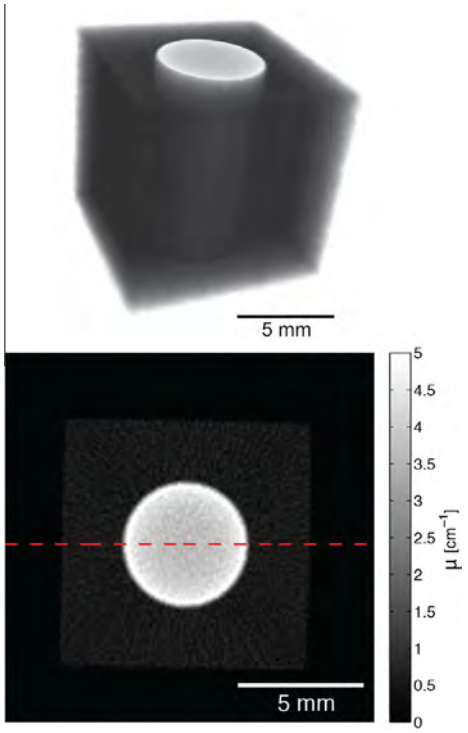

Fig. 5. Top: 3D reconstruction of the PMMA cube with the aluminium cylinder in the centre from 401 simulated projections with 10^8 rays per projections. Bottom: Single horizontal slice of the tomographic reconstruction for experimental data. Grey scale is given by the attenuation coefficient, μ [cm^{-1}].

line is the experimental data and the bottom line is the simulated data for each sample. Overall there is a good agreement between simulations and experimental data. The deviation is about 2% for the low absorbing PMMA cube and 3% for the highly absorbing Al cylinder. The difference between attenuation coefficients for the PMMA cylinder embedded in the Al cube is about 8% and for the surrounding cube the difference is about 5%, suggesting that the higher the absorption in the samples the larger is the difference between experimental data and simulations.

The signal-to-noise ratio ($\langle\mu\rangle/\sigma$) in the reconstructions is higher for the measurement than for the simulations when simulating 10^8 rays. In the projection images the standard deviation of the transmitted signal through air is about 5 times higher in the simulated than in the experimental data. For the simulations the number of events, N, in the detector pixels can be considered Poisson distributed and therefore the estimated standard deviation proportional to $\frac{1}{\sqrt{N}}$. It means by simulating 25 times more photons the standard deviation in the simulated projection images will be comparable to the experimental data.

The difference between the simulated and experimental data is largest at the edge of the samples, most pronounced for the aluminium cube where the difference is about 0.5 cm^{-1} (see Fig. 6(bottom)). The difference at the edge will appear if either the edges of the physical sample are not perfectly sharp, the sample is slightly tilted in the beam, or if the sample slightly vibrates during the measurement. All these effects give a reduced attenuation at the edges when reconstructed.

3.2. Correction of beam hardening artefacts

The simulations reproduce the reconstructed attenuation coefficient very well and therefore the simulations can be used to correct the cupping effect in the experimental data. In the following we perform a linearisation of the experimentally obtained

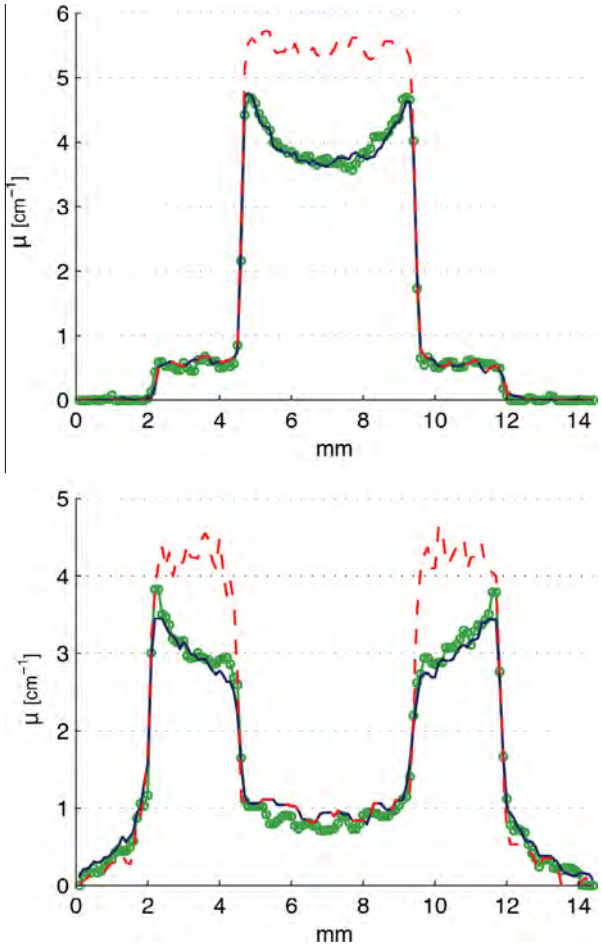

Fig. 6. Attenuation coefficient along a horizontal line through the centre of the cube for experimental data (solid blue), simulated data (green circles) and experimental data after beam hardening correction (red dashed). Top: PMMA cube with aluminium cylinder. Bottom: Aluminium cube with PMMA cylinder. (For interpretation of the references to colour in this figure legend, the reader is referred to the web version of this article.)

Table 1
Average attenuation coefficient ($\langle\mu\rangle$) and standard deviation (σ) of the voxels assigned as PMMA and Al for the experimental (first row) and simulated data (second row) for each of the phantom samples; the PMMA cube with a aluminium cylinder in the centre and the aluminium cube with a PMMA cylinder in the centre. The average is taken over the total volume of the cylinder and the cube, corresponding to about $12{\cdot}10^4$ and $50{\cdot}10^4$ voxels for the cylinder and cube, respectively. The standard deviation of the mean attenuation coefficient is less than 0.1% for all materials.

		PMMA	Al
$\langle\mu\rangle$ (σ) [cm^{-1}]			
PMMA cube	exp	0.54 (0.15)	4.03 (0.56)
10×10×10 mm^3	sim	0.55 (0.24)	4.17 (0.62)
Al cube	exp	1.06 (0.27)	3.10 (0.38)
10×10×10 mm^3	sim	0.98 (0.28)	3.26 (0.43)
Signal to noise ratio			
PMMA cube	exp	3.56	7.14
10×10×10 mm^3	sim	2.31	6.71
Al cube	exp	3.93	8.21
10×10×10 mm^3	sim	3.48	7.58

projections using a calibration curve calculated from simulated projections and show how the cupping effect can be significantly reduced by linearisation [14]. For each projection the transmitted intensity in the raw data is corrected according to the penetration length (l_{Al}) through the aluminium.

$$I_c(l_{Al}) = I_{\exp}(l_{Al}) + I_d(l_{Al}) \quad (2)$$

where I_c and $I_{\exp}$ is the corrected and the measured transmitted intensity, respectively. The correction term, I_d, is the difference between the transmission of a monochromatic and a polychromatic X-ray beam.

$$I_d(l_{Al}) = I_{\text{mono}}(l_{Al}) - I_{\text{poly}}(l_{Al}) \quad (3)$$

The monochromatic transmission at energy E and the polychromatic transmissions are theoretically given by

$$I_{\text{mono}}(E) = I_0(E)\exp\left(-\int d\mathbf{r}\mu(E,\mathbf{r})\right) \quad (4)$$

$$I_{\text{poly}} = \int dE I_0(E)D(E)\exp\left(-\int d\mathbf{r}\mu(E,\mathbf{r})\right) \quad (5)$$

To calculate the correction term, $I_d(l_{Al})$, the monochromatic and polychromatic transmission must be known as function of the sample thickness, l_{Al}.

For the aluminium cylinder the transmission of polychromatic radiation, $I_{\text{poly}}(l_{Al})$, as a function of aluminium thickness is obtained by simulating a aluminium box of varying thickness. The box is embedded in a $10 \times 10 \times 10\ \text{mm}^3$ PMMA cube. Fig. 7 shows the attenuation, $-\ln(I_{\text{poly}}/I_0)$, as function of the thickness of the aluminium box (dots), where $I_0 = \int dE I_0(E)D(E)$. This relationship has been fitted to a third order polynomial (solid line). For monochromatic radiation the attenuation, $-\ln(I_{\text{mono}}(E)/I_0(E))$, increases linear with the sample thickness. Instead of simulating a monochromatic beam, $I_{\text{mono}}(l_{\text{Al}})$ is obtained using the slope of the polynomial fit at $x = 0$ (dashed line). For the aluminium cube the calibration curve is calculated from the simulation of the sample itself.

To apply Eq. (2) the penetration length through aluminium must be calculated for each pixel in the projection images. This is done by segmenting the aluminium cylinder in the reconstruction and make the segmented image binary. The penetration length is calculated by ray tracing and the value is assigned to the corresponding transmission. The monochromatic and polychromatic transmission is calculated from the corresponding calibration curve for each pixel in the projection images and finally the original projection is corrected according to Eq. (2).

A single slice of the reconstruction before (left) and after correction (right) is shown in Fig. 8 for the aluminium cylinder (top) and aluminium cube (bottom). The grey scale is chosen to go from 3 to 6 cm^{-1} for the aluminium cylinder and 2–5 cm^{-1} for the aluminium cube, to accentuate the variations in the attenuation coefficient. It is clearly seen how the cupping artefacts are reduced and in Fig. 6 the attenuation coefficient along a horizontal line through the centre is compared for the uncorrected (blue solid line) and corrected reconstruction (red dashed line) for both the cylinder (top) and the cube (bottom). The overall cupping has, however, been reduced by almost a factor of 5, estimated from Fig. 8.

The phantom samples illustrated have a simple geometry and since PMMA is very weakly absorbing, the aluminium part can be considered as a single material sample and therefore the linearisation method is well adapted. For multi-material samples with complex geometry the artefacts are not easily corrected. McXtrace can be used to predict the beam hardening artefact samples with more complex geometry, one examples is shown in Fig. 9. The figure shows 3D reconstruction of a chess king made of PMMA with an aluminium box in the centre (right), based on simulated projections. The simulations are performed with the same beam geometry and filters as the phantom samples. The chess king has a width of 15 mm and the box is $2.8 \times 2.8 \times 3.5\ \text{mm}^3$. Fig. 9(right) shows the absorption coefficients along a horizontal line though the reconstruction with (blue circles) and without aluminium inclusion (dashed green), showing the cupping effect in the inclusion.

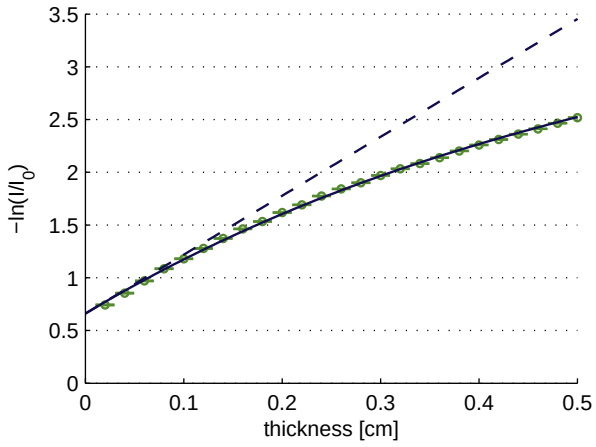

Fig. 7. Transmission through an aluminium box as function of the box thickness (simulated data) for polychromatic radiation (dots) fitted to a third order polynomial (solid line) and a first order polynomial (dashed line). The aluminium box is placed inside a $10 \times 10 \times 10\ \text{mm}^3$ PMMA cube. (For interpretation of the references to colour in this figure legend, the reader is referred to the web version of this article.)

4. Discussion

The attenuation coefficients in the simulated reconstructions agree well with the attenuation coefficients in the reconstructions obtained from experimental data. The deviation between the simulated and experimental data is in the order of 2-8%, increasing with increasing material density and thickness. This suggest that the higher the average energy of the beam is, when reaching a volume element in the sample, the higher is the deviation between the reconstructed absorption coefficient for the experimental and simulated data.

To achieve this good agreement between experimental and simulated data knowledge about the energy spectrum from the source, the sample and filter material composition and geometry, and energy efficiency of the detector is required. Information about the geometry of the sample can be obtained from the reconstruction based on the experimental data and implemented into a McXtrace simulation. The tolerance of the samples are in this case better than 0.1 mm. The filter thickness was adjusted with ± 0.03 mm, with only minor differences in the simulated reconstruction.

We have measured the X-ray spectrum experimentally, but McXtrace also has the source component `Source_lab`, which generates the spectrum from a theoretical approximation [25] and tabulated values for the energy distribution [26].

The energy efficiency of the detector is for our case simulated by the absorption in the active silicon layer with the thickness adapted from the manual. It have been shown by Schubert et al. [27] that for the standard Pilatus 100K detector, with an active layer of 320 μm silicon, charge sharing among different pixel elements will occur. It means that some of the low energy X-ray photons will not be detected while some of the high energy X-ray photons will be detected in more than one pixel. Therefore the transmission measured by the Pilatus 100K detector will be higher than the simulated transmission, since more high energy photons than low energy photons penetrate the sample. This causes the absorption coefficient in the reconstructions based on experimental data to be lower than in the reconstructions based on simulated data, as we observe. Therefore to further improve the accuracy of

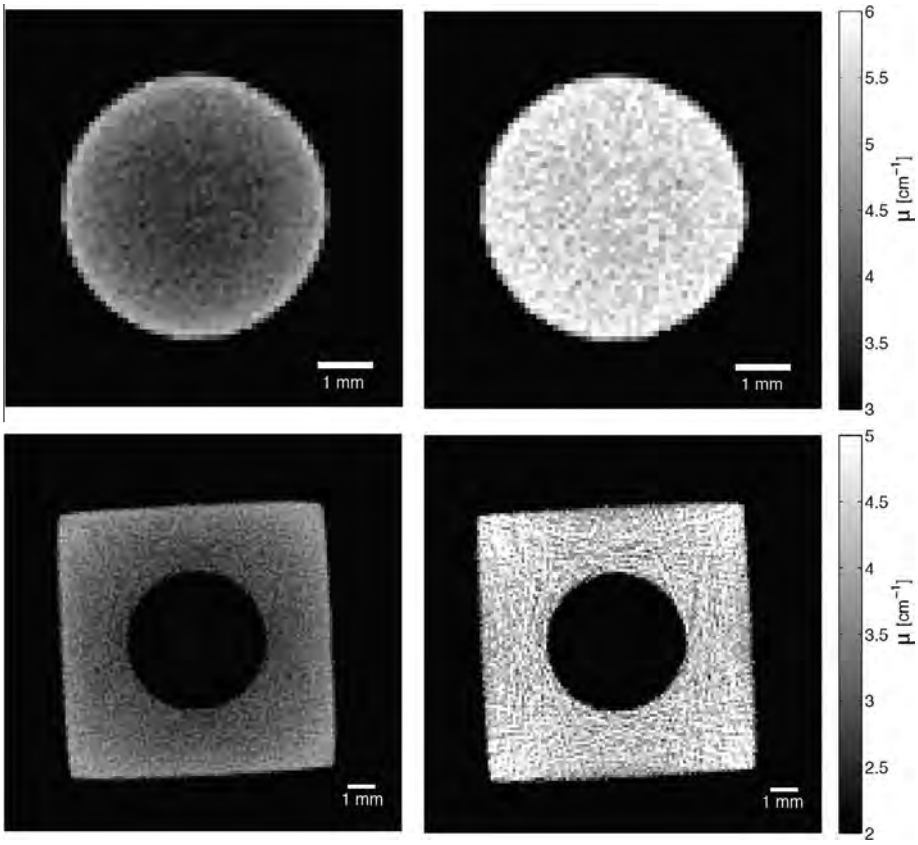

Fig. 8. Top: The reconstruction of the Al cylinder before (left) and after corrected for the cupping effect (right) (experimental data).Bottom: The reconstruction of the Al cube before (left) and after corrected for the cupping effect (right) (experimental data).

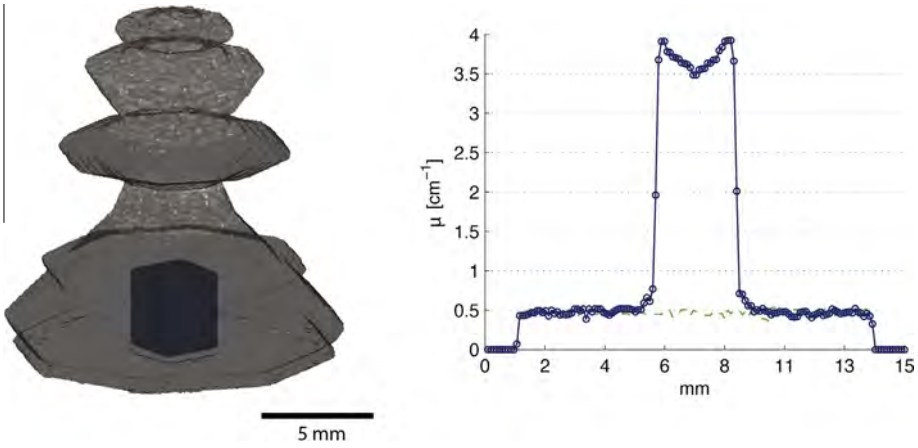

Fig. 9. Reconstruction of a chess king made from 401 simulated projections an $2.8 \times 2.8 \times 3.5$ mm^3 box in the centre and the reconstructed attenuation coefficient along a horizontal line though the centre (right). The chess king and the inclusion is made of PMMA and aluminium, respectively.

the simulations the energy efficiency of the detector must be known with higher accuracy.

In this study only absorption was included in the sample and filter components, but McXtrace offers components simulating scattering or diffraction. For further improvement of the tomography simulations these should be included in the absorption components.

The linearisation method requires knowledge about the transmission as function of sample thickness. Using simulations to obtain that knowledge saves both scan time and productions costs. Furthermore it is possible to simulated the transmission for samples, which can be hard to produce, which is the case for bone mineral density calibrations for instance [28].

5. Conclusion

We have shown how projections images, can be simulated by McXtrace and the 3D structure can be reconstructed using the standard filtered backprojection algorithm.

From the simulations the influence of the beam hardening on the reconstructed absorption coefficients can be predicted with

high accuracy. McXtrace is very flexible regarding the sample geometry and objects with different density and geometry can easily be combined. It means that beam hardening artefacts in samples with complex geometry can be predicted from simulated data and real variations in the material density can then be distinguished from the artificial variations introduced by the polychromatic X-ray spectrum. The geometry of the simulated samples can be based on the computer-aided design of the real sample and therefore simulations can be made prior to the experiment.

The good agreement between experimental and simulated data allows us to use simulated projections in the linearisation procedure for single material components. For the case of the homogeneous aluminium samples the overall cupping effect was reduced by almost a factor of 5. Furthermore the simulations can be used to optimise scan parameters, such as acceleration voltage and filtration of the beam, to improve the image contrast and reduce beam hardening.

Acknowledgement

We want to acknowledge Mikkel Schou Nielsen from the Niels Bohr Institute for help during the experiment. The experimental work has been financially supported by Novo Nordisk A/S and The Danish Agency for Science, Technology and Innovation through the NEXIM project. The McXtrace project was funded by the Danish Strategic Research Council.

References

[1] S. Nuzzo, F. Peyrin, P. Cloetens, J. Baruchel, G. Boivin, Quantification of the degree of mineralization of bone in three dimensions using synchrotron radiation microtomography, Med. Phys. 29 (2002) 2672.
[2] M. Ito, S. Ejiri, H. Jinnai, J. Kono, S. Ikeda, A. Nishida, K. Uesugi, N. Yagi, M. Tanaka, K. Hayashi, Bone structure and mineralization demonstrated using synchrotron radiation computed tomography (sr-ct) in animal models: preliminary findings, J. Bone Miner. Metab. 21 (5) (2003) 287–293.
[3] K. Chiba, N. Nango, S. Kubota, N. Okazaki, K. Taguchi, M. Osaki, M. Ito, Relationship between microstructure and degree of mineralization in subchondral bone of osteoarthritis: a synchrotron radiation μct study, J. Bone Miner. Res. 27 (7) (2012) 1511–1517. Jul;27(7):1511-7.
[4] R.A. Brooks, G. Di Chiro, Beam hardening in X-ray reconstructive tomography, Phys. Med. Biol. 21 (3) (1976) 390.
[5] J.A. Meganck, K.M. Kozloff, M.M. Thornton, S.M. Broski, S.A. Goldstein, Beam hardening artifacts in micro-computed tomography scanning can be reduced by X-ray beam filtration and the resulting images can be used to accurately measure bmd, Bone 45 (6) (2009) 1104–1116.
[6] G. Van Gompel, K. Van Slambrouck, M. Defrise, K.J. Batenburg, J. de Mey, J. Sijbers, J. Nuyts, Iterative correction of beam hardening artifacts in ct, Med. Phys. 38 (2011) S36.
[7] W. Zou, N. Hunter, M.V. Swain, Application of polychromatic μct for mineral density determination, J. Dent. Res. 90 (1) (2011) 18–30.
[8] R.J. Jennings, A method for comparing beam-hardening filter materials for diagnostic radiology, Med. Phys. 15 (4) (1988) 588–599.
[9] R.T. Lopes, E.B. Costa, E.F.O. de Jesus, Computed tomography with monochromatic bremsstrahlung radiation, Appl. Radiat. Isot. 53 (4) (2000) 665–671.
[10] Martin Petersilka, Herbert Bruder, Bernhard Krauss, Karl Stierstorfer, Thomas G. Flohr, Technical principles of dual source ct, Eur. J. Radiol. 68 (3) (2008) 362–368.
[11] R.E. Alvarez, A. Macovski, Energy-selective reconstructions in X-ray computerised tomography, Phys. Med. Biol. 21 (5) (1976) 733.
[12] A.J. Coleman, M. Sinclair, A beam-hardening correction using dual-energy computed tomography, Phys. Med. Biol. 30 (11) (1985) 1251.
[13] G.T. Herman, Correction for beam hardening in computed tomography, Phys. Med. Biol. 24 (1) (1979) 81–106.
[14] P. Hammersberg, M. Mangard, Correction for beam hardening artefacts in computerised tomography, J. X-ray Sci. Technol. 8 (1) (1998) 75.
[15] D. Van Dyck, J. Sijbers, E. Van de Casteele, E. Raman, An energy-based beam hardening model in computed tomography, Phys. Med. Biol. 47 (2002) 4181–4190.
[16] E. B Knudsen, A. Prodi, J. Baltser, M. Thomsen, P.K. Willendrup, M. Sanchez del Rio, C. Ferrero, E. Farhi, K. Haldrup, A. Vickery, et al., Mcxtrace: a monte carlo software package for simulating X-ray optics, beamlines and experiments, J. Appl. Crystallogr. 46 (3) (2013) 679–696.
[17] Christian Schanzer, Peter Böni, Uwe Filges, Thomas Hils, Advanced geometries for ballistic neutron guides, Nucl. Instrum. Methods Phys. Res. Sect. A 529 (1) (2004) 63–68.
[18] K. Lefmann, P.K. Willendrup, L. Udby, B. Lebech, K. Mortensen, J.O. Birk, K. Klen Ø, E. Knudsen, P. Christiansen, J. Saroun, et al., J. Neutron Res. 16 (3-4) (2008) 97–111.
[19] L. Udby, P.K. Willendrup, E. Knudsen, C. Niedermayer, U. Filges, N.B. Christensen, E. Farhi, B.O. Wells, K. Lefmann, Analysing neutron scattering data using mcstas virtual experiments, Nucl. Instrum. Meth. Phys. Res. Sect. A 634 (1) (2011) S138–S143.
[20] M. Slaney, A. Kak, Principles of Computerized Tomographic Imaging, SIAM, Philadelphia, 1988.
[21] P. Kraft, A. Bergamaschi, Ch. Bronnimann, R. Dinapoli, E.F. Eikenberry, H. Graafsma, B. Henrich, I. Johnson, M. Kobas, A. Mozzanica, et al., Characterization and calibration of pilatus detectors, IEEE Trans. Nucl. Sci. 56 (3) (2009) 758–764.
[22] Amptek inc. http://amptek.com/, November 2013.
[23] Ge measurements & control. http://www.ge-mcs.com/en/, November 2013.
[24] C.T. Chantler, Detailed tabulation of atomic form factors, photoelectric absorption and scattering cross section, and mass attenuation coefficients in the vicinity of absorption edges in the soft X-ray ($z = 30–36$, $z = 60–89$, $e = 0.1$ kev–10 kev), addressing convergence issues of earlier work detailed tabulation of atomic form factors, photoelectric absorption and scattering cross section, and mass attenuation coefficients in the vicinity of absorption edges in the soft X-ray ($z = 30–36$, $z = 60–89$, $e = 0.1$ kev–10 kev), addressing convergence issues of earlier work, J. Phys. Chem. Ref. Data 29 (4) (2000) 597.
[25] Hendrik Anthony Kramers XCIII, On the theory of X-ray absorption and of the continuous X-ray spectrum, The London, Edinburgh, and Dublin, Philos. Mag. J. Sci. 46 (275) (1923) 836–871.
[26] Joyce Alvin Bearden, X-ray wavelengths, Rev. Mod. Phys. 39 (1) (1967) 78.
[27] A. Schubert, G.J. OKeefe, B.A. Sobott, N.M. Kirby, R.P. Rassool, Characterisation of individual pixel efficiency in the pilatus ii sensor, Radiat. Phys. Chem. 79 (11) (2010) 1111–1114.
[28] W. Zou, J. Gao, A.S. Jones, N. Hunter, M.V. Swain, Characterization of a novel calibration method for mineral density determination of dentine by X-ray micro-tomography, Analyst 134 (1) (2008) 72–79.

Paper III

M Thomsen, M Poulsen, M Bech, A Velroyen, J Herzen, F Beckmann, R Feidenhans'l and F Pfeiffer.
Visualization of subcutaneous insulin injections by x-ray computed tomography.
Physics in Medicine and Biology (2012) 57(21), pp. 7191-203. doi:10.1088/0031-9155/57/21/7191

Phys. Med. Biol. **57** (2012) 7191–7203 doi:10.1088/0031-9155/57/21/7191

Visualization of subcutaneous insulin injections by x-ray computed tomography

M Thomsen[1,2], M Poulsen[2], M Bech[3,4], A Velroyen[4], J Herzen[4], F Beckmann[5], R Feidenhans'l[1] and F Pfeiffer[4]

[1] Niels Bohr Institute, University of Copenhagen, Universitetsparken 5, DK-2100 Copenhagen, Denmark
[2] Device R&D, Novo Nordisk A/S, Brennum Park 20, DK-3400 Hillerød, Denmark
[3] Medical Radiation Physics, Lund University, Barngatan 2:1, SE-22185 Lund, Sweden
[4] Technical University Munich, James-Franck-Straße 1, D-85748 Garching, Germany
[5] Institute of Materials Research, Helmholtz-Zentrum Geesthacht, Max-Planck-Str. 1, D-21502 Geesthacht, Germany

E-mail: mariath@fys.ku.dk

Received 13 April 2012, in final form 15 August 2012
Published 12 October 2012
Online at stacks.iop.org/PMB/57/7191

Abstract
We report how the three-dimensional structure of subcutaneous injections of soluble insulin can be visualized by x-ray computed tomography using an iodine based contrast agent. The injections investigated are performed *ex vivo* in porcine adipose tissue. Full tomography scans carried out at a laboratory x-ray source with a total acquisition time of about 1 min yield CT-images with an effective pixel size of $109 \times 109\ \mu m^2$. The depots are segmented using a modified Chan–Vese algorithm and we are able to observe differences in the shape of the injection depot and the position of the depot in the skin among equally performed injections. To overcome the beam hardening artefacts, which affect the quantitative prediction of the volume injected, we additionally present results concerning the visualization of two injections using synchrotron radiation. The spatial concentration distribution of iodine is calculated to show the dilution of the insulin drug inside the depot. Characterisation of the shape of the depot and the spatial concentration profile of the injected fluid is important knowledge when improving the clinical formulation of an insulin drug, the performance of injection devices and when predicting the effect of the drug through biomedical simulations.

(Some figures may appear in colour only in the online journal)

1. Introduction

In healthy people the blood sugar level is controlled by the release of insulin from the pancreas. Persons with diabetes have insufficient production of insulin and/or a reduced cell response

to insulin. Diabetic patients are treated with insulin injected subcutaneously, since insulin is a polypeptide and will by oral intake be broken down by the gastric acid or enzymes in the intestine. Even though the injections are performed in a similar manner following a detailed procedure, the patients experience large variations in the action of the insulin drug. Therefore the action of insulin drugs after subcutaneous injection has been intensively investigated and it has been shown that the variations are influenced by several factors like, e.g., the subcutaneous blood flow (Lauritzen *et al* 1980), the injection site (Bantle *et al* 1990) and the insulin sensitivity of the cells (Heinemann *et al* 1998, Ziel *et al* 1988). The variabilities observed are both due to the pharmacokinetics (i.e. the absorption of insulin into the blood stream) and pharmacodynamics (i.e. the effect of the insulin on the glucose uptake) of the insulin drug (Heinemann 2002).

The variability of the absorption of insulin from the injection site was first investigated by Moore *et al* (1956) by injecting radioactively labelled insulin both subcutaneous and intramuscular. The absorption rate was measured indirectly by measuring the decay in γ-radiation above the injection site. The pharmacokinetics of insulin drugs has been investigated in several studies using this technique (Binder 1969, Lauritzen *et al* 1980, Kølendorf *et al* 1983, de Meijer *et al* 1990). The absorption of insulin has also been investigated by measuring the elevation of the serum insulin (Galloway *et al* 1981, Berger *et al* 1982). The results of these studies have been summarized in a review by Heinemann (2002) in which he concludes that there is a variability in the absorption kinetics up to 15% intra-individual and up to 30% inter-individual. To our knowledge, the observed variability has not been related to the microscopic structure of the depot.

The microscopic structure of an injection depot is normally visualized by histology, which is a time consuming method and, therefore it is tedious to inspect the three-dimensional (3D) structure of the depot in this way. X-ray tomography offers a high spatial resolution and a measuring time much shorter than the time needed to prepare histology slices. The purpose of our work is to use a laboratory x-ray source and synchrotron radiation to visualize the 3D structure of injection depots on a micrometer scale and from the tomographic reconstructions analyse the shape of the depot and calculate the spatial concentration distribution of the drug in the tissue. For the development of this method we have used injections performed in porcine adipose tissue *ex vivo*, because porcine tissue was easily available and by making the injections *ex vivo* no ethical approval of the experiments were needed. For *ex vivo* injections the tissue sample has no vascular flow, a lower temperature and lower pH than living tissue. These differences are of minor importance during development of the method, but to obtain results with the highest clinical relevance the injections must be performed *in vivo*.

At the laboratory x-ray source it was possible to make fast tomography scans, such that the depot could be visualized just after injection and significant diffusion of the injected fluid during the measuring time was prevented. In that way we avoid freezing the sample, which will cause a deformation of the injection depot. From these tomographic reconstructions we want to investigate how different amounts of injected drug spread in the tissue. The reconstructions obtained using a polychromatic x-ray source will be affected by beam hardening artefacts, which makes a prediction of the spatial concentration distribution of the drug in the tissue uncertain. For a quantitative prediction of the spatial concentration distribution of the drug just after injection, we have visualized two injection depots using synchrotron radiation. From these reconstructions the volume of injection fluid inside the visualized depot has been calculated and compared with the amount injected to evaluate the sensitivity of the method. The spatial concentration distribution calculated from the monochromatic data was used as a reference measurement to evaluate how well the concentration distribution can be predicted from polychromatic data.

2. Materials and methods

To distinguish the injection from the adipose tissue in the radiological images we mixed the insulin drug with the water soluble contrast agent Xenetix 300 based on iobitridol. The mixture contains 30% Xenetix 300 and 70% insulin drug, corresponding to a concentration of 8.4% of iodine. The concentration was chosen as a trade off between good visibility of the depot in the radiological images and smallest possible influence on the insulin drug. Notably, addition of the contrast agent increases the viscosity of the drug and for the dilution used the viscosity was increased by about 50% compared to the pure insulin drug, which has a viscosity of about 1.1 mPa s at 20 °C.

To see if the distribution of the iodine visualized in the tomographic reconstruction represents the distribution of insulin, we made a comparison of an injection depot visualized by histological dyeing and by radiology. A volume of 100 μL was injected into the subcutaneous fat layer at the neck of an anaesthetized pig, which was put down immediately after. A biopsy, including the injection site, was cut out and snap frozen. The sample was cut into 2 mm thick slices and a radiological image was made for each of the slices. The slices were afterwards cut into slices with a thickness of 20 μm and the insulin was dyed. It was not possible to visualize the depot in a 20 μm slice by x-rays, so it was necessary to make the visualization first by radiology for 2 mm thick slices and afterwards cut up the slices for histology.

2.1. Tissue samples

The skin consists of three layers; epidermis, dermis and the subcutis. Below the skin are the bones or muscles. Ideally the insulin injections must be placed in the subcutis, which mainly consists of white adipose tissue, connective tissue, blood and nerve vessels (Agache and Humber 2004). All the investigated injections were performed in porcine adipose tissue *ex vivo*. Pigs are used as research animals for testing the effect of new insulin drugs, because pigs are one of the animals that are physiologically nearest to men. The skin structure, the blood circulation and digestion are very similar for pigs and men (Douglas 1972).

The tissue samples were taken from the neck of the pig, which is the anatomical region often used when injecting insulin drugs into pigs. Just after the pigs were put down, the tissue was cut off, frozen and stored at −20 °C. The tissue was thawed and cut out into pieces of about 2.5×2.5 cm^2 up to 5.0×5.0 cm^2 depending on the volume injected. The injections were made with a standard insulin injection device and the needle has a length of 6 mm and a diameter of 0.25 mm.

At the laboratory x-ray source we have visualized injections of 100, 400 and 700 μL of drug, where 700 μL was the maximum possible with the injection device used. The tissue sample were scanned just after the injection was performed and in total 20 samples were measured.

At the synchrotron radiation facility two injections each of 100 μL were visualized and the same two injections were visualized at the laboratory x-ray source to compare the two techniques. The samples were snap frozen in liquid nitrogen just after the injections were performed and kept frozen during the measurements. The samples were stored at −80 °C for about three weeks between the measurements at the laboratory x-ray source and the synchrotron radiation facility.

2.2. Laboratory x-ray source

We used a laboratory x-ray source with a molybdenum target and the acceleration voltage and current were set to 50 kV and 75 mA, respectively, to give approximately 10^5 counts s^{-1} in each pixel of the detector. To reduce beam hardening artefacts in the reconstructions and avoid the detector from being saturated, the beam was filtered by a 2 mm aluminium filter. The Pilatus 100K detector used in this experiment is a solid state detector with a pixel size of 172 $\times$ 172 μm^2, a fast read out time and high signal-to-noise ratio (Bech *et al* 2008). This setup allows us to carry out a tomography scan with 401 projections in 72 s. For the experiments performed the exposure time was 140 ms per projection and the read out time of the detector was 40 ms. A read out time of 40 ms was necessary for reading out the data from the detector and storing it. The sample was rotated continuously with a frequency of 5.0 $^\circ s^{-1}$, so no additional time for motor movements was added to the total acquisition time. We carried out scans of plastic tubes containing water and found that, except for a slight blurring of the edges of the sample, the continuous rotation gives no artefacts in the reconstructed images. The reconstructions were made with the standard filtered back projection algorithm for parallel beam geometry (Kak and Slaney 1988). The magnification was 1.58$\times$ and the effective pixel size of the detector was 109 $\times$ 109 μm^2. The grey scale values in the reconstructions have been divided by the effective pixel size to give the absorption coefficient in units of cm^{-1}.

2.3. Synchrotron radiation

The visualizations using synchrotron radiation were carried out at the synchrotron radiation facility DESY in Hamburg at the W2 (HARWII-II) beamline. This beamline has an energy range from 20 to 200 keV for imaging (Beckmann *et al* 2007). The tomography scans were carried out at 34 keV, an energy just above the K_α-edge of iodine. The energy was calibrated using two pure foils made of molybdenum and tin, which have the K_α-edge at 20 and 29 keV, respectively. The gap of the wiggler was chosen such that the intensity of the higher harmonics was very low, which was checked by placing an aluminium filter of several millimetres in the beam. No transmission through the aluminium filter was seen for a beam energy of 34 keV, meaning that there was no significant number of high energy photons in the beam. The field of view was 20.9 $\times$ 20.9 mm^2, which means that the scan was carried out as an off-axis tomography scan in three height steps to cover almost the whole tissue sample. The sample size was about 25 $\times$ 25 mm^2 and the tomography scans have 720 projections over 360°. The detector at the beam line is a CCD with a scintillator with a pixel size of 12 $\times$ 12 μm^2. (Beckmann *et al* 2007) . The limited field of view, the small pixel size of the detector and the time for motor movements means that the acquisition time was about 2 h for a full tomography scan at this experimental setup. Prior to reconstructions a 4 $\times$ 4 binning was applied to the projections, giving an effective pixel size of 27 $\times$ 27 μm^2.

2.4. Depot formation in the skin

To analyse the shape of the depots, the injections were segmented from the surrounding tissue by a slightly modified Chan–Vese algorithm (Chan and Vese 2001). To make a proper segmentation, a smearing of the tissue background was included in the algorithm.

To characterize the shapes of the depots, the surfaces have been fitted to an ellipsoidal shape, since an ellipsoid is a simple geometrical shape that describes the extension of the depot. The fits were made in MatLab by finding the minimum volume enclosing ellipsoid, and the fit gives the size of the depot in two perpendicular directions in a horizontal plane, referred

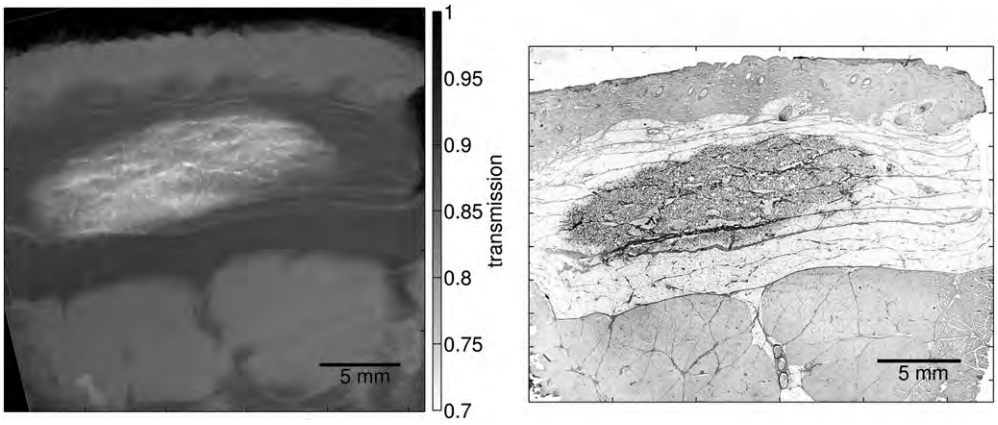

Figure 1. X-ray projection image (left) compared to a histological image (right). The injected volume is 100 μL and the sample thickness is 2 mm and 20 μm for the x-ray projection image and the histological image, respectively. The distribution of the contrast agent and the insulin drug appear almost identical.

to as *a* and *b* where $a \leqslant b$, and one in the vertical direction, referred to as *c* (Moshtagh 2012). The vertical direction is roughly parallel to the needle.

2.5. Spatial concentration distribution of the drug

For the two 100 μL injections measured both at the laboratory x-ray source and the synchrotron radiation facility, the spatial concentration distribution was calculated. For the monochromatic measurements the depots were segmented using a standard threshold segmentation and the polychromatic data were segmented using the Chan–Vese algorithm. The average concentration as a function of the radial distance from the centre of mass of the depot was found, by calculating the average concentration of iodine inside spherical shells centred at the centre of mass and with increasing radii. We have chosen to calculate the spatial concentration profile in this way, as currently used in simulations (Søborg *et al* 2009).

To calculate the absorption coefficient for an iodine dilution as a function of the iodine concentration for the polychromatic data, we have estimated the effective energy of the beam from reconstructions of cylindrical plastic tubes containing water, with diameters of 10 and 20 mm, respectively.

3. Experimental results

3.1. Distribution of the insulin drug and the contrast agent

Figure 1 shows an injection made *in vivo* visualized in a radiological image (left) compared to one of the corresponding histological images (right). The thickness of the sample was 2 mm for radiography and 20 μm for histology. The radiological image shows the distribution of iodine, while the histological image shows the distribution of insulin. The sample has been stretched during the histological preparation, but apart from that the shape and size of the injection depot are almost identical in the two images, confirming that no separation of the insulin drug and the contrast agent occurs.

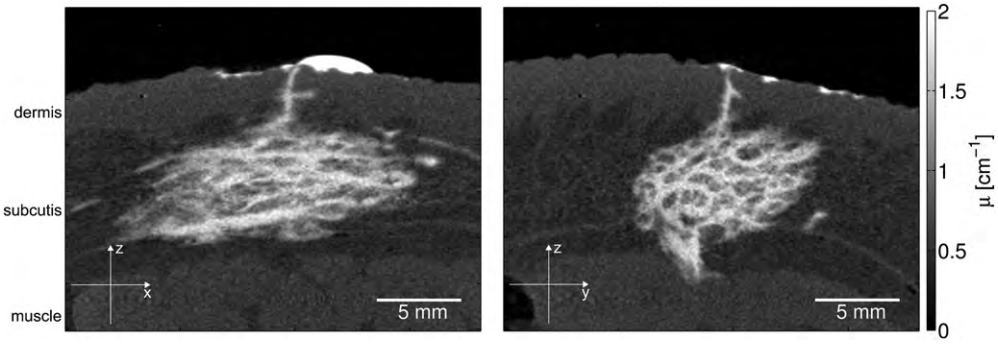

Figure 2. Tomographic reconstruction of an insulin injection cropped along two vertical planes perpendicular to each other. The injected volume is 400 μL. The different layers dermis, subcutis, and the muscles can be identified from the reconstruction. The grey scale is given by the x-ray attenuation coefficient (cm^{-1}).

Figure 3. The 3D structure of two injection depots, with an injected volume of 400 μL, segmented using the Chan–Vese algorithm. The depot shown to the left is the one illustrated in figure 2, and the depot to the right is the one shown in figure 4 (right, bottom).

3.2. Depot formation in the skin

Among the 20 samples measured, we observed large differences in both shape and position of the depot in the skin. Figure 2 shows one example of a tomographic reconstruction of an injection depot, where the injected volume is 400 μL. The figure shows the reconstructed depot cropped along two perpendicular vertical planes both passing through the injection channel. The injection fluid forms a depot in subcutis, and the fluid is pressed back through the injection channel, forming a droplet on the top of the skin, in the following referred to as the back flow. From the tomographic reconstruction it is possible to distinguish the different skin layers dermis, subcutis and the muscles, annotated in figure 2 (left). Epidermis and dermis cannot be distinguished, either because of the resolution in the reconstructions or because of too low a density difference between the two layers.

The depots were segmented and the 3D structure of two depots is shown in figure 3. The surfaces of the depots were fitted to ellipsoidal shapes and figure 4 (left) shows the average size in two directions in the horizontal plane, *a* and *b* (green dotted and blue crossed curve) and in the vertical direction, *c* (red squared curve) as a function of the injected volume. The shape of the enclosing ellipsoids is on average tri-axial, meaning that length of the semi-axis in the horizontal plane (*a* and *b*) is larger than the semi-axis in

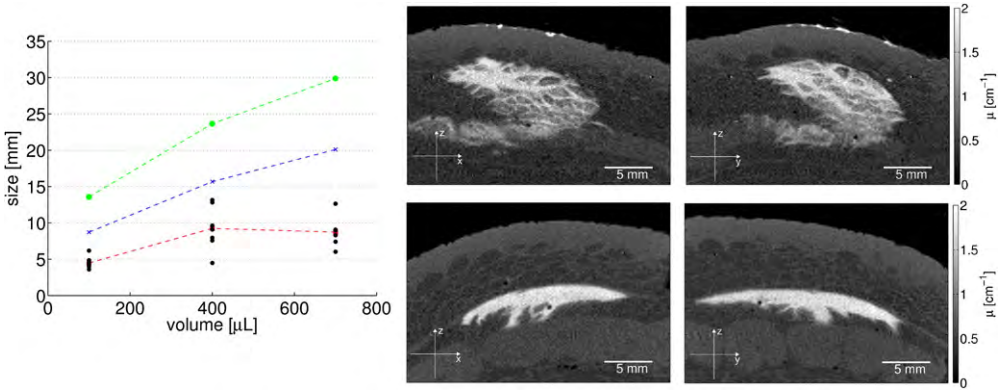

Figure 4. Left: average size of the injection depots in the horizontal plane (blue and green curves) and the vertical direction (red curve). The vertical size of individual injections is shown in order to illustrate the variation among depots (black dots). Right: the tomographic reconstructions of two insulin injections cropped along two vertical planes perpendicular to each other. The injected volume is 700 μL (top) and 400 μL (bottom). The injection of 700 μL exerts a pressure at the skin and a bump is formed at the surface. The injection of 400 μL forms a circular disk in subcutis as fixed in between two layers of connective tissue and no back flow was observed. The grey scale is given by the x-ray attenuation coefficient (cm^{-1}).

the vertical direction (c), $a, b > c$ and that one of the semi-axis in the horizontal plane is bigger the other, $a < b$. Thus, the fluid does not spread isotropically in the subcutis. On average the size of the depots in the horizontal direction increases with increasing volume, but the size in the vertical direction is almost constant when increasing the volume from 400 to 700 μL. The size of the depot in the vertical direction is in some cases limited by the thickness of the subcutaneous fat layer, as shown for the 700 μL injection in figure 4 (right, top). The injection fluid exerts a pressure at the skin and a bump on the skin surface is formed, but the fluid does not spread into the dermis. The injection fluid has spread into a region of the tissue with lower density, either the muscle or an inhomogeneity in the adipose tissue. The subcutaneous fat layer and the muscle are separated by a layer of connective tissue, called the fascia. In the same way the subcutaneous tissue is in some anatomical regions divided into two different layers separated by a membrane of connective tissue (Nakajima *et al* 2004). This may explain why the spread of the injection fluid into this layer is not isotropic but rather appears as if a channel in a membrane has been formed.

There are large variations in the size of the depot among injections of equal volume. Figure 4 (left) shows the size in the vertical direction for the individual injections (black dots). For the injections of 400 μL the average vertical size is about 9 mm, but one injection has a size of only 4.5 mm, shown in figure 4 (right, bottom). In this case the depot has a disk-like shape as fixed in between two layers of connective tissue and there is no back flow.

We have observed that the injection fluid does not spread isotropically in the fat tissue, but in most cases has a preferred direction. Figure 5 (left) shows the ratio a/b for the individual injections (black dots) and the average for each injected volume (red curve). It is seen that the ratio is almost independent of the injected volume, but varies from injection to injection when injecting the same volume. Figure 5 (right) shows two injection depots each with an injected volume of 100 μL. For the depot shown in figure 5 (right, top) the ratio a/b is about 0.5, giving a depot with a

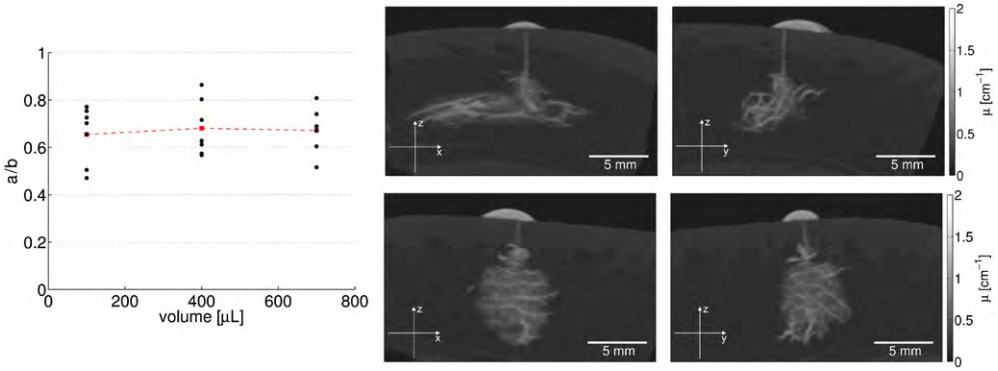

Figure 5. Left: ratio of the size of the depot in the two perpendicular directions in the horizontal plane. The average ratio (red curve) is seen not to depend on the injected volume, but a large variation among depots is observed (black dots). Right: the tomographic reconstructions of two insulin injections cropped along two vertical planes perpendicular to each other, each with an injected volume of 100 μL. One of the depots is cigar-shaped (top) and the other is more spherical (bottom). The grey scale is given by the x-ray attenuation coefficient (cm^{-1}).

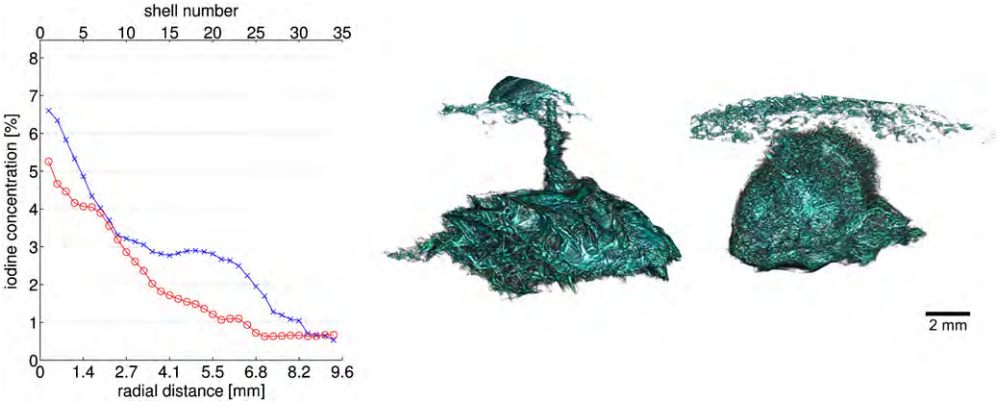

Figure 6. Left: spatial concentration distribution of iodine inside the injection depot for two injections, calculated from monochromatic data. The injected volume is 100 μL for both depots. The distances are the radii of the spherical shells measured from the centre of mass of the depot. Middle and right: 3D structure of injection depots visualized by monochromatic radiation. The spatial concentration distribution represented by the blue crosses and red circles relates to the injection depot in the middle and to the right respectively.

cigar shape, while the depot shown in figure 5 (right, bottom) is more spherical with $a/b = 0.7$.

3.3. Spatial concentration distribution of the drug

Here the spatial concentration distribution of the insulin drug calculated from monochromatic and polychromatic data will be compared. The 3D structures of two injections, visualized using both the x-ray tube and synchrotron radiation, are shown in figure 6 (middle and right). The reconstructions shown are for the monochromatic data and the depots are segmented by

threshold segmentation. The threshold was set to 0.51 cm^{-1}, which corresponds to an iodine concentration of 0.4% to make a proper segmentation of the depot.

The average concentrations as a function of distance from the centre of mass of the depot are illustrated in figure 6 (left). The radii of the spherical shells are given at the horizontal axis on the bottom and the corresponding shell number is given on the horizontal axis on the top. The average concentration of iodine decreases strongly with increasing distance from the centre for both depots. At a radial distance of about 2 mm the concentration is about half of the concentration of the drug injected (8.4% of iodine). We note that the concentration profile varies considerably among injections.

For these injections it was possible to retrieve 59 μL (red circles) and 87 μL (blue crosses) out of the 100 μL injected. Since only concentrations down to 0.4% can be separated from the adipose tissue the most diluted injection fluid will be lost and because the injected fluid is more diluted for one of the depots (red circles) than for the other (blue crosses) a larger amount of the drug will be lost for that injection. It should be noted that the back flow has not been included in these calculations, since the top part of the skin was not fully covered in the tomography scan in order to reduce the measuring time. Therefore the total volume calculated will be smaller than the amount injected even if it had been possible to resolve the total amount of injection fluid in the depot.

To estimate the spatial concentration distribution from the polychromatic data, we have calculated the effective energy of the x-ray beam from measurements of cylindrical plastic tubes containing water. The average reconstructed absorption coefficient for water is 0.69 and 0.60 cm^{-1} for the plastic tube with a diameter of 10 and 20 mm, respectively, corresponding to an effective energy of 21.7 and 23.3 keV. The effective energy increases with increasing size of the sample due to beam hardening.

Figure 7 shows the spatial concentration distribution for the two depots at an effective energy of 21.7 keV (red squares) and 23.3 keV (blue crosses) compared to the spatial concentration distribution calculated from monochromatic data (black diamonds). The overall shape of the concentration profile for the polychromatic data is comparable to that obtained for the monochromatic data. However for the depot shown in figure 7 (left) the concentration increases at a radial distance of about 4 mm from the centre for the polychromatic data, while for the monochromatic data the concentration is more constant. For the depot shown in figure 7 (right) the concentration decreases as a function of radial distance from the centre for both the polychromatic and monochromatic data, but the concentration decreases more slowly when calculated from polychromatic data.

The segmented depot is smaller for the polychromatic data than for the monochromatic data, as seen by the smaller radial spreading in figure 7, because the reconstructions obtained using the synchrotron radiation have a higher signal to noise ratio and better contrast between the depot and the tissue compared to the polychromatic data. Therefore lower concentrations of iodine can be separated from the tissue for the monochromatic data than for the polychromatic data.

The concentrations calculated from polychromatic data increase with increasing effective energy and the variation in the reconstructed absorption coefficient for the polychromatic data is both due to a dilution of the drug and the cupping effect. We have measured plastic tubes with a diameter of 10 mm containing a homogeneous dilution of 30% Xenetix 300 and 70% insulin drug (8.4 % iodine), corresponding to the concentration of the injected fluid, and 10% Xenetix 300 and 90% insulin drug (2.9% iodine), which approximates the average concentration in the depots, as calculated from monochromatic data.

For an iodine concentration of 8.4% the absorption coefficient decreases by about 0.4 cm^{-1} from the edge to the centre of the cylinder and for an iodine concentration of 2.9% the

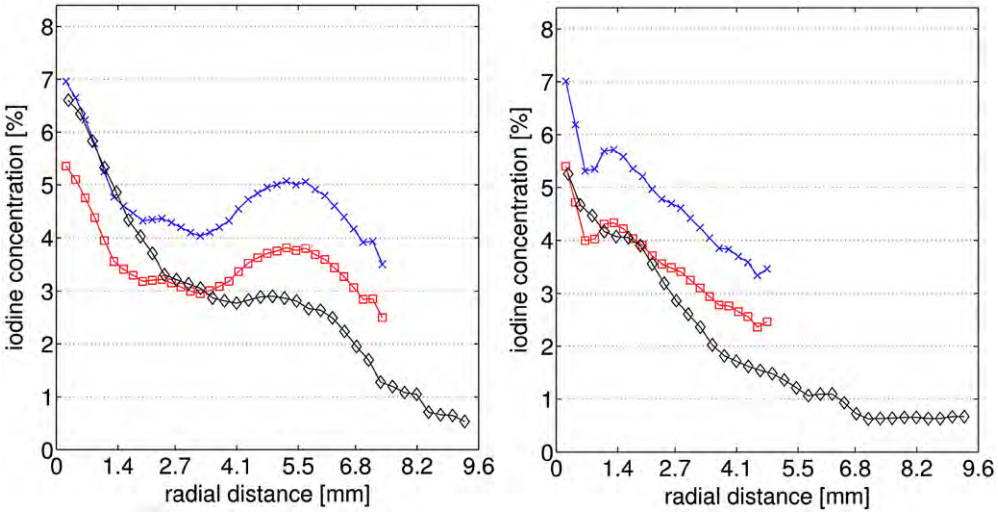

Figure 7. Spatial concentration distribution of iodine inside the injection depot for two injections calculated from both polychromatic and monochromatic data. The profile shown to the left is for the depot illustrated in figure 6 (middle) and the profile shown to the left is for the depot illustrated in figure 6 (right). For the polychromatic data the concentration profile is calculated for an effective energy of 21.7 keV (red squares) and 23.3 keV (blue crosses). The monochromatic data (black diamonds) are shown for comparison.

absorption coefficient decreases by about 0.1 cm^{-1} from the edge to the centre. Thus calculating the spatial concentration distribution using a fixed effective energy, the concentration of iodine in the centre pixels will be underestimated compared to the concentration of iodine in the pixels at the edge of the depot. Because of the cupping effect the concentration decreases by about 3–3.5% from the centre to the edge of the depot for the polychromatic data, while for the monochromatic data, the concentration decreases by 4–5% over the same distance.

4. Discussion

The advantage of performing a fast tomography scan is that the injection fluid will not diffuse significantly during the time of measuring and therefore we can avoid freezing the samples. By measuring on injections performed *ex vivo* and unfrozen we have no deformation of the depot. For identical injection conditions and in neck tissue from pigs, the presented depots show large differences in shape. The presented method makes it possible to investigate a large number of samples due to the short measuring time at the laboratory x-ray source and is therefore suitable for systematic investigations of how the depot is affected by the skin structure, the injection technique and the drug injected.

Information about the spatial concentration distribution of iodine can be obtained from the measurements at the synchrotron radiation facility, but for polychromatic data the spatial concentration profile calculated is less accurate because of beam hardening artefacts. We have observed that the effective energy of the polychromatic beam depends on the geometry of the sample, even for a low absorbing material such as water. Without making any correction for beam hardening artefacts, the overall shapes of the spatial concentration profile for different depots can be compared, but in order to obtain an accurate prediction of the spatial concentration distribution from polychromatic data the beam hardening artefacts must be

estimated. We are working on developing a virtual experiment of the experimental setup at the laboratory x-ray source from which the effective energy inside the tissue sample and the cupping effects can be estimated. Imaging using synchrotron radiation is relatively inaccessible since it is restricted to take place at large scale radiation facilities, but laboratory x-ray source and conventional μCT-scanner systems are widely available. Therefore improving the calculation of the concentration distribution from polychromatic data makes it possible to implement this method in the daily research and development of diabetic treatments.

The monochromatic data have a higher signal to noise ratio and better contrast between the injection fluid and the tissue and therefore a larger fraction of the injected volume could be retrieved. For the polychromatic data the contrast can be optimized by changing the acceleration voltage and filtering the x-ray beam. A decrease in the acceleration voltage and additional filtering of the beam will lower the flux meaning that the measuring time must be extended in order to obtain the same signal to noise ratio. Extending the measuring time means that the sample must be frozen to avoid diffusion of the drug.

The injections presented were made *ex vivo*, but this method can equally well be used for injections performed *in vivo*. When performing injections in pig tissue *in vivo*, the pig must be put down immediately after and the tissue sample including the injection site must be cut out and snap frozen. The freezing causes a deformation of the tissue and thereby also of the depot, but this deformation can be evaluated for injection performed *ex vivo* by measuring the same sample before and after freezing. The main changes in the adipose tissue after slaughtering is a decrease in temperature, the absence of blood and vascular flow and a decrease in pH. The decrease in temperature from body temperature to about 20°C causes the stiffness of the tissue to increase (Geerligs *et al* 2008). To get results with the highest clinical relevance, the injections must be made *in vivo*.

One approach to make visualizations of insulin injections *in vivo* in humans is high-resolution peripheral quantitative CT (HR-pQCT). It has been shown that to cover a region of 9 mm of an arm or a leg the scan time is about 3 min at a resolution of 82 μm (Boutroy *et al* 2005). We find that a standard insulin injection of 400 μL has a size of the order of 25 mm, meaning that the scan time will be extended. In order to use HR-pQCT to visualize insulin injection depots *in vivo* it must be considered how the acquisition time can be limited such that diffusion of the drug during the scan can be avoided. Since HR-pQCT is based on a polychromatic x-ray source like μCT, so beam hardening artefacts must be taken into account when evaluating the spatial concentration distribution of the drug (Sekhon *et al* 2009).

Both the shape of the depot and the spatial concentration profile inside the depot can be related to the variability in the insulin absorption rate through simulations of the pharmacokinetics of the insulin drug. In the models of the absorption kinetics of insulin simulated so far it has been assumed that the shape of the depot is spherical and that the concentration distribution is constant over the injection depot just after injection (Søborg *et al* 2009). Our experiments show that this approximation is too simple and is therefore an important input to improve the reliability of the biomedical simulations.

5. Conclusion

We have shown how the 3D structure of subcutaneous injections of soluble insulin can be visualized by x-ray absorption tomography. The setup at the rotating anode allows us to perform a full tomography scan in about 1 min. Due to the short measuring time and optimized segmentation methods it is possible to evaluate both the position of the depot in the tissue and the shape of the depot for a large number of samples. Thereby knowledge about the variability in the size and the shape of depots can be obtained. The investigated injections

were all performed *ex vivo* with the same injection device, the same kind of needle and the tissue samples were all taken from the same anatomical region of the pigs. In spite of these similarities the reconstructed depots showed large differences in shape. It has been shown that the injection fluid does not spread isotropically in the subcutaneous fat layer. The extent of the depot in the vertical direction is in some cases limited by the thickness of the subcutis and we have observed that the injection fluid can exert a pressure on dermis and spread into lower layers of the tissue. Since the structure of the skin and the blood flow differ for different layers of the skin this might affect the pharmacokinetics of the drug.

We have also shown that a quantitative measure of the spatial concentration distribution of the injected fluid inside the depot can be obtained from tomographic reconstructions when using monochromatic x-ray. In order to predict the spatial concentration distribution accurately from polychromatic data, beam hardening must be taken into account. A correction for beam hardening artefacts will make the calculation of the concentration profile from polychromatic data more accurate and the reconstructions obtained using synchrotron radiation must be used as references when developing such a correction scheme.

Identifying the parameters affecting the depot formation, and linking the changes in the shape, position and spatial concentration profile of the depot to the uptake of the drug is a crucial step on the way to a better-controlled treatment of diabetes.

Acknowledgments

We acknowledge Jonas Kildegaard and Susanne Primdahl from the Imaging Team at Novo Nordisk A/S, Måløv, for providing the tissue samples and the histological dyeing of the injections and Bente Eyving and Dan Nørtoft Sørensen from Experiments at Novo Nordisk A/S, Hillerød, for discussions about the measurements at the laboratory x-ray source. We want to thank Professor Mads Nielsen and Assistant Professor Francois Lauze for discussions about and implementation of the segmentation algorithms. For assistance with the experiments performed at the synchrotron radiation facility DESY we acknowledge Hilmar Burmester. This work has been financially supported by the Center of Industrial Application of CT-scanning (CIA-CT) and DanScatt.

References

Agache P and Humber P 2004 *Measuring the Skin: Non-invasive Investigation, Physiology, Normal Constants* ed M Philipp (Berlin: Springer) pp 401–28

Bantle J P, Weber M S, Rao S M S, Chattopadhyay M K and Robertson R P 1990 Rotation of the anatomic regions used for insulin injections and day-to-day variability of plasma glucose in type 1 diabetic subjects *J. Am. Med. Assoc.* **263** 1802–6

Bech M, Bunk O, Kraft P, Brönnimann C, Eikenberry E F and Pfeiffer F 2008 X-ray imaging with the PILATUS 100k detector *Appl. Radiat. Isot.* **66** 474–8

Beckmann F, Dose T, Lippmann T, Martins R V and Schreyer A 2007 The new materials science beamline HARWI II at DESY *Proc. 9th Int. Conf. on Synchroton Radiation Instumentation; AIP Conf Proc.* **879** 746–9

Berger M, Cüpper H J, Herger H, Jîrgens V and Berchtold P 1982 Absorption kinetics and biologic effects of subcutaneously injected insulin preparations *Diabetes Care* **5** 77–91

Binder C 1969 Absorption of injected insulin. A clinical-pharmacological study *Acta Pharmacol. Toxicol.* **27** 1–87

Boutroy S, Bouxsein M L, Munoz F and Delmas P D 2005 *In vivo* assessment of trabecular bone microarchitecture by high-resolution peripheral quantitative computed tomography *J. Clin. Endocrinol. Metab.* **90** 6508–15

Chan T F and Vese L A 2001 Active contours without edges *IEEE Trans. Image Process.* **10** 266–77

de Meijer P H, Lutterman J A, van Lier H J and vant Laar A 1990 The variability of the absorption of subcutaneously injected insulin: effect of injection technique and relation with brittleness *Diabet. Med.* **7** 499–505

Douglas W R 1972 Of pigs and men and research *Origins Life Evol. Biospheres* **3** 226–34

Galloway J A, Spradlin C T, Nelson R L, Wentworth S M, Davidson J A and Swarner J L 1981 Factors influencing the absorption, serum insulin concentration, and blood glucose responses after injections of regular insulin and various insulin mixtures *Diabetes Care* **4** 366–76

Geerligs M, Peters G W M, Ackermans P A J, Oomens C W J and Baaijens F P F 2008 Linear viscoelastic behavior of subcutaneous adipose tissue *Biorheology* **45** 677–88

Heinemann L 2002 Variability of insulin absorption and insulin Action *Diabetes Technol. Ther.* **4** 673–82

Heinemann L, Weyer C, Rauhaus M, Heinrichs J and Heise T 1998 Variability of the metabolic effect of soluble insulin and the rapid acting insulin analogue aspart *Diabetes Care* **21** 1910–4

Kak A C and Slaney M 1988 *Principles of Computerized Tomography Imaging* (Piscataway, NJ: IEEE) pp 49–112 http://www.slaney.org/pct/pct-toc.html

Kølendorf K, Bojsen J and Deckert T 1983 Clinical factors influencing the absorption of ^{125}I-NPH insulin in diabetic patients *Horm. Metab. Res.* **15** 274–8

Lauritzen T, Binder C and Faber O K 1980 Importance of insulin absorption, subcutaneous blood flow, and residual beta-cell function in insulin therapy *Acta Paediatr.* **69** 81–4

Lauritzen T, Faber O K and Binder C 1979 Variation of ^{125}I-insulin absorption and blood glucose concentration *Diabetologia* **17** 291–5

Moore E W, Mitchell M L and Chalmers T C 1956 Variability in absorption of insulin-I-131 in normal and diabetic subjects after subcutaneous and intramuscular injection *J. Clin. Invest.* **38** 1222–7

Moshtagh N 2012 Minimum volume enclosing ellipsoids http://www.mathworks.se/matlabcentral/

Nakajima H, Imanishi N, Minabe T, Kishi K and Aiso S 2004 Anatomical study of subcutaneous adipofascial tissue: a concept of the protective adipofascial system (PAFS) and lubricant adipofascial system (LAFS) *Scand. J. Plast. Reconstr. Surg. Hand Surg.* **38** 261–6

Sekhon K, Kazakia G J, Burghardt A J, Hermannsson B and Majumdar S 2009 Accuracy of volumetric bone mineral density measurement in high-resolution peripheral quantitative computed tomography *Bone* **45** 473–9

Søborg T, Rasmussen C H, Mosekilde E and Coldin-Jørgensen M 2009 Absorption kinetics of insulin after subcutaneous administration *Eur. J. Pharm. Sci.* **36** 78–90

Ziel F H, Davidson M B, Harris M D and Rosenberg C S 1988 The variability in the action of unmodified insulin is more dependent on changes in tissue insulin sensitivity than on insulin absorption *Diabet. Med.* **5** 662–6

Paper IV

M. Thomsen, C.H. Rasmussen, H.H.F. Refsgaard, K.M. Pedersen, R.K. Kirk, M. Poulsen, R. Feidenhans'l.
Spatial distribution of soluble insulin in pig subcutaneous tissue: Effect of needle length, injection speed and injected volume.
European Journal of Pharmaceutical Science (submitted for internal review in Novo Nordisk A/S).

Spatial distribution of soluble insulin in pig subcutaneous tissue: Effect of needle length, injection speed and injected volume

Maria Thomsen[a,b,*], Christian Hove Rasmussen[a], Hanne H.F. Refsgaard[a], Karen-Margrethe Pedersen[a], Rikke K. Kirk[a], Mette Poulsen[a], Robert Feidenhans'l[b]

[a]*Novo Nordisk A/S, Novo Allé, DK-2880 Bagsværd, Denmark*
[b]*Niels Bohr Institute, University of Copenhagen, Blegdamvej, DK-2100 Copenhagen, Denmark*

Abstract

The distribution of a soluble insulin formulation was visualized in pig subcutaneous tissue and the spatial drug distribution was quantified in 3-dimensions using x-ray computed tomography. Pig subcutaneous tissue has very distinct tissue layers, which could be separated in the tomographic reconstruction and the amount of drug in each tissue class was quantified. With a scan time of about 45 min per sample, and a semi-automatic analysis pipeline it was possible to analyse differences in the spatial drug distribution between several similar injections.

We have studied how the drug distribution was effected by needle length, injection speed and injected volume. An injected volume of 0.1 mL and injection depth of 8 mm gave about 50% risk of partly intramuscular injections. Using a 5 mm needle resulted purely in subcutaneous injections with minor differences in the spatial drug distribution between injections. Varying the injection speed from 25 μL/s up to 300 μL/s gave no changes in the drug concentration distribution. Increasing the injected volume from 0.1 mL to 1 mL did not increase the intramuscular volume fraction, but gave a significantly higher volume faction placed in the subcutaneous fascia layer.

The method presented gives novel insight into subcutaneous injections of soluble insulin drugs and can be used to optimize the injection technique for subcutaneous drug administration.

Keywords: subcutaneous injections, drug distribution, x-ray computed tomography, insulin aspart

1. Introduction

Insulin dependent diabetic patients perform several subcutaneous injections daily in order to keep their blood glucose level within specific physiological limits. The injected insulin forms a bolus in the subcutaneous tissue from where it is absorbed into the blood stream. Large inter- and intra-patient variability is observed in the metabolic effect among similar injections for all kinds of insulin formulations (Heinemann, 2002; Gin and Hanaire-Broutin, 2005; Guerci and Sauvanet, 2005). The effect of an insulin bolus injection depends on several factors and some of those are related directly to the injection technique and the injection site (Ogston-Tuck, 2014). The absorption time have been shown to depend on the injection site and depth (Frid and Linde, 1992; Rave et al., 1998; Karges et al., 2005; Gupta et al., 2011), the local subcutaneous blood flow (Vora et al., 1993) and skin temperature (Cengiz et al., 2014; Pfützner et al., 2015). Furthermore the absorption is effected by the injection technique (Mader et al., 2012; Engwerda et al., 2013).

Insulin Aspart (IAsp) is a fast-acting insulin analogue with a single amino acid substitution and has a reduced tendency for the insulin monomers to self-associate into dimers (Brange et al., 1988). Fast acting insulin drugs have a higher elimination rate from the blood stream than the absorption rate from the injection site, meaning that the metabolic effect is controlled by the absorption from the injection site (Rasmussen et al., 2013). Therefore the drug distribution and concentration at the injection site is important for the time action of the insulin injection.

The absorption process has been evaluated directly by radioactive labelling of the insulin molecule. In these studies the absorption rate is estimated by measuring the remaining radioactivity at the injection site as function of time (Lauritzen et al., 1980; Vora et al., 1993).

In vivo ultra sound measurements have been used to study the injection depth. The insulin can be visualized directly (Polak et al., 1996) or presented by an air injection (Hofman et al., 2010). Insulin mixed with a food colorants have been visualized for *ex vivo* injections in adipose pig tissue (Jockel et al., 2013). In this study the tissue biopsies including the injection site were snap frozen and cut into thin sections. The drug distribution was visualized in each slice and the slices stacked to form the 3-dimensional (3D) structure.

In this study we propose a method to visualize and quantify the spatial drug distribution at micrometer resolution. The method is based on x-ray computed tomography (μCT) (Thomsen et al., 2012). The insulin drug is mixed with an iodine based contrast agent, to be distinguishable from the adipose tissue in the radiographic images. A scan time of the order 1 hour per injection and a semi-automatic analysis pipeline, make it possi-

*Tel: 4442 3501, mobile: +453079 5050
Email address: mtmx@novonordisk.com (Maria Thomsen)

ble to investigate the variability in the drug distribution among several similar injections. The injections presented were performed *ex vivo* in subcutaneous pig tissue. This approach allowed us to include injection parameters that are not yet appropriate for preclinical testing and make several injections in tissue from the same animal.

We present a visualization of the injection bolus for different injections depths, speeds and volumes. From the tomographic reconstructions we were able to quantify the spatial drug distribution, obtain the injection depth, and estimate the drug distribution among the different tissue layers; dermis, subcutis and the muscle tissue. The variabilities in the drug distribution is discussed in relation to the pharmacokinetic variability.

2. Materials and Methods

2.1. Ethical approval

The study was performed in LYD (The crossbred Landrace & Yorkshire & Duroc) pigs after the animals were sacrificed. Before this study the pigs had been included in investigations approved by the Danish Animal Experiment Inspectorate.

2.2. Sample preparation

The injections were performed with an motor driving injection device where the injection speed and volume were digitally controlled. 30G 8 mm needles were used, and the injection depths were adjusted by needle stops. The study of the spatial drug distribution was divided into two part. In part 1 we study the effected of the needle length (group 1-2). In part 2 we studied the effect of the injection speed (group 3-5) and injected volume (group 6-7). The groups are listed in table 1.

The injections were placed at the neck of the pig, shown in Figure 1. The injections sites were examined with ultrasound, to localize the region with the thickest subcutaneous layer and no underlying muscle tissue.

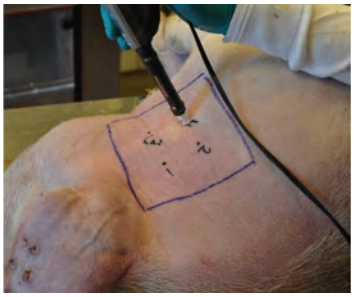

Figure 1: Injection site at the neck region of the LYD pig.

Sixteen injections were performed using a 5 mm (group 1) and 8 mm (group 2) needle, respectively. Eight pigs were used for this part, four pigs for each group. For group 1, where the injections were performed with a 5 mm needle, the injection bolus were placed very close to the junction between subcutis and dermis, and therefore a 6 mm needle was chosen for group 3-7 to place the injections as central in subcutis as possible.

Eight injections of 0.1 mL were performed with an injection speed at 25 µL/s, 100 µL/s and 300 µL/s, respectively (group 3-5 in Table 1). Furthermore eight injections at 1 mL were performed at an injection speed of 25 µL/s and 100 µL/s, respectively (group 6-7 in Table 1). Six pigs were used for this part and the injections were randomized among the pigs. One injection of 0.1 mL (group 5) and one of 1 mL (group 6) was excluded as a part of the injection was missing after cutting out the tissue biopsy.

The injections were performed and the tissue biopsies were cut out and snap frozen in 2-Methylbutane and dry ice. All done within 15 minutes after termination of the pig. The tissue samples were stored at -80°C until the CT-scans were performed. The tissue samples were about 30×30×30 mm^3 with one injection in each sample.

The contrast in the CT-reconstructions given by the local x-ray attenuation length in the sample. The x-ray attenuation length depends on the atomic number and the mass density, so in order to distinguish the injection from the surrounding tissue in the CT-reconstructions the soluble fast acting insulin drug was mixed with x-ray contrast agent Xenetix300 based on iobitridol. The mixture have an iobitridol concentration of 90 mg/mL (30% Xenetix300), giving an increased density (1.07 g/cm^2), but also increased viscosity (1.1 mPa·s at 20°C). Xenetix300 is a nonionic, low-osmolality contrast agent, which distributes in the interstitial space and not penetrates into cells (Dencausse et al., 1995).

2.3. Histological staining

In order to make as close to an one to one comparison of the insulin and iodine distribution as possible, ten of the tissue samples was trimmed into 2 mm slabs and visualized by X-ray radiography. Afterwards one slice from each of the samples was cryo fixed and 10 µm sections were cut and placed on SuperFrost+glas slides. The slices were fixated in 10% buffered formalin, blocked with Dual Peroxidase Blocking (DAKO, DK), pre-incubation with 5% skim milk in TBS for 30 minutes and incubated for 1 hour with the primary anti-insulin antibody (mAb HUI18, 2µg/ml). The staining was visualized using Envision Mouse system (DAKO, DK) and DAB+ for 20 minutes and counter-stained with haematoxylin. Between steps the sections were rinsed in TBS-T and lastly the sections were rehydrated and mounted with Pertex.

2.4. X-ray computed tomography

The tomography scans were preformed on the CT-scanner, XRadia Versa VRM-410 (ZEISS), at the Imaging Industrial Portal, the Technical University of Denmark. The acceleration voltage and current were set to 80 kV and 125 µA, respectively. A low absorbing polymer LE3 filter was placed in front of the beam slit to improve image contrast and reduce beam hardening artefacts. The CT-scans had 401 projections with an exposure time of 5 s per projections, giving a total scan time of about 45 minutes, including motor movements. The reconstructions had an effective voxel size of 50 µm and resolution at 120 µm. The tissue samples were kept frozen at about -15°C during the scans,

Group	Number of injections	Needle length [mm]	Volume [mL]	Speed [μL/s]
1	16	5	0.1	100
2	16	8	0.1	100
3	8	6	0.1	25
4	8	6	0.1	100
5	8	5	0.1	300
6	8	5	1	25
7	8	6	1	100

Table 1: Study parameters for the seven study groups. Group 3-4 and 6-7 were pooled in the analysis of small and large injection volumes.

by having them placed in a cooling chamber made of extruded polystyrene foam (XPS) and cooled with a Peltier elements.

2.5. Segmentation

The tomographic reconstructions can be considered to consist of four classes, which are distinguishable by their differences in the x-ray attenuation length. The four classes are air, dermis and muscle tissue, the subcutaneous fat layer, and the contrast agent. The muscle tissue and dermis are indistinguishable in the reconstructions. The grey scale values for each class overlap, so a simple threshold segmentation is insufficient. We use the Markov Random Field Algorithm (Geman and Geman, 1984; Li, 2009), which is robust against image noise, and the segmentation is not influenced by small local variations in tissue density. The segmentations gives a labelled image, with one label for each class.

After segmentation the injection depot was digitally removed. The boundary between dermis and subcutis, and subcutis and the muscle tissue was found semi-automatically. Planes were placed manually at the boundaries in the segmented image, and the points at the planes were moved iteratively until they reach the boundary. The points missing, where the injection bolus were placed, were interpolated by fitting the points at the boundary to a smooth surface.

Let $\mathcal{I}$ be the set of points segmented as the injection bolus. For $\mathbf{x}_i \in \mathcal{I}$ is the subset of points in the muscular tissue layers given as

$$M = \{\mathbf{x}_i \mid \forall \mathbf{x}_i \in \mathcal{I} : d_M(\mathbf{x}_i) < d_M(\mathbf{x}_i + \mathbf{n}_M)\} \tag{1}$$

where $d_M(\mathbf{y}_i)$ gives the shortest Euclidean distance from the point $\mathbf{y}_i$ to the boundary between subcutis and the muscle, and $\mathbf{n}_M$ is the normal vector to the plane pointing from the muscle to the subcutaneous layer.

The points in the dermal layer are found in a similar way, and the remaining points are assigned to belong to subcutis.

2.6. Density calibration

The grey scale value in each segmented image voxel was related to iodine concentration through a series of calibration measurements. The calibration phantom used was a 30×30×30 mm^3 cube made of Polymethyl Methacrylate (PMMA), with a density of 1.19 g/cm^2. PMMA was used as a soft tissue equivalent (Zou et al., 2011; Chantler, 2000). A step-weight was drilled in the center of the cube, with a diameter of 12 mm at the top and 4 mm at the bottom. The step weight was filled with mixtures of IAsp and Xenetix300, where the Xenetix300 concentration was varied from 5% to 30%. The grey scale value in the tomographic reconstruction was calculated for each of the concentrations and the relation was fitted to a linear function. No severe cubbing artefacts were observed for the calibration measurements, and therefore no corrections for beam hardening artefacts were made. The segmentation gave a cut off at a drug concentration of about 2.5% of drug (0.2% of iodine), which corresponds to the grey scale value of the subcutaneous tissue plus 2 times its standard deviation. It means that drug, which have become more diluted than that will be lost in the segmentation.

Each voxel in the reconstructed image is an average over a volume of about $(120\ \mu m)^3$, set by the image resolution. The individual fat cell have a size of about 50-100 μm (Hausman and Martin, 1981), and can not be seen in the images. Therefore reflects the calculated average concentration distribution both of the tissue porosity and drug distribution. Since the porosity is lower in the muscle tissue, than in the adipose tissue, a lower average concentration was seen in the muscle.

2.7. Spatial drug distribution

The tissue biopsies were cut out after the injections were performed. This caused the tissue to subtract, and the freezing also expanded the sample. It means that the tissue layer thickness measured in the tomographic reconstructions were larger than the thickness measured *in vivo*. To compare the injection depth the boundary between dermis and subcutis was taken as the reference plane. The injection depth was defined as the distance between this plane, and a parallel plane, that divides the injection bolus in half.

The texture of the injection bolus was used as a measure for the overall variation in the drug distributions. The texture index was calculated as

$$T = \frac{\sum_i \nabla I_i}{V} \tag{2}$$

where ∇I_i is the image gradient in each voxel, V is the total segmented volume. It means the more inhomogeneous the

drug distribution the higher is the texture measure. The texture features were extracted using learning dictionaries (Dahl and Larsen, 2011).

The overall spatial drug distributions were represented by the image histograms (H_i). The difference between histograms in each of the study groups were quantified in term of the χ^2 difference

$$\chi^2 = \sum_i^M \frac{2(H_i + \tilde{H}_i)^2}{H_i - \tilde{H}_i} \quad (3)$$

where H_i is the histogram for one injection with M-bins, and $\tilde{H}_i$ is the mean histogram for the group.

2.8. Statistical analysis

Data from the two parts in the study were analysed by analysis of variance (ANOVA).
Part 1: Histogram difference (χ^2), texture index (T), and injection depth were analysed with the individual pig and needle length as factors.
Part 2: Average concentration, texture index, and injection depth were analysed with the individual pig, injected volume and injection speed as factors.

3. Results

3.1. Comparison with histology

Figure 2 shows a histological image (A) and a radiographic image (B) of a single slice of a 1 mL injection. The periphery of the injection bolus as seen in the histological image is marked in the radiographic image as a red curve. A part from a slight deformation, very good agreement between the IAsp and Xenetix300 distribution was seen, and based on these results we assume that the Xenetix300 distribution represent the insulin distribution well.

3.2. Visualization by μCT

Figure 3 shows examples of different depots for 0.1 mL injections performed with a 8 mm needle (group 2). It is seen that the different skin layers, dermis, subcutis and muscle tissue, can be distinguished in the tomographic reconstruction. One injection placed in the muscle tissue (A), one in the lower subcutis beneath the fascia layer (red arrow) (B), and one placed in the fascia between subcutis and the muscle (C). The color scale present the average concentration of the injected fluid in each voxel. The grey scale is proportional to the x-ray attenuation length, where a lighter color means a higher attenuation length.

Both the spatial drug distribution and shape were seen to vary from injection to injection. The shape have been characterized by a number of parameters; the variation from a spherical shape, the elongation of the bolus in the plane parallel to the skin surface (xy-plane), and the hight in $z-$direction. All parameters had a CV of the order 20-50% (data not shown).

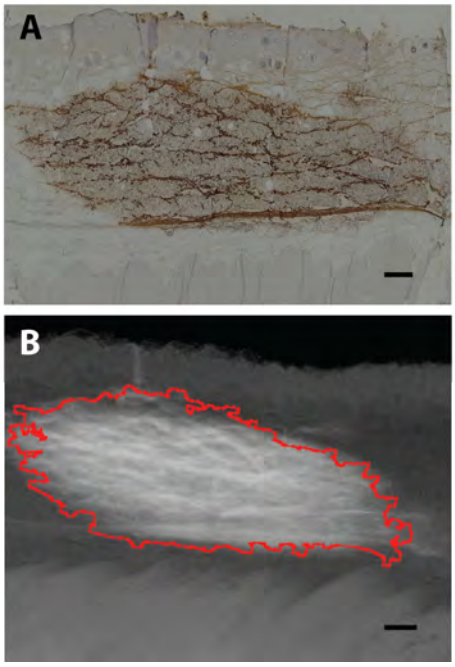

Figure 2: Comparison between histology image, where the insulin was stained by HUI18 (A) and radiographic image of the iodine distribution (B) for a 1 mL injections.The boarder of the insulin distribution found in (A) is shown as in (B) (red curve). The scalebar is 2 mm.

3.3. Spatial drug distribution

The injection channel and the drug at the skin surface (the backflow) was removed digitally and only the injection bolus analysed (see Figure 3 (C)).

The total volume was calculated as a weighted sum over all the voxels in the injection bolus. In the injection bolus 70-95% of the injected drug volume could be recovered from the tomographic reconstruction. The variations did not correlate with the individual animal.

3.3.1. Effect of needle length

Figure 4 (top) shows an image histogram of the segmented voxels for group 1 (5 mm needle) (blue) and group 2 (8 mm needle) (red). A similar drug distribution was seen for the injections performed with the 5 mm needle, compared to injections performed with the 8 mm needle, reflected by a lower variation in χ^2 (Table 2). The drug distribution also became more homogeneous when using a 5 mm needle, compared to the 8 mm needle, seen from the texture index listed in Table 2.

For group 2 (8 mm needle) some of the histograms had a peak at low concentrations. This corresponds to the volume fraction placed intramuscular, shown in Figure 3 (A). Two injections had a peak at an average drug concentration about 80%. Both of these injections were placed in the lower subcutaneous fat layer, shown in Figure 3 (B). The injected drug was not seen to accumulated around the injection site in the same way for all injections placed in this layer.

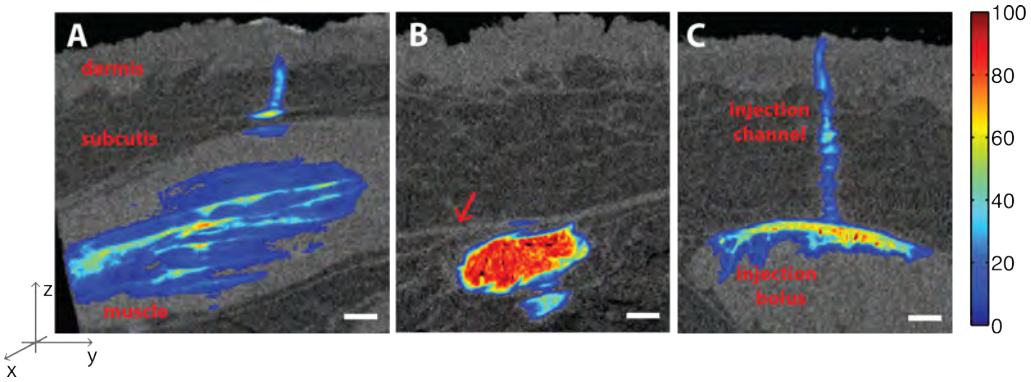

Figure 3: Three examples of injections performed with a 8 mm needle. The tissue layers can be distinguished by their density difference. One injection is placed totally inter-muscular (A), in the lower subcutaneous fat layer (B) beneath the fascia in subcutis (red arrow), and in the fascia between the muscle tissue and subcutis (C). The scalebar is 2 mm.

Group (inj. volume, needle length)	Histogram diff. (χ^2)	Texture (T)	Depth [mm]
1 (0.1 mL, 5 mm)	0.059 (0.68)	0.056 (0.13)	1.54 (0.38)
2 (0.1 mL, 8 mm)	0.35 (0.80)	0.087 (0.37)	7.74 (0.18)

Table 2: Mean value with CV in parentheses of the histogram difference (χ^2), texture index (T) and injection depth for group 1 and 2. The texture index was calculated from Eq. (2) and the histogram difference was calculated from Eq. (3).

The histogram over the intramuscular volume fraction is shown in Figure 4 (bottom) for the injections performed with the 5 mm needle (blue) and 8 mm needle (red).

Figure 5 shows an example of a 3D rendering of an injection depot, where each voxel were assigned to either dermis (grey), subcutis (yellow) or the muscle (purple). Using the 5 mm needle the injections were placed totally subcutaneously, while for the 8 mm needle 50% of the injections had more than 20% of the injected fluid placed intramuscularly. This is also seen from the injection depth, which was about 5 times higher when using a 8 mm needle compared to a 5 mm needle. The large variations in the injection depth and intramuscular volume fraction for the 8 mm needle showed that the injection depth was not only given by the needle length, but also effected by the structure of the tissue. Using a 8 mm needle the fascia between subcutis and the muscle might be penetrated by the needle tip, and the volume was placed beneath the needle, and not surrounding the needle, as it seemed to be the case for the injections performed with the 5 mm needle.

For the intramuscular volume fraction, texture index and injection depth there was a significant effect of the needle length.

3.3.2. Effect of injected volume

Tabel 3 lists the histogram difference (χ^2), the texture index (T) and the injection depth for the 0.1 mL (group 3-5) and the 1 mL injections (group 6-7) all performed with a 6 mm needle. Large variations was seen in the histograms for all groups, however no statistical significant effect of the individual pigs was observed. The average drug concentration, the texture index and injection depth were significantly effected of the injected volume, but the injection speed did not effect these parameters.

We therefore pooled group 3-4 and group 6-7 in the comparison between the 0.1 mL and 1 mL injection volumes, as these were performed with the same injection speed. This gave fifteen injections in each group.

Figure 6 (top) shows the histogram of the average drug concentration for the 0.1 mL injections (green) and the 1 mL injections (purple). Two of the 0.1 mL injections had a peak at low concentrations (~10%), and for these 60-80% of injected volume was placed intramuscular, shown in Figure 6 (bottom) (green). The three 0.1 mL injections with an intramuscular volume fraction above 30%, were the tissue samples with the smallest subcutaneous thickness. The thickness was about 10% smaller than in the remaining tissue samples, estimated from the 3D reconstructions. The intramuscular volume fraction was not increased when increasing the injected volume, shown in Figure 6 (bottom) (purple).

Three of the 1 mL injections had a peak at an average drug concentration about 80%, one example shown in Figure 7 (A). These injections were all placed in the lower part of the subcutaneous tissue layer, as it was the case for the two injections performed with the 8 mm needle with a high drug concentration. The regions were segmented by learning dictionaries, and the volume fractions in the fascia were 80-90%.

The histogram showed that the remaining injections had distributions similar to the distribution seen for the 0.1 mL injections. Two examples are shown in Figure 7 (B-C). For the injection in (C) a part of the injected volume was placed in the fascia in the subcutaneous fat layer (black arrow). This was not reflected in the histogram (Figure 6 (top)), but observed for nine of the injections. The volume was segmented and the volume fractions placed in the fascia layer were calculated to

Group (inj. speed, volume)	Histogram diff. (χ^2)	Texture (T)	Injection depth [mm]
3 (25 µL/s, 0.1 mL)	0.15 (0.79)	0.10 (0.16)	5.23 (0.21)
4 (100 µL/s, 0.1 mL)	0.096 (1.27)	0.10 (0.16)	5.37 (0.20)
5 (300 µL/s, 0.1 mL)	0.076 (0.67)	0.095 (0.10)	5.54 (0.19)
6 (25 µL/s, 1 mL)	0.18 (0.81)	0.085 (0.22)	7.01 (0.18)
7 (100 µL/s, 1 mL)	0.16 (0.91)	0.087 (0.19)	6.28 (0.14)

Table 3: Mean value with CV in parentheses of the histogram difference (χ^2), texture index (T) and injection depth for injection performed with varying injection speed and volume.

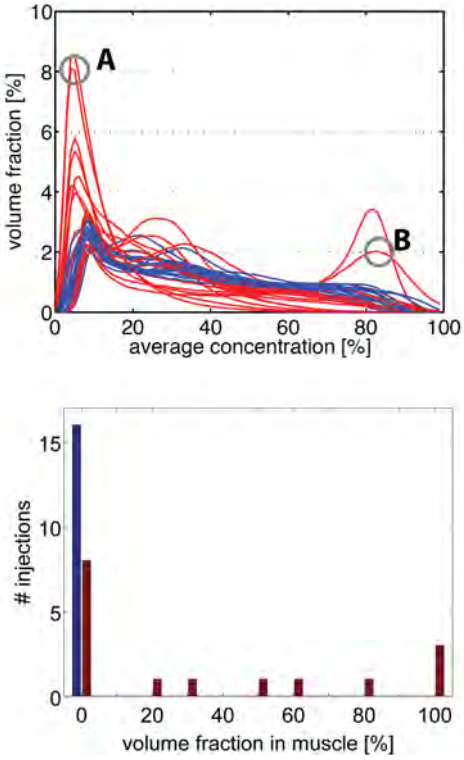

Figure 4: **Top:** Average concentration distribution for injections performed with a 5 mm (blue) and 8 mm needle (red). An intramuscular part of an injection was seen as a peak in the histogram at low average concentrations. One example marked with **A** refer to the injection shown in Figure 3 (A). Two injections had a peak at high concentrations. One example marked with **B** refer to the injection shown in Figure 3 (B). **Bottom:** Histogram of the volume fraction placed intramuscular for the injections using a 5 mm needle (blue) and 8 mm needle (red).

be between 10-50% for these injections. The same was only seen for four of the 0.1 mL injections in group 3-5, and for these injections the volume fraction was between 15-50%.

4. Discussion

The purely subcutaneous injections had a homogeneous distribution with little variation among injections. The variations in the drug distribution were effected mainly by the needle length. The variability in drug distribution seen for

Figure 5: 3D rendering of an injection bolus where the individual voxels are assigned to the dermal layer (grey), subcutis (yellow) or the muscle layer (purple). The boundary between dermis and subcutis and subcutis and the muscle layer is shown as transparent grey surfaces.

the injections performed with the 5 mm needle was related to variations in the tissue structure.

As the injections were performed *ex vivo* no direct link between the inspected depots and the pharmacokinetics could be established. The pharmacokinetic of IAsp were measured for similar injections using a 5 mm needle. CV for $C_{\max}$, the maximum insulin plasma concentration, were measured to be about 45% (n=305) (data not shown). Since the spatial distribution were seen to be similar for these injections, most of the variability in $C_{\max}$ is likely to be related to other factors than the spatial concentration distribution, e.g. differences in the local blood flow, diffusion capacity of the drug and the level of physical activity of the pigs.

The variability in the pharmacokinetics introduced by the partly intramuscular injections were not measured directly, but can be estimated using the semi-mechanistic model proposed by Rasmussen et al. (2013) for insulin aspart. The input parameters for the model were estimated from two independent clinical studies of T1 diabetics (Thorisdottir et al., 2009; Ma et al., 2012), and the intramuscular absorption rate was estimated from data presented by Hildebrandt et al. (1985) to be about 40% higher than from the subcutaneous fat layer. Using these parameters and the intramuscular volume fraction found for the injections performed with the 8 mm needle in this study, CV for $C_{\max}$, was increased by about 15% compared to the

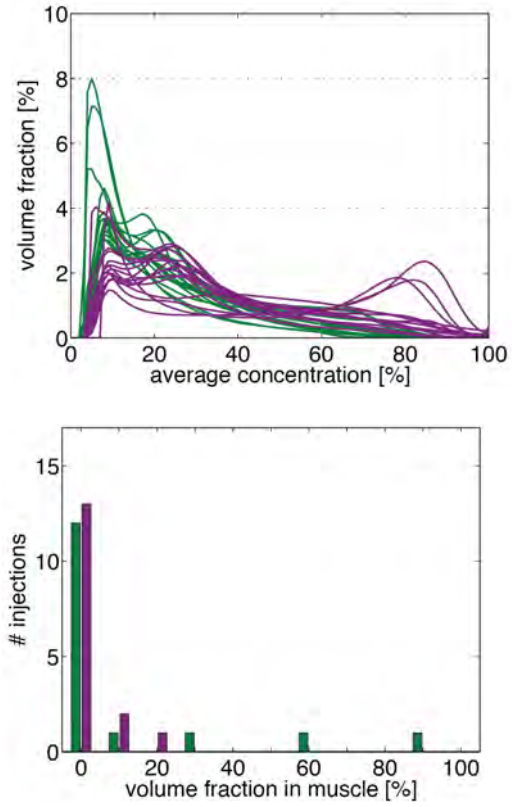

Figure 6: **Top:** Average concentration distribution of the 0.1 mL injections (green) and 1 mL injections (purple). The histogram for the two 0.1 mL injections that were partly intramuscular have a peak at low concentrations.**Bottom:** Histogram of the intramuscular volume fraction for the 0.1 mL injections(green) and 1 mL injections (purple).

purely subcutaneous injections. The overall CV for $C_{\max}$ in the clinical studies (Thorisdottir et al., 2009; Ma et al., 2012), was estimated from data to be about 35%. It means that accidental intramuscular injections can contribute significantly to the overall variability.

The injected volume of 1 mL had similar intramuscular volume fraction as the 0.1 mL injections, but for ten out of the fifteen 1 mL injections a substantial amount of the volume was placed in the fascia layer in the subcutaneous fat layer. To our knowledge it is not known how this will effect the absorption kinetics.

Since we wanted to evaluate how the injection bolus were effected by the injection parameters, the injections were performed right after the pig was put down. If the injections were performed when the pig was still alive, the diffusion and absorption of the drug would take place. Since the pigs were terminated before injection no blood flow and vascular flow were present at the injection time, and this might influence drug distribution.

The Markov Random Field segmentation algorithm and the learning dictionary algorithm have been shown to be very robust also for noisy images. Therefore the presented analysis pipeline can be implemented to *in vivo* μCT-reconstructions, where the image quality is reduced by limitations in the acceptable radiation dose given to the animals (Ford et al., 2003), and the temporal resolution needed, due to the absorption kinetics of the drug. Preclinical μCT scanners have become a standard tool for diagnostics studies of rodents (Bouxsein et al., 2010; Campbell and Sophocleous, 2014). This setup makes it possible to perform the injections *in vivo* and link the initial drug distribution presented by the iodine contrast agent to the pharmacokinetics of the insulin drug.

5. Conclusion

We have quantified the spatial drug distribution of subcutaneous injected soluble insulin in pigs *ex vivo* using μCT, and presented a semi-automatic analysis tool, which makes it possible to analyse several injections and study the variability among equally performed injections. We have shown large variability in the position of the injection bolus in the tissue layers, especially for longer needles (8 mm) and larger injection volumes. We saw no effect of changing the injection speed on the spatial drug distribution. The intramuscular volume fraction was comparable for the small and large volumes, but for larger volumes a higher fraction of the injected drug was placed in the fascia in the subcutaneous fat layer .

The concentration and distribution of the drug is an important model parameter when predicting the action of soluble insulin formulations under *in vivo* conditions. If the injected volume was placed totally in subcutis the average concentration distribution was similar from injection to injection, and therefore only expected to account for a minor part of the variability seen in pre-clinically studies. A proper examination of the injection site (e.g by ultra sound) and well controlled injection parameters can potentially reduce the variability in preclinical studies.

The presented technique can directly implemented for *in vivo* preclinical μCT studies.

6. Acknowledgement

We thank the Imaging Industry Portal at the Technical University of Denmark for access to the tomography instrument. From DTU Compute at the Technical University of Denmark we acknowledge Hildur Einarsdottir, Anders Dahl and Vedrana Andersen Dahl for help with the image segmentation.

7. References

Bouxsein, M. L., Boyd, S. K., Christiansen, B. A., Guldberg, R. E., Jepsen, K. J., Müller, R., 2010. Guidelines for assessment of bone microstructure in rodents using micro–computed tomography. Journal of Bone and Mineral Research 25 (7), 1468–1486.

Brange, J., Ribel, U., Hansen, J., Dodson, G., Hansen, M., Havelund, S., Melberg, S., Norris, F., Norris, K., Snel, L., et al., June 1988. Monomeric insulins obtained by protein engineering and their medical implications. Nature 333.

Campbell, G. M., Sophocleous, A., 2014. Quantitative analysis of bone and soft tissue by micro-computed tomography: applications to ex vivo and in vivo studies. BoneKEy reports 3.

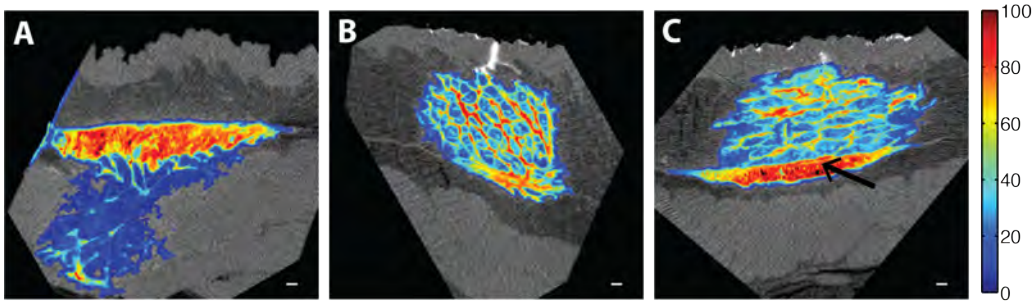

Figure 7: 2D slice of the 3D tomographic reconstruction for three 1 mL injections. The grey scale is proportional to the x-ray attenuation length and the color scale present the drug concentration.

Cengiz, E., Weinzimer, S. A., Sherr, J. L., Tichy, E. M., Carria, L., Cappiello, D., Steffen, A., Tamborlane, W. V., 2014. Faster in and faster out: accelerating insulin absorption and action by insulin infusion site warming. Diabetes technology & therapeutics 16 (1), 20–25.

Chantler, C., 2000. Detailed tabulation of atomic form factors, photoelectric absorption and scattering cross section, and mass attenuation coefficients in the vicinity of absorption edges in the soft x-ray (z= 30-36, z= 60-89, e= 0.1 kev-10 kev), addressing convergence issues of earlier work detailed tabulation of atomic form factors, photoelectric absorption and scattering cross section, and mass attenuation coefficients in the vicinity of absorption edges in the soft x-ray (z= 30-36, z= 60-89, e= 0.1 kev-10 kev), addressing convergence issues of earlier work. Journal of Physical and Chemical Reference Data 29 (4), 597.

Dahl, A. L., Larsen, R., 2011. Learning dictionaries of discriminative image patches. In: 22nd British Machine Vision Conference.

Dencausse, A., Violas, X., Feldman, H., Havard, P., Chambon, C., 1995. Pharmacokinetic profile of iobitridol. Acta radiologica. Supplementum 400, 25–34.

Engwerda, E. E., Tack, C. J., de Galan, B. E., 2013. Needle-free jet injection of rapid-acting insulin improves early postprandial glucose control in patients with diabetes. Diabetes care 36 (11), 3436–3441.

Ford, N., Thornton, M., Holdsworth, D., 2003. Fundamental image quality limits for microcomputed tomography in small animals. Medical physics 30 (11), 2869–2877.

Frid, A., Linde, B., 1992. Intraregional differences in the absorption of unmodified insulin from the abdominal wall. Diabetic medicine 9 (3), 236–239.

Geman, S., Geman, D., 1984. Stochastic relaxation, gibbs distributions, and the bayesian restoration of images. Pattern Analysis and Machine Intelligence, IEEE Transactions on (6), 721–741.

Gin, H., Hanaire-Broutin, H., 2005. Reproducibility and variability in the action of injected insulin. Diabetes & metabolism 31 (1), 7–13.

Guerci, B., Sauvanet, J., 2005. Subcutaneous insulin: pharmacokinetic variability and glycemic variability. Diabetes & metabolism 31 (4), 4S7–4S24.

Gupta, J., Park, S. S., Bondy, B., Felner, E. I., Prausnitz, M. R., 2011. Infusion pressure and pain during microneedle injection into skin of human subjects. Biomaterials 32 (28), 6823–6831.

Hausman, G., Martin, R. J., 1981. Subcutaneous adipose tissue development in yorkshire (lean) and ossabaw (obese) pigs. Journal of animal science 52 (6), 1442–1449.

Heinemann, L., 2002. Variability of insulin absorption and insulin action. Diabetes technology & therapeutics 4 (5), 673–682.

Hildebrandt, P., Sejrsen, P., Nielsen, S., Birch, K., Sestoft, L., 1985. Diffusion and polymerization determines the insulin absorption from subcutaneous tissue in diabetic patients. Scandinavian Journal of Clinical and Laboratory Investigation 45 (8), 685–690.

Hofman, P. L., Derraik, J. G. B., Pinto, T. E., Tregurtha, S., Faherty, A., Peart, J. M., Drury, P. L., Robinson, E., Tehranchi, R., Donsmark, M., et al., 2010. Defining the ideal injection techniques when using 5-mm needles in children and adults. Diabetes Care 33 (9), 1940–1944.

Jockel, J. P. L., Roebrock, P., Shergold, O. A., Huwiler, C., 2013. Insulin depot formation in subcutaneous tissue. Journal of diabetes science and technology 7 (1), 227–237.

Karges, B., Boehm, B., Karges, W., 2005. Early hypoglycaemia after accidental intramuscular injection of insulin glargine. Diabetic Medicine 22 (10), 1444–1445.

Lauritzen, T., Binder, C., Faber, O., 1980. Importance of insulin absorption, subcutaneous blood flow, and residual beta-cell function in insulin therapy. Acta Paediatrica 69, 81–84.

Li, S. Z., 2009. Markov random field modeling in image analysis. Springer.

Ma, Z., Parkner, T., Frystyk, J., Laursen, T., Lauritzen, T., Christiansen, J. S., 2012. A comparison of pharmacokinetics and pharmacodynamics of insulin aspart, biphasic insulin aspart 70, biphasic insulin aspart 50, and human insulin: a randomized, quadruple crossover study. Diabetes technology & therapeutics 14 (7), 589–595.

Mader, J. K., Birngruber, T., Korsatko, S., Deller, S., Köhler, G., Boysen, S., Augustin, T., Mautner, S. I., Sinner, F., Pieber, T. R., et al., 2012. Enhanced absorption of insulin aspart as the result of a dispersed injection strategy tested in a randomized trial in type 1 diabetic patients. Diabetes care.

Ogston-Tuck, S., 2014. Subcutaneous injection technique: an evidence-based approach. Nursing Standard 29 (3), 53–58.

Pfützner, A., Raz, I., Bitton, G., Klonoff, D., Nagar, R., Hermanns, N., Haak, T., 2015. Improved insulin absorption by means of standardized injection site modulation results in a safer and more efficient prandial insulin treatmenta review of the existing clinical data. Journal of diabetes science and technology 9 (1), 116–122.

Polak, M., Beregszaszi, M., Belarbi, N., Benali, K., Hassan, M., Czernichow, P., Tubiana-Rufi, N., 1996. Subcutaneous or intramuscular injections of insulin in children: Are we injecting where we think we are? Diabetes Care 19 (12), 1434–1436.

Rasmussen, C., Røge, R., Ma, Z., Thomsen, M., Thorisdottir, R., Chen, J., Mosekilde, E., Colding-Jørgensen, M., 2013. Insulin aspart pharmacokinetics: an assessment of its variability and underlying mechanisms. European Journal of Pharmaceutical Sciences. Submitted.

Rave, K., Heise, T., Weyer, C., Herrnberger, J., Bender, R., Hirschberger, S., Heinemann, L., 1998. Intramuscular versus subcutaneous injection of soluble and lispro insulin: comparison of metabolic effects in healthy subjects. Diabetic medicine 15 (9), 747–751.

Thomsen, M., Poulsen, M., Bech, M., Velroyen, A., Herzen, J., Beckmann, F., Feidenhans'l, R., Pfeiffer, F., 2012. Visualization of subcutaneous insulin injections by x-ray computed tomography. Phys. Med. Biol. 57, 7191–7203.

Thorisdottir, R. L., Parkner, T., Chen, J.-W., Ejskjær, N., Christiansen, J. S., 2009. A comparison of pharmacokinetics and pharmacodynamics of biphasic insulin aspart 30, 50, 70 and pure insulin aspart: a randomized, quadruple crossover study. Basic & clinical pharmacology & toxicology 104 (3), 216–221.

Vora, J., Burch, A., Peters, J., Owens, D., 1993. Absorption of radiolabeled soluble insulin in type 1 (insulin-dependent) diabetes: Influence of subcutaneous blood flow and anthropometry. Diabetic medicine 10 (8), 736–743.

Zou, W., Hunter, N., Swain, M., 2011. Application of polychromatic μct for mineral density determination. Journal of Dental Research 90 (1), 18–30.

Paper VI

M. Thomsen, M. Strobl, K. Lefmann
Neutron Imaging. Book chapter in *Neutron Scattering: Theory, Instrumentation and Simulation*
(2014) (lecture notes), University of Copenhagen.

Chapter 8

Imaging

Authors:
Maria Thomsen, Niels Bohr Institute, University of Copenhagen
Markus Strobl, European Spallation Source, Lund, Sweden

8.1 Introduction

In neutron imaging the interior structure of a sample is visualised in real space with a resolution of the order 10-100 micrometer, unlike scattering experiments where the information is obtained in reciprocal space and is an average over the sample volume illuminated. Like the scattering techniques, the imaging method is non-destructive and has been used in a wide variety of applications ranging from inspection of objects of preservation interest (*e.g.* cultural heritage) and industrial components to visualization and quantification of interior dynamical processes (*e.g.* water flow in operational fuel cells).

Neutron imaging is in general restricted to take place at large scale facilities. One example is the ICON beamline at SINQ, PSI, where a schematic illustration is shown in Figure 8.1 [64].

One aspect of imaging is radiography. Here, a two-dimensional (2D) map of the transmitted neutrons are obtained at the detector screen, similar to X-ray radiography known from the hospitals. Section 8.2 deals with the instrumentation needed for neutron imaging, including spatial and temporal image resolution and the detector system. Another aspect of imaging is computed tomography (CT), which is well known for X-rays, but also feasible with neutrons. Here, the sample is rotated around an axis perpendicular to the beam direction and radiographic projection images are obtained stepwise from different view angles. These images are combined mathematically to give the three-dimensional (3D) map of the attenuation coefficient in the interior of the sample. This will be explained in detail in section 8.3.

8.1.1 Attenuation

The neutron attenuation can happen either by absorbtion or scattering. The corresponding cross sections are given in Table 2.1 for some elements. In Figure 8.2, we show the attenuation coefficient for all elements as a function of atomic number for thermal neutrons (25 meV), compared to the absorption cross section for X-rays (100 keV). Whereas neutrons interact with the nuclei of matter, X-rays interact with its electrons. With X-rays, the attenuation is higher, the higher the electron density (the higher the atomic number). There is no such regular correlation for the interaction between neutrons and matter, and hence the attenuation coefficients are irregularly distributed independent of the atomic number. In the figure the mass attenuation coefficients are given as μ/ρ, with ρ being the density. The linear attenuation coefficient, μ, has the unit of reciprocal length. The relationship between the attenuation coefficient and the cross section is given by

$$\frac{\mu}{\rho} = \frac{N_a}{M}\sigma \tag{8.1}$$

where N_a is Avogadros number, M is the molar mass, and σ is the total cross section.

It is seen from the figure that the light elements, such as hydrogen and boron, have a very low absorption cross section for X-rays while they strongly scatter (blue) or absorb (red) neutrons. In contrast, many important metals can much easier be penetrated by neutrons than by X-rays (Al, Fe, Sn, and Pb are marked in Figure 8.2 as examples).

Neutron imaging can in many cases be used as a complementary technique to the X-ray radiography. This is illustrated in Figure 8.3, which shows a radiographic image of an analog camera obtained with X-rays (a) and neutrons (b). In the X-ray image the metal parts from the battery are attenuating strongly, but seem totally transparent to neutrons. Neutrons, on the other hand, display strong contrast to image the lighter polymer (plastic) parts containing significant amounts of hydrogen. Because neutrons interact directly with the nuclei, the attenuation coefficient differs even between isotopes (unlike the X-ray attenuation), making is possible to distinguish for example the water types: hydrogen oxide (normal water, H_2O) and deuterium oxide (heavy water, D_2O), because the total cross section for hydrogen is 40 times that of deuterium, see Table 2.1.

8.2 Radiography

We first repeat the result from section 2.1.5 that the neutron flux, Ψ, inside a sample is exponentially damped (the Beer - Lambert law):

$$\Psi(z) = \Psi(0)\exp\left(-\int_0^z \mu(z')dz'\right) \tag{8.2}$$

where z is the depth in the sample and $\mu(z')$ is the total attenuation coefficient at the given position in the sample. The total attenuation is the sum of the

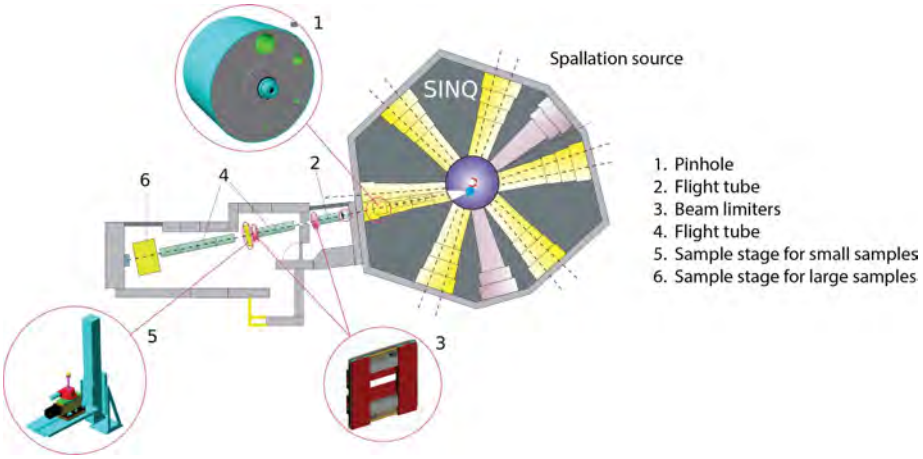

Figure 8.1: Schematic illustration of the ICON beamline at SINQ, PSI. Figure is adapted from [64].

absorption and scattering attenuations.

$$\mu = \mu_a + \mu_s, \tag{8.3}$$

Hydrogen and boron both give a strong attenuation of the neutron beam, but in the case of hydrogen the attenuation is mainly due to scattering, while for boron the attenuation is dominated by absorption, see Figure 8.2. The two processes can not be distinguished in the radiographic images, as only the transmitted neutrons are detected.

The experimental set-up is relatively simple, as it is a basic pinhole geometry due to the limited potential of optics with neutrons. The set-up is illustrated in Figure 8.4. In such a set-up the available flux is strongly coupled with the achievable spatial resolution. Like in many other cases and techniques, increasing resolution directly implies a trade-off in available flux and hence increases the exposure time.

The spatial resolution in an image gives the size of the structures that can be investigated, e.g. how close points in an object can be to each other but still be distinguished. The temporal resolution in a series of radiographic images is related to the acquisition time for a single image and is especially important when considering dynamic processes. Both the temporal and spatial resolution depend on the pinhole size, the collimation length (flight path), and the detector system, to be explained in the following.

8.2.1 Spatial resolution

Currently, the spatial resolution at state-of-the-art instruments is of the order of 100 μm down to 20 μm. The spatial resolution is limited by two factors:

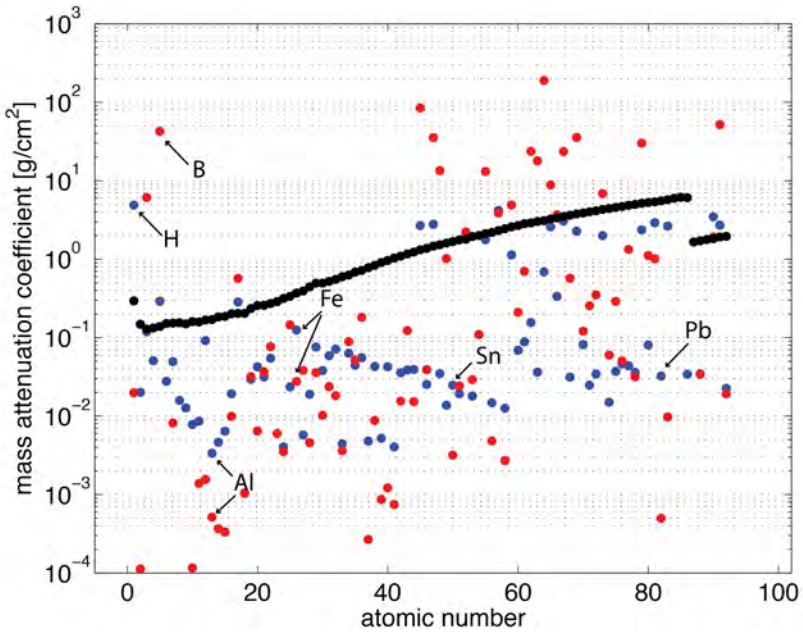

Figure 8.2: Absorption (red) and scattering (blue) coefficients for thermal neutrons with energy 25 meV (2200 m/s), compared to the attenuation coefficient for X-rays with energy 100 keV. Adapted from `http://www.psi.ch/niag/what-is-neutron-imaging`.

- The geometry of the pinhole set-up, including the pinhole size, the pinhole-sample and sample-detector distances.
- The intrinsic detector resolution, i.e. the uncertainty of the determination of the position in the physical and digital detection process.

In the basic pinhole geometry, illustrated in Figure 8.5, the optimum source for imaging is a point source, but at a real beam line, a pinhole with a finite size has to be used. For such a geometry it can easily be derived that for a pinhole with diameter D, the resolution is limited geometrically by the image blur, given by [65]

$$d = D\frac{l}{L}. \tag{8.4}$$

where L and l is the pinhole-sample and sample-detector distance, respectively, defined in Figure 8.5.

The collimation ratio is defined as the ratio between the pinhole-sample distance and the pinhole size, L/D, and is a key parameter for a set-up. The higher the collimation ratio, the better the spatial resolution for a finite sample-

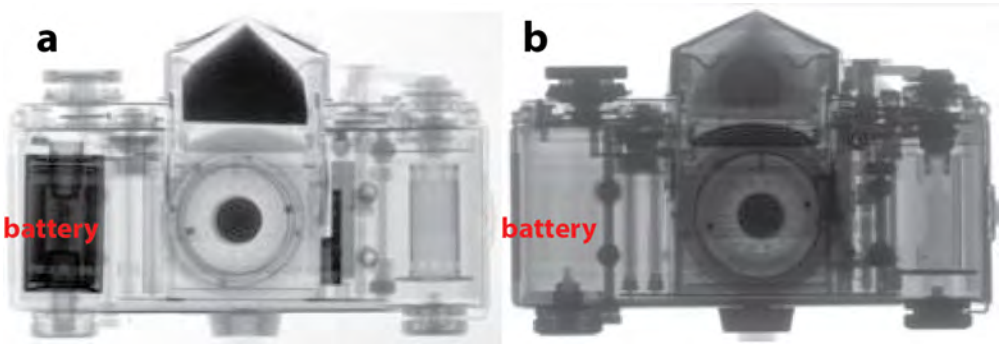

Figure 8.3: Radiography image of a camera obtained with X-rays (a) and neutrons (b). Adapted from `http://www.psi.ch/niag/what-is-neutron-imaging`.

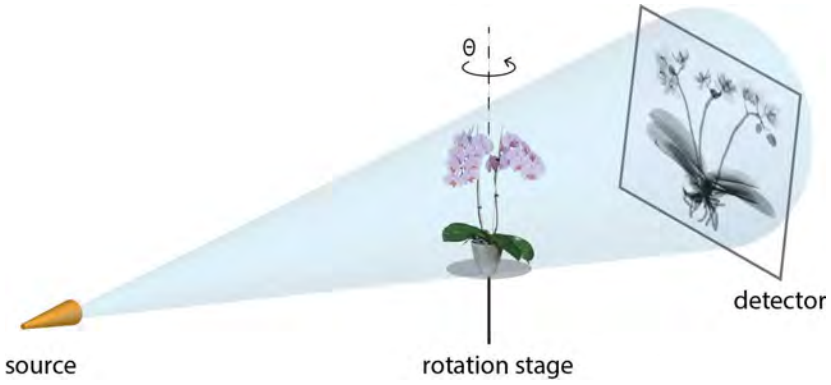

Figure 8.4: Schematic illustration of the experimental set-up for neutron imaging.

detector distance, l. The sample is placed as close as possible to the detector system, in order to achieve high resolution.

The collimation ratio can be increased by decreasing the pinhole diameter or increasing the pinhole-sample distance. Due to the divergence of the beam in the pinhole (of magnitude a few degrees), the beam opens into a cone and the flux decreases as the inverse square of the distance from the pinhole. Therefore, increasing the collimation ratio by a factor of two, either by increasing the distance or decreasing the pinhole diameter, reduces the flux by a factor four.

The second aspect of the spatial resolution is related to the detector system and depends on the size of the pixel elements and the precision in position by with the neutron can be detected. A neutron hitting one pixel element might also be counted in neighbouring pixels, meaning that the spatial resolution often is less than the actual detector pixel size will allow. By definition, the spatial resolution cannot be better than two times the pixel size. The basic principles will be explained in section 8.2.3.

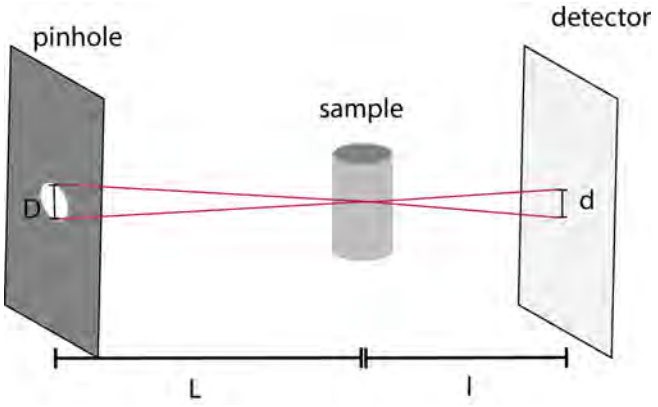

Figure 8.5: Schematic illustration of the geometric resolution (d) and its dependence on the size of the pinhole (D), the source to sample distance (l) and the sample to detector distance (L).

8.2.2 Temporal resolution

The achievable time resolution in kinetic studies depends on the available flux and the detector efficiency. The required exposure time is ruled by the signal-to-noise ratio. The relative image noise decreases when the number of counts in a detector pixel increases. Hence, the signal-to-noise ratio depends on the source flux, the size of the pinhole, the source-detector distance, the exposure time, the attenuation of the sample, the detector efficiency and additional detection noise, e.g. dark current and read out noise. Therefore the best trade off between spatial resolution and the signal-to-noise ratio has to found for each (in particular kinetic) experiment. Other sources of noise are, however, given by e.g. gamma radiation and fast neutrons reaching the detector. These background noise sources are to be avoided as much as possible through instrumentation means like shielding, filters, and avoiding a direct line of sight from the detector to the neutron source.

Neglecting the detector and background noise, it can be assumed that the counting statistics of the detector is Poisson distributed and the signal-to-noise ratio is given by $\sigma(N)/N = 1/\sqrt{N}$, where N is the number of counts in a single detector pixel.

To improve the spatial resolution both the geometric resolution, d, and the effective pixel size must be reduced. Both decrease the counting number in each detector pixel, meaning that the exposure time has to be increased correspondingly to have unchanged signal-to-noise ratio. In the most efficient case the resolution of the detector system matches the geometric resolution of the set-up. The higher the signal-to-noise ratio the better objects with similar attenuation coefficients (and thickness's) can be distinguished in a radiographic image. The neutron flux at most beam lines is of the order $10^6 - 10^8$ neutrons/cm^2/s and with a pixel size of the order 100 μm the number of counts per pixel is $10^3 - 10^6$

neutrons/s.

8.2.3 Detection

As outlined above, the main parameters characterizing an imaging detector are the detection efficiency, the electronic noise and the intrinsic spatial resolution. The most common detectors used for neutron imaging are scintillator screens in conjunction with CCD (charge-couple-device) cameras and flat amorhous-Si detectors[65, 66], but meanwhile also MCP (microchannel plate) based detectors [67]. In the scintillator screen the neutrons are absorbed and visible light is emitted, which can be detected by the CCD. The most commonly used scintillator material is crystalline ^{6}LiF/ZnS:Ag, where the neutrons are converted by the Li-atoms in order to produce light by the ZnS scintillator material [68]. The doping with silver shifts the light emission to be around 450 nm, which is in the range where the CCD is most efficient. The thickness of the scintillator screen is between 0.03 mm and 0.2 mm. The thicker the screen the more neutrons are absorbed, but the spatial resolution decreases correspondingly.

Not all neutrons will be absorbed in a scintillator screen and the CCD chip will suffer from radiation damage if placed directly behind the scintillator screen. Therefore a mirror is placed in an angle of 45° behind the scintillator screen and the light is reflected to the CCD chip. A lens system is placed between the mirror and the CCD in order to record an image of the light from the scintillator on the chip, illustrated in Figure 8.6.

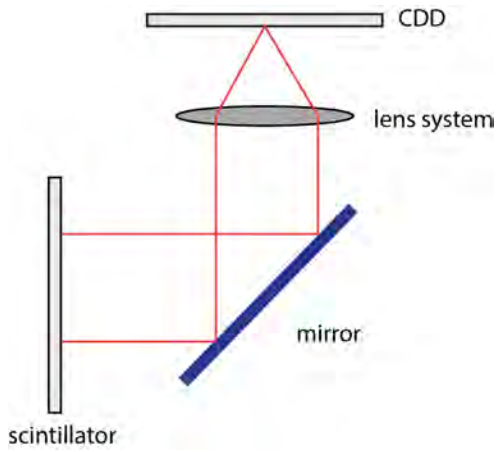

Figure 8.6: Schematic illustration of the scintillator screen coupled to a CCD detector.

Amorphous Si-detectors and MCP detectors can be placed directly in the beam and function without optics. Both the amorhous-Si and the MCP detectors require a converter, typically based on ^{10}B, which has a high absorption cross section for thermal neutrons. The neutrons are captured by ^{10}B to produce

^{7}Li and α-particles. For the Si-detector, the α-particles pass on to the detection layer, a biased silicon layer [69]. For the MCP detector the α-particles and lithium nuclei liberate free secondary electrons into the adjacent evacuated channel, illustrated in an animation (http://www.novascientific.com/neutron.html).

Experimental considerations. In the experimental set-up factors such as electronic noise and inhomogeneities in the detector efficiency and variation in the incident beam intensity both temporally and in time, effects the image quality.

To improve image quality three images are combined to form the final image; a projection image of the sample, a dark-field and a flat-field image. The dark-field image is a image with the beam turned off used to corrected for dark-current in the detector system, meaning counts in the detector not related to the neutron beam. These counts must be subtracted from the projection images. A flat-field image is an image with open beam shutter, but without the sample placed in the beam path. The flat-field image is used to correct for inhomogeneities in the beam profile and in the detector screen. The projections (transmission image) are for each pixel corrected with both the dark-field and the flat-field images.

$$T_\theta = \frac{I_\theta - DF}{FF - DF} \tag{8.5}$$

with I_θ being the original projection image, DF is the dark field image and FF is the flat-field image.

8.3 Computed tomography

Computed tomography (CT) is most commonly know for X-rays in the field of medical imaging, which is extensively used for diagnostics at hospitals. In computed tomography the interior 3D structure is reconstructed from a series of radiographic images obtained from different angles and have successfully been applied for neutrons.

Consider the case of a 2D sample, shown in 8.7(a) with the gray scale representing the interior attenuation coefficient, $\mu(x, y)$. When illuminated by the neutron beam the projection image, $T_\theta(x')$ is given by Eq. (8.5) and shown in 8.7(b). Projections taken from several angles are collected in a *sinogram*, shown in Figure 8.7(c).

The aim of the tomographic reconstruction is to go from the projections back to the function $\mu(x, y)$. The algorithm used for that is called the Filtered Backprojection Algorithm and will be derived in the following sections for a 2D sample and in the case where the beam rays are all parallel. To obtain the 3D reconstruction of the attenuation coefficient, $\mu(x, y, z)$, the projections are measured stepwise in height and the reconstructed 2D slices are stacked to obtain the 3D structure. The derivation given below follows [70].

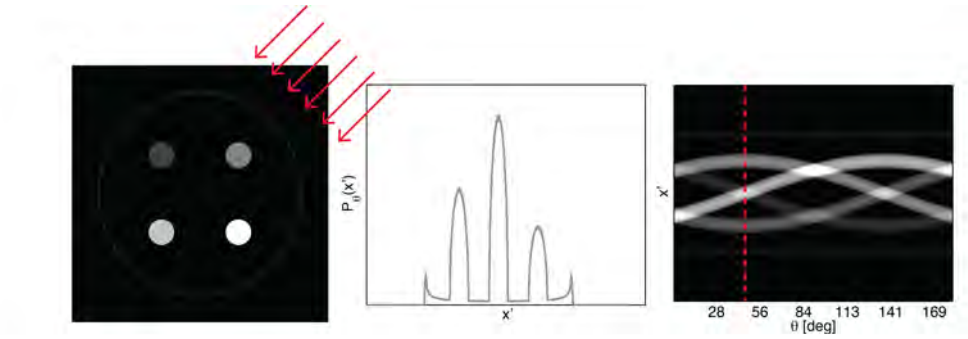

Figure 8.7: 2D object (a) projected from an angle of 45° degrees (b). The beam direction is shown as red arrows. Projections from 128 angles covering 180° collected in a sinogram (c). The red line indicates the projection at 45°.

8.3.1 Tomographic reconstruction

A projection image can be mathematically expressed as an integral of the object function, $f(x, y)$, along the beam path

$$\begin{aligned} P_\theta(x') &= \int_{-\infty}^{\infty} dx \int_{-\infty}^{\infty} dy f(x,y)\delta(x\cos(\theta) + y\sin(\theta) - x') \\ &= \int_{-\infty}^{\infty} f(x', y')dy' \end{aligned} \tag{8.6}$$

where the variables are defined in Figure 8.8 and $\delta(x)$ is the Dirac-delta function. The total projection is obtained by measuring $P_\theta(x')$ for all x'.

The coordinate system (x', y') is the coordinate system (x, y) rotated by the angle θ:

$$\begin{pmatrix} x' \\ y' \end{pmatrix} = \begin{bmatrix} \cos\theta & \sin\theta \\ -\sin\theta & \cos\theta \end{bmatrix} \begin{pmatrix} x \\ y \end{pmatrix} \tag{8.7}$$

The projection, $P_\theta(x')$, is known as the Radon transformation of the function of $f(x, y)$ [71]. In the case of neutron (or X-ray) imaging the object function, $f(x, y) = \mu(x, y)$, the interior attenuation coefficient. For the projection to be the Radon transformation of $\mu(x, y)$ it is seen from Eq. (8.2) that $P_\theta(x') = -\ln(T_\theta(x'))$.

The Fourier Slice Theorem

The Filtered Backprojection Algorithm is based on the Fourier Slice Theorem, which states that: *The Fourier transformation of projection $\tilde{P}_\theta(w)$ is equal to the Fourier transformation of the object, $\tilde{f}(u, v)$, along a line through the origin in the Fourier domain.*

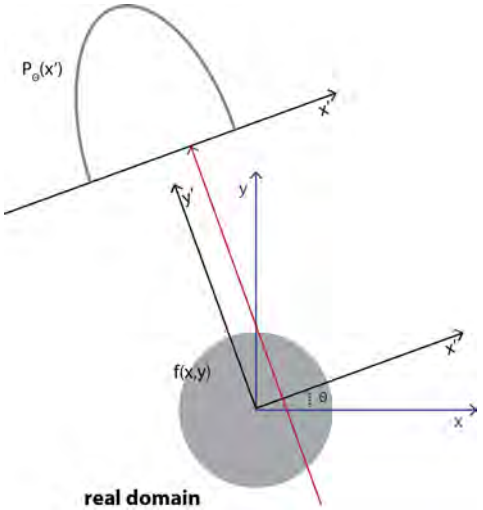

Figure 8.8: Projection, $P_\theta(t)$, of the object $f(x, y)$, along a line parallel to y'.

The theorem is illustrated in Figure 8.9(a), where the Fourier transformation of $P_\theta(x')$ is shown as a grey line in the Fourier domain. The line is rotated an angle θ with respect to the u-axis.

The Fourier Slice Theorem can be proven directly, by taking the Fourier transform of the projection of the object, $P_\theta(x')$ with respect to the spatial frequency w:

$$\begin{aligned}
\tilde{P}_\theta(w) &= \int_{-\infty}^{\infty} dx' P_\theta(x') \exp\left(-i2\pi(x'w)\right) \\
&= \int_{-\infty}^{\infty} dx' \int_{-\infty}^{\infty} dy' f(x', y') \exp\left(-i2\pi(x'w)\right) \\
&= \int_{-\infty}^{\infty} dx \int_{-\infty}^{\infty} dy f(x, y) \exp\left(-i2\pi w(x\cos\theta + y\sin\theta)\right) \\
&= \int_{-\infty}^{\infty} dx \int_{-\infty}^{\infty} dy f(x, y) \exp\left(-i2\pi(xu + yv)\right) \\
&= \tilde{f}(u, v) \qquad (8.8)
\end{aligned}$$

We here identify the spatial frequencies u and v as: $(u, v) = (w\cos\theta, w\sin\theta)$, meaning that

$$\tilde{P}_\theta(w) = \tilde{f}(w\cos\theta, w\sin\theta) \qquad (8.9)$$

8.3.2 Filtered Backprojection Algorithm

Before going into the mathematical derivation of the Filtered Backprojection Algorithm the main idea will be summarized.

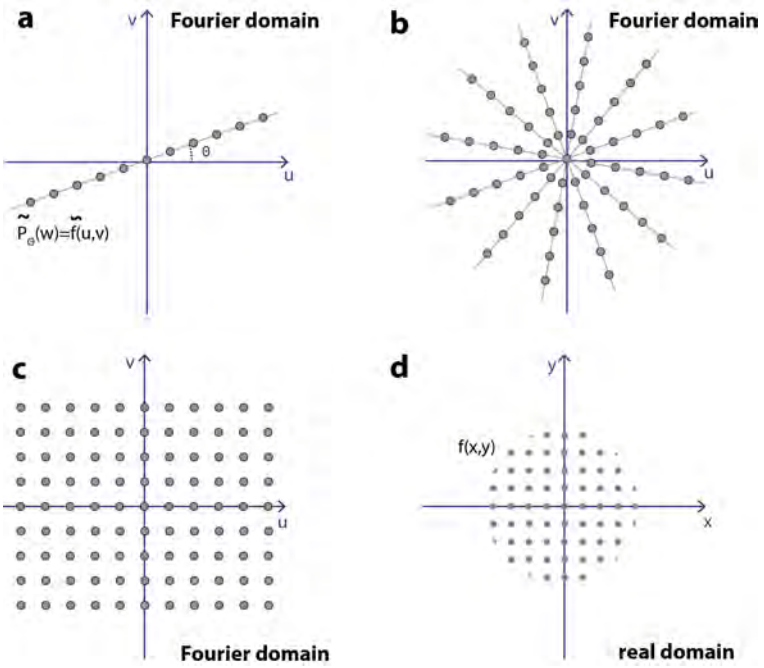

Figure 8.9: a) The Fourier transformation of the projection, $\tilde{P}_\theta(w)$ equals the Fourier transformation of the object, $\tilde{f}(u,v)$, along a single line in Fourier domain. **b)** Measuring $P_\theta(t)$ for different angles gives $\tilde{f}(u,v)$ in a number of lines in the Fourier domain. **c)** Interpolation of $\tilde{f}(u,v)$ in the parts of the Fourier domain not covered by the projection measurement. **d)** Inverse Fourier transformation to recover the object function.

Having obtained the projection from several angles, the Fourier transform of the object is known along several lines in the Fourier domain, shown in Figure 8.9(b). In order to calculate the object function by taking the inverse Fourier transformation, the Fourier transformation must be known regularly in the whole Fourier domain, as shown in Figure 8.9(c).

For this to be the case the Fourier transformation of each projection should form a pie shape in the Fourier domain, as shown in Figure 8.10(a). However, the Fourier Slice Theorem says that the Fourier Transformation is only known along a line, as illustrated in Figure 8.10(b). To approximate the ideal situation in Figure 8.10(a) a filter of the form $|w|$ is applied to $\tilde{f}(u,v)$ before taking the inverse Fourier transform, shown in Figure 8.10(c). From the mathematical derivation it is seen that the filter appears as the Jacobian determinant when changing from Cartesian to polar coordinates in the Fourier Domain.

The mathematical derivation of the algorithm goes backwards and starts by

Figure 8.10: Schematic illustration of the Fourier transformation of the projections. **a)** The ideal case where the data covers a pie shape in Fourier domain and the object can be obtained by taking the inverse Fourier transform. **b)** Fourier transformation of a measured projection. **c)** In the Filtered Backprojection Algorithm a filter is applied to the data in (b) to approximate the situation in (a).

taking the inverse Fourier Transform of $\tilde{f}(u, v)$.

$$f(x,y) = \int_{-\infty}^{\infty} du \int_{-\infty}^{\infty} dv \tilde{f}(u,v) \exp\left(i2\pi(xu+yv)\right) \tag{8.10}$$

$$= \int_{0}^{2\pi} d\theta \int_{0}^{\infty} dw w \tilde{f}(w,\theta) \exp\left(i2\pi w(x\cos\theta + y\sin\theta)\right) \tag{8.11}$$

$$= \int_{0}^{\pi} d\theta \int_{-\infty}^{\infty} dw |w| \tilde{f}(w,\theta) \exp\left(i2\pi w(x\cos\theta + y\sin\theta)\right) \tag{8.12}$$

where the coordinate transformation from (u, v) to (w, θ) have introduced the Jacobian determinant, w. Note that the integration limits are changed from step 2 to 3, due to the periodic properties of the Fourier Transform, which gives the filter $|w|$.

$$\tilde{f}(w, \theta + \pi) = \tilde{f}(-w, \theta) \tag{8.13}$$

Substituting in the projection, using the Fourier Slice Theorem gives that

$$f(x,y) = \int_{0}^{\pi} d\theta \int_{-\infty}^{\infty} dw |w| \tilde{P}_\theta(w) \exp\left(i2\pi w x'\right) \tag{8.14}$$

The Fourier transform of the projection, $\tilde{P}_\theta(w)$ is filtered by $|w|$, before taking the inverse Fourier transform and backprojected by integrate over all angles in the real domain. Therefore the name Filtered Backprojection. The filter $|w|$ is called the Ram-Lak filter, but for some applications other filters is used in order to reduce noise in the reconstructed images [70].

To use this formula, the projection must be known continuously for the angle θ in the interval $[0, \pi]$ and in space x' in the interval $[-\infty, \infty]$. In practice the projections are measured in discrete points corresponding the pixel size of the detector and for a finite number of angle steps. Therefore the integrals in Eq. (8.14) are replaced by sums, illustrated by the point in Figure 8.9.

In summary, the Filtered Backprojection Algorithm goes in the following steps:

- Collect the projections $P_\theta(x')$ from a number of angle steps and number of points.

- Calculate the (discrete) Fourier Transformation, $\tilde{P}_\theta(w)$ of each projection, Figure 8.9(a-b)
- Apply the filter $|w|$ in Fourier domain, to approximate the ideal case where the measured points are equally distributed in Fourier space, Figure 8.9(c).
- Take the inverse Fourier Transformation of the filtered projection $|w|\tilde{P}_\theta(w)$ and make a sum over all angles to make the reconstruction, Figure 8.9(d).

Figure 8.11 shows the reconstruction of a 2D object, using 4 (a), 8 (b), 32 (c) and 128 projections (d) over 180°. It is seen how the reconstruction algorithm smear the projection images back on the image plane and that the reconstruction is improved when using more projections.

To speed up the measurements a cone beam instead of a parallel beam is used in practice, illustrated in Figure 8.4. The change in beam geometry effects the reconstruction algorithm in Eq. (8.14), since the path of the beam is changed, but the basic principle is the same. The derivation can be found in [70]. For most neutron imaging set-ups the distance between be pinhole and the detector is so large that for practical implementation the beam can be considered parallel.

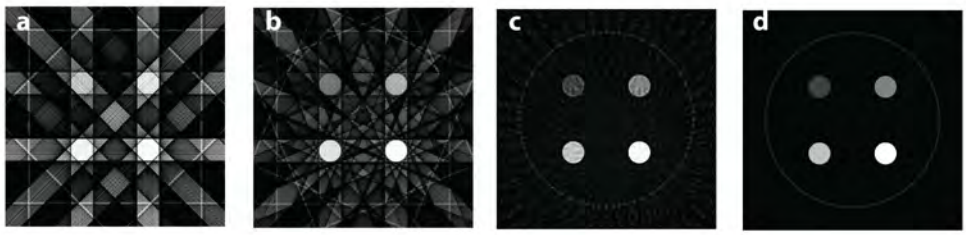

Figure 8.11: Reconstruction of the 2D object shown in Figure 8.7(a) using 4, 8, 32 and 128 projections (a-d) over 180 degrees.

8.4 Applications of neutron imaging

A particular strength of neutron imaging is the sensitivity to hydrogen, combined with the ability to penetrate bulk metal parts. Therefore water, plastic, glues, hydrogen, and organic materials can be detected in even small amount and in dense materials. This section presents examples, where neutron imaging gives novel insight.

8.4.1 Water transport in fuel cells

Fuel cells operate by converting a fuel into electrical power via a chemical reaction. One type of fuel cells is the hydrogen-oxygen proton exchange membrane fuel cell (PEMFCs), where hydrogen is used as the fuel and reacts with oxygen

to form water. A schematic presentation of a PEMFC is shown in Figure 8.12 [72]. The water must be removed through flow channels for the fuel cell to work properly and if water is not formed in an area of the fuel cell it indicates a defective area. The metallic shell of the fuel cell is almost transparent to neutrons and the interior water content can be quantified due to the high scattering cross section of hydrogen. Therefore the dynamics of the water can be quantified in a unmodified and full functional fuel cell (*in situ*) by neutron radiography or tomography [73].

To follow the dynamics, good temporal resolution is required, as the exposure time for each projection image is limited by the time scale of the transport process. The time resolution for neutron radiography is of the order of seconds, which is well suited for these processes [74]. The difference in the attenuation coefficient of water (H_2O) and heavy water (D_2O), makes it possible not only to study the water accumulation, but also the water exchange in operational fuel cells by neutron radiography, demonstrated by [75]. Switching from hydrogen to deuterium gas, the deuterium gas is reduced to D_2O in the catalyst layer and gradually replaced water, seen in the radiographic images as a decrease in neutron attenuation. Thereby the exchange time can be measured by measuring the change in image intensity, shown in Figure 8.13(left).

The radiographic images are normalized to the dry fuel, such that only the water content is seen and the color scale displays the local water thickness. At time $t = 0$ the fuel cell is saturated and the H_2 feed gas is exchange with the D_2 gas. After 24.75 min (Figure 8.13 (left)(d)) nearly all the water has been replace by heavy water, and the gas feed in again switched back to H_2. The neutron beam attenuation increases, seen in Figure 8.13 (left)(e)-(f). The amount of water is calculated from the attenuation in the red marked area in Figure 8.13 (left)(a) for about the first 10 sec, shown in Figure 8.13 (right). This show that neutron radiography can be used not only to visualize but also quantify the flow process *in situ*.

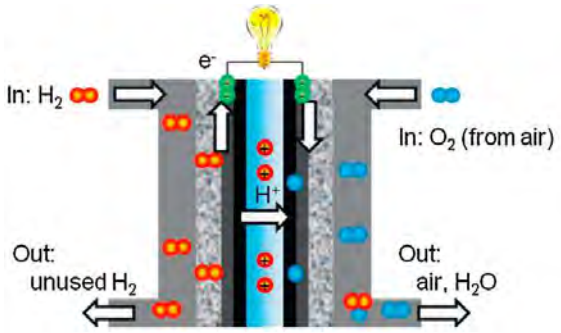

Figure 8.12: Schematic illustration of a PEMFC. Figure is adapted from [72].

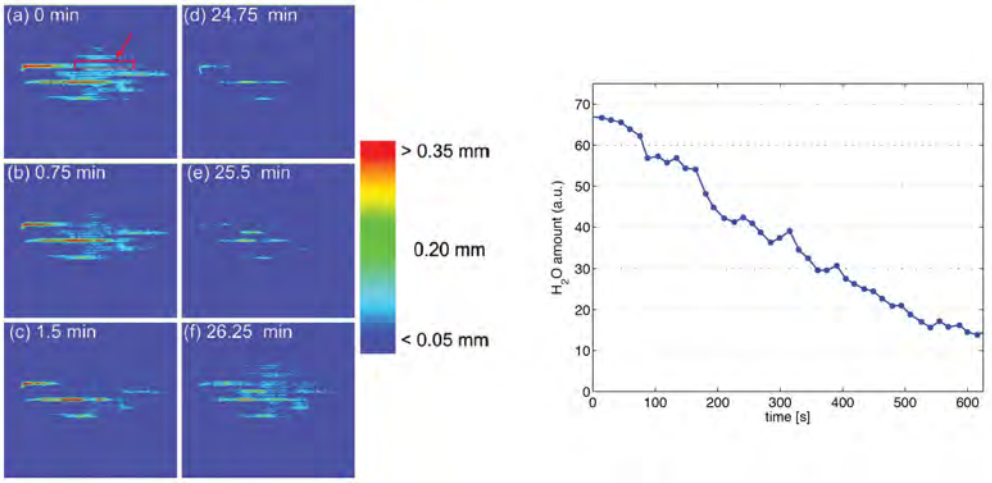

Figure 8.13: Left: Radiographic neutron images normalized to the dry fuel cell. Color scale display the water thickness. Figures are adapted from [75]. **Right:** Change in the water thickness in area marked by the red box in (a) after switching the gas feed from H_2 to D_2. Data is digitalized from [75].

8.4.2 Water uptake in plants

The difference in the attenuation coefficient of light and heavy water also makes it possible to study the water uptake in plants [76, 77, 78]. Figure 8.14(left)**a** shows a neutron radiographic image of roots in soil. The surface is irrigated with 3 mL of D_2O and radiographic images are obtained 15 min, 30 min, 6 h and 12 h after irrigation, shown at Figure 8.14 (left)**b-e**. The images are normalized to the original images, meaning that in the white areas H_2O has been replaced by D_2O. The soil to the left becomes wet and the roots takes up water (WR). The soil to the right side remains dry (S) for the whole experiment, but water is transported to the roots (DR). The relative change in neutron transmission makes it possible to compare the water uptake in the different areas of the roots, Figure 8.14 (right). The water uptake by the roots placed in the moist soil is significant higher, than in the dry soil. After 6-12 h it is seen that water is transported to the stem, Figure 8.14 (left)**d-e**.

8.4.3 Cultural heritage

Imaging of cultural heritage ranges from archaeological objections to pieces of art. Here, the preserving interest is important and non-destructive testing techniques are required. Therefore, neutron tomography is a well-suited technique.

El violinista (1920) is a sculpture by the Catalan artist Pablo Gargallo. The sculpture is composed of the wooden core on which thin sheets of lead is fixed by needles and soldering. Figure 8.15 shows a photography of the sculpture (a)

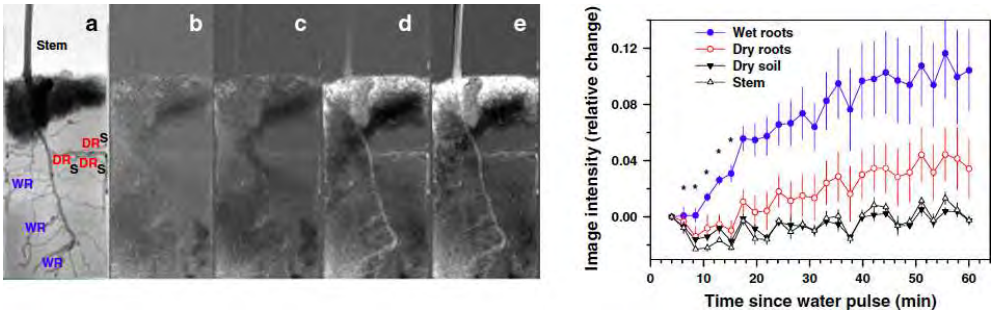

Figure 8.14: Left: (**a**) Roots system from Zea mays, prior to exposure of 3 mL of D_2O to the surface. (**b-e**) The same plant 0.25, 0.5, 6 and 12 h after the surface has been irrigated with D_2O. The images are divided by the initial image (a). Light areas represent displacement of H_2O with D_O. **Right:** Relative change in image intensity for roots placed in moist soil (WR), dry soil (DR) and the dry soil (S). The figures are adapted from [76].

and the 3D rendering of the tomographic reconstruction, showing the wooden core (b). The sculpture shows signs of corrosion, which is most likely due to organic vapours from the wood. This can be visualized by neutron tomography, due to the hydrogen sensitivity, shown as red areas in Figure 8.15(c).

Figure 8.15: The lead and wood sculpture *El violinista* (1920) (a). 3D rendering of the wood core (b) and map of the areas (c) effected by corrosion (red) and needle fixations (blue) obtained by neutron tomography. Figure adopted from [79].

An other example is a Buddhist bronze statue. Figure 8.16 (top row) shows a photograph (left) and neutron radiography image (right) of a 15th century Bodhisattva Avaloktesvara [79]. The objects placed inside the statue can be investigated closely by neutron tomography without effecting the statue, shown in Figure 8.16 (bottom raw). Three objects are identified. A small heart-shaped capsuled (turquoise) wrapped in a piece of close is placed in the chest of the statue. A scroll (brown) probably containing a religious text, and a pouch

(violet) containing some spherical objects and tied up with string.

Figure 8.16: Top: Photography (a) and neutron radiography image (b) of a Buddhist bronze statue. **Bottom**. 3D rendering obtained by neutron tomography. (a) shows a virtual cut through the sculpture. (b) and (c) show the segmentation of three discernable objects; a small wrapped capsule (turquoise), a scroll (brown) and a pouch (violet) containing some spherical objects (green, grey, yellow) and tied up with string (red). Figure adopted from [79].